Structure-borne sound transmission between isotropic, homogeneous plates and periodic ribbed plates

Thesis submitted in accordance with the requirements of the University of Liverpool for the degree of Doctor of Philosophy

by

Jianfei Yin

November 2012

Abstract

The prediction of sound and vibration transmission in built-up structures is important for human comfort, health and safety. For structural reasons, engineering structures often incorporate periodic ribbed plates to increase stiffness and stability whilst reducing the weight. However, vibration propagation on periodic ribbed plates is complex due to the existence of stop/pass bands. This thesis is concerned with predicting vibration transmission between isotropic, homogeneous plates and periodic ribbed plates. The objectives are to investigate the use of Statistical Energy Analysis (SEA) and develop and validate advanced SEA (ASEA) using ray tracing to incorporate tunnelling mechanisms.

Two approaches were considered for modelling the periodic ribbed plate: either representing it as a single subsystem or representing each bay as a single subsystem in the high-frequency range (above the fundamental local mode of the bay). In the low-frequency range (below the fundamental local mode of the bay) Finite Element Methods (FEM) and laboratory experiments show that the periodic ribbed plate can be adequately modelled in SEA using wave approaches from periodic structure and orthotropic plate theories. In the high-frequency range a significant decrease in energy along successive bays was identified using FEM leading to the conclusion that it is not appropriate to model a periodic plate as a single subsystem. SEA models were therefore investigated that treated each bay as an individual subsystem using wave theory. For different L-junctions formed from an isotropic, homogeneous plate and a periodic ribbed plate, SEA significantly underestimated the response in the bays. Experimental SEA (ESEA) was used to investigate these discrepancies which confirmed the existence of tunnelling mechanisms between physically unconnected subsystems. In contrast to SEA which gave errors up to 60 dB for the furthest bay from the junction, ASEA gave errors less than 6 dB when the mode count for the bay was greater than five.

A range of two- and three- plate structures with different periodic ribbed plates or periodic folded plate have been modelled with ASEA. The results all lead to the conclusion that ASEA can successfully incorporate tunnelling mechanisms and provide a significantly more accurate approach to predicting high-frequency vibration transmission across periodic ribbed plates than SEA.

Acknowledgements

I would like to express my sincere thanks to my supervisor, Dr. Carl Hopkins, for his guidance, help and encouragement throughout the duration of my study at the Acoustics Research Unit. He has made these past four years an enjoyable and valuable learning experience for me, both academically and personally.

I would like to thank Dr. Gary Seiffert for his help and advice in the preparation for my experiments and his unfailing support throughout my study. My thanks also go to Prof. Barry Gibbs whose guidance and encouragement are much appreciated and will not be forgotten. I would like to extend my thanks to all the staff in the ARU, Prof. David Oldham and Dr. Chris Egan for their advice on my research work.

To my friends and colleagues at the Acoustics Research Unit, their generous help and support are deeply appreciated. In particular, I would like to thank Matthew and Christoph for helping me with the experiments and David for many useful and valuable discussions on my research topic.

I would also like to thank my teachers and friends in the National University of Defence Technology in Changsha, China. In particular, I'm grateful to Professor Xisen Wen and Professor Jihong Wen for offering me the great opportunity to pursue my PhD abroad and for their constant support and encouragement during my time in the UK. I would also like express my gratitude to Dr. Xiaoyun Han for his help with my work during his visit to ARU. His help greatly accelerated my work and it is very much appreciated. I would also like to thank Dr. Dianlong Yu for his help and support on many matters for the past four years. My thanks also extend to all my friends in NUDT, in particular, to Yong Xiao and Linmei Lv.

I'm also grateful for the funding provided by the China Scholarship Council, the Acoustics Research Unit at the University of Liverpool and the National University of Defense Technology.

Last but not least, I would like to thank my parents for their love, support, understanding and always being there for me unconditionally.

Contents

List of symbols

A	Energy transfer matrix from available to available energy
B	Bending stiffness or flexural rigidity (N·m) or frequency bandwidth (Hz)
B	Energy transfer matrix from available to unavailable energy
$D(\theta)$	Weighting function for probability of wave propagation angle θ
D_E	Energy level difference (dB)
E	Young's modulus ($N \cdot m^{-2}$)
E'	Equivalent Young's modulus ($N \cdot m^{-2}$)
E_i	Energy of subsystem i (J)
E_{ij}	Energy of subsystem i where the source subsystem is j (J)
F	Force, shear force (N)
G	Shear modulus ($N \cdot m^{-2}$)
H	Loss factor matrix or geometric mean of the bending stiffness for orthotropic plates
I	Energy intensity (Watt/m) or moment of inertia of the beam
J	Torsional constant (m^4)
L	Length (m)
M	Bending moment (N·m) or Modal overlap factor or diagonal modal overlap factor matrix
M_{av}	Geometric mean of the modal overlap factor
N	Mode count
P	Available power input matrix
Q	Unavailable power input matrix
S	Surface area (m^2)
T	Reverberation time (s)
TOB	One-third octave band

U	Perimeter of the surface
W	Power (watt)
Y	Mobility ($m \cdot N^{-1} \cdot s^{-1}$)
Z	Impedance ($N \cdot s/m$)
b_b	Beam width (m)
c_B	Bending phase speed (m/s)
c_g	Group speed (m/s)
c_L	Longitudinal wave speed (m/s)
d_{mfp}	Mean free path (m)
$\mathbf{d}$	'Unavailable' modal energy or column vector of modal energies (watt·Hz or watt·rad/s)
e	Modal energy (watt·Hz)
$\mathbf{e}$	Column vector of modal energies (watt·Hz)
e_{mesh}	Mesh error (%)
f	Frequency (Hz)
f_c	Band centre frequency
h_p	Plate thickness (m)
i	$\sqrt{-1}$
k	Wavenumber (rad/m)
m	Mass (kg)
n	Modal density ($mode \cdot Hz^{-1}$)
r_{rd}	Distance at which direct field equals reverberant field (m)
s	Standard deviation
t	Time (s)
$t_{v,0.975}$	Student t-distribution for 95% confidence interval with a degree of freedom of v
v	Velocity (m/s)

α	Receptance (m/N or Rad·N^{-1} m^{-1} for rotational receptance)
γ	Reflection coefficient
ε	Energy density over plate surface (J/ m^2) or strain
ζ	Fraction of critical damping
η_{ij}	Coupling loss factor from subsystem *i* to subsystem *j*
η_{ii}	Internal loss factor of subsystem *i*
η_i	Total loss factor of subsystem *i*
θ	Wave heading angle or incident wave angle (rad)
κ	Distance parameter (m)
λ	Propagation constant
μ	Poisson's ratio
ξ	Lateral displacement (m)
π	3.1415926…
ρ	Mass density (kg/m^3)
ρ_s	Surface density or mass per unit area (kg/m^2)
σ	Stress (N·m^{-2})
τ	Transmission coefficient
ψ	Mode shape
ω	Angular frequency (rad·s^{-1})
ϕ	Characteristic beam function
Θ	Range of wave angles
Re{}	Real part of a complex value
Im{}	Imaginary part of a complex value
∇^4	Differential factor $\partial^4/\partial x^4 + 2\partial^4/(\partial x^2 \partial y^2) + \partial^4/\partial y^4$
*	Complex conjugate

$< >_{sa}$ Spatial average

$\rightarrow$ Vector

Subscripts:

B, L, T	Bending (B), quasi-longitudinal (L), transverse shear waves (T)
b	Beam
dp	Driving-point
equiv	Equivalent value
inc	Incident wave
in-plane	In-plane waves
mfp	Mean free path
nf	Nearfield
p	Plate
reflect	Reflected wave
trans	Transmitted wave
x, *y*, *z*	*x*, *y*, *z* directions

List of figures

List of tables

1 Introduction

1.1 Background and motivation

The ability to predict sound and vibration transmission in built-up structures such as buildings, ships, trains and automobiles is important for human comfort, health and safety. It is also the result of stringent legislation introduced in many countries by specifying a maximum allowable sound pressure level or vibration level to provide a safe and comfortable environment (for example, see [1] for ship noise legislation, [2, 3] for automobile industries and [4] for building design). In addition, for existing structures with high levels of sound and vibration, an understanding of the transmission mechanisms is needed to make effective noise or vibration control decisions.

For structural reasons, engineering structures often incorporate periodic ribbed plates to increase the strength, static stiffness and stability whilst reducing the weight. In terms of vibration propagation on periodic ribbed plates, they often exhibit a stop/pass band feature where in certain frequency bands (stop bands) waves cannot propagate and will attenuate exponentially and in other frequency bands (pass bands) waves can propagate freely [5]. To-date there has been limited focus on the wave transmission in built-up structures when periodic ribbed plates are incorporated. Therefore, the primary motivation for this thesis is to predict sound and vibration transmission in built-up structures that comprise both isotropic, homogeneous plates and periodic ribbed plates. The research in this thesis is purely on vibration transmission.

In engineering fields, two approaches are generally used for predicting vibration transmission in built-up structures; either deterministic or statistical methods. The most common deterministic approach is the Finite Element Method (FEM) [6]. At low frequencies (large wavelengths), FEM can provide quick, efficient calculations of the structural response. However at high frequencies (small wavelengths), deterministic models can be impractical due to the high computational cost and the fact that the uncertainty in describing the physical properties of the structure meaning that it is not possible to accurately predict the response at any one point on the structure. For this reason, statistical approaches

are used at high frequencies, such as Statistical Energy Analysis (SEA) [7]. SEA predicts the spatial-average energies on subsystems that represent cavities, beams or plates. Calculation of the energy flow between subsystems requires determination of statistical parameters such as coupling loss factor. Although, experimental techniques either from physical or numerical experiments are studied to obtain this parameter (for example, Bies and Hamid [8] and Hopkins [9]), theoretical models based on a wave approach are most commonly used to determine coupling loss factors.

Theoretical analysis using a wave approach is often applied to structures formed from simple and continuous elements such as plates, shells or beams. However, wave theory is well-suited to modelling sound and vibration transmission across isolated junctions rather than large built-up structures which incorporate periodic ribbed plates.

Combining the wave approach and Bloch theory, Tso and Hansen [10] considered an L-junction comprised of a periodic ribbed plate and an isotropic homogeneous plate. This allowed them to model the periodic ribbed plate as a single subsystem whilst incorporating stop/pass band feature of the periodic structure. This thesis will reconsider the validity of using such an approach at high frequencies through comparison with FEM and measurements.

Langley [11] proposed Wave Intensity Analysis (WIA) for high frequency vibration problems where SEA was significantly in error due to the absence of diffuse fields. In WIA, the directional wave intensity is represented by a Fourier series, and the order of the Fourier series is calculated from the associated power balance equation. For the first order of Fourier series, WIA is equivalent to SEA. For coupled subsystems where there is a spatial wave filtering effect at the interface of the subsystem, SEA can significantly underestimate the energy transmission across the subsystems. WIA is able to take into account spatial filtering and in situations where the subsystems do not have diffuse fields, provides considerable improvement to SEA.

It has been proposed that the inadequacies of SEA could be overcome by using indirect coupling loss factors between physically unconnected subsystems. Langley and Bercin [12] proposed that WIA can also be cast into the form of SEA

with the addition of indirect coupling loss factors. The existence and importance of indirect coupling loss factors has also been discussed by Mace [13], Blakemore *et al*. [14, 15] etc. This topic is considered in a more detailed review of the literature in section 2.4.1.

Heron [16] proposed that indirect coupling loss factors (referred to as a tunnelling mechanism) could be incorporated by using ray tracing in an advanced form of SEA (ASEA). Heron validated ASEA using an in-line array of beams and made a proposal for its extension to plate systems. However, the latter was not implemented and validated and no published literature using ASEA for plate systems has been found. In addition, neither ASEA nor WIA has previously been considered for periodic ribbed plates. Hence in this thesis, ASEA is implemented to assess its potential to incorporate indirect coupling in structures formed from isotropic, homogeneous plates and periodic ribbed plates.

1.2 Objectives

This thesis is concerned with the prediction of vibration transmission between isotropic, homogeneous plates and periodic ribbed plates. The main objectives are to develop and validate a methodology using SEA or ASEA for the analysis of isolated plate junctions and to incorporate this approach in the modelling of larger built-up structures. The validation will initially be carried out using FEM, and then confirmed with physical experiments. Two distinct frequency ranges will be considered for the periodic ribbed plate: a low-frequency range where the plate can be modelled as a single subsystem (either as an orthotropic plate or incorporating periodic theory) and a high-frequency range where each bay on the ribbed plate can be modelled as a subsystem in an SEA or ASEA model.

1.3 Chapter layout

The layout of the chapters in this thesis is as follows.

Chapters 2, 3, 4 and 5 predominantly describe the theory that is used in the thesis.

Chapter 2 reviews the prediction of structure-borne sound transmission using statistical approaches based upon statistical energy analysis. This includes experimental statistical energy analysis which is used with the output from finite element models to determine structural coupling parameters. This chapter describes an advanced from of statistical energy analysis (ASEA) which is used in this thesis to incorporate tunnelling mechanisms.

Chapter 3 discusses the vibration field on isotropic and orthotropic plates for bending and in-plane waves.

Chapter 4 focuses on descriptions of vibration propagation on periodic ribbed plates of infinite extent. It investigates the role of pass and stop bands on periodic ribbed plates which are further explored in terms of the natural frequencies of the bays formed between the ribs using receptance method. The analysis in this chapter is needed to calculate coupling loss factors for SEA models which treat the periodic ribbed plate as a single subsystem.

Chapter 5 presents theoretical models for wave transmission between coupled plates across structural junctions considering bending only models and bending and in-plane wave models.

Chapter 6 applies SEA, ESEA and ASEA with the main aim of predicting vibration transmission through L-junctions comprising an isotropic, homogeneous plate and a periodic ribbed plate. In this chapter, these models are validated against numerical experiments with FEM.

Chapter 7 contains the validation of SEA, ESEA and ASEA using physical experiments on L-junctions in the laboratory.

Chapter 8 applies ASEA to other L-junctions with different damping and different periodic features to further prove the validity of ASEA. It also investigates the validity of using ASEA on larger structures that incorporate these L-junctions.

Chapter 9 contains the conclusions and considers future work.

The novelty and originality in this thesis stems from demonstrating that indirect coupling is important for structure-borne sound transmission at high frequencies involving individual bays on a periodic plate when each bay supports local modes. The thesis shows that the assumption that the periodic ribbed plate can be treated as a single subsystem in SEA at high frequencies can be invalid due to a significant decrease in vibration across the ribs. To model this behaviour, ASEA has been implemented as described by Heron [16] and adapted to ribbed plates with long narrow bays in order to incorporate tunnelling mechanisms. ASEA has subsequently been validated using both FEM and laboratory experiments.

2 Statistical and numerical models for structure-borne sound transmission: SEA, ESEA, ASEA and FEM

2.1 Introduction

In engineering, numerical methods such as Finite Element Method (FEM) are often used to predict the modal response of complex structures. However, the large size of the models and expense in computation resources often limit the accurate prediction to relatively low frequencies with large wavelength. For small wavelengths at high frequencies, uncertainties arise in FEM due to the high sensitivity of mode shapes and modal resonant frequencies to small variations of the geometry. Similarly, numerical methods are known to be rather inaccurate with high order of modes, even for idealized models [17].

Due to uncertainties and large computational expense using FEM at high frequencies, statistical methods such as Statistical Energy Analysis (SEA) are developed to calculate the response of the systems using statistical modal parameters. As a result, a large structure is divided into subsystems which are expressed using statistical modal parameters, and then responses of the system are calculated in terms of total time-average distribution of energy among subsystems rather than exact displacements or forces. The average response of subsystems using SEA is more reliable than the numerical prediction since it eliminates the effects of small variations of the structure. This is extremely useful at the design stage where the details of the structures are not available to engineers. Since the development of SEA by Lyon in the 1960s [18], it has been widely and successfully applied in various engineering fields such as buildings, aerospace, naval and automobile industries.

This thesis is based around the use of statistical methods as a framework of analysis for structure-borne sound transmission in built-up structures. Hence this chapter describes such methods, namely Statistical Energy Analysis (SEA), Experimental Statistical Energy Analysis (ESEA) and Advanced Statistical Energy Analysis (ASEA). The latter is used to incorporate tunnelling mechanisms between physically unconnected subsystems. The thesis uses numerical experiments with Finite Element Method (FEM) to provide the data to test the

statistical approaches and therefore the approach to FEM is also described in this chapter.

2.2 Statistical Energy Analysis (SEA)

2.2.1 Literature review

This section reviews the literature relating to the concepts, main assumptions of and some limitations of SEA.

2.2.1.1 Concepts and assumptions

The origins of SEA concern the analysis of a linear system comprised of two 'weakly' coupled oscillators excited by independent broadband random noise [7]. It is found that power flow is proportional to the difference in energies of uncoupled resonators and it always flows from the resonator with higher energy to the one with lower energy. The analysis was extended to solve more complicated multi-modal subsystems under the assumption that the energy flow between two multi-modal subsystems is proportional to the difference in their modal energies. However, this statement can only be justified under the following assumptions [17]:

(1) 'Weak' or 'light' coupling between subsystems

In a modal approach, weak coupling can be considered to occur when the local modes of an uncoupled subsystem hardly change when it is coupled to other subsystems so that energy flow can be related to the local modal energies [19]. In terms of waves, weak coupling requires the wave field incident upon either side of the junction between two subsystems to be incoherent [20]. In the case of weak coupling, the energy flow is only dependent on the local properties of the subsystems, whilst if it is strong coupling, energy flow between subsystems is largely dependent on the global properties of the system where standard SEA formulation will no longer hold. Various criteria have been proposed to evaluate the validity of the condition of weak coupling and the applicability of SEA in previous studies. Langley [21, 22] proposed a definition of weak coupling where the difference between the Green function of a coupled subsystem and that of the uncoupled subsystem is sufficiently small. Fahy and James [23, 24] extended

Langley's definition and proposed a practical method to determine the strength of coupling between two subsystems by using the time delay in the rise of kinetic energy of one subsystem when an impulsive excitation is injected to the other subsystem. Mace [25] gave a simple evaluation of coupling strength both from the modal analysis and the wave analysis. All of these methods try to ensure a well-conditioned energy response matrix in SEA for the matrix inversion.

(2) Equipartition of modal energy in subsystems

This assumption means that each mode of the subsystem carries equal amount of energy. The modal responses for subsystems are also assumed to be incoherent. To satisfy these assumptions requires a selection of similar mode groups to form subsystems often based on the similarity of geometries of the structures. It is often considered that subsystems with low damping tend to get close to the condition of equipartition of modal energy. The extreme situation of 'true' equipartition of modal energies can only be achieved when the subsystem damping is zero [7]. However, Yap and Woodhouse [26] indicated a contrary conclusion against the classical SEA prediction that subsystems with low damping didn't always yield equipartition of the modal energies and SEA could significantly overestimate the modal energies of those subsystems that are not physically connected to the source subsystem (for example, a chain of subsystems).

(3) Subsystem response to be dominated by the reverberant field

Under this assumption, the energy in a subsystem can be considered uniformly distributed. With highly damped subsystems, however, this assumption will not be true.

(4) Equal probability of natural frequencies occurring in the interested frequency bands

This assumption means that each subsystem is a member of a population of systems that are generally physically similar, but different enough to have randomly distributed parameters [18].

(5) Statistically independent excitation on subsystems

Such excitation applies equal modal forces to all the subsystem modes and injects energy into the direct wave field equally at all points of the excited subsystem [27] so that the basic SEA assumption of equal partition of modal energies among subsystems is satisfied. Statistically independent excitations are described as over the plate surface with constant amplitude but with phase randomly distributed with location. Under this type of excitations, the energy response can be calculated by summing the energy response due to excitation applied to each point in the excited subsystem [28]. It can be realized using rain-on-the-roof excitation where the complex forces are delta-correlated, broadband excitations applied on the subsystem with magnitude at any location proportional to the local mass density and the phase follows a uniform probability in the range of $(0, 2\pi)$. Ideal rain-on-the-roof can excite the local modes of the excited subsystem equally [28].

2.2.1.2 Limitations

Limitations of SEA result from the constraints of the assumptions that the development of SEA is based upon.

SEA can only give the estimate of the statistically averaged global response for a subsystem and cannot predict the distributions of the energy field. This may cause significant error or even the failure of SEA if the local response within a subsystem dominates the total response instead of the global response. In other words, the assumption of equipartition of modal energies is not satisfied. Therefore, additional procedures need to be taken in order to incorporate the large local response. This assumption of equipartition of modal energies in the modelling was removed by Maxit and Guyader [29] by incorporating the modal energy distribution in the SEA formulation. The modal information of subsystems needs to be calculated and for complex structures, this can be achieved using the Finite Element Method (FEM). This procedure is only applied to those subsystems for which equipartition doesn't occur. The rest of the subsystems are modelled using classical SEA theory.

Another issue that limits the application of SEA is in frequency bands where the subsystems have low mode count and low modal overlap (more discussions see

section 2.2.4). Craik *et al.* [30] discussed the application of SEA at low frequencies where low mode count and modal overlap occurs. Theoretical models by spatially averaging the mobilities of the subsystem were used to determine the coupling loss factors. It was stated that "modal properties of the receiving subsystem affect coupling between two subsystems". Large fluctuations of coupling loss factors from the measurements were observed at low frequencies and they seemed to follow the same manner as the mobility of the receiving subsystem. The theoretical method was also able to give the upper and lower limit of coupling loss factor at low frequencies. Hopkins [31] investigated the application of SEA for different structural junctions with low modal overlap and mode count. It was shown that small variation of material properties can cause significant differences in the coupling parameters. Therefore, it is necessary to use numerical or experimental ensemble average to determine the coupling loss factors instead of one single deterministic analysis.

The assumption of weak coupling is also one of the concerns in the application of SEA as in many engineering structures the coupling between subsystems can be considered as 'strong'. Although weak coupling has been considered as one of the basic assumptions in the derivation of SEA, Scharton and Lyon [32] showed that this assumption could actually be removed in SEA by redefining the subsystem 'blocked' energies. Mace and Rosenberg [33] related the coupling strength to the damping of the subsystems and it was indicated that when the coupling is strong (small damping), more information is needed for each subsystem than normal SEA in order to give accurate predictions (i.e. the coupling loss factor results can be sensitive to the shape of the subsystem).

2.2.2 General formulation of SEA

The SEA model is based on energy balance for groups of resonant modes within a structure. A complex built-up structure is modelled as an assembly of coupled mode groups named subsystems. The modes for each subsystem are considered statistically and the calculated responses are spatial averaged energies for each subsystem. As the response of a subsystem is based on its resonant modes, SEA should be used at frequencies above the fundamental mode of the subsystem.

Figure 2.1 illustrates a general linear system consisting two subsystems in SEA. The direction of energy flow is represented by arrows. The input power is applied to subsystem 1 as W_{in}, the transferred power between subsystem 1 and 2 is labelled as W_{12} and W_{21}, and the dissipated powers for the two subsystems are labelled as W_{1d} and W_{2d}.

Conservation of energy requires that the energy entering one subsystem must equal the energy leaving that subsystem. Energy leaving each subsystem is partly transferred to other coupled subsystems and partly dissipated due to internal losses such as damping. The power balance equations for the system in Figure 2.1 can be expressed as:

$$W_{in} + W_{21} = W_{1d} + W_{12} \tag{2.1}$$

$$W_{12} = W_{21} + W_{2d} \tag{2.2}$$

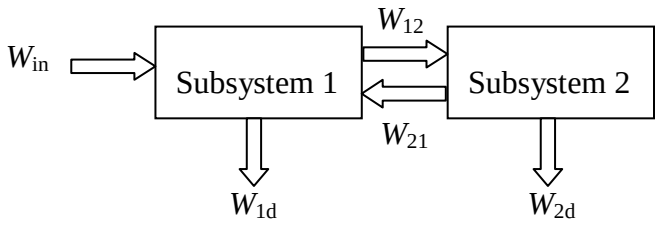

Figure 2.1 Schematic of a two-subsystem model

The power transfer from subsystem 1 to subsystem 2, W_{12}, can be expressed in terms of coupling loss factor, η_{12} which in SEA is defined as the fraction of energy transferred per radian cycle and the energy in subsystem 1, E_1 as:

$$W_{12} = \omega \eta_{12} E_1 \tag{2.3}$$

Dissipated power within subsystem 1 due to internal damping can be quantified using the internal loss factor, η_{11}:

$$W_{1\mathrm{d}} = \omega \eta_{11} E_1 \tag{2.4}$$

Substituting equations (2.3) and (2.4) into equations (2.1) and (2.2), a matrix form of the power balance equations can be written as:

$$\begin{bmatrix} W_{\mathrm{in}} \\ 0 \end{bmatrix} = \omega \begin{bmatrix} \eta_{11} + \eta_{12} & -\eta_{21} \\ -\eta_{12} & \eta_{21} + \eta_{22} \end{bmatrix} \begin{bmatrix} E_1 \\ E_2 \end{bmatrix} \tag{2.5}$$

The above matrix equation can be extended to a more general form for an SEA model with N subsystems as shown in equation (2.6).

$$\begin{bmatrix} W_1 \\ W_2 \\ \vdots \\ \vdots \\ W_N \end{bmatrix} = \omega \begin{bmatrix} \sum_{k=1}^{N} \eta_{1\mathrm{k}} & -\eta_{21} & \cdots & -\eta_{N1} \\ -\eta_{12} & \sum_{k=1}^{N} \eta_{2\mathrm{k}} & \cdots & -\eta_{N2} \\ \vdots & & \ddots & \vdots \\ -\eta_{1N} & \cdots\cdots & & \sum_{k=1}^{N} \eta_{N\mathrm{k}} \end{bmatrix} \begin{bmatrix} E_1 \\ E_2 \\ \vdots \\ \vdots \\ E_N \end{bmatrix} \tag{2.6}$$

where W_i is the input power into subsystem i and E_i is the energy of subsystem i. If the input powers and the loss factors are known, energies for all subsystems can be calculated using matrix inversion.

The leading diagonal elements of the $N \times N$ matrix in equation (2.6) characterize the total power leaving each subsystem, and define the total loss factor, η_i:

$$\eta_i = \sum_{k=1}^{N} \eta_{ik} = \eta_{ii} + \sum_{\substack{k=1 \\ k \neq i}}^{N} \eta_{ik} \tag{2.7}$$

The total energy E_i can also be expressed using modal energy e_i as average energy per mode:

$$e_i = E_i / n_i \tag{2.8}$$

where n_i is the modal density of subsystem i, which can be a function of frequency. Equation (2.6) can now be rewritten in terms of modal energy as:

$$\begin{bmatrix} W_1 \\ W_2 \\ \vdots \\ \vdots \\ W_N \end{bmatrix} = \omega \begin{bmatrix} n_1\eta_{11} + \sum_{k=2}^{N} n_1\eta_{1k} & -n_2\eta_{21} & \cdots & -n_N\eta_{N1} \\ -n_1\eta_{12} & n_2\eta_{22} + \sum_{\substack{k=1 \\ k\neq 2}}^{N} n_2\eta_{2k} & \cdots & -n_N\eta_{N2} \\ \vdots & & \ddots & \vdots \\ -n_1\eta_{1N} & \cdots\cdots & & n_N\eta_{NN} + \sum_{\substack{k=1 \\ k\neq N}}^{N} n_N\eta_{Nk} \end{bmatrix} \mathbf{e} \tag{2.9}$$

where **e** is a column vector of modal energies:

$$\mathbf{e} = \begin{bmatrix} E_1 / n_1 & E_2 / n_2 & \cdots & E_N / n_N \end{bmatrix}^{\mathrm{T}} \tag{2.10}$$

2.2.3 Determination of subsystems

Subsystems are often defined on the basis of the similarity of the physical components and the existence of the physical boundaries of the whole system. However, this is not always appropriate. For example, sometimes the definition of a subsystem will change depending on the frequency range under consideration.

Structural subsystems such as plates and beams can often support more than one wave type, e.g. a plate can support bending, quasi-longitudinal and transverse shear motion at the same time [34]. As each wave type will result in a group of modes with different properties and energies, they have to be considered as separate subsystems in the SEA model. These subsystems may also be coupled to each other at structural junctions where the conversion of wave types occurs.

2.2.4 Modal density and modal overlap

Since SEA calculates the energy power flow between groups of modes, modal density is an effective measure of the energy storage capability of a subsystem. Modal density, $n(f)$, describes the number of modes ΔN in a frequency band Δf with central frequency f. Frequency-average modal density is defined as:

$$n(f) = \lim_{\Delta\omega \to 0} \frac{\Delta N}{\Delta f} = \lim_{\Delta\omega \to 0} \frac{N(f + \Delta f) - N(f)}{\Delta f} \tag{2.11}$$

Statistical mode counts, $N(f)$, can be determined in wavenumber space [7] for equation (2.11), or alternatively, the modal density can be determined using theoretical, numerical or experimental methods.

Although theoretical modal densities can be used for simple homogeneous elements, many structures are not homogeneous or are sufficiently complex to model that experimental methods are the only practical method to obtain the modal densities.

Modal densities can be estimated using equation (2.12) from either numerical or physical experiments to determine the driving-point mobility such as the method discussed by Clarkson and Pope [35] using the equation as:

$$n(f) = \frac{1}{f_2 - f_1} \int_{f_1}^{f_2} 4\rho_S S \,\mathrm{Re}\{Y\}\, \mathrm{d}\omega \tag{2.12}$$

Where $\mathrm{Re}\{Y\}$ is the real part of the driving-point mobility. $n(f)$ gives a band-averaged modal density in the frequency band with lower and upper limits f_1 and f_2 and centre frequency f.

For simple structures, the driving-point mobility can also calculated using theoretical models.

(1) Driving-point mobility for infinite thin plates

For an infinite thin plate, the driving-point mobility is real and given by Cremer *et al*. [34] as:

$$Y_{\mathrm{dp}} = \frac{1}{8\sqrt{B_{\mathrm{p}}\rho_{\mathrm{s}}}} \tag{2.13}$$

where B_{p} is the bending stiffness of the plate.

(2) Driving-point mobility for rectangular thin plates

For a rectangular thin plate with dimensions of $L_x \times L_y \times h_{\mathrm{p}}$, the driving-point mobility at position (x, y) can be calculated using the modal summation method [36]:

$$Y_{\mathrm{dp}}(x, y) = i\omega \sum_{m=1}^{\infty}\sum_{n=1}^{\infty} \frac{\psi_{mn}^2(x, y)}{\rho h_p L_x L_y \left[\omega_{mn}^2(1+i\eta) - \omega^2\right]} \tag{2.14}$$

where η is the damping loss factor of the plate and $\psi_{mn}(x, y)$ is the mode shape of the $(m, n)^{\mathrm{th}}$ mode and ω_{mn} is the corresponding natural frequency, which can be calculated using the equation given by Warburton [37]:

$$\omega_{mn} = \sqrt{\frac{Eh_{\mathrm{p}}^2}{12\rho(1-\mu^2)}} \cdot \left(\frac{\pi}{L_x}\right)^2 q_{mn} \tag{2.15}$$

where E, ρ, μ are the Young's modulus, density and Poisson's ratio of the plate respectively, and q_{mn} can be calculated from:

$$q_{mn} = \sqrt{G_x^4(m) + G_y^4(n)(L_x / L_y)^4 + 2(L_x / L_y)^2[\mu Q_x(m)Q_y(n) + (1+\mu)J_x(m)J_y(n)]} \tag{2.16}$$

The parameters G_x, Q_x, J_x and G_y, Q_y, J_y are given in Table 1 for free-free (FF) and simply-supported-simply-supported (SS) boundary conditions along two opposite edges of the plate.

The mode shape $\psi_{mn}(x, y)$ can be calculated from characteristic beam functions for x- and y-directions given in [38]:

$$\psi_{mn}(x, y) = \phi(x)\phi(y) \tag{2.17}$$

where the characteristic beam function for simply-supported boundary conditions can be calculated from [38]:

$$\phi_m(x) = \sqrt{2}\sin\left(\frac{m\pi x}{L_x}\right), \qquad \phi_n(y) = \sqrt{2}\sin\left(\frac{n\pi y}{L_y}\right) \tag{2.18}$$

N.B. The use of beam functions for free-free boundary conditions results in errors (particularly for the low order modes) as noted by Leissa [39]. However, this boundary condition is not used to determine the driving-point mobility in this thesis.

Modal overlap describes the degree of overlap in modal response and is defined by the ratio of the half-power bandwidth to the average frequency spacing between mode frequencies [7]. It is often used to assess whether various forms of modelling are appropriate in SEA [31]. The modal overlap factor of subsystem i, M_i, can be calculated from the modal density and total loss factor of the subsystem as shown in equation (2.19) [7] as:

$$M_i(f) = f\eta_i n_i(f) \tag{2.19}$$

When the plates and/or beams are coupled with each other to form a more complicated structure, geometric mean modal overlap, M_{av}, can be used to

evaluate the modal overlap proposed by Fahy and Mohammed [40]. For two subsystems *i* and *j*, M_{av} can be calculated from:

$$M_{\text{av}} = \sqrt{M_i M_j} \tag{2.20}$$

Table 1: Mode parameters for rectangular thin plate used to calculate natural frequencies

Boundary condition	Mode number (*n*)	*G*(n)	*Q*(n)	*J*(n)
Free-Free	1	0	0	0
	2	0	0	1.216
	3	1.506	1.248	5.017
	n (*n*>3)	*n*-1.5	$(n-1.5)\left[1-\frac{2}{(n-1.5)\pi}\right]$	$(n-1.5)^2\left[1+\frac{6}{(n-1.5)\pi}\right]$
Simply-supported - Simply-supported	1	0	0	*J*=*Q*
	2	2	4	
	3	3	9	
	n (*n*>3)	*n*	n^2	

2.2.5 Internal loss factor

For structural vibration problems, the internal loss factor often describes the material damping. Internal loss factors are generally obtained experimentally by measuring the energy dissipation in each subsystem while it is decoupled from the whole structure. The internal loss factors vary with the wave types, but in noise control, bending waves are usually the primary concern as they are the main cause of sound radiation.

The reverberation time, *T*, is commonly used to measure internal loss factors for subsystems that are *isolated* from the whole system. The reverberation time is the time needed for the subsystem response to drop by 60 dB after the excitation has been interrupted. The experimental measurement of reverberation time is discussed in section 7.2. The relationship between the reverberation time and the internal loss factor for subsystem *i*, η_{ii}, is given by Cremer *et al.* [34], which is expressed as:

$$\eta_{ii} = \frac{2.2}{fT} \tag{2.21}$$

When *T* is measured *in-situ* where the subsystem is coupled to other subsystem(s), instead of internal loss factor, the total loss factor of the subsystem is obtained:

$$\eta_i = \eta_{ii} + \sum_{j=1}^{N} \eta_{ij} = \frac{2.2}{fT} \qquad (i \neq j) \tag{2.22}$$

Although equation (2.22) is used for the evaluation of the total loss factors, if the internal loss factor is much larger than the sum of the coupling loss factor, this equation can also be used to give an estimate of the internal loss factors. Note that the sum of the coupling loss factors $\sum_{j=1}^{N} \eta_{ij}$ is not only dependent on the number of subsystems that are coupled to subsystem *i*, but also dependent on the frequency. Therefore when equation (2.22) is used to estimate the internal loss factor, it may give a good estimation in certain frequency range but inaccurate prediction at frequencies outside this range.

2.2.6 Coupling loss factor

The subsystems are coupled together in SEA to allow the transfer of energy. This coupling can be quantified by Coupling Loss Factor (CLF) which describes the fraction of energy transmitted from one subsystem to another per radian cycle. The evaluation of coupling loss factors is a key process in SEA modelling and they can be determined either from theoretical or experimental approaches.

(1) Theoretical determination of coupling loss factors

Most models in this thesis consider the coupling between two plate subsystems along a line junction, such as the structure shown in Figure 2.2. The energy intensity in plate i, $\mathrm{d}I_i(\theta)$ in the angle range of (θ, $\theta+\mathrm{d}\theta$) can be calculated from:

$$\mathrm{d}I_i(\theta) = \varepsilon_i c_{\mathrm{g},i} D(\theta) \frac{\mathrm{d}\theta}{\Theta} \tag{2.23}$$

Where ε_i is energy density over the plate surface as $\varepsilon_i = E_i / S_i$ (S_i is the surface area of the plate and E_i is the energy of subsystem i). $c_{\mathrm{g},i}$ is the group speed of subsystem i which is used to describe the velocity at which energy is conveyed along the wave. Θ is the range of wave angles (i.e. for a diffuse field, $\Theta=2\pi$). $D(\theta)$ is a weighting function concerning the probability of wave propagation directions [7]. If subsystem i is an isotropic plate and characterized by a diffuse field so that waves have equal probability over of all directions, $D(\theta)$ =1 is applied. The intensity impinging upon the junction line only considers the projection along the coupling length. If the wave transmission across the junction is characterised by an angle-dependent transmission coefficient $\tau_{ij}(\theta)$ as $\mathrm{d}I_j=\tau_{ij}(\theta)\mathrm{d}I_i$, the total power transferred from plate i to j can be calculated from:

$$W_{ij} = \int_{-\pi/2}^{\pi/2} \tau_{ij}(\theta) L_{ij} \cos\theta \mathrm{d}I_i(\theta) \tag{2.24}$$

Where L_{ij} is the length of the coupling line, $L_{ij}\cos(\theta)$ represents the projection of the intensity onto the junction line.

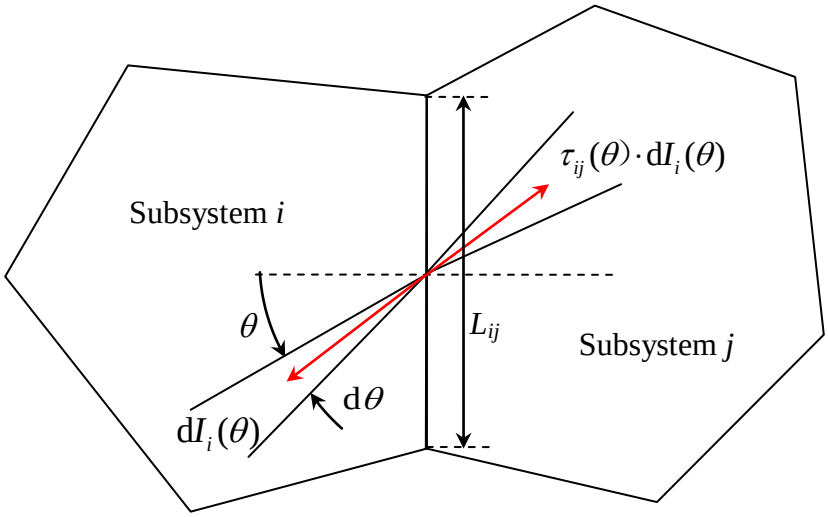

Figure 2.2 Two plates coupled though a line junction

Using equation (2.23), (2.24) can be rewritten as:

$$W_{ij} = \frac{E_i c_{\mathrm{g},i} L_{ij}}{\pi S_i} \int_0^{\pi/2} \tau_{ij}(\theta) \cos\theta \mathrm{d}\theta \tag{2.25}$$

Putting equation (2.25) into (2.3), the coupling loss factor from subsystem i to j can be obtained:

$$\eta_{ij} = \frac{c_{\mathrm{g},i} L_{ij}}{\omega \pi S_i} \overline{\tau}_{ij} \tag{2.26}$$

where $\overline{\tau}_{ij}$ is the angular-average transmission coefficient which can be expressed as:

$$\overline{\tau}_{ij} = \int_0^{\pi/2} \tau_{ij}(\theta) \cos\theta \mathrm{d}\theta \tag{2.27}$$

Equations (2.26) and (2.27) are only valid for isotropic homogeneous plates due to spatially equal distribution of energy over all directions where the weighting function $D(\theta)$ =1. For orthotropic plates, this criterion no longer holds, so angle-

dependent $D(\theta)$ needs to be introduced to consider the orthotropicity and is derived in Chapter 5.

(2) Experimental determination of coupling loss factors

Coupling loss factors can be evaluated from physical experiments by measuring the input power as well as the distribution of the vibration energy, such as the works by Lalor [41], Bies and Hamid [42]. This will be discussed in detail in Chapter 7.

Numerical experiments using Experimental Statistical Energy Analysis (ESEA) can also be used to calculate coupling loss factors and is discussed in section 2.3.

2.2.7 Consistency relationship

The consistency relationship in SEA is based on the assumption that there is no energy dissipation at the coupling junction. The coupling loss factors between two subsystems *i* and *j* are related as:

$$n_i \eta_{ij} = n_j \eta_{ji} \tag{2.28}$$

Mace [43] pointed out that this relationship only holds when the coupling between subsystems is conservative where there is no energy dissipation at the coupling junction. It is shown that with non-conservative coupling, significant error may occur in using the consistency relationship.

2.2.8 Requirements on dimensions of plate subsystem due to high internal losses

One of the SEA assumptions requires the uniform distribution of energy over each subsystem or a reverberant field on the subsystem. If there is a significant decrease in energy level in a subsystem due to high internal damping or large subsystem size, this assumption will no longer hold. This does not necessarily mean that SEA should fail to work as Yap and Woodhouse [26] have shown that

if the excitation is distributed over the surface of the subsystem such as rain-on-the-roof, SEA would still give reasonable prediction despite of the high internal damping. However, this situation still needs to be considered in SEA.

Lyon proposed an upper limit for subsystem size with the aim of significant decay with distance within the subsystem with relatively high damping using the maximum subsystem dimension, $L_{\max,\,i}$, as [7]:

$$L_{\max,i} < \frac{0.5 c_{g,i}}{\pi f \eta_{ii}} \tag{2.29}$$

No derivation or validation of this requirement was provided by Lyon [7]; hence an alternative approach is considered below for subsystem representing plates.

Assuming power input into subsystem *i* along one of the plate edges, we consider another edge that is connected to another subsystem. The average distance that wave travels from the starting edge to the coupling edge can be characterized using the mean free path, d_{mfp}, which is defined as:

$$d_{\mathrm{mfp}} = \frac{\pi S}{U} \tag{2.30}$$

where U is the perimeter ($U=2L_x+2L_y$ for rectangular plate) and S is the surface area.

A requirement on subsystem damping can be found by assuming that the power dissipated due to internal damping must be significantly smaller than the power available to be transmitted to other subsystems. Assuming an energy level difference of at least 10 dB leads to the following requirement:

$$10 \lg \frac{W_{\mathrm{trans}}}{W_{\mathrm{dissipated}}} \geq 10 \text{ dB} \tag{2.31}$$

If a unity power input is assumed, the power dissipated over the distance of the mean free path can be calculated from:

$$W_{\text{dissipated}} = \exp(-2\pi f \eta_{ii} d_{\text{mfp}} / c_{\text{g},\,i}) \tag{2.32}$$

Therefore, at the coupling edge, the power available for transmission is:

$$W_{\text{trans}} = 1 - W_{\text{dissipated}} = 1 - \exp(-2\pi f \eta_{ii} d_{\text{mfp}} / c_{\text{g},\,i}) \tag{2.33}$$

Substituting (2.32) and (2.33) into(2.31) gives:

$$d_{\text{mfp}} \le \frac{1.2 c_{\text{g},\,i}}{\pi f \eta_{ii}} \tag{2.34}$$

If the dimensions of the subsystems are known, equation (2.34) can be used to estimate an upper frequency limit that satisfies this criterion. This requires the use of the largest mean free path, $\max\{d_{\text{mfp},\,i}\}_{i=1}^{N}$ after evaluating all N subsystems. As the group speed is also dependent on the frequency, for bending wave propagation, the group speed can be calculated using the following equation given in[34]:

$$c_{\text{g},\,i} = 2c_{\text{B},\,i} = 2\sqrt{\frac{\pi f h_{\text{p}} c_{\text{L},\,i}}{\sqrt{3}}} \tag{2.35}$$

where h_{p} is the thickness of the plate and $c_{\text{L},\,i}$ is the quasi-longitudinal wave speed of the plate subsystem i.

Then equation (2.34) can be re-written as equation (2.36) to calculate the upper frequency limit:

$$f \le \frac{h_{\text{p}} c_{\text{L},i}}{\left(\eta_{ii} \max\{d_{\text{mfp},\,i}\}_{i=1}^{N}\right)^2} \tag{2.36}$$

Using the above approach, it is found that Lyon's criterion is actually based on the rule that the dissipated power is half of the transmitted power so that instead of a 10 dB difference in equation (2.31), Lyon chose 3 dB such that the dissipated

power is equal to half of the transmitted power and the waving travelling distance used the largest dimension of the subsystem instead of mean free path. The validity of this requirement will be considered in chapter 6 for specific SEA models.

2.3 Experimental Statistical Energy Analysis (ESEA)

2.3.1 Literature review

When theoretical determination of coupling loss factors fails due to the complexity of the subsystems and coupling junctions, experimental methods such as Experimental Statistical Energy Analysis (ESEA) can be used to obtain coupling loss factors.

ESEA is developed from SEA power balance equations to determine the unknown loss factors *in situ* using either physical or numerical experiments. Lyon and Dejong [7] proposed the possibility of using both experimental and numerical means to predict the coupling loss factor for SEA. By using broad band excitation on the source subsystem, the coupling loss factor can be obtained by measuring the energies on the source and receiving subsystems. They acknowledged the difficulty to predict accurate CLFs with low modal overlap however didn't propose any solutions.

Many works relating to ESEA focused on how to accurately measure the responses of the subsystems that is valid to be used in the frame work of SEA. Bies and Hamid [8] proposed a power injection method to measure the coupling loss factors *in situ* based on an inverse SEA procedure. Power was injected using point excitation at several randomly chosen positions on each subsystem to ensure the statistical independence of modes which is a basic requirement for SEA. For each excitation position, the response of the subsystem was measured from ten randomly chosen positions and the CLF is calculated from an average of the ensemble measurement. They also used the reverberant decay method to measure the loss factor in comparison with power injection method which was a steady-state technique. It was shown that the *in situ* power injection method for loss factor measurement gave good agreement with the steady-state measurement

when the subsystem is decoupled from the structure. The steady-state method consistently gave higher loss factors than the transient decay method, and this discrepancy was explained as because "energy distribution among modes of the system (in this case a lightly damped plate) during reverberant decay is not in steady state equilibrium" [8].

Clarkson and Ranky [44] carried out the similar ESEA procedure proposed by Bies and Hamid using transient excitation as power input to determine the coupling loss factor between two coupled plates. It is indicated that condition of the energy matrix from measurement can significantly affect the accuracy of the ESEA prediction. Woodhouse [45] also showed small errors in measurement that were used in the ESEA matrix inversion may result in larger error in the prediction of loss factors and proposed a matrix-fitting method to assess whether the system can be modelled on the basis of SEA. Clarkson and Ranky [44] successfully applied this method to the coupled plates, and Hodges *et al.* [46] optimized the matrix-fitting routines to increase the efficiency and accuracy of measurement matrix inversion. However, this method is still largely dependent on the accuracy of the measurement data.

Lalor [41, 47, 48, 49] carried out loss factor measurements by using the power injection method but predominantly addressed the problem of ESEA matrix condition for large complex structures. The occurrence of an ill-conditioned energy matrix is related to the insensitivity of SEA subsystem energy distribution to the change of coupling loss factor. The matrix condition can be improved by rearranging the SEA power balance matrix to eliminate the internal loss factors and the coupling loss factors can be expressed in terms of the measured input power and subsystem energies. For complex structures, the calculation of the subsystem energies from measurement was discussed by introducing the concept of equivalent mass. This can be calculated from measured power input, total loss factor and velocity levels of the subsystem [50]. It was also suggested that the uncertainty in determining subsystem modal densities can be overcome by using the consistency relationship between two subsystems.

Hopkins [9, 51] applied ESEA by using the data from numerical experiments with Finite Element Method (FEM). It was demonstrated that the use of ESEA can be

extended to the situation of low modal overlap and mode count by using ensemble average. Bending and in-plane wave conversion at structural junctions was also identified by FEM with ESEA as this is often difficult to identify in physical experiments.

2.3.2 Simplified ESEA

Based on the SEA power balance equations in (2.1) and (2.3), the coupling loss factor from subsystem *i* to *j* can be estimated by assuming that there is negligible power flowing back from *j* to *i* and that all transmission takes place along the direct transmission path from *i* to *j*. This is given by Craik [52]:

$$\eta_{ij} = \frac{E_j}{E_i}\eta_i \tag{2.37}$$

If the internal loss factor of subsystem *i* is much larger than the total loss factor of this subsystem, equation (2.37) can be further simplified as:

$$\eta_{ij} \approx \frac{E_j}{E_i}\eta_{ii} \tag{2.38}$$

2.3.3 General ESEA matrix formulation

The general formulation of ESEA can be expressed in the following form [31]:

$$\begin{bmatrix} \sum_{n=1}^{N}\eta_{1n} & -\eta_{21} & -\eta_{31} & \cdots & -\eta_{N1} \\ -\eta_{12} & \sum_{n=1}^{N}\eta_{2n} & -\eta_{32} & & \\ -\eta_{13} & -\eta_{23} & \sum_{n=1}^{N}\eta_{3n} & & \vdots \\ \vdots & & & \ddots & \\ -\eta_{1N} & & \cdots & & \sum_{n=1}^{N}\eta_{Nn} \end{bmatrix} \begin{bmatrix} E_{11} & E_{12} & E_{13} & \cdots & E_{1N} \\ E_{21} & E_{22} & E_{23} & & \\ E_{31} & E_{32} & E_{33} & & \vdots \\ \vdots & & & \ddots & \\ E_{N1} & & \cdots & & E_{NN} \end{bmatrix} = \begin{bmatrix} W_1/\omega & 0 & \cdots & \cdots & 0 \\ 0 & W_2/\omega & & & \vdots \\ \vdots & & W_3/\omega & & \vdots \\ \vdots & & & \ddots & 0 \\ 0 & \cdots & 0 & & W_N/\omega \end{bmatrix} \tag{2.39}$$

where E_{ij} is the energy of subsystem *i* with power input into subsystem *j*.

ESEA requires power input into each of the subsystems in turn and for each power input, the spatial averaged energy on all subsystems need to be measured and inserted into the ESEA formulation. Determination of the input powers and subsystem energies allows inversion of the energy matrix to calculate the coupling loss factors.

The inversion of the matrix may result in some negative coupling loss factors which are clearly physically impossible. For the energies and powers measured with physical experiments, this may be caused by the measurement uncertainty [53]. Sheng *et al.* [54] investigated negative coupling loss factors in ESEA and considered that they could be caused by non-conservative coupling which means that there is energy dissipated at the junction which standard SEA does not incorporate. If the coupling loss factors are obtained from numerical experiments with FEM, errors due to discretization can be evaluated using element mesh error, which will be discussed in section 2.5.3. The negative coupling loss factors are caused by an ill-conditioned matrix. A possible solution is to rearrange the ESEA formulations and mathematically improve the matrix condition. If the negative coupling loss factors still occur, they have to be considered as invalid data.

2.3.4 Alternative ESEA matrix formulations

In order to reduce the chance of having ill-conditioned matrices, one possible alternative ESEA formulation is proposed by Lalor [55] as shown in equation (2.40) by eliminating internal loss factors in the power balance equations, which may increase the matrix condition numbers compared with the general formulation.

$$\begin{bmatrix} \eta_{1i} \\ \vdots \\ \eta_{ri} \\ \vdots \\ \eta_{Ni} \end{bmatrix}_{r \neq i} = \frac{W_i}{\omega E_{ii}} \begin{bmatrix} \left(\frac{E_{11}}{E_{i1}} - \frac{E_{1i}}{E_{ii}}\right) & \cdots & \left(\frac{E_{r1}}{E_{i1}} - \frac{E_{ri}}{E_{ii}}\right) & \cdots & \left(\frac{E_{N1}}{E_{i1}} - \frac{E_{Ni}}{E_{ii}}\right) \\ \vdots & \ddots & & & \vdots \\ & & \left(\frac{E_{rr}}{E_{ir}} - \frac{E_{ri}}{E_{ii}}\right) & & \\ \vdots & & & \ddots & \vdots \\ \left(\frac{E_{1N}}{E_{iN}} - \frac{E_{1i}}{E_{ii}}\right) & \cdots & \left(\frac{E_{rN}}{E_{iN}} - \frac{E_{ri}}{E_{ii}}\right) & \cdots & \left(\frac{E_{NN}}{E_{iN}} - \frac{E_{Ni}}{E_{ii}}\right) \end{bmatrix}^{-1} \begin{bmatrix} 1 \\ \vdots \\ \vdots \\ \vdots \\ 1 \end{bmatrix}$$

(2.40)

Using equation (2.40) for each subsystem, one gets N sets of matrix equations for the coupling loss factors $\{\eta_{ri}\}$ relating to subsystem i. Compared with the standard ESEA doing a matrix inversion with $N \times N$ size, equation (2.40) reduces the matrix size to only $(N\text{-}1) \times (N\text{-}1)$ so that the matrix could be better conditioned.

The internal loss factors are calculated separately using equation (2.41).

$$\begin{bmatrix} \eta_{11} \\ \\ \vdots \\ \\ \eta_{NN} \end{bmatrix} = \frac{1}{\omega} \begin{bmatrix} E_{11} & E_{12} & E_{13} & \cdots & E_{1N} \\ E_{21} & E_{22} & E_{23} & & \\ E_{31} & E_{32} & E_{33} & & \vdots \\ \vdots & & & \ddots & \\ E_{N1} & & \cdots & & E_{NN} \end{bmatrix}^{-1} \begin{bmatrix} W_1 \\ \vdots \\ \vdots \\ \vdots \\ W_N \end{bmatrix} \tag{2.41}$$

Assuming weak coupling, Lalor considered the coupling between physically unconnected subsystems to be negligible so that these indirect coupling loss factors can be treated as equal to zero. Based on this, equation (2.40) can be altered to further improve the matrix condition [47].

Considering a three-subsystem model shown in Figure 2.3, the subsystems are connected in a chain where subsystem 1 and 3 are not directly connected. In the absence of indirect coupling, η_{13} and η_{31} are set to be zero in the formulation of ESEA.

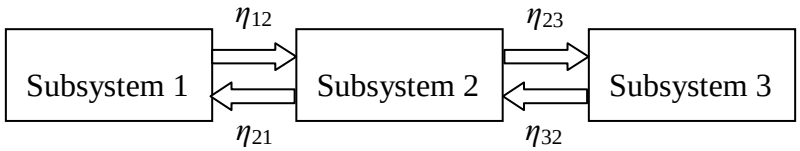

Figure 2.3 Three subsystems in a chain

By rearranging and partitioning the matrices in equation (2.40) for three-subsystem model, all the zero coupling loss factors are placed together

$$\begin{matrix} \\ \eta_{12} \\ \eta_{21} \\ \eta_{23} \\ \eta_{32} \\ \hdashline \eta_{13} \\ \eta_{31} \end{matrix} \begin{matrix} \\ (\eta_{12}) \\ (\eta_{21}) \\ (\eta_{23}) \\ (\eta_{32}) \\ \hdashline (\eta_{13}) \\ (\eta_{31}) \end{matrix} = \frac{1}{\omega} \left[\begin{array}{cccc:cc} (\frac{E_{11}}{E_{21}}-\frac{E_{12}}{E_{22}}) & 0 & 0 & (\frac{E_{31}}{E_{21}}-\frac{E_{32}}{E_{22}}) & 0 & 0 \\ 0 & (\frac{E_{22}}{E_{12}}-\frac{E_{21}}{E_{11}}) & 0 & 0 & 0 & (\frac{E_{32}}{E_{12}}-\frac{E_{31}}{E_{11}}) \\ 0 & 0 & (\frac{E_{22}}{E_{32}}-\frac{E_{23}}{E_{33}}) & 0 & (\frac{E_{12}}{E_{32}}-\frac{E_{13}}{E_{33}}) & 0 \\ (\frac{E_{13}}{E_{23}}-\frac{E_{12}}{E_{22}}) & 0 & 0 & (\frac{E_{33}}{E_{23}}-\frac{E_{32}}{E_{22}}) & 0 & 0 \\ \hdashline 0 & 0 & (\frac{E_{21}}{E_{31}}-\frac{E_{23}}{E_{33}}) & 0 & (\frac{E_{11}}{E_{31}}-\frac{E_{13}}{E_{33}}) & 0 \\ 0 & (\frac{E_{23}}{E_{13}}-\frac{E_{21}}{E_{11}}) & 0 & 0 & 0 & (\frac{E_{33}}{E_{13}}-\frac{E_{31}}{E_{11}}) \end{array}\right]^{-1} \left[\begin{array}{c} W_2/E_{22} \\ W_1/E_{11} \\ W_3/E_{33} \\ W_2/E_{22} \\ \hdashline W_3/E_{33} \\ W_1/E_{11} \end{array}\right]$$

(2.42)

As η_{13} and η_{31} are both zero, only the upper left sub-matrix needs to be considered and (2.42) can be replaced by (2.43) to calculate the coupling loss factors.

$$\begin{bmatrix} \eta_{12} \\ \eta_{21} \\ \eta_{23} \\ \eta_{32} \end{bmatrix} = \frac{1}{\omega} \begin{bmatrix} (\frac{E_{11}}{E_{21}}-\frac{E_{12}}{E_{22}}) & 0 & 0 & (\frac{E_{31}}{E_{21}}-\frac{E_{32}}{E_{22}}) \\ 0 & (\frac{E_{22}}{E_{12}}-\frac{E_{21}}{E_{11}}) & 0 & 0 \\ 0 & 0 & (\frac{E_{22}}{E_{32}}-\frac{E_{23}}{E_{33}}) & 0 \\ (\frac{E_{13}}{E_{23}}-\frac{E_{12}}{E_{22}}) & 0 & 0 & (\frac{E_{33}}{E_{23}}-\frac{E_{32}}{E_{22}}) \end{bmatrix}^{-1} \begin{bmatrix} W_2/E_{22} \\ W_1/E_{11} \\ W_3/E_{33} \\ W_2/E_{22} \end{bmatrix} \quad (2.43)$$

Hopkins [31] shows that the general ESEA formulation often gives the lowest condition numbers while Lalor's formulation can sometimes slightly improve the matrix condition by giving a lower condition number. However, both methods may still produce negative coupling loss factors depending on the number of subsystems.

2.4 Advanced Statistical Energy Analysis (ASEA)

2.4.1 Literature review: Tunnelling mechanism in the application of SEA

SEA has been successfully used in the area of noise and vibration prediction. However, when applied to complex structural assemblies, SEA predictions often exhibit some errors due to the complexity of various wave and power transmission mechanisms among which the tunnelling mechanism occurs when indirect coupling exists between two SEA subsystems that are physically separated from each other by other subsystems.

The concept of a tunnelling mechanism originated from quantum mechanics which describes the phenomenon that a particle tunnels through a barrier that it classically could not surmount [56]. Conceptually, the tunnelling mechanism in SEA occurs when two physically unconnected subsystems are coupled together. It is also sometimes referred to as indirect coupling.

An important tunnelling example was studied by Price and Crocker [57] for the coupling between two rooms separated by a wall. The tunnelling was explained as the result of non-resonant (mass law) transmission where power flow between the two rooms is contributed by "non-resonant modes with small amplitudes but acting as efficient radiators" [58]. Leppington *et al.* [59] incorporated this energy transmission mechanism into the theory of SEA by adding the mass law contribution. They also indicated the non-resonant transmission not only depended on the mass of the plates, but also on the incident wave angle and frequency.

For structural vibration problems, Blakemore *et al*. [14, 15] investigated wave transmission in perfect and imperfect periodic systems found in submarines. In

both situations, it was found that SEA significantly underestimated the subsystem response. The reason for this error was explained by Langley [60] as the result of a spatial wave filtering effect at the interface of the subsystems. Even if a diffuse field is generated in the excited subsystem, the wave filtering will result in a less and less diffuse field as the wave propagates through successive subsystems.

Langley and Bercin [61] took account of the wave directional filtering effect at the structural junctions and proposed a wave intensity analysis to calculate the subsystem response. The analysis results can be expressed in the form of conventional SEA with additional coupling loss factors between physically unconnected subsystems. It was shown that these indirect coupling loss factors, may be very small compared with other coupling loss factors, but could play a very important role in the vibration transmission in structures.

Cuschieri and Sun [62] suggested that there were three reasons that may cause indirect coupling for vibration problems: Firstly, the directly coupled subsystems are strongly coupled; secondly, the sizes of the subsystems are smaller than the wavelength; thirdly, the junction between the subsystems is in the nearfield of another junction. Lalor [47] considered three flat plates connected in a chain forming two L-junctions and tunnelling occurs at low frequencies when the flexural modes of the two physically unconnected subsystems are coupled via in-plane motion of the middle plate so that it is acting as a connector. For this type of tunnelling mechanism, it has been already modelled into the existing SEA theory by including the in-plane subsystems. Langley [21, 22] used a power flow method to analyze complex dynamic systems in the framework of SEA and showed that for certain weakly coupled systems, tunnelling can occur, however standard SEA can still give accurate results if every subsystem is subject to excitation. If only one subsystem is excited, SEA may have errors especially for subsystems distant from the excitation.

Heron [16] studied a chain of one-dimensional rods using ray theory to track the power flowing around the SEA subsystems at high frequencies and then used the standard SEA to take care of the residual power. This approach is referred to as Advanced Statistical Energy Analysis (ASEA). Heron applied ASEA to a one-dimensional model and suggested it could be extended to two-dimensional plate

network but indicated that “the actual implementation could well be computationally expensive”.

Fredö [63] suggested the reason that standard SEA failed to predict the indirect coupling for highly damped subsystems was because it neglected the energy decay of the subsystems. He proposed a modification of the SEA power balance to introduce a decay factor that accounted for the drop of energy across a subsystem.

This thesis makes use of ASEA for two-dimensional plate systems. The basic concept of ASEA is first introduced in a qualitative description. Then the general formulations of ASEA are derived. A detailed algorithm for ray tracing that is used in ASEA is discussed and a complete ASEA algorithm for two-dimensional subsystems is presented.

2.4.2 Qualitative description of ASEA

In SEA, we assume all power transfer occurs between available power per unit modal energy in one subsystem to available power per unit modal energy in the same or another subsystem. In ASEA, it is necessary to refer to available and unavailable power per unit modal energy. The concept of unavailable power is introduced to describe power losses within the subsystems which will not be available for further transmission.

In ASEA, each subsystem is considered in turn as the ‘chosen’ subsystem. In this chosen subsystem, all the junctions that connect this subsystem to all other subsystems are identified. For each of these junctions, the available power per unit modal energy that is incident upon the junction at one angle of incidence is calculated. Then Snell’s law, ray tracing and wave theory are used to track this available power and calculate two types of power transfer. Firstly, power transfer from available power in the chosen subsystem that is reflected back from the junction as available power as well as available power that is transmitted to available power in other connected subsystems. Secondly, power transfer from available power in the chosen subsystem to unavailable power in the chosen subsystem and all other connected subsystems. These calculations are repeated for

all the junctions in all the subsystems. How far the available power per unit modal energy in the chosen subsystem is tracked is determined by an ASEA level number which denotes the number of transfers of available to unavailable power per unit modal energy on each subsystem. For example, ASEA1 means that when we have considered power incident on all junctions in each subsystem there will have been one transfer of available to unavailable power per unit modal energy on each subsystem. With a level number of zero (i.e. ASEA0) there is no transfer from available power to unavailable power and therefore ASEA0 is equivalent to SEA. For each angle of incidence, all transfers of power are entered into a pair of coupling matrices, **A** and **B**. Matrix **A** describes available to available power transfers and matrix **B** describes available to unavailable power transfers. When a diffuse field is assumed for each subsystem, this calculation is repeated until all possible angles of incidence have been considered. A diffuse field version of matrices **A** and **B** is calculated by integrating over all angles of incidence. When the chosen level number of calculation has been reached, the residual power is accounted in matrix **A** to maintain the power balance. The final step is to assign power input to corresponding subsystem(s) and solve the ASEA energy balance equations involving matrices **A** and **B** to calculate the subsystem responses.

2.4.3 General ASEA formulation

In SEA, the responses of all subsystems are steady-state and with the input power known, the energies of subsystems can be calculated from equation (2.9). This equation can also be expressed as follows to make a clear link to ASEA as:

$$\mathbf{P} = (\mathbf{H} + \mathbf{M})\mathbf{e} \tag{2.44}$$

where **e** is a column vector of SEA modal energies as:

$$\mathbf{e} = \begin{bmatrix} E_1 / n_1 & E_2 / n_2 & \cdots & E_N / E_N \end{bmatrix}^{\mathrm{T}} \tag{2.45}$$

and **P** is the column vector of input powers, and **M** is a diagonal matrix of modal overlap factors as shown in equation (2.46) with each element calculated using equation (2.19).

$$\mathbf{M} = \omega \begin{bmatrix} \eta_1 n_1 & 0 & \cdots & 0 \\ 0 & \eta_2 n_2 & & \vdots \\ \vdots & & \ddots & 0 \\ 0 & \cdots & 0 & \eta_N n_N \end{bmatrix} \tag{2.46}$$

H is a matrix determined by the coupling loss factors and modal densities of SEA subsystems as:

$$\mathbf{H} = \omega \begin{bmatrix} \sum_{k\neq 1}^{N} n_1 \eta_{1\mathrm{k}} & -n_2 \eta_{21} & \cdots & -n_N \eta_{N1} \\ -n_1 \eta_{12} & \sum_{k\neq 2}^{N} n_2 \eta_{2\mathrm{k}} & \cdots & -n_N \eta_{N2} \\ \vdots & & \ddots & \vdots \\ -n_1 \eta_{1N} & \cdots\cdots & & \sum_{k\neq N}^{N} n_N \eta_{N\mathrm{k}} \end{bmatrix} \tag{2.47}$$

Where η_{ij} is the coupling loss factor from subsystem *i* to *j*. It is worth noting that the sum of each column of matrix **H** should equal zero due to the power balance requirement. **H** is a symmetric matrix because of the consistency relationship in SEA in equation (2.28).

In standard SEA, all subsystem energies are stored modal energies which are available for transmission to other subsystems. In ASEA, the energy in each subsystem is divided into two parts as available energy and unavailable energy. Therefore, ASEA divides equation (2.44) into two parts as proposed by Heron [16]:

$$\mathbf{P} = \mathbf{Ae} + \mathbf{Me} \tag{2.48}$$

$$\mathbf{Q} = \mathbf{Be} + \mathbf{Md} \tag{2.49}$$

where the available modal energy is denoted by ***e*** and the unavailable modal energy is denoted by **d**. Here the term 'unavailable modal energy' may be considered rather inappropriate for power dissipated due to wave propagation which does not involve subsystem modes. However, it is still used in the formulation of ASEA in order to maintain a link to the framework of SEA. Accordingly, column vectors **P** and **Q** are available power input and unavailable power input respectively. For N subsystems, **A** and **B** are $N \times N$ matrices that represent the power transfers where element (j, i) of matrix **A** represents the available power per unit modal energy transferred from subsystem i to available power in subsystem j and the element (j, i) of matrix **B** represents the available power per unit modal energy transferred from subsystem i to unavailable power in subsystem j. The response of the subsystems can be calculated from **e**+**d** once **A**, **B**, **P** and **Q** are known.

In equation (2.48) the physical meaning of matrix **A** is the power transfer from available power in a particular subsystem to available power in another subsystem (including that subsystem itself) while matrix **B** in equation (2.49) represents the transfer of available power to unavailable power. The terms **M**·**e** and **M**·**d** in equation (2.48) and (2.49) give the available power lost and unavailable power lost within each subsystem.

From Equation (2.48) and (2.49), the sum of the modal energies can be written as:

$$\mathbf{e} + \mathbf{d} = \mathbf{M}^{-1}(\mathbf{Q} + \mathbf{R}) \tag{2.50}$$

where

$$\mathbf{R} = (\mathbf{M} - \mathbf{B})(\mathbf{M} + \mathbf{A})^{-1}\mathbf{P} \tag{2.51}$$

For rain-on-the-roof excitation on a subsystem, all the input power is available for transmission, so it can be treated as available power input whilst the unavailable power input **Q** is zero. Then the above equation can be simplified as follows:

$$\mathbf{P} = (\mathbf{M} + \mathbf{A})(\mathbf{M} - \mathbf{B})^{-1}\mathbf{M}(\mathbf{e} + \mathbf{d}) \tag{2.52}$$

Combining equations (2.48) and (2.49) gives,

$$\mathbf{P} + \mathbf{Q} = (\mathbf{A} + \mathbf{B})\mathbf{e} + \mathbf{M}(\mathbf{e} + \mathbf{d}) \tag{2.53}$$

Comparing equation (2.53) with (2.44), it is seen that **A**+**B** must obey the same relationship concerning the sum of each column to zero as **A**+**B** corresponds to **H** in the SEA formulation shown in equation (2.44). This requirement serves as an important check of validity of ASEA throughout the calculation process. ASEA requires calculating the elements of matrices **A** and **B** in order to obtain the subsystem response.

2.4.4 Power transfer across subsystems

The key component of ASEA is to determine the power transfer matrices **A** and **B**. This is achieved by tracing the power across the subsystems.

Consider the energy field on a subsystem *i* with modal energy of e_i. Note that this subsystem doesn't necessarily have to be the subsystem where the structure is actually excited because ASEA needs to perform the following calculation for all subsystems.

If a diffuse vibration field in the subsystems is assumed, the available power in subsystem *i* impinging upon the coupling junction for one- and two-dimensional subsystems is calculated as follows.

(1) One-dimensional subsystems

For a one-dimensional subsystem such as a beam with length, L_i, the time, *t*, for waves to travel from one end of the beam to the other end can be calculated from:

$$t = \frac{d_{\text{mfp}}}{c_g} = \frac{L_i}{c_{g,i}} \tag{2.54}$$

where d_{mfp} is the mean free path representing the average distance that wave travels between two boundaries. For a one-dimensional subsystem, d_{mfp} equals the beam length, L_i and $c_{\text{g},\,i}$ is the group velocity of subsystem i.

As the waves travel both from left to right and right to left along the beam, the power flow in one direction can be calculated from the following equation:

$$W_i = \frac{E_i / 2}{t} \tag{2.55}$$

Combining equations (2.54) and (2.55) gives:

$$E_i / L_i = 2W_i / c_{\text{g},\,i} \tag{2.56}$$

The modal density expression for beams is given by:

$$n(f) = \frac{2L_i}{c_{\text{g},\,i}} \tag{2.57}$$

Using modal energy e_i to replace E_i allows equation (2.56) can be written as:

$$W_i = e_i \tag{2.58}$$

Thus we define the available power per unit modal energy at each end of beam subsystem i for potential transportation to other subsystems as:

$$W_{\text{a},i} = W_i / e_i = 1 \tag{2.59}$$

(2) Two-dimensional subsystems

For a diffuse vibration field on subsystem i, the incident energy is uniformly distributed in angle, and the intensity $\mathrm{d}I_i(\theta)$ associated with a narrow range of angles, $\mathrm{d}\theta$ is given based on equation (2.23) as:

$$\mathrm{d}I_i(\theta) = \frac{E_i c_{\mathrm{g},i}}{S_i}\frac{\mathrm{d}\theta}{2\pi} \tag{2.60}$$

where E_i can be expressed in terms of modal energy e_i and modal density n_i using equation (2.8) where the modal density for a plate can be calculated from:

$$n_i(f) = \frac{k_i S_i}{c_{\mathrm{g},i}} \tag{2.61}$$

where k_i is the wavenumber of subsystem i for a certain wave type, which is defined as $k_i=\omega/c_i$.

Substituting equation (2.61) into equation(2.60) gives:

$$\frac{\mathrm{d}I_i(\theta)}{\mathrm{d}(\theta)} = \frac{e_i k_i}{2\pi} \tag{2.62}$$

Considering only bending wave transmission on the plate, k_i can be replaced by bending wavenumber k_B can be expressed as:

$$k_\mathrm{B} = \frac{\omega}{c_\mathrm{B}} = \sqrt{\frac{2\sqrt{3}\omega}{h_\mathrm{p} c_\mathrm{L}}} \tag{2.63}$$

Where h_p is the thickness of the plate and c_L is the quasi-longitudinal wave speed of the plate.

Therefore, the power per unit modal energy impinging upon a fraction of the boundary line, $\mathrm{d}U_i$, at an angle of incidence, θ, perpendicular to this boundary can be calculated from:

$$W_{\mathrm{a},\,i} = \frac{\mathrm{d}I_i(\theta)}{\mathrm{d}(\theta)}\cos(\theta)\mathrm{d}U_i / e_i = \frac{e_i k_i \cos(\theta)}{2\pi}\mathrm{d}U_i \cdot \frac{1}{e_i} = \frac{k_i \cos(\theta)}{2\pi}\mathrm{d}U_i \qquad (2.64)$$

With $W_{\mathrm{a},i}$ as the initial available power in subsystem i, we can now proceed with the calculation of matrices **A** and **B** by tracing this initial power across the subsystems with the following steps:

Step 1: All elements in the $N \times N$ matrices **A** and **B** are set to zero at the beginning of the calculation. The elements in these matrices are filled and updated during the power tracking procedure.

Step 2: The initial available power, $W_{\mathrm{a},\,i}$, at an incident wave angle, θ, is added to element (i, i) of matrix **A** as the available power originating in subsystem i which is currently in subsystem i as available power. Further power transfer from available to available power will be recorded and accumulated at the corresponding element in matrix **A**. Note that it is not critical which subsystem is chosen as subsystem i because all subsystems will eventually be considered and the power is always normalized to modal energy.

Step 3: If subsystem j is coupled to subsystem i, the available power that can flow into subsystem j is calculated using the transmission coefficient as shown in equation (2.65). This transmitted available power now becomes the 'starting available power' in subsystem j for further tracking.

$$W_{\mathrm{s},\,j} = \tau_{ij} W_{\mathrm{a},\,i} \qquad (2.65)$$

All subsystems which are coupled to subsystem i must be considered as forming different paths to track. It is noted that the case when $j = i$ also needs to be considered, which means that power reflected back into subsystem i as new 'starting available power' in subsystem i can be calculated using the reflection coefficient r_{ij} as in equation (2.66).

$$W_{\mathrm{s},\,i} = r_{ij} W_{\mathrm{a},\,i} \qquad (2.66)$$

The reflected power from a junction may, or may not be tracked further. If it is not to be tracked any further, it must be considered as residual power, $W_{\mathrm{r},\,j}$, which is then subtracted from element (j, i) of matrix **A**.

It is noted that in standard SEA, the calculation proceeds as discussed in section 2.2.6 using:

$$\omega n_i \eta_{ij} = \int_0^{L_{ij}} \int_{-\pi/2}^{\pi/2} W_{\mathrm{a},\,i} \mathrm{d}\theta \mathrm{d}l_i \tag{2.67}$$

where the length of the junction connecting subsystems i and j is L_{ij}. Thus the coupling loss factor can be calculated from:

$$\eta_{ij} = \frac{L_{ij} k_i}{\pi \omega n_i} \overline{\tau}_{ij} \tag{2.68}$$

where the angular-average transmission coefficient is given in equation (2.27).

Step 4: Track the 'starting available power' $W_{\mathrm{s},\,j}$ in subsystem j. As the wave propagates across the subsystem, the available power will be dissipated due to internal loss depending on the distances that the wave travels. Consider when the wave reaches another coupling junction, the wave has travelled a distance of κ_j, then the remaining available power $W_{\mathrm{e},\,j}$ can be calculated from:

$$W_{\mathrm{e},\,j} = W_{\mathrm{s},\,j} \exp(-\omega \eta_{jj} \kappa_j / c_{\mathrm{g},\,j}) \tag{2.69}$$

Note that this differs from the proposal by Heron [16] which used an average distance for polygonal plates, whereas here the exact distance travelled can be calculated using ray tracing algorithm described in the next section.

The power loss due to internal dissipation is given by:

$$W_{\mathrm{l},\,j} = W_{\mathrm{s},\,j} - W_{\mathrm{e},\,j} \tag{2.70}$$

This part of power is no longer available for further transmission, and should be subtracted from element (j, i) of matrix **B** as the power transfer from available power that originated in subsystem i to unavailable power in subsystem j. Subtraction instead of summation is due to the mathematical arrangement of the equations and to satisfy the power balance equations. It is worth mentioning that since all of the power traced in this process originated in subsystem i, it is only column i of matrices **A** and **B** that require updating due to the power balance relationship. As noted previously, the power balance can be checked at any time by summing each column of **A**+**B** to ensure it is equal to zero.

For one-dimensional subsystems, the wave propagation distance in subsystem j, κ_j, in equation (2.69) is only related to the length of the beam subsystem. However, for two-dimensional plate subsystems, the travelling distance requires geometric calculations to track the wave propagation path from one junction to another. Considering the initial available power $W_{a,\,i}$, in order to determine the exact wave propagation path, there are two factors to take into account. As shown in equation (2.64), $W_{a,\,i}$ is dependent on the incident wave angle; hence different wave angles result in different propagation paths. Another important factor is the position along the coupling junction where $W_{a,\,i}$ is injected. The power injection position along the coupling junction does not only affect the wave propagation path, but also determines the power injection position at the next junction. Only with this knowledge can the power flow be tracked further. Therefore, both factors need to be incorporated into the geometrical calculation. Section 2.4.5 introduces a geometric ray tracing theory to determine the wave propagation path within a subsystem.

If the initial power, $W_{a,\,i}$, is associated with an incident wave angle, θ, and the power injection position occurs at the coordinate l_{ij} along the junction between subsystem i and j where $0 \leq l_{ij} \leq L_{ij}$ (L_{ij} is the length of this junction). Hence the resulting ASEA matrices **A** and **B** will be a function will be functions of θ and l_{ij}, denoted as $A_{ij}^{\theta,l_{ij}}$ and $B_{ij}^{\theta,l_{ij}}$ respectively. ASEA calculation has to consider every position along the junction with the length of L_{ij} and every possible incident wave angle. This can be achieved by performing an integral for all possible incident wave angles and all power injection positions along the junction as:

$$\mathbf{A}_{ij} = \int_0^{L_{ij}} \int_{-\pi/2}^{\pi/2} A_{ij}^{\theta, l_{ij}} \mathrm{d}\theta \mathrm{d}l_{ij} \tag{2.71}$$

$$\mathbf{B}_{ij} = \int_0^{L_{ij}} \int_{-\pi/2}^{\pi/2} B_{ij}^{\theta, l_{ij}} \mathrm{d}\theta \mathrm{d}l_{ij} \tag{2.72}$$

Step 5: Take $W_{\mathrm{e},j}$ as the injected power and keep tracking the power by repeating the procedure from Step 3. Matrices **A** and **B** are used as accumulators with the elements in column *j* being updated throughout this process. The whole process can stop at any stage leaving the remaining power $W_{\mathrm{r},j}$. This residual power must be subtracted from element (*j*, *i*) of matrix **A** in order to satisfy the power balance equations. The convergence of ASEA depends on how far the power is tracked. This is indicated by the number of subsystems across which the power is tracked, resulting in an ASEA level number. For example, by the end of the calculation, if the power has been tracked across each subsystem twice, it indicates an ASEA level number of two i.e. ASEA2. If the level number is very large, such that matrix **A** is effectively zero, ASEA is equivalent to a ray tracing procedure where all phase effects are ignored.

Step 6: After finishing an ASEA calculation for one coupling junction on subsystem *i*, the same procedure is repeated for all the other junctions with subsystem *i* restarting from Step 2.

Step 7: After completing the calculations for all the junctions in subsystem *i*, repeat the same procedure for all the other subsystems from Step 2.

Step 8: The final results of matrices **A** and **B** that will be used in equation (2.50) to calculate subsystem responses are summations of the **A** and **B** results obtained from Step 7 for each subsystem:

$$\begin{aligned} \mathbf{A} &= \sum_{k=1}^{J_1} \mathbf{A}_{1k} + \ldots + \sum_{k=1}^{J_i} \mathbf{A}_{ik} + \ldots \sum_{k=1}^{J_N} \mathbf{A}_{Nk} \\ \mathbf{B} &= \sum_{k=1}^{J_1} \mathbf{B}_{1k} + \ldots + \sum_{k=1}^{J_i} \mathbf{B}_{ik} + \ldots \sum_{k=1}^{J_N} \mathbf{B}_{Nk} \end{aligned} \tag{2.73}$$

where $J_1, J_2, ..., J_N$ is the number of junctions for each subsystem and N is the number of subsystems. Note that $\mathbf{A}_{ik}$ and $\mathbf{B}_{ik}$ correspond to the coupling between subsystem i ($1 \leq i \leq N$) and another subsystem through junction k ($1 \leq k \leq J_i$). So here k does not represent subsystem number as in equation (2.71) and (2.72).

Substituting equation (2.71) into (2.73) gives:

$$\mathbf{A} = \sum_{i=1}^{N} \sum_{k=1}^{J_i} \int_0^{L_{ik}} \int_{-\pi/2}^{\pi/2} A_{ik}^{\theta, l_{ik}} \mathrm{d}\theta \mathrm{d}l_{ik} \tag{2.74}$$

$$\mathbf{B} = \sum_{i=1}^{N} \sum_{k=1}^{J_i} \int_0^{L_{ik}} \int_{-\pi/2}^{\pi/2} B_{ik}^{\theta, l_{ik}} \mathrm{d}\theta \mathrm{d}l_{ik} \tag{2.75}$$

This derivation is based on only considering bending wave transmission. If in-plane waves need to be taken into account, the ASEA calculation needs to start again from Step 1 for in-plane transmission and the entire process is repeated.

Step 9: Solve equation (2.50) using matrices **A** and **B** and by assigning the power input for rain-on-the-roof in matrix **P**.

2.4.5 ASEA for two-dimensional subsystems using ray tracing

Heron [64] successfully applied Advanced Statistical Energy Analysis to one-dimensional rod systems. However, when it comes to a two-dimensional subsystems, as indicated by equations (2.74), Heron noted that the ASEA calculation could be intensive.

The key issue in applying ASEA to two-dimensional plate systems is to determine the wave propagation path used in (2.69) with the knowledge of the incident wave angle and position of wave injection. The theory of Geometrical Ray Tracing (GRT) often used in the area of optics and room acoustics is used to calculate the wave propagation paths.

2.4.5.1 Brief review of ray tracing theory in acoustics and structural vibration

Ray tracing theory is used in the study of geometrical room acoustics to model the sound propagation path in space at high frequencies where the sound waves can be considered to propagate along straight lines [65]. When the propagation of a wave is obstructed by geometrical boundaries of the space, it is either modelled as a specular reflection, diffraction or diffusion. By tracing the rays, not only the propagation paths can be determined, but also the sound energy distribution in space can be obtained by summing the acoustic energy traces at receiver positions. However, the energy summation can only be carried out on the basis that the energies carried by rays are uncorrelated.

For vibration fields, Cremer [34] applied the concept of ray tracing to calculate the responses of a simple rod by using wave summation. Gunda *et al.* [66] used image source method to analyze a square plate structure. Cotoni and Le Bot [67] extended the ray tracing methods to coupled thin plate structures to deal with both specular and diffuse reflection. The high frequency ray tracing methods allow calculation of the energy distribution across the subsystem with certain level of accuracy instead of obtaining a spatially averaged response as in SEA. However, this accuracy is at the cost of computational efforts as numerous rays need to be generated in order to use the energy summation method to get reasonable accuracy.

Compared with the above ray tracing methods for structural problems, the computation load is relatively low for ASEA as the energy distribution in the subsystem is not calculated. With the incident wave angle and wave injection position known for a specific ray, all that is needed is to calculate is the propagation path, position and wave angle when the ray strikes the next junction.

2.4.5.2 Mathematical description of ray tracing

Assume that the plate subsystem has polygonal shape with junctions and uncoupled boundaries as shown in Figure 2.4. If we only consider specular reflection, then the angles of incidence and transmission follow Snell's law.

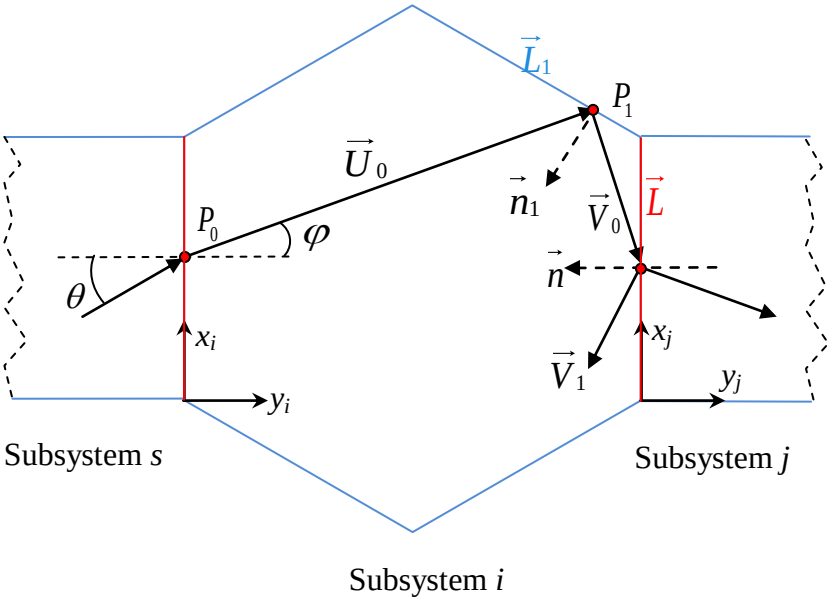

Figure 2.4 Geometric ray tracing for polygon plate subsystem (The blue coloured lines are referred to as boundaries which are not connected to other subsystems; the red lines are referred to as junctions which are connected to at least one other subsystem.)

Consider a wave injected from subsystem s to subsystem i at position P_0 with an incident wave angle of θ, the transmitted wave angle φ in subsystem i is calculated using Snell's law as:

$$k_s \sin\theta = k_i \sin\varphi \tag{2.76}$$

where k_s and k_i are wavenumbers of subsystems *s* and *i*.

When the wave travels across subsystem *i*, a local coordinate system x_i-y_i is used for calculation. The waves can be represented by unit vectors {*m*, *n*} pointing in the direction of propagation. The transmitted wave is expressed by vector $\vec{U}_0$; hence for the transmitted wave angle φ and injection position coordinate $P_0(x_{i0}, y_{i0})$. $\vec{U}_0$ can be expressed as:

$$\vec{U}_0 = \begin{bmatrix} m \\ n \end{bmatrix} = \begin{bmatrix} \cos\varphi \\ \sin\varphi \end{bmatrix} \tag{2.77}$$

The ray function can then be calculated from:

$$\begin{aligned} &\frac{x_i - x_{i0}}{m} = \frac{y_i - y_{i0}}{n} \\ \Rightarrow &\frac{x_i - x_{i0}}{\cos\varphi} = \frac{y_i - y_{i0}}{\sin\varphi} \end{aligned} \tag{2.78}$$

Equation (2.78) can also be written in a general form as

$$Rx_i + Ty_i + C = 0 \tag{2.79}$$

where *R*, *T* and *C* are constants for a known wave.

When the wave strikes the first boundary $\vec{L}_1$ as shown in Figure 2.4, the reflected wave is represented by vector, $\vec{V}_0$, which can be calculated using equation (2.80).

$$\vec{V}_0 = \vec{U}_0 - 2(\vec{U}_0 \cdot \vec{n}_1)\cdot\vec{n}_1 \tag{2.80}$$

where the unit vector $\vec{n}_1$ is a normal vector at the intersection point between the wave and the first reflecting boundary so that $\vec{n}_1 \times \vec{L}_1 = 0$.

The intersection point between the wave and the reflecting boundary $\vec{L}_1$, is $P_1(x_{i1}, y_{i1})$, can be calculated from:

$$\begin{bmatrix} x_{i1} \\ y_{i1} \end{bmatrix} = \begin{bmatrix} x_{i0} \\ y_{i0} \end{bmatrix} - \frac{Rx_{i0} + Ty_{i0} + C}{Rm + Tn} \begin{bmatrix} m \\ n \end{bmatrix} \tag{2.81}$$

As the boundary $\vec{L}_1$ is bounded within a certain length, it is necessary to find out whether the intersection point is inside or outside the perimeter of the subsystem.

The boundary $\vec{L}_1$ is bounded by two points $P_{1-L}(x_{i1-L}, y_{i1-L})$ and $P_{2-L}(x_{i2-L}, y_{i2-L})$, such that the intersection point $P_1(x_{i1}, y_{i1})$ is only within the boundary by satisfying the following equation:

$$\begin{bmatrix} |x_{i1-L} - x_{i2-L}| \\ |y_{i1-L} - y_{i2-L}| \end{bmatrix} = \begin{bmatrix} |x_{i1} - x_{i1-L}| \\ |y_{i1} - y_{i1-L}| \end{bmatrix} + \begin{bmatrix} |x_{i1} - x_{i2-L}| \\ |y_{i1} - y_{i2-L}| \end{bmatrix} \tag{2.82}$$

If the intersection point is located on the boundary, the distance D between P_1 and P_0 can be calculated from:

$$D = \sqrt{(x_{i0} - x_{i1})^2 + (y_{i0} - y_{i1})^2} \tag{2.83}$$

The incident wave angle, θ_{inc}, impinging upon the junction can also be calculated from vector $\vec{U}_0$ using:

$$\theta_{\text{inc}} = \arctan\left(\frac{n}{m}\right) \tag{2.84}$$

If the boundary is a reflecting boundary such as $\vec{L}_1$ shown in Figure 2.4, ASEA calculation requires ray tracing theory to keep tracking the wave until a junction obstructs the ray such that the propagation distance should be the summation of the propagation distance calculated after each reflection. If there is more than one

junction in the subsystem, it is always the first junction that needs to be considered as the reflected power will no longer be traced and treated as residual power in ASEA matrices.

When the ray hits the junction, it will be transmitted to the next subsystem. With the knowledge of the intersection position and the wave vector, the calculation repeats from the beginning of the derivation of Section 2.4.5.2 for the next subsystem until it meets the required ASEA level number.

2.4.5.3 Flow chart of the ray tracing algorithm

Based on the above mathematical description of the ray tracing theory for ASEA to calculate wave propagation distance, the following flow chart shown in Figure 2.5 demonstrates the algorithm used for ray tracing in ASEA when power is injected into one subsystem.

The input parameters include (a) the geometry of each subsystem in the local coordinate system where all the boundaries and junctions are labelled from 1 to N_b; (b) the coordinate of the power injection position and (c) the transmitted wave angle.

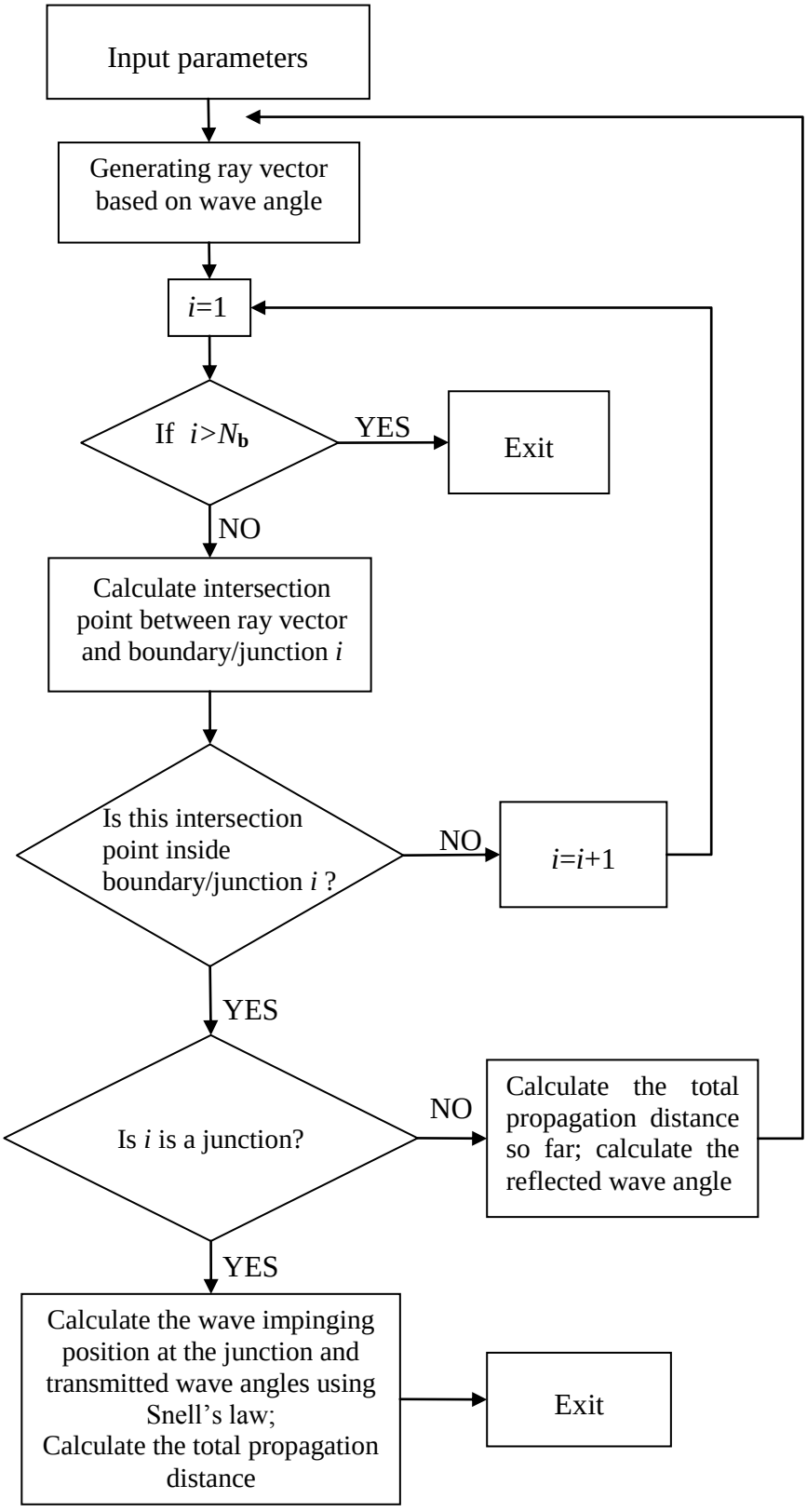

Figure 2.5 Flow chart of geometrical ray tracing across plate subsystems for ASEA

2.5 Numerical modelling using Finite Element Method (FEM)

2.5.1 Literature review: the application of FEM in structural vibration

The finite element method is widely used in solving complex elasticity and structural analysis problems in civil and aeronautical engineering. In FEM, continuous structures are discretized into a set of elements connected through nodal points [6] and the responses of these nodal points are calculated from the equations of motion including a mass and stiffness matrix. This section reviews the application of FEM specifically in the area of structural dynamic analysis for coupled plates.

Simmons [68] used FEM to calculate the vibration transmission across L- and H-junctions of plates. The energies of the plates calculated from FEM were then used to determine the coupling loss factors in SEA. It was observed that responses predicted from FEM at individual positions and frequencies are not reliable in the context of SEA due to the discrepancies between the real structure and the numerical models in terms of material properties and boundary conditions, which will result in a shift in eigenfrequencies and error in mode shapes. Therefore, spatially averaged energies of the plates in frequency bands are required for the analysis. The results were found to be in good agreement with theoretical and measurement results.

Steel and Craik [69] used FEM to predict the coupling loss factors at low frequencies with low mode overlap down to the fundamental mode. It was found that at the fundamental mode, coupling loss factors calculated from FEM agrees well with the theoretical method using the method proposed by Craik *et al.* [30] by spatially averaging point mobilities of the receiving subsystem. However, discrepancies occured above the fundamental frequency and it was indicated that this could be caused by errors in accurately modelling the real structure in FEM.

Hopkins [51, 70] used a Monte Carlo method with FEM to determine coupling loss factors where subsystems had low mode counts and low modal overlap. The comparison between FEM predictions, measured data and SEA using a wave

approach confirmed the existence of wave conversion between bending and in-plane waves at the structural junction.

Mace and Shorter [28] used FEM to analyze energy flow among subsystems. The nodal responses of the subsystems to distributed time harmonic excitation were decomposed into global modes so that better computational efficiency could be achieved. Mace and Rosenberg [33] extended this method to investigate the effect of subsystem irregularity on the coupling loss factors between two plates. It was concluded that coupling power is sensitive to the subsystem irregularity when the coupling is strong, normally the cases with low damping.

Fredö [71] used FEM in combination with SEA to determine the power transmission between coupled plates. It was indicated that the use of FEM can overcome many deficiencies of SEA such as the abilities of dealing with complicated subsystems, narrow band sources and non-resonant transmission. The Energy Flow Coefficient (EFC) between two subsystems calculated from FEM was case specific however it tended towards the CLF at high frequencies. It was also shown that the existence of negative EFCs was the results of substantial non-resonant transmission.

2.5.2 FEM modelling

2.5.2.1 Shell element S4R

In this thesis, finite element analysis is carried out using commercial software ABAQUS 6.10. A rectangular four-node, shell element, S4R is used to model isotropic, homogeneous plates and periodic ribbed plates. The S4R element is a general purpose element which is quoted as giving "robust and accurate solutions in all loading conditions for thin and thick shell problems" [72]. It uses Kirchhoff's thin plate theory when plate thickness is small and changes to Mindlin–Reissner's thick plate theory as the thickness increases. The thin plate limit is assessed in section 3.1.3 by using the comparison between the plate thickness and the wavelength.

In order to make a preliminary assessment of the S4R element, Figure 2.6 compares FEM calculations of the driving-point mobility on a rectangular simply-supported plate with infinite plate theory for a thin plate calculated using equation (2.13). Mobilities are calculated in narrow bands with 2 Hz resolution and averaged into one-third octave bands. The plate has a thickness of 13 mm and the element size is chosen to be 10 mm which allows seven elements per wavelength at the highest frequency of interest at 10 kHz. The close agreement between FEM and infinite plate theory between 1 kHz and 5 kHz indicates that the S4R element adequately represents thin plate theory. However, there appears to be a distinct offset from infinite plate theory of up to 2 dB between 6.3 kHz and 10 kHz. The thin plate limit calculated using equation (3.28) is 9038 Hz. Hence it is possible that this small discrepancy is due to the FEM element reproducing thick plate behaviour near and above the thin plate limit.

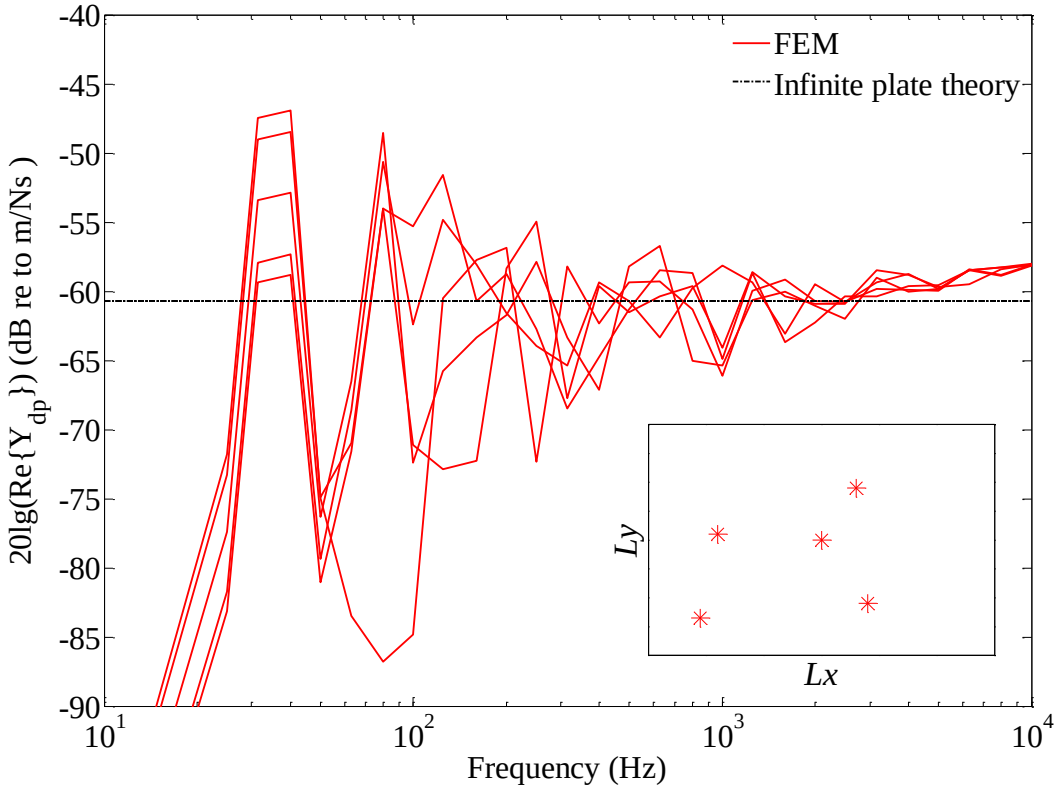

Figure 2.6 Driving-point mobilities from five randomly chosen positions (indicated by *) on a simply-supported, rectangular plate calculated using FEM averaged in one-third octave bands compared with infinite plate theory. ($L_x \times L_y$=1.2 m ×0.8 m, h_p= 0.013m, ρ=1180 kg/m^3, E=5.93 ×10^9 N·m^{-2} and μ=0.3)

2.5.2.2 Excitation: rain-on-the-roof

Statistically independent excitation is applied to each subsystem by using rain-on-the-roof (ROTR) excitation on all the unconstrained nodes over the plate surface with complex forces of unity magnitude and random phase. However, on ribbed plates these forces are only applied to nodes in the bays (i.e. not on the ribs). In this thesis, ten sets of different rain-on-the-roof are used to calculate the average responses with confidence intervals.

2.5.2.3 Damping

Ignoring the loss due to sound radiation, the internal loss factor is solely determined by the damping effects of the subsystems. Damping is introduced in FEM using the fraction of critical damping, ζ, which is related to the internal damping loss factor by Cremer *et al*. [34] and Crede and Harris [73]:

$$\eta_{ii}=2\zeta \tag{2.85}$$

This relation is only valid for the damping–controlled modal response and when ζ <0.1 based on Cremer *et al*. [34] and Crede and Harris [73].

All FEM models presented in this thesis use constant damping values which are entered into ABAQUS by using the values of the fraction of critical damping.

2.5.2.4 Boundary conditions

In this thesis, the term ‘bending wave only models’ is used where only bending waves are transmitted across the junction. The junction nodes are simply-supported (or ‘pinned’) to prevent displacement in the three coordinate directions. Hence only bending moments can be transmitted and in-plane waves cannot be generated at the junction. For ‘bending and in-plane wave models’ the junction nodes are unconstrained to allow displacement and rotation which allows conversion between bending and in-plane waves at the junction.

2.5.2.5 Post-processing

Individual frequency results from FEM are combined into one-third-octave bands for ESEA analysis. There are two reasons that a frequency band average should be used instead of using individual frequencies directly. Firstly, errors in calculating eigenfrequencies occur at high frequencies even with accurate finite element models due to the discretization of the structure. Secondly, for complex models, discrepancies in material properties, boundary conditions and geometries of the models between the FEM and the real structure are almost inevitable. Therefore, it is often experienced that a frequency shift occurs in eigenfrequencies between the FEM and real structure. However, if the responses are combined into wide frequency bands, it is shown to be able to give a sufficiently accurate estimate of the response of the structures.

2.5.2.6 Computational resources

Computation is carried out using High Performance Computing Clusters provided by the University of Liverpool on 8 dual processor dual core 2.4 GHz nodes with 8 GB of RAM.

2.5.3 FEM element mesh error

In FEM calculations, inadequate mesh refinement can be a source of error. For reasonable accuracy, it is usually recommended that at least six representative elements should fit into the shortest wavelength present in the analysis. For improved accuracy, ten or more elements can be used at the shortest wavelength, but the computation time and memory requirements rapidly increase.

To balance computational efficiency and accuracy, a method of evaluating the adequacy of the element size and mesh by comparing the input power with the total power contained in the system is used as described by Hopkins [74].

The total power input into a subsystem can be calculated from equation (2.86) using the complex forces applied on N unconstrained nodes and their displacements.

$$W_{\text{in}} = \frac{\omega}{2}\sum_{n=1}^{N}\left(\text{Im}\left\{\underline{\hat{F}}\right\}\text{Re}\left\{\underline{\hat{\xi}}\right\} - \text{Re}\left\{\underline{\hat{F}}\right\}\text{Im}\left\{\underline{\hat{\xi}}\right\}\right)_n \tag{2.86}$$

The power dissipated by the subsystem after response, W_{out}, can be calculated from equation (2.87):

$$W_{\text{out}} = \omega\eta_i E_i \tag{2.87}$$

For bending waves, E_i can be calculated using equation (2.88) from the displacement perpendicular to the plate surface for all N elements in the FEM model.

$$E_i = m_i\left\langle v^2\right\rangle = \omega^2\left[\frac{1}{2}\sum_{n=1}^{N} m_n\left|\underline{\hat{\xi}}_n\right|^2\right] \tag{2.88}$$

The mesh and element size can be evaluated by calculating the element mesh error, $e_{\text{mesh,}}$ between W_{in} and W_{out}, as shown in equation (2.89).

$$e_{\text{mesh}} = \frac{\left|W_{\text{out}} - W_{\text{in}}\right|}{W_{\text{in}}}\times 100\% \tag{2.89}$$

Because e_{mesh} is dependent upon the damped modal response, it is only strictly valid at frequencies under damping control. As e_{mesh} only considers bending wave energy, e_{mesh} will be large when there is significant in-plane wave energy.

Hopkins [74] has shown that whilst the mesh error is usually close to 0% in the vicinity of the global eigenfrequencies when the element size is adequate, the error is highly dependent upon the excitation, for example, there can be large variations between different sets of ROTR. Mesh errors ranging between 0% and 40% were typically found to indicate satisfactory element sizes.

2.6 Conclusions

This chapter reviewed and described the principles of SEA, FEM and ASEA as prediction models for structure-borne sound transmission that will be used in this thesis.

ESEA was introduced as an approach to estimate coupling loss factors from numerical experiments with FEM which will be compared with coupling loss factors determined from wave theory that will be described in chapter 5.

ASEA was introduced as an extension to SEA which can incorporate tunnelling mechanisms between physically unconnected subsystems. ASEA will be tested on structural junctions including periodic ribbed plates in chapters 6, 7 and 8. A ray-tracing algorithm used to track power flow among subsystems in ASEA was described in detail.

The models in this chapter were described in a generic form that applies to many different kinds of vibration fields. Therefore the next chapter, Chapter 3, describes the specifics of vibration fields on isotropic and orthotropic plates that are the subject of this thesis.

3 Vibration field on isotropic and orthotropic plates

This chapter presents theoretical models based on the wave approach for the vibration propagation on plate structures.

It begins with the discussion of free vibration in thin isotropic, homogeneous plates. Three different wave types that are supported by the plate are described including bending, quasi-longitudinal and transverse shear waves. The equation of motion governing the wave propagation is presented for all three wave types, along with the thin plate limit and other properties of isotropic plates such as modal density and modal overlap.

Structures consisting of thin plates stiffened or reinforced by a periodic array of ribs are widely used in aircraft, ships and buildings. The reason that these types of structures are widely used is primarily for their advantageous elastic properties. It is shown that rearranging the distribution of material in structural members is the most efficient way to resist stress [75], and also result in stronger structures, more economical in material. Although the ribs normally take a relatively small part of the total weight of the structures, they substantially influence the strength, stiffness and stability of the plates [75], and also affect the dynamic behaviour of the plates. Unlike isotropic homogeneous structures where elastic properties in all directions are found to be identical, the ribbed plates often exhibit different elastic properties in two mutually perpendicular directions and therefore can be considered as orthotropic. It is noted that these types of structures are often regarded as structurally orthotropic to distinguish them from naturally orthotropic materials such as timber. In this thesis, only structurally orthotropic plates are discussed so that the materials of the separate plates as well as the ribs are always homogeneous and isotropic.

Since the elastic properties strongly affect the wave propagation supported by the plates, the wave propagation on a periodic ribbed plate can be analyzed by considering the orthotropic properties of the entire structure. The dynamic behaviour of a ribbed plate can be described by considering an equivalent flat plate with orthotropic elastic properties. The equations of motion for thin orthotropic plates are derived in a similar manner to the isotropic plates. However,

the description of orthotropic plates is more complex due to the angle-dependent elastic properties.

3.1 Wave propagation on thin, isotropic, homogeneous plates

An isotropic, homogeneous thin plate typically supports three different types of waves in the audio frequency range: bending, quasi-longitudinal and transverse shear waves [34]. The latter two are described as in-plane waves due to the motion staying in the same plane as the structure.

Among these three wave types, bending waves tend to be the most important for many structure-borne sound transmission problems due to the sound radiation caused by their out-of-plane displacements. However, for wave propagation across large distances where several structural junctions are involved in the transmission path, conversion between bending and in-plane waves will occur and needs to be considered [76] as for built-up structures it can make a significant contribution to the total change of energy in the modelling of SEA [51, 77]. Therefore, in this section, the equations of motion for all three types are presented.

3.1.1 Bending waves

Applying the classical thin plate theory [78] where the bending wavelength is larger than the plate thickness, the equation of motion for a bending wave travelling in the *x*-*y* plane (see Figure 3.1) can be expressed as a function of the lateral displacement, ξ, in the following form

$$\nabla^4 \xi + \frac{\rho h_\mathrm{p}}{B_\mathrm{p}} \frac{\partial^2 \xi}{\partial t^2} = 0 \tag{3.1}$$

where ρ is the plate density, h_p is the thickness of the plate and B_p is bending stiffness (or flexural rigidity). For isotropic plate, B_p can be calculated from:

$$B_\mathrm{p} = \frac{E h_\mathrm{p}^2}{12(1-\mu^2)} \tag{3.2}$$

where E is Young's modulus and μ is the Poisson's ratio of the plate material.

with the fourth-order differential factor ∇^4 defined as:

$$\nabla^4 = \frac{\partial^4}{\partial x^4} + 2\frac{\partial^4}{\partial x^2 \partial y^2} + \frac{\partial^4}{\partial y^4} \tag{3.3}$$

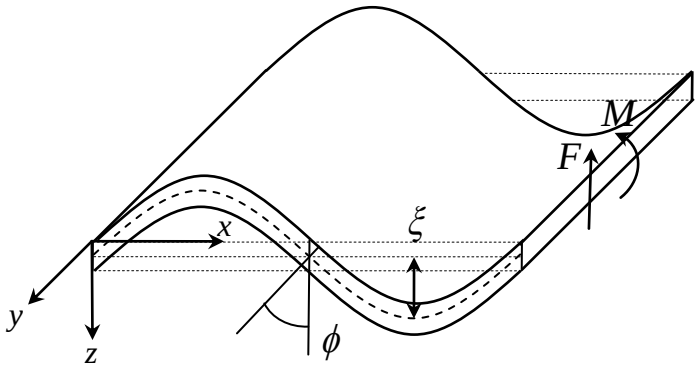

Figure 3.1 Bending wave propagating along a plate element (NB lateral displacement ξ and angular displacement ϕ are exaggerated on the diagram)

Figure 3.1 shows the parameters describing bending wave motion on a plate for a plane harmonic bending wave travelling in a direction characterized by a propagation heading angle, θ, on the positive x-y plane. The solution to equation (3.1) can be written as:

$$\xi(x, y, t) = A\exp[k(x\cos\theta + y\sin\theta)]\exp(i\omega t) \tag{3.4}$$

where A is the complex wave amplitude.

Substituting equation (3.4) into (3.1) leads to two pairs of solutions for k as:

$$k = \pm ik_{\mathrm{B}} \tag{3.5}$$

$$k = \pm k_{\mathrm{B}} \tag{3.6}$$

Where k_{B} is defined as bending wavenumber given as:

$$k_{\mathrm{B}} = \left(\frac{\rho h_{\mathrm{p}} \omega^2}{B_{\mathrm{p}}} \right)^{\frac{1}{4}} \tag{3.7}$$

The imaginary wavenumbers in equation (3.5) represent the propagating waves with '$-$' indicating the positive direction and '+' indicating negative direction of propagation. The real wavenumbers in equation (3.6) represent the near-field which decays exponentially.

Therefore, the general solutions of the bending wave equation for an isotropic plate have four complex amplitudes corresponding to the two pairs of wavenumbers shown as:

$$\begin{aligned} \xi(x,y,t) = \{ & A_1 \exp[ik_{\mathrm{B}}(x\cos\theta + y\sin\theta)] + A_2 \exp[-ik_{\mathrm{B}}(x\cos\theta + y\sin\theta)] + \\ & A_3 \exp[k_{\mathrm{B}}(x\cos\theta + y\sin\theta)] + A_4 \exp[-k_{\mathrm{B}}(x\cos\theta + y\sin\theta)] \} \exp(i\omega t) \end{aligned} \tag{3.8}$$

The four unknown amplitudes $\{A_1, A_2, A_3, A_4\}$ can be calculated by applying the corresponding boundary conditions or continuity relations.

The bending wave phase velocity is calculated from:

$$c_{\mathrm{B}} = \frac{\omega}{k_{\mathrm{B}}} = \left(\frac{\omega^2 B_{\mathrm{p}}}{\rho h_{\mathrm{p}}} \right)^{\frac{1}{4}} \tag{3.9}$$

The group velocity is defined as the velocity of the overall shape of the wave and it represents the velocity with which wave energy propagates. For bending wave, it is given as:

$$c_{\mathrm{g,B}} = \frac{\mathrm{d}\omega}{\mathrm{d}k_{\mathrm{B}}} = 2c_{\mathrm{B}} \tag{3.10}$$

Now only consider the wave propagation in *x*-direction, the bending wave can also be characterized by the rotation of the plate cross-section about *y*-axis, ϕ, which can be calculated from the lateral displacement ξ as:

$$\phi = \frac{\partial \xi}{\partial x} \tag{3.11}$$

At a cross-section perpendicular to *x*-axis, the moment acting on the edge due to bending wave propagation (see Figure 3.1) is given by:

$$M = -B_{\mathrm{p}}\left(\frac{\partial^2 \xi}{\partial x^2} + \mu \frac{\partial^2 \xi}{\partial y^2}\right) \tag{3.12}$$

The force at the edge is a combination of a shear force and a force that resists twisting at the boundary (see Figure 3.1) and is given as:

$$F = B_{\mathrm{p}}\left[\frac{\partial^3 \xi}{\partial x^3} + (2-\mu)\frac{\partial^3 \xi}{\partial x \partial y^2}\right] \tag{3.13}$$

The energy per unit width carried by bending wave can be characterized by the wave intensity with propagation amplitude *A* [34].

$$I_{\mathrm{B}} = |A|^2 B_{\mathrm{p}} \omega k_{\mathrm{B}}^3 \tag{3.14}$$

3.1.2 In-plane waves

The equations of motion for quasi-longitudinal wave and transverse shear wave in thin isotropic homogeneous plates are given by [34]:

$$\left(\frac{E}{(1-\mu^2)}\frac{\partial^2}{\partial x^2}+G\frac{\partial^2}{\partial y^2}-\rho\frac{\partial^2}{\partial t^2}\right)\xi_x+\frac{E}{2(1-\mu)}\frac{\partial^2\xi_y}{\partial x\partial y}=0 \tag{3.15}$$

$$\left(G\frac{\partial^2}{\partial x^2}+\frac{E}{(1-\mu^2)}\frac{\partial^2}{\partial y^2}-\rho\frac{\partial^2}{\partial t^2}\right)\xi_y+\frac{E}{2(1-\mu)}\frac{\partial^2\xi_x}{\partial x\partial y}=0 \tag{3.16}$$

Where ξ_x and ξ_y brepresent the in-plane displacement in the *x*- and *y*-directions respectively. *G* is the shear modulus given as:

$$G=\frac{E}{2(1+\mu)} \tag{3.17}$$

The solution of ξ_x and ξ_y can be obtained by introducing a displacement potential Φ and scalar function Ψ to uncouple the motion equations (3.15) and (3.16) developed by Cremer *et al.* [34] as:

$$\xi_x=\frac{\partial\Phi}{\partial x}+\frac{\partial\Psi}{\partial y} \tag{3.18}$$

$$\xi_y=\frac{\partial\Phi}{\partial y}-\frac{\partial\Psi}{\partial x} \tag{3.19}$$

The displacement potential Φ describes rotational part of the displacement which incorporates the quasi-longitudinal wave. The divergence-free part of the displacement which represents transverse wave is described by the stream function Ψ. Therefore, the general solution of the in-plane wave equations for harmonic wave propagating in the angle of θ can be similarly written as bending wave as:

$$\Phi(x,y,t)=\{A_1\exp[ik_{\mathrm{L}}(x\cos\theta+y\sin\theta)]+A_2\exp[-ik_{\mathrm{L}}(x\cos\theta+y\sin\theta)]\}\exp(i\omega t) \quad (3.20)$$

$$\Psi(x,y,t)=\{A_3\exp[ik_{\mathrm{T}}(x\cos\theta+y\sin\theta)]+A_4\exp[-ik_{\mathrm{T}}(x\cos\theta+y\sin\theta)]\}\exp(i\omega t) \quad (3.21)$$

where the in-plane quasi-longitudinal and transverse shear wavenumbers are given as:

$$k_{\mathrm{L}}=\omega\sqrt{\frac{\rho(1-\mu^2)}{E}} \quad (3.22)$$

$$k_{\mathrm{T}}=\omega\sqrt{\frac{\rho}{G}} \quad (3.23)$$

Thus, the phase velocities of the corresponding in-plane waves can be calculated:

$$c_{\mathrm{L}}=\frac{\omega}{k_{\mathrm{L}}}=\sqrt{\frac{E}{\rho(1-\mu^2)}} \quad (3.24)$$

$$c_{\mathrm{T}}=\frac{\omega}{k_{\mathrm{T}}}=\sqrt{\frac{G}{\rho}} \quad (3.25)$$

Compared with the bending wave solution in equation (3.8) where the wave field is represented by four amplitude variables, for quasi-longitudinal and transverse shear waves, each only need two amplitude variables to characterize the wave propagation.

As the in-plane waves travels in the *x*-*y* plane, it induces a normal force F_x and an in-plane shear force F_y. The two forces at θ=0 ° can be expressed in terms of in-plane displacements given by Timoshenko [78] as:

$$F_x = \frac{Eh_\mathrm{p}}{(1-\mu^2)}\left(\frac{\partial \xi_\mathrm{L}}{\partial x} + \mu \frac{\partial \xi_\mathrm{T}}{\partial y}\right) \tag{3.26}$$

$$F_y = Gh_\mathrm{p}\left(\frac{\partial \xi_\mathrm{L}}{\partial y} + \frac{\partial \xi_\mathrm{T}}{\partial x}\right) \tag{3.27}$$

3.1.3 Thin plate limit

Equations (3.1) and (3.15) for bending and quasi-longitudinal waves are both based on the assumption that the plate is thin enough that the wavelength is much larger than the plate thickness. This places an upper limit to the frequency of analysis because at higher frequencies, the shear strain and hence the shear stress across the plate thickness which is not considered in the thin plate theory cannot be neglected [79]. Cremer *et al.* [34] suggested the frequency limits in thin plate theory for both bending and quasi-longitudinal waves at which the relative errors in the phase velocity is 10% and 3% respectively. For bending waves, it is approximately equivalent to the condition that bending wavelength equals six times of the plate thickness. Therefore, the thin plate limit for bending waves can be evaluated using equation (3.28). Similarly, for quasi-longitudinal waves, the thin plate limit for the use of equation (3.15) is given in equation (3.29). It is noted that thin plate limits are only required for bending and quasi-longitudinal waves which both have contributions to the lateral displacement while for transverse shear waves, there is no such requirement in the formulation of the wave equations.

$$f_{\mathrm{B,thin}} < \frac{c_\mathrm{L}}{20h_\mathrm{p}} \tag{3.28}$$

$$f_{\mathrm{L,thin}} < \frac{c_\mathrm{L}}{3h_\mathrm{p}} \tag{3.29}$$

3.1.4 Modal density

Modal density for two-dimensional subsystems is strongly dependent on the geometry as well as the boundary conditions. However, Xie *et al.* [80] show that for homogeneous elements such as beams and uniform plates, the modal density will converge to asymptotic values regardless of the boundary conditions at high frequencies. Therefore the asymptotic modal densities can be used to represent *in-situ* subsystem modal densities without considering the boundary conditions.

Modal density of plate subsystems corresponding to different wave types are given in [19] as:

$$n_{\mathrm{B}}(f) = \frac{S\sqrt{3}}{h_{\mathrm{p}} c_{\mathrm{L}}} \quad \text{for bending waves (thin plate)} \tag{3.30}$$

$$n_{\mathrm{T}}(f) = \frac{4\pi f S}{c_{\mathrm{L}}^2 (1\text{-}\mu)} \quad \text{for transverse shear waves} \tag{3.31}$$

$$n_{\mathrm{Q}}(f) = \frac{2\pi f S}{c_{\mathrm{L}}^2} \quad \text{for quasi-longitudinal waves} \tag{3.32}$$

where μ is the Poisson's ratio of the plate material, and S is the surface area of the plate.

3.2 Wave propagation on thin, orthotropic plates

3.2.1 Literature review: orthotropic plate vibration

There is a large amount of literature on orthotropic plates; hence only the major contributions to the research on plate vibration are reviewed here.

Early investigations on the topic of orthotropic structures were generally based on the fact that natural materials are generally anisotropic. Toritsky [75] gave a review of some of the earliest works on the elasticity of orthotropic bodies. These works were purely theoretical and only considered naturally orthotropic structures.

Lechnitsky [81, 82] investigated the strain-stress relations and elastic properties for structurally orthotropic plates. Expressions were derived to characterize the elastic properties for stiffened plates as equivalent orthotropic plates. Based on this, the estimation of natural frequency for orthotropic plates with various boundary conditions was also presented.

Toritsky [75] investigated stiffened plates as structurally orthotropic plates and presented theoretical and empirical solutions for stiffened plates considering both bending and in-plane displacements.

Rao *et al.* [83] formulated bending wave propagation on orthotropic plates using the finite element method. However, this formulation couldn't incorporate in-plane waves due to the assumption of very large lateral displacements compared with in-plane displacement to simplify the geometric stiffness matrix.

Deobald and Gibson [84] applied the Rayleigh-Ritz method to model the bending of rectangular orthotropic plates and used finite element analysis to validate the analytical results. They also proposed a method to use natural frequencies of orthotropic plates from measurements to determine the elastic properties of the orthotropic plates.

3.2.2 Orthotropic plate theory

Timoshenko *et al.* [78] gave the relations between the stress and strain components for the case of plane stress in *x*-*y* plane as shown in Figure 3.2 (the stress in *z*-direction σ_z is ignored) written as:

$$\begin{bmatrix} \sigma_x \\ \sigma_y \\ \tau_{xy} \end{bmatrix} = \begin{bmatrix} E_x' & \mu_{yx}E_x' & 0 \\ \mu_{xy}E_y' & E_y' & 0 \\ 0 & 0 & G_{xy} \end{bmatrix} \begin{bmatrix} \varepsilon_x \\ \varepsilon_y \\ \gamma_{xy} \end{bmatrix} \tag{3.33}$$

where:

$$E_x' = \frac{E_x}{1-\mu_{xy}\mu_{yx}} \qquad E_y' = \frac{E_y}{1-\mu_{yx}\mu_{xy}} \tag{3.34}$$

According to Betti's reciprocity theorem for symmetry condition of the stiffness, the following relationship applies [75]:

$$E_x\mu_{yx} = E_y\mu_{xy} \tag{3.35}$$

The elastic modulus in the two principal directions E_x and E_y, shear modulus G_{xy} and Poisson's ratio μ_{xy} and μ_{yx} are used to characterize the equivalent material properties.

In this thesis, since the dynamic behaviour of orthotropic plates is only considered to be caused by the geometry of the plate cross-section due to the periodic stiffened ribs, the orthotropicity of the plate material is not considered so that all the structures discussed in this thesis are made of homogeneous materials. However, the equivalent elastic properties in two orthotropic directions of the periodic plate may not be equal to the material elastic properties. As a result, the equivalent properties must be used.

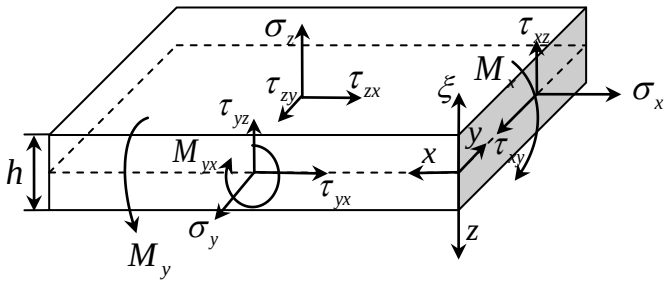

Figure 3.2 Stress-strain, resulting moment and lateral displacement of a plate element

3.2.3 Bending waves and angle-dependent bending stiffness

Considering bending wave propagating on the orthotropic plate, the strain components in equation (3.33) can be expressed as:

$$\varepsilon_x = -z\frac{\partial^2 \xi}{\partial x^2} \qquad \varepsilon_y = -z\frac{\partial^2 \xi}{\partial y^2} \qquad \gamma_{xy} = -2z\frac{\partial^2 \xi}{\partial x \partial y} \tag{3.36}$$

Substituting equation (3.36) into (3.33) gives:

$$\sigma_x = -z\left(E_x{}' \frac{\partial^2 \xi}{\partial x^2} + \mu_{yx} E_y{}' \frac{\partial^2 \xi}{\partial y^2} \right) \tag{3.37}$$

$$\sigma_y = -z\left(E_y{}' \frac{\partial^2 \xi}{\partial y^2} + \mu_{xy} E_x{}' \frac{\partial^2 \xi}{\partial x^2} \right) \tag{3.38}$$

$$\tau_{xy} = -2G_{xy} z \frac{\partial^2 \xi}{\partial x \partial y} \tag{3.39}$$

With the expressions of the strain components, the bending and twisting moments are given as:

$$M_x = \int_{-h/2}^{h/2} \sigma_x z \mathrm{d}z = -\left(B_x \frac{\partial^2 \xi}{\partial x^2} + \mu_{yx} B_y \frac{\partial^2 \xi}{\partial y^2} \right) \tag{3.40}$$

$$M_y = \int_{-h/2}^{h/2} \sigma_y z \mathrm{d}z = -\left(B_y \frac{\partial^2 \xi}{\partial y^2} + \mu_{xy} B_x \frac{\partial^2 \xi}{\partial x^2} \right) \tag{3.41}$$

$$M_{xy} = -\int_{-h/2}^{h/2} \tau_{xy} z \mathrm{d}z = 2B_{xy} \frac{\partial^2 \xi}{\partial x \partial y} \tag{3.42}$$

Similarly to the isotropic plate, the equation of motion for bending waves can be expressed as:

$$B_x \frac{\partial^4 \xi}{\partial x^4} + 2H \frac{\partial^4 \xi}{\partial x^2 \partial y^2} + B_y \frac{\partial^4 \xi}{\partial y^4} + \rho h \frac{\partial^2 \xi}{\partial t^2} = 0 \tag{3.43}$$

where H is:

$$H = \mu_{xy} B_y + 2B_{xy} \tag{3.44}$$

H describes the torsional effects of the plate, which can be estimated using a geometrical mean of the bending stiffness in two orthotropic directions as:

$$H = \sqrt{B_x B_y} \tag{3.45}$$

Troitsky [75] notes that equation (3.45) is only valid when the thickness of the plate is constant, the deflection of the plate is relatively small and the deformations can be considered to be fully elastic.

Consider a specific orthotropic plate consisting of an isotropic plate with periodic stiffened ribs as shown in Figure 3.3, the bending stiffness components are given in [85] as:

$$B_x = \frac{E_x' h_\mathrm{p}^3}{12} = \frac{E h_\mathrm{p}^3}{12(1-\mu^2)} \tag{3.46}$$

$$B_y = \frac{E_y' h_\mathrm{p}^3}{12} = \frac{E h_\mathrm{p}^3}{12(1-\mu^2)} + \frac{E I_{\mathrm{bx}}}{l} \tag{3.47}$$

$$B_{xy} = \frac{G_{xy} h_\mathrm{p}^3}{12} \tag{3.48}$$

where h_p is the thickness of the plate. It is assumed that both the ribs and plate are made of the same material with Young's modulus E and Poisson's ratio μ. Equivalent shear modulus G_{xy} can be calculated using equation (3.17) if the plate is isotropic, but with orthotropic plates, it is normally determined from

experiments although approximate estimations may exist for some cases. I_{bx}, the moment of inertia of the rib, can be calculated using equation (3.49).

$$I_{bx} = \frac{b_b h_b^3}{12} \tag{3.49}$$

Where b_b and h_b are the width and the thickness of the rib as shown in Figure 3.3 (b).

For the periodic ribbed plate in Figure 3.3, H is given in [85] as:

$$H = \frac{E}{12(1-\mu^2)} \tag{3.50}$$

The bending wavenumber for an orthotropic plate can be determined using the similar procedure to section 3.1.1, which also leads to four components to characterize the bending wave propagation and near-fields. For an orthotropic plate, the bending wavenumber is not only dependent on frequency, but also dependent on the wave heading angle. The angle-dependent wavenumber $k_B(\theta)$ can be calculated from:

$$k_B(\theta) = \sqrt{\omega} \sqrt[4]{\frac{\rho h_p}{B(\theta)}} \tag{3.51}$$

where the angle-dependent bending stiffness per unit width $B(\theta)$ is given in [86] as:

$$B(\theta) = B_x \cos^4\theta + 2(\mu_{xy} B_y + 2B_{xy}) \cos^2\theta \sin^2\theta + B_y \sin^4\theta \tag{3.52}$$

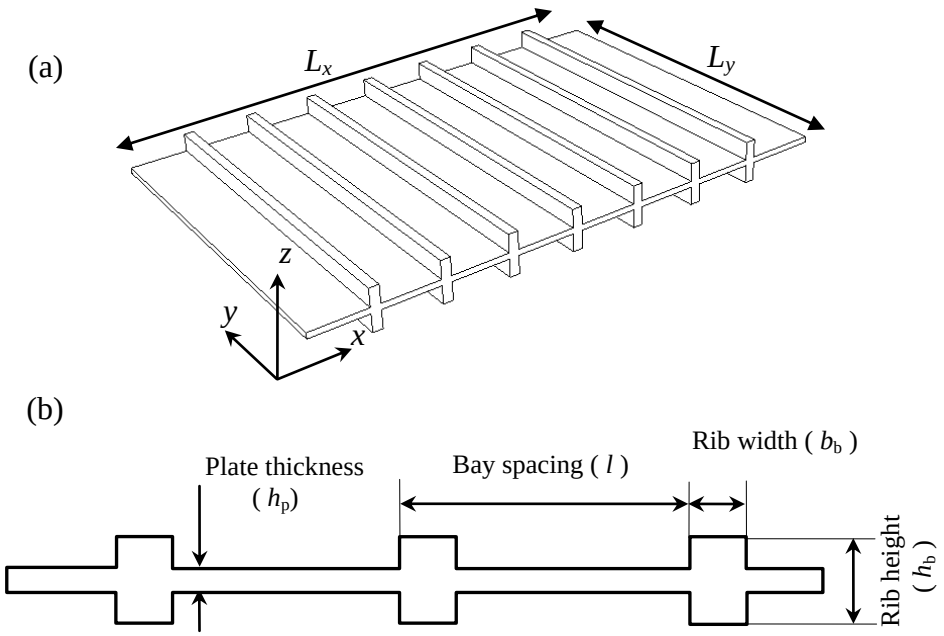

Figure 3.3 (a) Plate with periodic ribs symmetrically arranged around the centre line of the plate; (b) Dimension parameters of the periodic ribbed plate

Consider an orthotropic plate as shown in Figure 3.3 with dimensions and material properties shown in Table 2. Figure 3.4 shows the angle-dependent wavenumber for the ribbed plate at different frequencies. At low frequencies, the variation of the absolute values of bending wavenumber with the change of wave heading angle is small. This is because the bending wavelength is much larger than the rib spacing so the contribution of the stiffened ribs on the overall elastic properties of the plate is also small. However, at high frequencies where the bending wavelength is similar or smaller than the rib spacing, the values of wavenumber vary significantly. Note from equation (3.51) the ratio between the wavenumber at 0 ^{o}and 90 ^{o}is $\sqrt{B_x / B_y}$ and is independent of frequency. When the wave heading angles are close to the two principal directions (0 º10 ^{o}and 80 º90 º), the wavenumber does not show significant variance with heading angle .

Table 2: Dimension and material properties of a ribbed plate as shown in Figure 3.3

Dimensions	Material properties
$L_x \times L_y$=1.2 m ×0.8 m	ρ=1180 kg/m^3
h_p=13 mm; l=150 mm;	c_L=2350 m/s
b_b=30 mm; h_b=50 mm.	μ=0.3

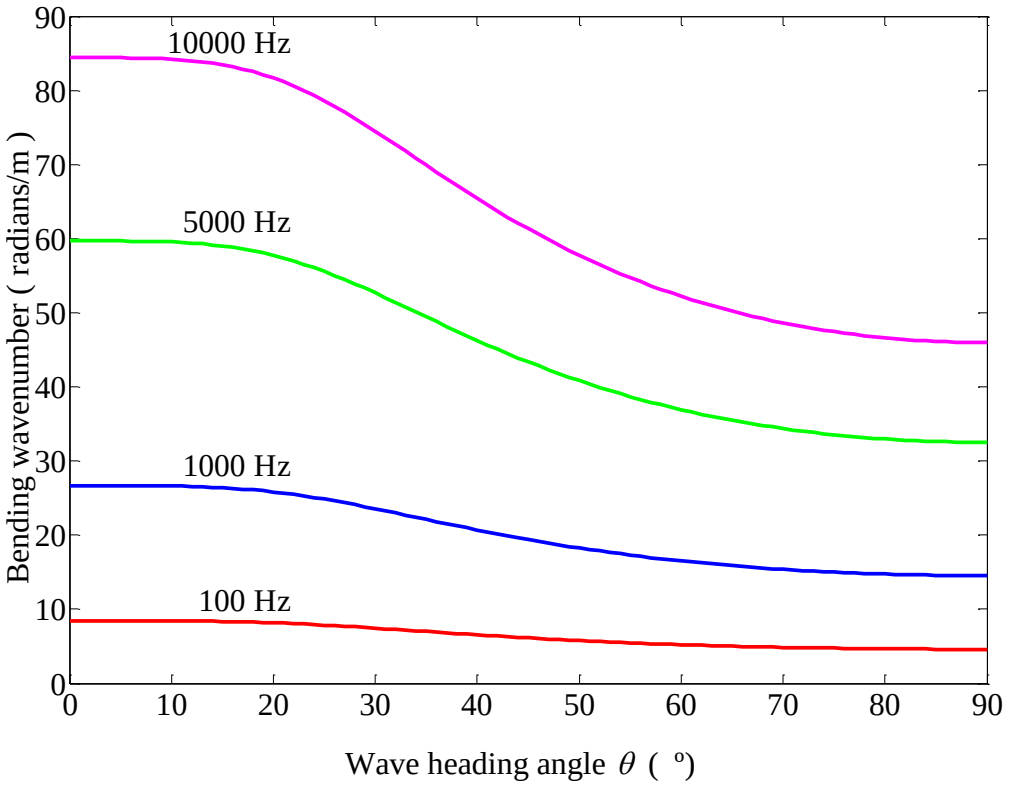

Figure 3.4 Angle-dependent bending wavenumber for a periodic ribbed plate shown in Figure 3.3 (dimensions and material properties see Table 2) at different frequencies

Figure 3.5 shows the variation of bending stiffness with the change of wave heading angles considering different geometric parameters of the ribbed plate. In general, at the wave heading angles of 0^{o} (in the x-direction) and 90^{o} (in the y-direction), the orthotropic plate behaves exactly as isotropic plate with bending stiffnesses of B_x and B_y respectively. Therefore when only the arrangement of the ribs (rib width, height or spacing) changes, the bending stiffness at 0^{o} heading angle stays the same as an isotropic plate without the ribs. For all other wave angles, the shear modulus G_{xy} influences the variation of the bending wavenumber. As the orthotropicity of the plate elastic properties induces in-plane shear [87] while bending only induces normal stress parallel to principal material directions, the overall bending stiffness in an arbitrary heading angle is not only dependent on the bending stiffness in its two principal directions but also on the shear modulus.

It is shown in Figure 3.5 that by increasing the rib width and rib height, or reducing the rib spacing, the bending stiffness in y-direction will be increased resulting in an increase in bending stiffness at all heading angles except 0^{o}. When the plate thickness varies, there is a more significant effect on the bending stiffness in the x-direction than y-direction because the main contribution to the bending stiffness in the y-direction is due to the ribs.

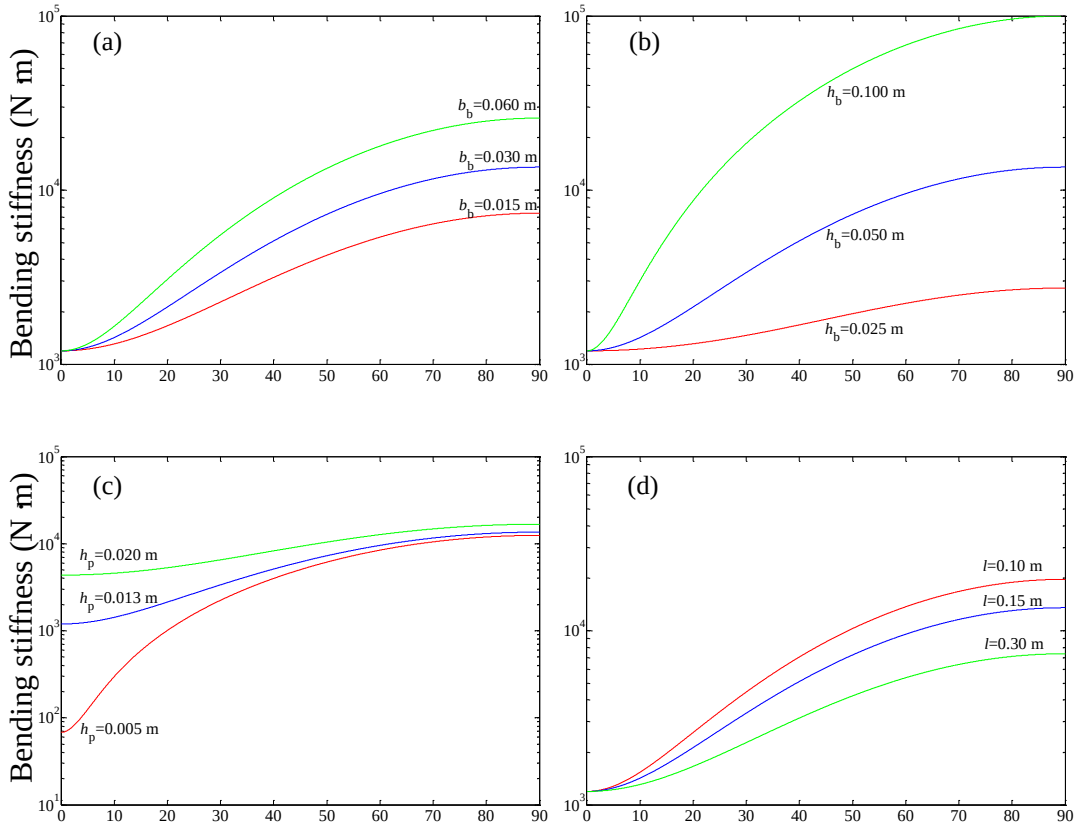

Figure 3.5 Angle-dependent bending stiffness for a periodic ribbed plate shown in Figure 3.3 (dimensions and material properties see Table 2) with different geometric parameters (only one parameter is chosen as a variable in each graph with all the others geometries fixed where the blue curves represent the default values): (a) rib width; (b) rib height; (c) plate thickness; (d) rib spacing. Wave heading angle of 0 ºcorresponds to the *x*-direction and 90 ºcorresponds to *y*-direction.

3.2.4 Approximate natural frequencies of orthotropic plates

Exact natural frequencies of a periodic ribbed plate are difficult to obtain using theoretical methods. Numerical calculation can be both time consuming and computationally expensive for complicated large structures or at high frequencies. However, many approximate theoretical methods have been developed. These normally consider the plate as orthotropic plate and simplify the geometry of the structure into a uniform plate with orthotropic elastic properties.

Dickinson [88] gives an approximate solution to calculate natural frequencies for an orthotropic plate using the Rayleigh-Ritz method:

$$f_{mn} = \frac{\pi}{2\sqrt{\rho_s}} \left\{ \frac{G_x^4(m)B_x}{a^4} + \frac{G_y^4(n)B_y}{b^4} + \frac{2Q_x(m)Q_y(n)H}{a^2b^2} + \frac{4B_{xy}[J_x(m)J_y(n) - Q_x(m)Q_y(n)]}{a^2b^2} \right\}^{1/2} \tag{3.53}$$

where mode number parameters G_x, Q_x, J_x and G_y, Q_y, J_y are dependent on the boundary conditions and can be calculated from Table 1 with the corresponding mode number. H is the bending stiffness parameter from equation (3.44). Bending stiffness as B_x, B_y and B_{xy} can be obtained from equation (3.46), (3.47) and (3.48) for the periodic ribbed plate with an overall dimension of $a \times b$ and an equivalent mass per unit area, ρ_s.

Table 3 shows the natural frequency calculated from equation (3.53) compared with FEM where the element size is chosen to be 0.01 m which is smaller than one tenth of the wavelength at 500 Hz. Below the 10^{th} mode, the relative error compared with numerical method is less than 12% which indicates the achievable accuracy of the Rayleigh-Ritz method when considering the ribbed plate as an orthotropic plate. Note that error does not linearly increase with increasing mode number. As the mode count increases, as shown in Figure 3.6, the Rayleigh-Ritz method also misses a significant number of modes. This is mainly due to the

limitations of the method being unable to incorporate the local modes of the rectangular bays separated by stiffened ribs whose fundamental mode occurs at 637.3Hz.

Table 3: Natural frequencies of a periodic ribbed plate (dimensions and material properties see Table 2) calculated from Rayleigh-Ritz method compared with numerical results using finite element method

Mode number	Rayleigh-Ritz method (Hz)	Finite element method (Hz)	Relative error to FEM results (%)
1	62.38	58.08	7.40
2	75.18	73.55	2.22
3	105.15	104.12	0.99
4	154.32	150.27	2.69
5	221.61	210.58	5.24
6	240.82	215.28	11.86
7	249.51	227.59	9.63
8	268.01	250.93	6.81
9	300.71	282.29	6.53
10	305.98	287.41	6.46

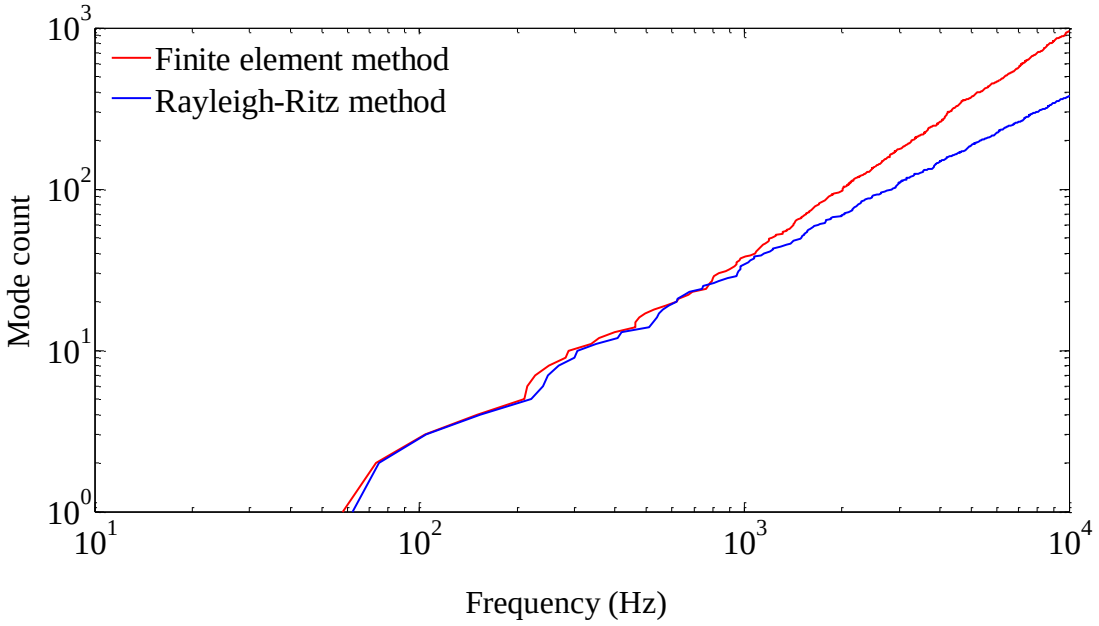

Figure 3.6 Mode count for a periodic ribbed plate (dimensions and material properties see Table 2) calculated from the Rayleigh-Ritz method compared with numerical results using finite element method

3.2.5 In-plane waves

The equations of motion for quasi-longitudinal and transverse shear waves in orthotropic plate are given by Bosmans [87] in (3.54) and (3.55) based on the strain-stress relations in *x*- and *y*-directions.

$$\left(E_x' \frac{\partial^2}{\partial x^2} + G_{xy} \frac{\partial^2}{\partial y^2} - \rho \frac{\partial^2}{\partial t^2} \right) \xi_x + (\mu_{yx} E_x' + G_{xy}) \frac{\partial^2 \xi_y}{\partial x \partial y} = 0 \tag{3.54}$$

$$\left(G_{xy} \frac{\partial^2}{\partial x^2} + E_y' \frac{\partial^2}{\partial y^2} - \rho \frac{\partial^2}{\partial t^2} \right) \xi_y + (G_{xy} + \mu_{xy} E_y') \frac{\partial^2 \xi_x}{\partial x \partial y} = 0 \tag{3.55}$$

Equation (3.54) and (3.55) have similar expressions compared with the in-plane wave equations for isotropic plate. However, unlike equations (3.15) and (3.16), in-plane wave equations for orthotropic plates cannot be separated into uncoupled equations for pure quasi-longitudinal and transverse shear wave equations because in an orthotropic structure, the compression causing longitudinal waves always induces shear at the same time in a direction that is not one of the principal material directions [87].

Similarly to bending wave propagation on an orthotropic plate, the in-plane wavenumber for an orthotropic plate are also angle-dependent. The general expression of the angle-dependent in-plane wavenumber is given as:

$$k(\theta) = \omega \sqrt{\frac{\rho}{E_x' \cos^2\theta + G_{xy} \sin^2\theta + (\mu_{yx} E_x' + G_{xy}) V(\theta) \sin\theta \cos\theta}} \tag{3.56}$$

where $V(\theta)$ is the solution of the wave equations (3.54) and (3.55) when considering sinusoidal harmonic in-plane motion on the othotropic plate. The problem can be simplified as:

$$aV^2 + bV + c = 0 \tag{3.57}$$

where

$$a=(\mu_{yx}E'_x+G_{xy})\sin\theta\cos\theta \tag{3.58}$$

$$b=E'_x\cos^2\theta-E'_y\sin^2\theta+G_{xy}(\sin^2\theta-\cos^2\theta) \tag{3.59}$$

$$c=-a \tag{3.60}$$

The two roots of equation (3.57) are:

$$V_1(\theta)=\frac{-b+\sqrt{b^2+4a^2}}{2a} \tag{3.61}$$

$$V_2(\theta)=\frac{-b-\sqrt{b^2+4a^2}}{2a} \tag{3.62}$$

The decision to use V_1 or V_2 in equation (3.56) is determined by the relative values of Young's modulus and shear modulus.

At θ=0 º, the in-plane wavenumber is equal to the quasi-longitudinal wavenumber in the *x*-direction, or the transverse shear wavenumber.

$$k_{\mathrm{L}}(0)=\omega\sqrt{\frac{\rho}{E'_x}} \qquad k_{\mathrm{T}}=\omega\sqrt{\frac{\rho}{G_{xy}}} \tag{3.63}$$

At θ=90 º, the in-plane wavenumber equals the quasi-longitudinal wavenumber in the *y*-direction, or the same transverse shear wavenumber as in equation (3.63).

$$k_{\mathrm{L}}(90^\circ)=\omega\sqrt{\frac{\rho}{E'_y}} \tag{3.64}$$

3.2.6 Modal density

The modal density for an orthotropic plate can be calculated using a similar approach to that in section 2.2.4 with the knowledge of the natural modes of the orthotropic plate which could be obtained from section 3.2.4 using the Rayleigh-Ritz method or from either numerical or physical experiments.

For bending waves, the modal density is given by Bosmans and Vermeir [89] for an orthotropic plate:

$$n(f) = \frac{S\sqrt{\rho_s}}{\pi} \int_0^{\pi/2} \frac{1}{\sqrt{B(\theta)}} d\theta \tag{3.65}$$

where ρ_s is the equivalent mass per unit area of the orthotropic plate including the mass of the ribs. Angle-dependent bending stiffness $B(\theta)$ can be obtained from equation (3.52).

Lyon [7] replaced the integral in equation (3.65) to give an approximate estimation of the modal density for an orthotropic plate using the bending stiffness in two principal directions of the plate:

$$n(f) \approx \frac{S\sqrt{\rho_s}}{4} \left(\frac{1}{\sqrt{B_x}} + \frac{1}{\sqrt{B_y}} \right) \tag{3.66}$$

Heckl [90] also proposed an alternative method to calculate the modal density using a geometrical average bending stiffness.

$$n(f) \approx \frac{S\sqrt{\rho_s}}{2} \frac{1}{\sqrt[4]{B_x B_y}} \tag{3.67}$$

The modal density for the periodic ribbed plate calculated using equations (3.65), (3.66) and (3.67) are shown in Figure 3.7 for comparison with numerical results using FEM. The results show that although Lyon and Heckl's methods only consider the bending stiffness in two principal directions and are independent of

shear modulus G_{xy}, the agreement with Bosmans and Vermeir's method is excellent and all three methods give close estimations compared with FEM. Bosmans and Vermeir's results are almost identical with Heckl's in this example as the later can be derived from the former by approximating the bending stiffness in the two principal directions, B_x and B_y, with the geometrical mean of the bending stiffness, $\sqrt{B_x B_y}$.

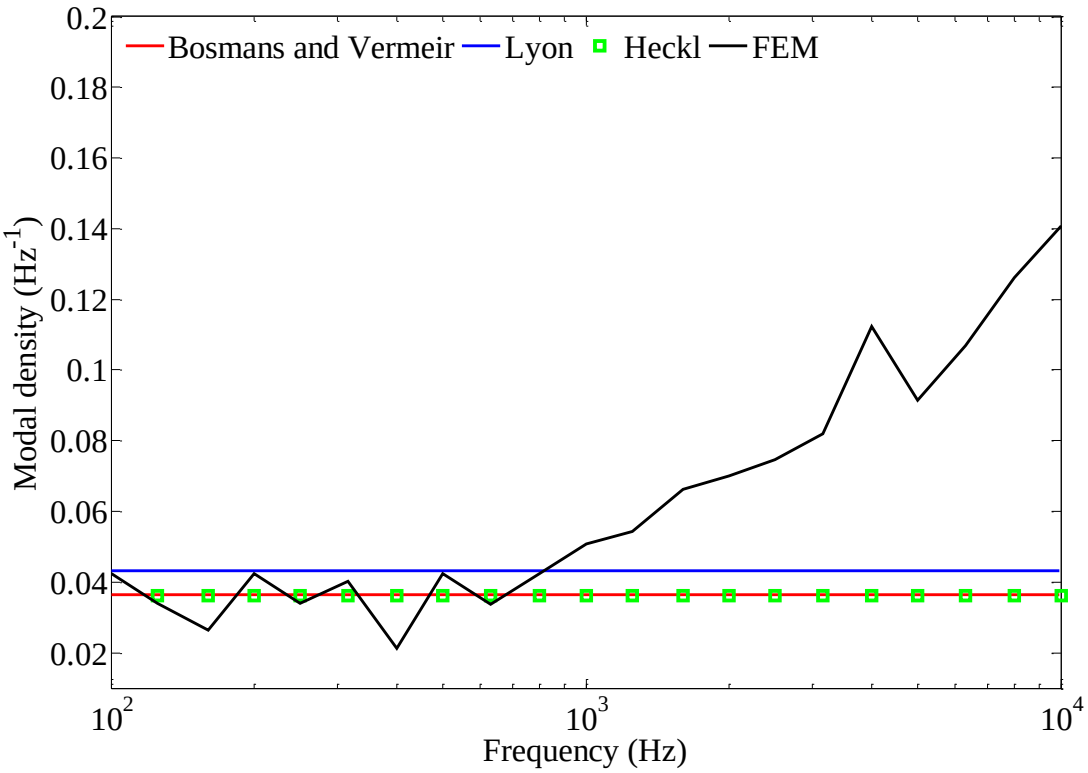

Figure 3.7 Modal density of the periodic ribbed plate calculated using different theoretical methods considering the ribbed plate as an orthotropic plate compared with the results obtained from numerical experiments.

3.2.7 FEM modelling for orthotropic plates

Orthotropic plates in FEM software ABAQUS can be modelled using the same shell element as isotropic plates but assigning orthotropic material properties. Based on the strain-stress relations for an orthotropic plate as shown in equation (3.33), equivalent Young's modulus E'_x , E'_y, shear modulus G_{xy} and Poisson's ratio μ_{xy} need to be input into the FEM model. In addition, shear moduli G_{xz} and G_{yz} are also included because they may be required for modelling transverse shear

deformation in a shell [72]. These parameters are usually obtained from laboratory measurement. However, for structural orthotropic plates made of isotropic homogeneous materials, they can also be estimated analytically. For the periodic ribbed plate as shown in Figure 3.3, E_x', E_y', and G_{xy} can be calculated using equations as (3.46), (3.47) and (3.17). The shear modulus G_{xz} and G_{yz} would have little effect on the results when bending waves and in-plane waves travelling in *x-y* plane are considered. They are estimated using the following equations:

$$G_{xz}=G_{xy} \tag{3.68}$$

$$G_{yz}=\frac{E_y'}{2(1+\mu_{yz})} \tag{3.69}$$

The orthotropic material properties in ABAQUS have to comply with the following material stability requirements for plane stress [72]:

$$E_x', E_y', G_{xy}, G_{xz}, G_{yz}>0 \tag{3.70}$$

$$\left|\mu_{xy}\right|<\sqrt{E_x'/E_y'} \tag{3.71}$$

3.3 Conclusions

This chapter described the theory for bending and in-plane wave fields on isotropic and orthotropic plates. Calculations were carried out for a periodic ribbed plate treated as an orthotropic plate to illustrate the important features that will be relevant to the predictions in chapters 5 and 6.

Concerning the prediction of eigenfrequencies on a periodic ribbed plate, it was shown that the Rayleigh-Ritz method missed a significant number of modes at high frequencies in comparison with FEM. For modal densities, approximated equations from both Lyon and Heckl give close estimations of the modal densities compared with the theory from Bosmans and Vermeir.

4 Wave theory for predicting vibration propagation on periodic ribbed plates

4.1 Introduction

This chapter focuses on wave descriptions of vibration propagation on periodic ribbed plates of infinite extent. These theories are needed in chapter 5 to calculate coupling loss factors for SEA models which treat the periodic ribbed plate as a single subsystem. This chapter also investigates the role of pass and stop bands on two-dimensional structures (i.e. plates) which are further explored in terms of the natural frequencies of the bays formed between the ribs.

4.2 Literature review: vibration of periodic ribbed plates

This section gives a brief overview of literature concerning structure-borne sound transmission on periodic plates, primarily focussing on periodic *ribbed* plates.

Brillouin [5] first studied wave propagation on periodic structures using Bloch theory and showed that waves travelling in periodic structures could display a distinctive frequency band gap property referred to as stop bands in which waves cannot propagate in the structure. These exist alongside pass bands in which waves can travel freely in the structure without any attenuation. Since then, much work has been done on the dynamic features of periodic structures. Due to the large quantity of literature, this section only reviews the studies on vibration of periodic ribbed/stiffened plates.

Heckl [91] first discussed the bending wave propagation on a plate with periodic attached beams. It was shown that when beam spacing is shorter than 1/4 of the bending wave length it is possible to treat the ribbed plate as an orthotropic plate. When the beam spacing is similar to, or larger than the bending wavelength, Heckl related the vibration field of two adjacent periodic elements by introducing a propagation constant using Brillouin's method for periodic structures. The propagation constant was derived and it was suggested that this general methodology could be extended to other periodic structures. Rumerman [92] further extended Heckl's method and derived the expression of forced response

and free modes of an infinite periodic stiffened plate and in this derivation, the ribs were idealized as parallel line attachments capable of exerting line forces and moments upon the plate. The motion of the ribs was ignored in this method so that this method could not cope with the case when an in-plane wave was generated at the junction.

In the work by Heckl and Rumerman a two-dimensional plate was simplified as an equivalent one-dimensional plate where only the normal incidence of bending waves was considered. Mead and Wilby [93] used a receptance method to analyze a two-dimensional periodic ribbed plate. This method allowed analysis of random incidence but vibration in the direction parallel to the ribs was considered as independent free sinusoidal motion; hence the analysis can be simplified to only consider the direction perpendicular to the ribs. The propagation constant in terms of receptance was given and the internal loss factor η was included using a complex bending stiffness, $B_p(1+i\eta)$.

A thorough review of work on wave propagation on periodic structures between 1964 and 1995 is given by Mead [94]. The paper reviews different methods available to analyze wave propagation on periodic structures including the receptance method, transfer matrix method and finite element method.

Classical periodic theory considers wave propagation on in finite periodic structure while in reality structures are finite. Clarkson and Mead [95] suggested that when a finite periodic structure is highly damped, the theory for infinite periodic structures can be used with sufficient accuracy. The 'exact' results for finite periodic structures can potentially be calculated by using the receptance method or the transfer matrix method.

When the periodic structure is coupled with other elements forming larger built-up structures, its pass/stop band features can affect the wave transmission and response distribution in the system. However, few research papers have been found to focus in this area. Tso and Hansen [10] carried out analysis using the wave approach for vibration transmission across an L-junction comprised of an isotropic, homogeneous plate and a periodic ribbed plate. The vibration field of the periodic ribbed plate was described using the classical Bloch theory for infinite periodic structures and then incorporated into the calculation of

transmission coefficient between the two plates. It was found that the transmission coefficient is dependent upon the incident wave angle and frequency, and it shows the stop/pass band phenomenon. However when the angular averaged transmission coefficient is used to calculate the coupling loss factor in SEA, no distinct stop bands occurred, instead only some transmission troughs were found indicating the existence of the pass bands. Langley *et al*.[96] considered a model of three plates coupled in a chain including a periodic ribbed plate in the framework of SEA. The periodic ribbed plate was not modelled as a subsystem in this model, but as a non-conservative coupling element between two homogeneous, isotropic plate subsystems. The transmission and absorption coefficients associated with the ribbed plate were successfully introduced using the dynamic stiffness method and a computationally efficient approach based on a one-dimensional waveguide. This paper pointed out that the main advantage of this work compared with SEA and wave intensity analysis is that it enables to analyze the effect of stop/pass bands of the periodic structure on vibration transmission for coupled structures, while SEA may fail to model the periodic structure and the wave intensity analysis can offer a considerable improvement than SEA by incorporating the wave filtering effect but is still unable to capture the stop/pass band behaviour.

Another extensive review of literature was carried out by Mester and Benaroya [97] focusing on both 'perfect' and 'imperfect' periodic structures. In this thesis, only 'perfect' periodicity is considered whereas in reality there will be engineering tolerances. Work by several authors (e.g. Langley [60], Lin [98], Hodges and Woodhouse [99]) on imperfect finite periodic ribbed plates have shown that the rib spacing irregularity causes localization of high order modes resulting in a rise of the response near the and this phenomena cannot be predicted by classical periodic theory.

4.3 Vibration field on a periodic ribbed plate

An isotropic, homogeneous plate with periodically reinforced beams symmetrically attached on both sides of the plate is chosen for analysis as shown

in Figure 3.1. The ribs divide the isotropic plate into smaller plate elements and each element is referred to as a bay. This symmetrical arrangement of periodic ribs is used to avoid the generation of in-plane waves so that only bending waves are considered in the modelling.

In this section, a periodic ribbed plate of infinite extent is analyzed using the thin plate theory and Bloch theory to consider the periodicity of the structure. The stop/pass band characteristics of the periodic plate are studied in detail.

For a periodic structure, the wave motion in terms of the lateral (or out-of-plane) displacement, ξ, for an arbitrary element *n*, is related with its neighbouring element *n*+1 given by [5] using Bloch theory:

$$\xi_{n+1} = \exp(\lambda)\xi_n \tag{4.1}$$

where the propagation constant, λ, is a complex value. If λ is purely imaginary, waves will travel freely across the structure without any attenuation. The frequency range where this occurs is referred to as a pass band. On the other hand, if the propagation constant contains a non-zero real part, the wave will decay exponentially and the corresponding frequency range is referred to as a stop band.

For an infinite two-dimensional periodic system such as the case shown in Figure 3.3 (a), equation (4.1) can then be extended and written as:

$$\exp(\lambda)\xi_n(x_{\mathrm{n}}, y, t) = \xi_{n+1}(x_{\mathrm{n+1}}, y, t) \;\Rightarrow\; \exp(\lambda)\xi_n(x_{\mathrm{n}}, y, t) = \xi_{n+1}(x_n + l, y, t) \tag{4.2}$$

where *l* is the length of the bay between two ribs in the *x*-direction. If the width of the stiffened ribs is small enough to ignore, each periodic element of the structure is simplified to a bay which can be represented by a thin isotropic plate. Thus, *l* in equation (4.2) is equal to the length of the bay in the *x*-direction.

The following derivation follows the approach of Tso and Hansen [10] and incorporates the stiffened ribs in the modelling of the boundary conditions by considering torsional, bending and inertia effects.

Considering bending waves propagating in the *x*-*y* plane, the wave motion on each bay is governed by equation (3.1) for thin isotropic plates. As the stiffened ribs are parallel to the *y*-axis and extend to infinity towards both directions, the wave motion along the *y*-axis is continuous and is given by:

$$\xi(y) = \exp(\pm ik_{\mathrm{B}} y \sin\theta) \tag{4.3}$$

where k_{B} is the bending wavenumber of the plate and θ is the wave heading angle.

The displacement can therefore be described using:

$$\xi_n(x_n) = \exp(k_{mx} x_n)\exp(\pm ik_{\mathrm{B}} y \sin\theta)\exp(i\omega t) \tag{4.4}$$

Substituting equation (4.4) into (3.1) yields the bending wave motion on one bay as:

$$\xi_n(x_n, y, t) = \left[\sum_{m=1}^{4} A_m \exp(k_{mx} x_n)\right]\exp(\pm jk_{\mathrm{B}} y \sin\theta)\exp(i\omega t) \tag{4.5}$$

The four wavenumbers in the *x*-direction can be obtained from:

$$\begin{gathered} k_{1\mathrm{x}} = ik_{\mathrm{B}}\cos\theta, \qquad k_{2\mathrm{x}} = -ik_{\mathrm{B}}\cos\theta, \\ k_{3\mathrm{x}} = k_{\mathrm{B}}\sqrt{(1+\sin^2\theta)}\,,\ k_{4\mathrm{x}} = -k_{\mathrm{B}}\sqrt{(1+\sin^2\theta)} \end{gathered} \tag{4.6}$$

Bloch theory formed in equation (4.2) is applied for adjacent bays in conjunction with equation (4.5). The four unknown wave amplitudes (A_1, A_2, A_3, A_4) and the wave propagation constant, λ, need to be solved by considering the appropriate boundary conditions for the periodic element.

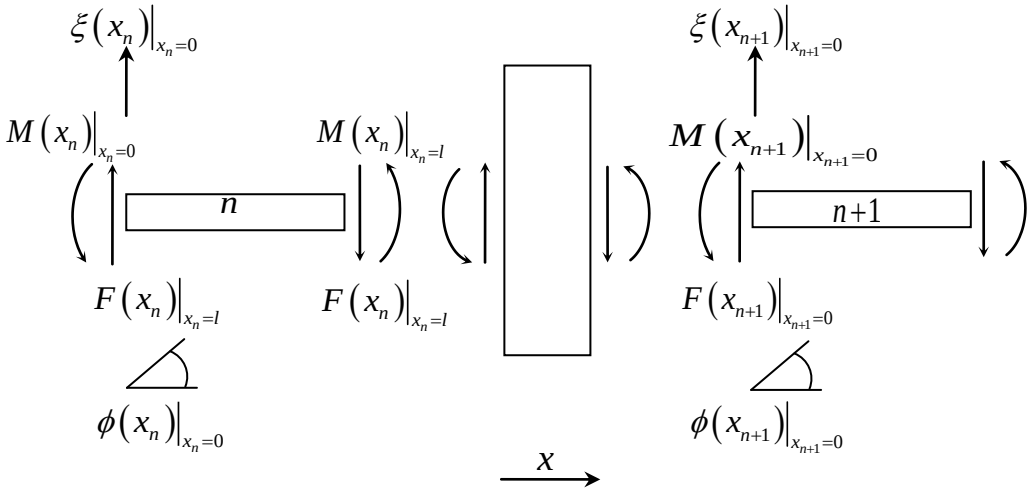

Figure 4.1 Forces, moments and displacements for two adjacent bays separated by a rib

Similarly as expressed in equation (4.2), Bloch theory gives the relationship between the displacement ξ, plate rotation ϕ, force F and moment M at the boundaries of two adjacent bays as:

$$\exp(\lambda)\,\xi(x_n)\big|_{x_n=0} = \xi(x_{n+1})\big|_{x_{n+1}=0} \tag{4.7}$$

$$\exp(\lambda)\,\phi(x_n)\big|_{x_n=0} = \phi(x_{n+1})\big|_{x_{n+1}=0} \tag{4.8}$$

$$\exp(\lambda)\,F(x_n)\big|_{x_n=0} = F(x_{n+1})\big|_{x_{n+1}=0} \tag{4.9}$$

$$\exp(\lambda)\,M(x_n)\big|_{x_n=0} = M(x_{n+1})\big|_{x_{n+1}=0} \tag{4.10}$$

The right-hand side of equations (4.7) and (4.8) can also be written in the following form according to the continuity conditions at the junction between the beam and the bay assuming that the width of the beam can be ignored:

$$\xi(x_{n+1})\big|_{x_{n+1}=0} = \xi(x_n)\big|_{x_n=l} \tag{4.11}$$

$$\phi(x_{n+1})\big|_{x_{n+1}=0} = \phi(x_n)\big|_{x_n=l} \tag{4.12}$$

The stiffened beam causes a discontinuity in the junction force and bending moment between the neighbouring elements, hence the above continuity conditions are not suitable for the junction force and bending moment. Instead, the equilibrium of the forces and moments at the junction must consider the torsional, bending and inertia effects of the stiffened beam.

The equilibrium of forces in *z*-direction needs to consider the shear force of the beam due to its bending motion in the *y*-*z* plane,

$$F(x_n)\big|_{x_n=l} - F(x_{n+1})\big|_{x_{n+1}=0} - \frac{\partial F_\mathrm{b}}{\partial y} = -\rho_\mathrm{b} S_\mathrm{b} \omega^2 \xi(x_n)\big|_{x_n=l} \tag{4.13}$$

where ρ_b, S_b are density and cross-sectional area of the beam respectively. F_b is the lateral shear force in the beam, which results from the bending of the beam in the *x*-*y* plane. It can be calculated by:

$$F_\mathrm{b} = B_\mathrm{b} \frac{\partial^3 \xi(x_n)}{\partial y^3} \tag{4.14}$$

where B_b is the bending stiffness of the rib. For a rectangular beam structure, it is given as:

$$B_\mathrm{b} = E_\mathrm{b} I_{\mathrm{b}x} \tag{4.15}$$

where the Young's modulus of the beam is E_b and $I_{\mathrm{b}x}$ is the moment of inertia of the beam about *x*-axis which can be calculated from equation (3.49).

Therefore, using equation (4.14) and (4.15), equation (4.13) can be rewritten as:

$$F(x_n)\big|_{x_n=l} - F(x_{n+1})\big|_{x_{n+1}=0} - E_{\mathrm{b}} I_{\mathrm{bx}} \left.\frac{\partial^4 \xi(x_n)}{\partial y^4}\right|_{x_n=l} = -\rho_{\mathrm{b}} S_{\mathrm{b}} \omega^2 \xi(x_n)\big|_{x_n=l} \tag{4.16}$$

The variation in plate rotation along the *y*-axis causes the beam to twist which results in a torsional moment. Considering the equilibrium of moment of the line parallel to the *y*-axis and passing through the beam centroid, the following equation of equilibrium for bending moment is given as:

$$M(x_n)\big|_{x_n=l} - M(x_{n+1})\big|_{x_{n+1}=0} - \frac{\partial M_{\mathrm{b}}}{\partial y} = -I_{\mathrm{bc}} \omega^2 \phi(x_n)\big|_{x_n=l} \tag{4.17}$$

where I_{bc} is the second moment of inertia per unit length of the beam about the centroid given as:

$$I_{\mathrm{bc}} = \frac{b_{\mathrm{b}} h_{\mathrm{b}}^3 + h_{\mathrm{b}} b_{\mathrm{b}}^3}{12} = \frac{S_{\mathrm{b}}^2}{12}\left(\frac{b_{\mathrm{b}}}{h_{\mathrm{b}}} + \frac{h_{\mathrm{b}}}{b_{\mathrm{b}}}\right) \tag{4.18}$$

The torsional moment of the beam M_{b} is related to the shear modulus, G_{b}, and the torsional constant, J_{b} for the beam as:

$$M_{\mathrm{b}} = -G_b J_b \frac{\partial \phi(x_n)}{\partial y} = -G_b J_b \frac{\partial \xi(x_n)}{\partial x_n \partial y} \tag{4.19}$$

where G_{b} can be calculated using equation (3.17) and the torsional constant for the beam , J_{b} , is given in [100] as:

$$J_{\mathrm{b}} = \frac{h_b b_b^3}{3}\left[1 - 192\frac{b_{\mathrm{b}}}{\pi^5 h_{\mathrm{b}}}\tanh\left(\frac{\pi h_{\mathrm{b}}}{2b_{\mathrm{b}}}\right)\right] \tag{4.20}$$

Therefore, equation (4.17) can be written as:

$$M(x_n)\big|_{x_n=l} - M(x_{n+1})\big|_{x_{n+1}=0} + G_{\mathrm{b}} J_{\mathrm{b}} \left.\frac{\partial^3 \xi(x_n)}{\partial x_n \partial y^2}\right|_{x_n=l} = -I_{\mathrm{bc}} \omega^2 \left.\frac{\partial \xi(x_n)}{\partial x_n}\right|_{x_n=l} \tag{4.21}$$

Replacing all the elements containing n+1 by the corresponding element of n using equations (4.7) to (4.10) and substituting equation (4.5) to equations (4.11), (4.12), (4.16) and (4.21) gives:

$$\sum_{m=1}^{4} A_m \exp(k_{mx} l) = \exp(\lambda) \sum_{m=1}^{4} A_m \tag{4.22}$$

$$\sum_{m=1}^{4} A_m k_{mx} \exp(k_{mx} l) = \exp(\lambda) \sum_{m=1}^{4} A_m k_{mx} \tag{4.23}$$

$$\sum_{m=1}^{4} (k_{mx}^2 - \frac{I_{\mathrm{bc}} S_{\mathrm{b}} \omega^2 k_{mx}}{B_{\mathrm{p}}} - \frac{G_{\mathrm{b}} J_{\mathrm{b}} k_{\mathrm{y}}^2 k_{mx}}{B_{\mathrm{p}}} + \mu k_{\mathrm{y}}^2) A_m \exp(k_{mx} l) = \exp(\lambda) \sum_{m=1}^{4} A_m (k_{mx}^2 + \mu k_{\mathrm{y}}^2) \tag{4.24}$$

$$\sum_{m=1}^{4} [k_{mx}^3 - \frac{\rho_{\mathrm{b}} S_{\mathrm{b}} \omega^2}{B_{\mathrm{p}}} - \frac{E_{\mathrm{b}} I_{\mathrm{bx}} k_{\mathrm{y}}^4}{B_{\mathrm{p}}} + (2-\mu) k_{\mathrm{y}}^2 k_{mx}] A_m \exp(k_{mx} l) = \exp(\lambda) \sum_{m=1}^{4} A_m [k_{mx}^3 + (2-\mu) k_{\mathrm{y}}^2 k_{mx}] \tag{4.25}$$

These four equations (4.22) to (4.25) can be written in matrix form as:

$$\begin{bmatrix} \exp(k_{1\mathrm{x}} l) & \exp(k_{2\mathrm{x}} l) & \exp(k_{3\mathrm{x}} l) & \exp(k_{4\mathrm{x}} l) \\ k_{1\mathrm{x}} \exp(k_{1\mathrm{x}} l) & k_{2\mathrm{x}} \exp(k_{2\mathrm{x}} l) & k_{3\mathrm{x}} \exp(k_{3\mathrm{x}} l) & k_{4x} \exp(k_{4\mathrm{x}} l) \\ u_1 & u_2 & u_3 & u_4 \\ z_1 & z_2 & z_3 & z_4 \end{bmatrix} \begin{bmatrix} A_1 \\ A_2 \\ A_3 \\ A_4 \end{bmatrix} = \exp(\lambda) \begin{bmatrix} 1 & 1 & 1 & 1 \\ k_{1x} & k_{2x} & k_{3x} & k_{4x} \\ q_1 & q_2 & q_3 & q_4 \\ p_1 & p_2 & p_3 & p_4 \end{bmatrix} \begin{bmatrix} A_1 \\ A_2 \\ A_3 \\ A_4 \end{bmatrix}$$

(4.26)

where

$$q_m = k_{mx}^2 + \mu k_{\mathrm{y}}^2$$

$$p_m = k_{mx}^3 + (2-\mu)k_y^2 k_{mx}$$

$$u_m = (k_{mx}^2 - \frac{I_{bc}\omega^2 k_{mx}}{B_p} - \frac{G_b J_b k_y^2 k_{mx}}{B_p} + \mu k_y^2)\exp(k_{mx} l)$$

$$z_m = [k_{mx}^3 + \frac{\rho_b S_b \omega^2}{B_p} - \frac{E_b I_{bx} k_y^4}{B_p} + (2-\mu)k_y^2 k_{mx}]\exp(k_{mx} l)$$

The matrix equation can be abbreviated as:

$$\mathbf{H_1}[A_m] = \exp(\lambda)\mathbf{H_2}[A_m] \tag{4.27}$$

Furthermore, equation (4.27) can be written in the form as:

$$\mathbf{H}[A_m] = \exp(\lambda)[A_m] \tag{4.28}$$

where $\mathbf{H} = \mathbf{H_2^{-1}H_1}$. This is a standard eigenvalue problem in which the eigenvalues of the matrix **H** are exp(λ). The solution of the corresponding eigenvectors gives the unknown wave amplitudes (A_1, A_2, A_3, A_4) for insertion in equation (4.5).

The calculation results in four propagation constants in two pairs with one exp(λ) from each pair being the reciprocal of the other. These correspond to waves which either decay or propagate in the positive and negative directions. If we consider waves that travel in one direction in general, only one positive and one negative free wave can occur at any frequency so that one pair of the eigenvalues is valid and either one of the eigenvalues in this pair can be used in further subsequent calculations. (In this thesis, the real part of the complex propagation constant is presented as positive.)

To illustrate the propagation constants, consider such a periodic ribbed plate as shown in Figure 3.3(a) made from Perspex. The geometrical dimensions are illustrated in Figure 3.3(b). Figure 4.2 shows the complex propagation constants for this structure with different propagation wave angles.

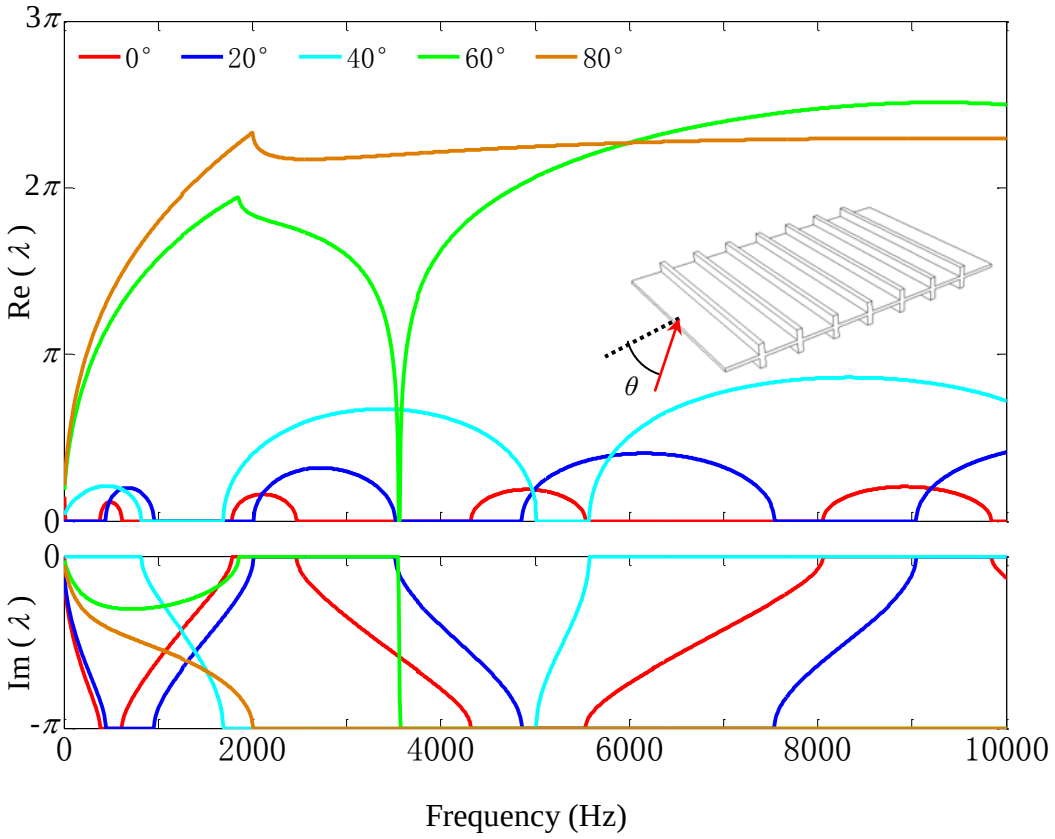

Figure 4.2 Real and imaginary parts of the propagation constant, λ, with different propagation wave angles for an infinite periodic ribbed plates (dimensions and material properties see Table 2)

If the propagation constant is purely imaginary, the bending wave will travel freely across the ribbed plate; hence the corresponding frequency falls within a pass band. Between two consecutive pass bands where the propagation constant has a non-zero real part, there will be no propagating wave and the frequency falls within a stop band.

As shown in Figure 4.2, the distribution of stop/pass bands is dependent upon the wave propagation angle as well as frequency. In general, with the increase of propagation wave angles, the width of the pass bands reduces while the band gap increases. At 0 °, when the real part is non-zero, the imaginary part is either zero or $-\pi$. Bending waves with propagation angle above ≈60 ° do not exhibit any pass bands anymore and the stop bands dominate the entire frequency range.

Figure 4.3 shows the bending wave propagation with wave heading angles from 0 ° to 90 ° on the periodic plate. The black shaded area represents purely imaginary

propagation constants, which can be referred to as a propagation zone. The white areas, on the other hand, are attenuation zones where a non-zero real part of the propagation constant exists. Bending wave fields on plates with only one specific propagation angle are rarely found in the real world, and usually contain many different angles. For example, in a diffuse vibration field the bending waves occur at all possible propagation angles. As shown in Figure 4.3, at any particular frequency the periodic plate doesn't exhibit a single pass or stop band, which is in contrast to the case of a one-dimensional periodic structure.

It is expected that the greatest vibration response will occur in pass bands. Hence it is of great importance for structural engineers to understand the band gap characteristics for periodic structures.

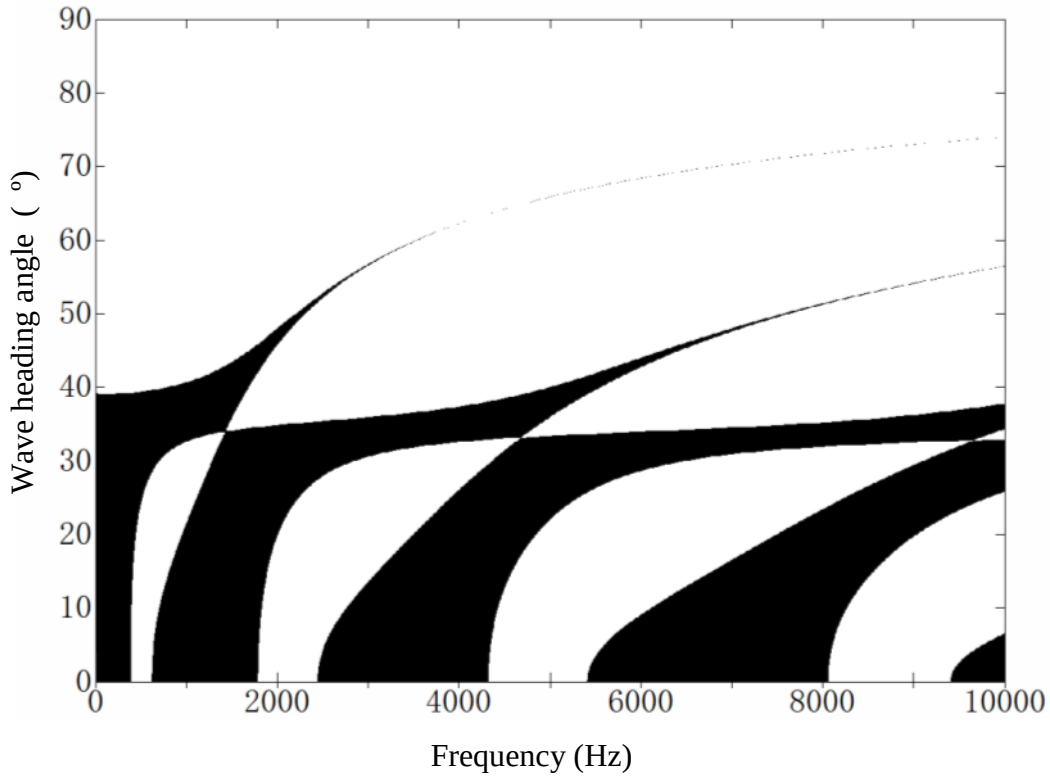

Figure 4.3 Propagation and attenuation zones of a periodic ribbed plate (black shaded areas: propagation zones; white areas: attenuation zones)

4.4 Effect of geometrical properties on stop/pass band distribution

Taking the default dimensions for the ribbed plate shown in Table 2, Figure 4.4 to Figure 4.7 show the variation in the distribution of propagation and attenuation zones when one parameter is changed from the default value.

- Figure 4.4 (a) and (b) show different widths for the rib. It can be seen that when the rib width is increased, the four attenuation zones surrounded by propagation zones cover a wider frequency range. However, the upper bounds of the propagation zones in terms of the wave heading angles remain the same.

- Figure 4.5 (a) and (b) show different heights for the rib. It can be seen that when the rib height is increased, the area of the propagation zones has been compressed both to a lower heading angle and in frequency range. Also the attenuation zones at small wave heading angles tends to move towards lower frequencies.

- Figure 4.6 (a) and (b) show different bay spacings. With increasing bay spacing, the width of each attenuation zone is compressed in frequency range and moves towards lower frequencies so that more propagation and attenuation zones appear below 10 kHz.

- Figure 4.7 (a) and (b) show different plate thicknesses. With increasing plate thickness, the propagation zones extend to higher wave heading angle while the attenuation zones are moved to higher frequencies so that less attenuation zones appear below 10 kHz.

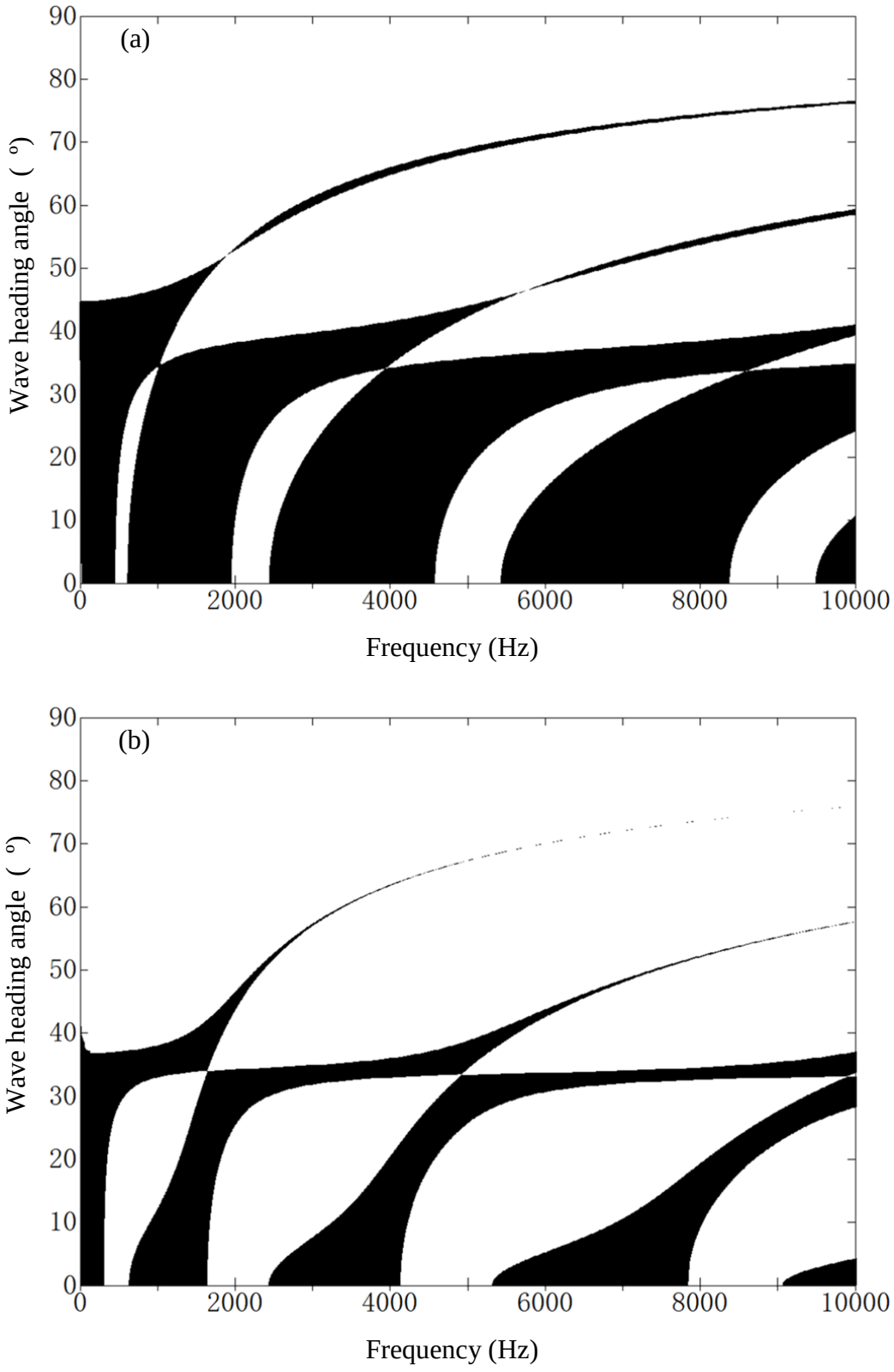

Figure 4.4 Variation of rib width (a) 15 mm, (b) 60 mm on the distribution of propagation and attenuation zones. (Compare with Figure 4.3 for 30 mm rib width where all other parameters remains the same with rib height: 50 mm, rib spacing: 150 mm and plate thickness: 13 mm)

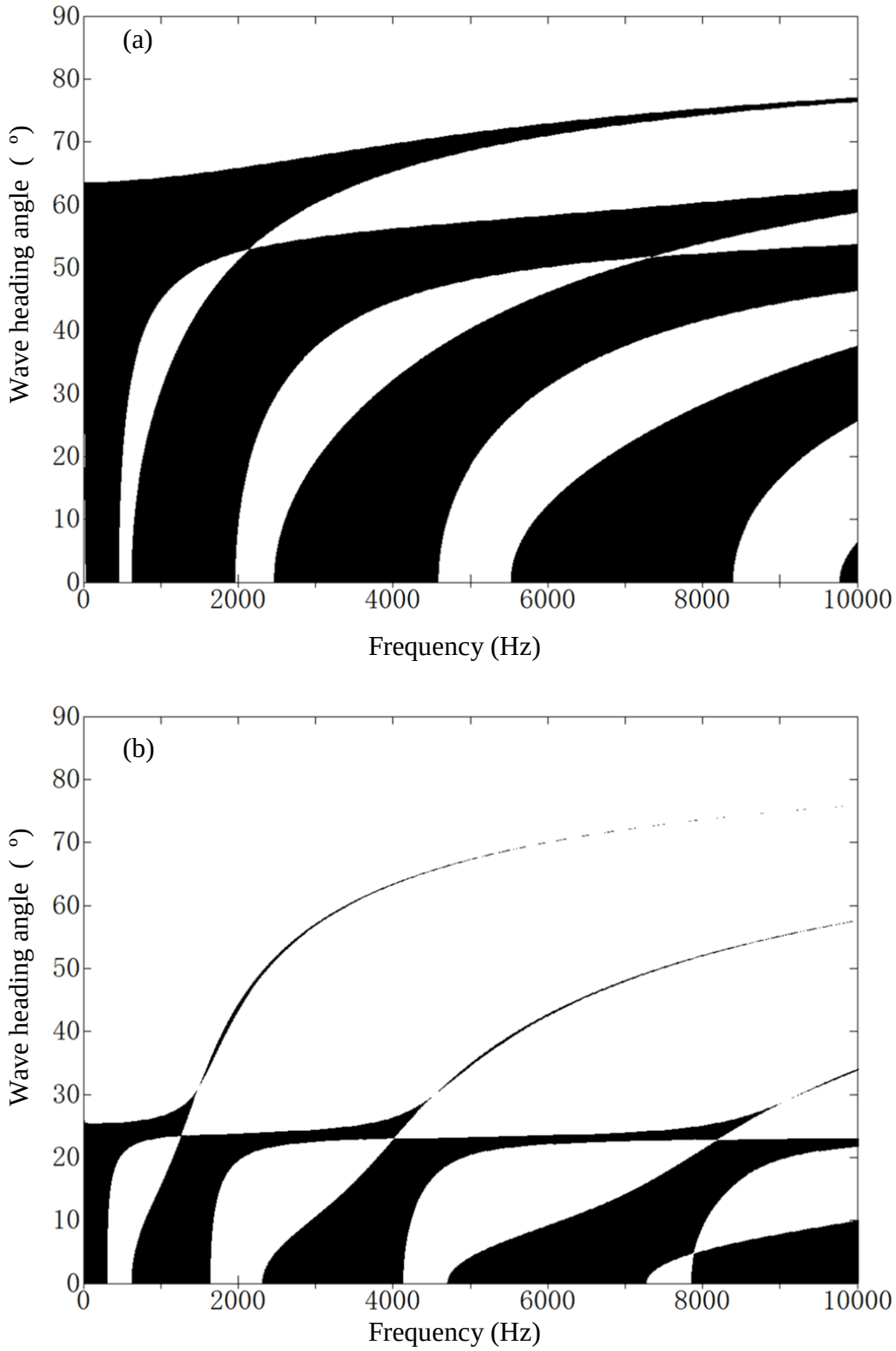

Figure 4.5 Variation of rib height (a) 25 mm, (b) 100 mm on the distribution of propagation and attenuation zones. (Compare with Figure 4.3 for 50 mm rib height where all other parameters remains the same with rib width: 30 mm, rib spacing: 150 mm and plate thickness: 13 mm)

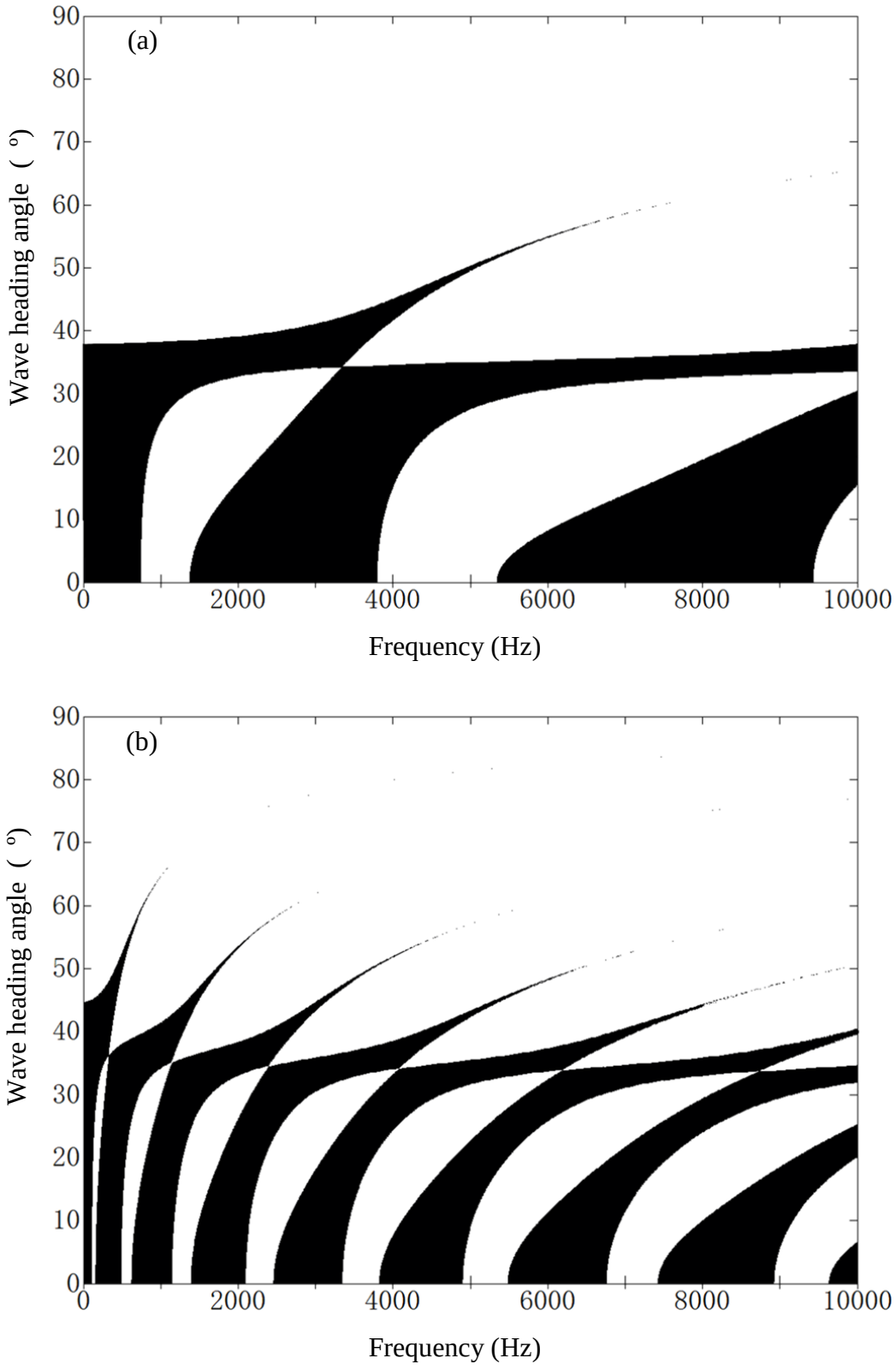

Figure 4.6 Variation of bay spacing (a) 100 mm, (b) 300 mm on the distribution of propagation and attenuation zones. (Compare with Figure 4.3 for 150 mm bay spacing where all other parameters remains the same with rib width: 30 mm, rib height: 50 mm and plate thickness: 13 mm)

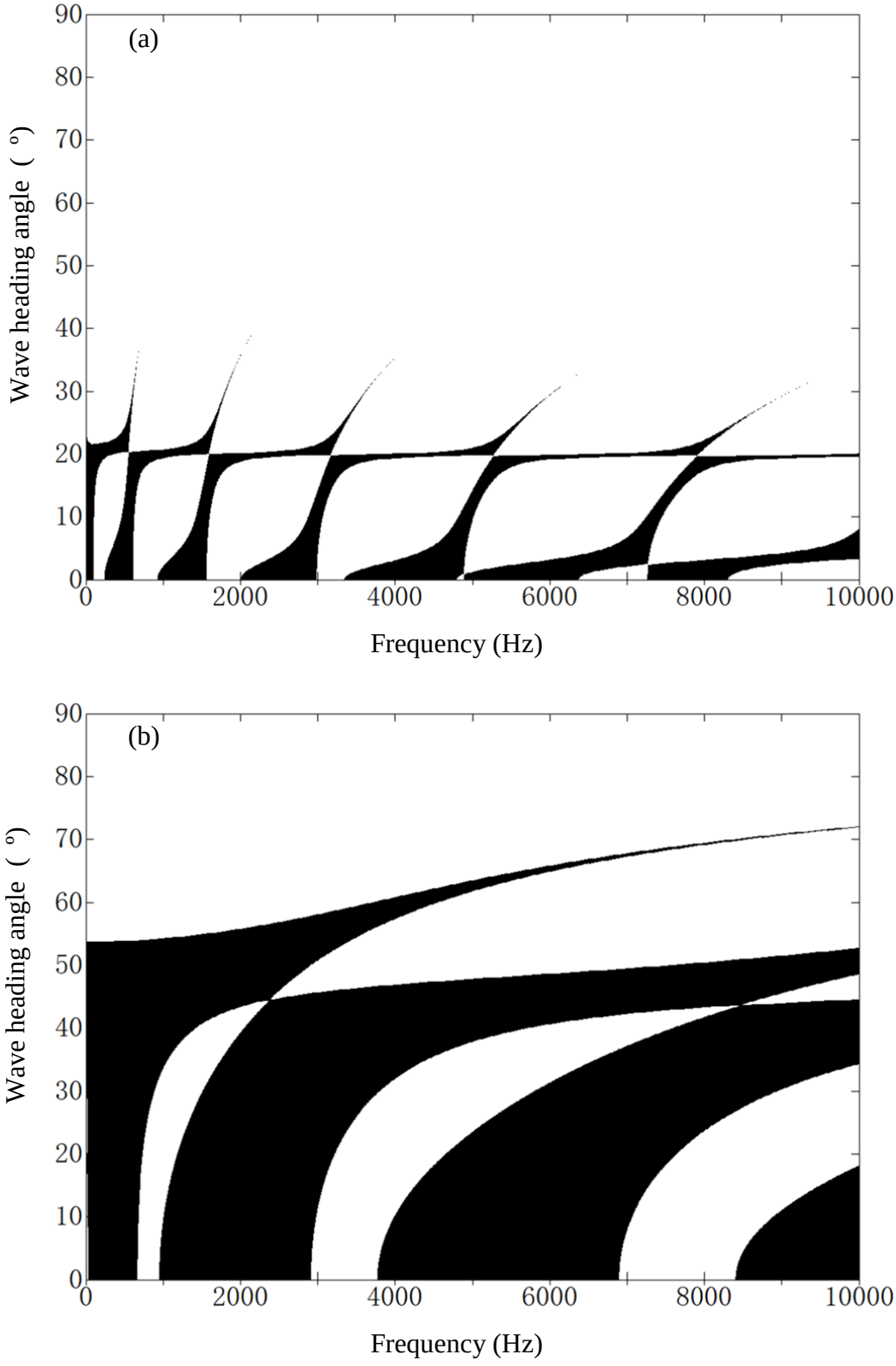

Figure 4.7 Variation of plate thickness (a) 5 mm, (b) 20 mm on the distribution of propagation and attenuation zones. (Compare with Figure 4.3 for 13 mm bay spacing where all other parameters remains the same with rib width: 30 mm, rib height: 50 mm and bay spacing: 150 mm)

4.5 Relationship between bounding frequencies of stop/pass bands and natural frequencies of the periodic element from a ribbed plate

4.5.1 Introduction

Previous studies by Gupta [101] and Mead [102] have found that for certain periodic structures, the upper and lower bounds of pass bands can be identified by the natural frequencies of a periodic element. In this section this is investigated because it is important to understand the relationship between the natural frequencies and the bounding frequencies of the pass bands for a two-dimensional periodic ribbed plate. In chapters 6 and 7, the bays of the periodic ribbed plate will be treated as individual subsystems in SEA and ASEA models; this is only possible once the bay supports local modes. For practical purposes, the fundamental mode is calculated for a bay with simply-supported boundaries. Therefore it is of interest to relate the fundamental mode of a bay (SSSS) to the first pass or stop band.

4.5.2 General approach for analysing periodic structures using the receptance method

Mead [102] introduced a receptance approach to calculate the propagation constant for general periodic structures and applied this method. Such receptance methods are thoroughly described by Bishop and Johnson [103] to calculate the vibration response of the whole system from analyzing individual components of the system. The receptance method is initially used in this section to determine the response of a general periodic system as shown in Figure 4.8 (a). This is then applied to a specific periodic system, a two- dimensional periodic ribbed plate in order to investigate the relationship between the natural frequencies and the bounding frequencies of the pass bands.

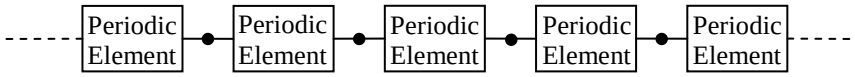

(a)

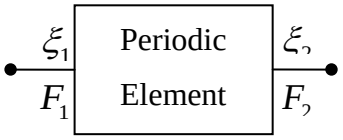

(b)

Figure 4.8 (a) Schematic of a general infinite periodic system; (b) forces and displacements at two coupling ends of one periodic element

In a periodic system, each periodic element can be characterized by its receptances which relate the force and displacement at its two coupling ends. Taking one of the periodic elements shown as in Figure 4.8 (b), the displacements and forces on the left and right ends of the element are related through the following receptance matrix.

$$\begin{bmatrix} \xi_1 \\ \xi_2 \end{bmatrix} = \begin{bmatrix} \alpha_{11} & \alpha_{12} \\ \alpha_{21} & \alpha_{22} \end{bmatrix} \begin{bmatrix} F_1 \\ F_2 \end{bmatrix} \tag{4.29}$$

where α_{11} and α_{22} are direct receptances and α_{12} and α_{21} are cross receptances. It is noted that the receptances can also be expressed as the ratio of rotational angle over moment at the two ends of the periodic element. This will be referred to as rotational receptances later in the thesis. In this case, equation (4.29) can be changed to:

$$\begin{bmatrix} \phi_1 \\ \phi_2 \end{bmatrix} = \begin{bmatrix} \alpha_{11} & \alpha_{12} \\ \alpha_{21} & \alpha_{22} \end{bmatrix} \begin{bmatrix} M_1 \\ M_2 \end{bmatrix} \tag{4.30}$$

For free motion on an infinite periodic system, Bloch theory yields the displacements and forces at the corresponding positions of two neighbouring periodic element is related through propagation constant λ as:

$$\xi_2 = \exp(\lambda)\xi_1 \tag{4.31}$$

$$F_2 = \exp(\lambda)F_1 \tag{4.32}$$

Substituting (4.31) and (4.32) into (4.29) gives:

$$\xi_1 = [\alpha_{11} - \exp(\lambda)\alpha_{12}]F_1 \tag{4.33}$$

$$e^{\lambda}\xi_1 = [\alpha_{12} - \exp(\lambda)\alpha_{22}]F_1 \tag{4.34}$$

Eliminating ξ_1 and F_1 by dividing (4.33) by (4.34) obtains:

$$\alpha_{11} + \alpha_{12} - [\exp(\lambda) + \exp(-\lambda)]\alpha_{12} = 0 \tag{4.35}$$

as $\exp(\lambda) + \exp(-\lambda) = 2\cosh(\lambda)$, equation (4.35) can be written as:

$$\cosh(\lambda) = \frac{\alpha_{11} + \alpha_{22}}{2\alpha_{12}} \tag{4.36}$$

When propagation constant λ is imaginary, $-1 \le \cosh(\lambda) \le 1$, and represents the wave inside a propagation zone. The bounding frequencies that define the boundaries of the propagation and attenuation zones are therefore positions that satisfy

$$\cosh(\lambda) = \pm 1 \tag{4.37}$$

4.5.3 Using the receptance method to calculate the natural frequencies of a periodic element

The natural frequencies of an individual periodic element are calculated in this section with different boundary conditions in order to find their relationship to the bounding frequencies of the pass bands of the complete periodic structure.

(1) Free boundary

Considering one periodic element taken out of the whole structure without any constraint at the boundary, the boundary receptance at natural frequencies will be infinite whilst the ratios $\alpha_{11}/\ \alpha_{22}$ and $\alpha_{11}/\ \alpha_{12}$, remain finite according to [101]. Bishop and Johnson [103] calculate $\alpha_{11}/\ \alpha_{22}$ and $\alpha_{11}/\ \alpha_{12}$ for symmetric elements where $\alpha_{11}=\alpha_{22}$. Hence the ratios will be either +1 or ± 1 so that they satisfy the equation $\cosh(\lambda) = \pm 1$. Therefore, the natural frequencies of the periodic element with free boundaries are located at the bounding frequencies of the pass bands.

(2) Simply-supported or Clamped boundaries

If the element is clamped or simply-supported at both its coupling ends, it will have different natural frequencies. Based on the boundary condition which yields zero translational displacement at both coupling ends, this gives:

$$\xi_1 = \alpha_{11}F_1 + \alpha_{12}F_2 = 0 \tag{4.38}$$

$$\xi_2 = \alpha_{21}F_1 + \alpha_{22}F_2 = 0 \tag{4.39}$$

In order to satisfy equation (4.38) and (4.39), the determinant of the receptance matrix:

$$\begin{vmatrix} \alpha_{11} & \alpha_{12} \\ \alpha_{21} & \alpha_{22} \end{vmatrix} = 0 \tag{4.40}$$

As $\alpha_{12} = \alpha_{21}$ for reciprocity requirement, equation (4.40) can be reduced to equation (4.41) for a symmetric element.

$$\alpha_{11}^2 - \alpha_{12}^2 = 0 \quad \Rightarrow \quad \frac{\alpha_{11}}{\alpha_{12}} = \pm 1 \tag{4.41}$$

Equation (4.41) is only satisfied at natural frequencies so that $\cosh(\lambda) = \pm 1$, therefore simply-supported or clamped boundaries also define the bounding frequencies of the pass bands.

4.5.4 Applying the receptance method to periodic ribbed plates

For one-dimensional periodic beam systems, the exact point receptances can be calculated theoretically. However, for some complex two-dimensional periodic structures such as the periodic ribbed plate shown in Figure 3.3, exact receptances of each element can be difficult to calculate using theoretical methods. Hence some simplifications have to be made. Therefore, the periodic element of the ribbed plate in Figure 3.3 is simplified to be a thin plate representing the bay and only considering the ribs in terms of their effect on the bay as structural line discontinuities.

Now we only consider one bay from the periodic plate as illustrated in Figure 4.9, the solution of equation (3.1) for bending wave motion in a thin plate can be expressed in relation with the mode number in *y*-direction given by [36].

$$\xi(x, y, t) = [A_1 \cosh(\kappa_a x') + A_2 \sinh(\kappa_a x') + A_3 \cos(\kappa_a' x') + A_4 \sin(\kappa_a' x')] \sin(n\pi y') \exp(i\omega t) \tag{4.42}$$

where $\{A_1, A_2, A_3, A_4\}$ are wave amplitude constants which are determined from the corresponding boundary conditions at the two coupling ends where x=0 and x=a. Also

$$x' = \frac{x}{a} \qquad y' = \frac{y}{b} \tag{4.43}$$

$$\kappa_a = \frac{a}{b} n\pi \sqrt{K+1} \qquad \kappa'_a = \frac{a}{b} n\pi \sqrt{K-1} \tag{4.44}$$

$$K = \frac{\omega}{(n^2\pi^2 / b^2)\sqrt{B_p / \rho h_p}} \tag{4.45}$$

where integer n=1, 2, 3... represents the mode number in y-direction, B is the bending stiffness, ρ is the density and h is the thickness of the plate in the bay. $\xi(x, y)$ is the mode shape corresponding to the natural frequency ω.

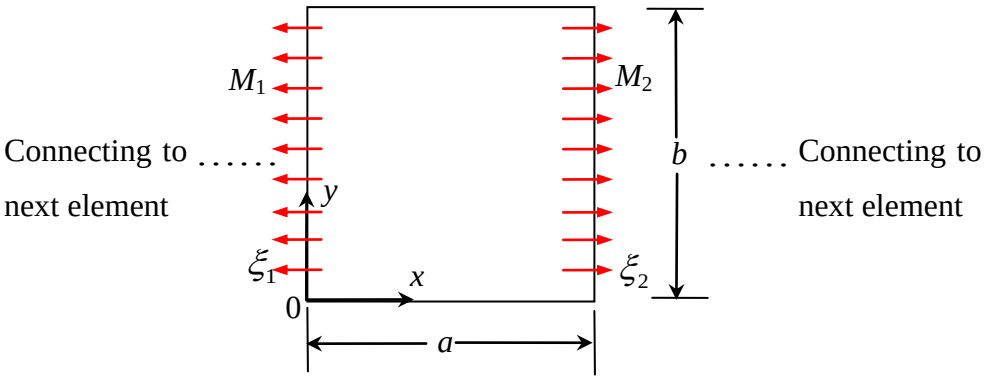

Figure 4.9 One periodic element as a thin rectangular plate

To calculate the receptance at the coupling lines of both right and left sides, the equation (4.42) need to be solved by applying the boundary conditions. First, simply-supported boundary conditions at the coupling edges of x=0 and x=a are considered. From equation (4.42), it can be shown that the bending moment and the responses in displacement in the y-direction both follow a sinusoidal distribution. Thus the formulation of receptance which is the ratio of the displacement and force will cancel the y-component and it will not be considered in the following derivation.

The simply-supported boundary conditions at the opposite coupling lines yield:

$$\xi(x,y,t)=0 \quad M=M_1 \quad \text{at } x=0$$
$$\xi(x,y,t)=0 \quad M=M_2 \quad \text{at } x=a \tag{4.46}$$

At natural frequencies, the mode shape $A_s(x,y)$ at the boundaries has:

$$A_s(x,y)=0 \text{ and } -B\frac{\partial^2 A_s}{\partial x^2}=M_1\sin(n\pi y') \quad \text{at } x=0$$
$$A_s(x,y)=0 \text{ and } -B\frac{\partial^2 A_s}{\partial x^2}=M_2\sin(n\pi y') \quad \text{at } x=a \tag{4.47}$$

where M_1 and M_2 are magnitudes of the bending moment per unit length along the coupling lines. Considering both boundaries, the overall solution for the mode shape is a sum of two parts where M_1 and M_2 are applied using equations from (4.47) respectively as:

$$A_s(x,y)=A_s(x,y)\big|_{M_1}+A_s(x,y)\big|_{M_2} \tag{4.48}$$

and

$$A_s(x,y)\big|_{M_1}=-\frac{M_1}{B_p}\frac{a^2}{(\kappa_a^2+\kappa_a'^2)}\left[\frac{\sinh(\kappa_a x')}{\sinh(\kappa_a)}-\frac{\sin(\kappa_a' x')}{\sin(\kappa_a')}\right]\sin(n\pi y') \tag{4.49}$$

$$A_s(x,y)\big|_{M_2}=-\frac{M_2}{B_p}\frac{a^2}{(\kappa_a^2+\kappa_a'^2)}\left[\frac{\sinh[\kappa_a(1-x')]}{\sinh(\kappa_a)}-\frac{\sin[\kappa_a'(1-x')]}{\sin(\kappa_a')}\right]\sin(n\pi y') \tag{4.50}$$

The rotational receptances for a plate are defined by Azimi *et al.* [104] as:

$$\alpha_{ij}=\frac{\partial A_s(x,y)\big|_{M_j}/\partial x}{(-1)^{j-1}M_j\sin(n\pi y')} \qquad \text{at } x=x_i \quad i=1,2,\ x_1=0 \text{ and } x_2=a \tag{4.51}$$

Substituting equation (4.49) and (4.50) into (4.51), the direct and cross receptances of the plate when two opposite coupling edges are simply-supported can be obtained and simplified as:

$$\alpha_{11}=\alpha_{22}=Ca\left[\kappa_a \coth(\kappa_a)-\kappa'_a \cot(\kappa'_a)\right] \tag{4.52}$$

$$\alpha_{12}=\alpha_{21}=Ca\left[\kappa_a / \sinh(\kappa_a)-\kappa'_a / \sin(\kappa'_a)\right] \tag{4.53}$$

where Ca is defined as:

$$Ca=-\frac{a}{B_{\mathrm{p}}(\kappa_a^2+\kappa_a'^2)} \tag{4.54}$$

$\alpha_{11}=\alpha_{22}$ because of the symmetrical nature of the structure and $\alpha_{12}=\alpha_{21}$ due to the reciprocity relationship.

For the periodic ribbed plate shown in Figure 3.3 (dimensions and material properties in Table 2), Figure 4.10 shows the receptances with the fundamental mode in *y*-direction (*n*=1 used in equation (4.44) and (4.45)) at the coupling lines for the bay element from the model. Figure 4.11 shows the corresponding $\cosh(\lambda)$ calculated from these receptances using equation (4.36). In Figure 4.10, each time the receptance jumps between positive and negative values corresponds to a position in Figure 4.11 where $\cosh(\lambda)=\pm 1$. It can be calculated from equation (4.29) that when $\cosh(\lambda)=1$, $\xi_1=\xi_2$ and $F_1=-F_2$ where the forces at both ends of the element have opposite phase whereas when $\cosh(\lambda)=-1$, $\xi_1=\xi_2$ and $F_1=F_2$ both forces have the same phase.

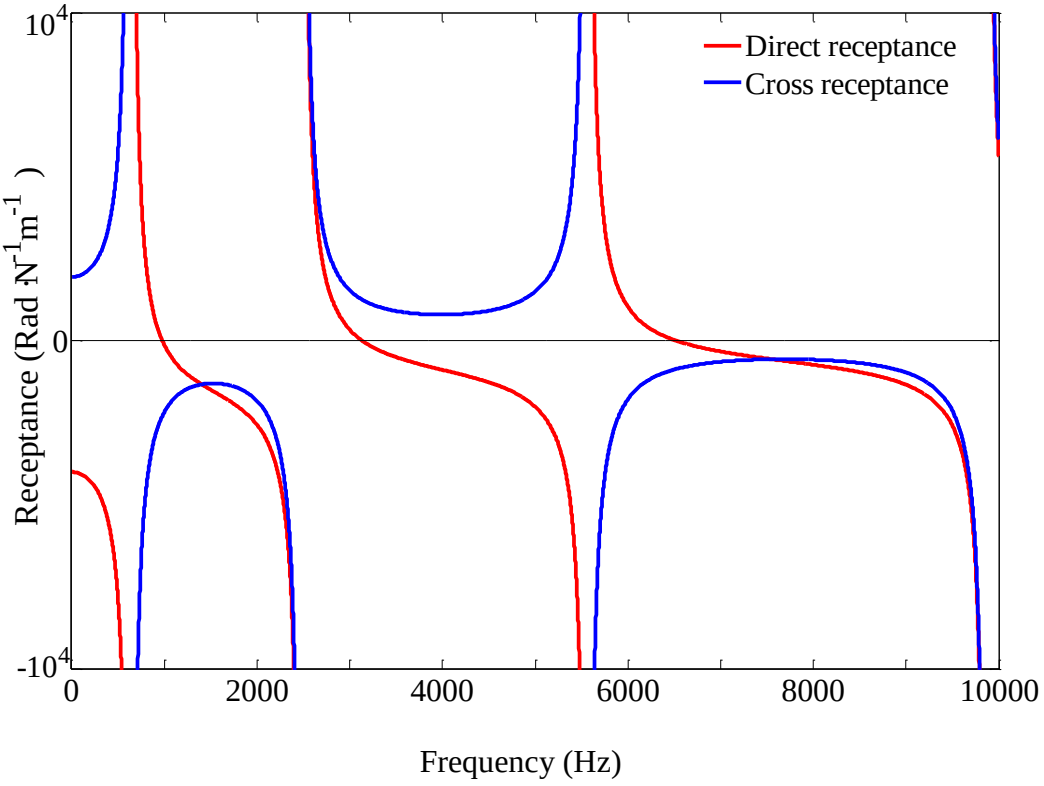

Figure 4.10 Direct and cross receptances for a rectangular thin plate

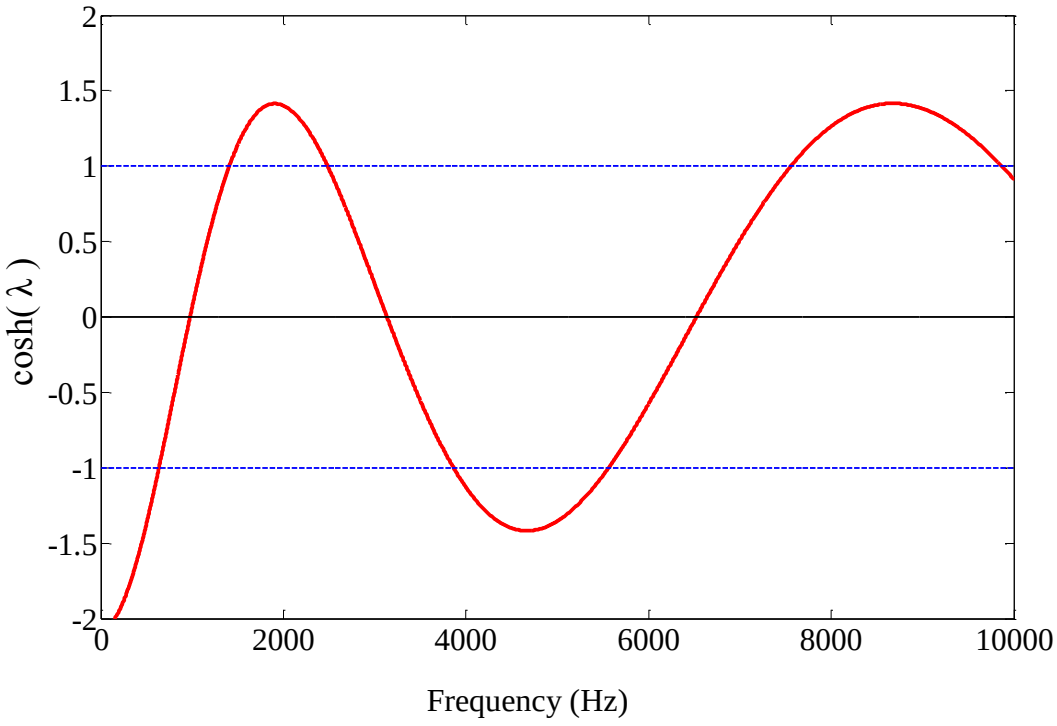

Figure 4.11 cosh(λ) variation with frequency for a rectangular thin plate

Figure 4.12 compares the propagation constants calculated using the receptance method and the wave approach. The propagation angle used in the wave approach is zero. This means that it does not contribute to the modal response in *y*-direction which is the closest equivalent situation to the calculation used in the receptance method. A noteworthy finding is that the receptance method and the wave approach give the same lower frequency limit for all pass bands; however for the upper frequency limit of each pass band, the receptance method gives a lower frequency than the wave approach. This discrepancy is caused due to the simplifications in the receptance method and the assumptions in the wave approach:

- In the wave approach, the plate element in *y*-direction is considered as infinite whereas the receptance method incorporates the modal response in the *y*-direction due to its finite length.

- The receptance method simplifies the stiffened rib to a continuous line discontinuity in the structure so that the effect of torsion and bending of the ribs on wave propagation between bays is ignored. In contrast, the wave approach takes account of this in the modelling. However, both methods ignore the finite width of the rib in the *x*-direction so that the periodic elements in the structure only consider the bays as thin plates.

Although there are differences between these two methods, this should not deter the usage of the receptance method to investigate the relationship between the bounding frequencies of the periodic structure and the natural frequencies of its periodic elements.

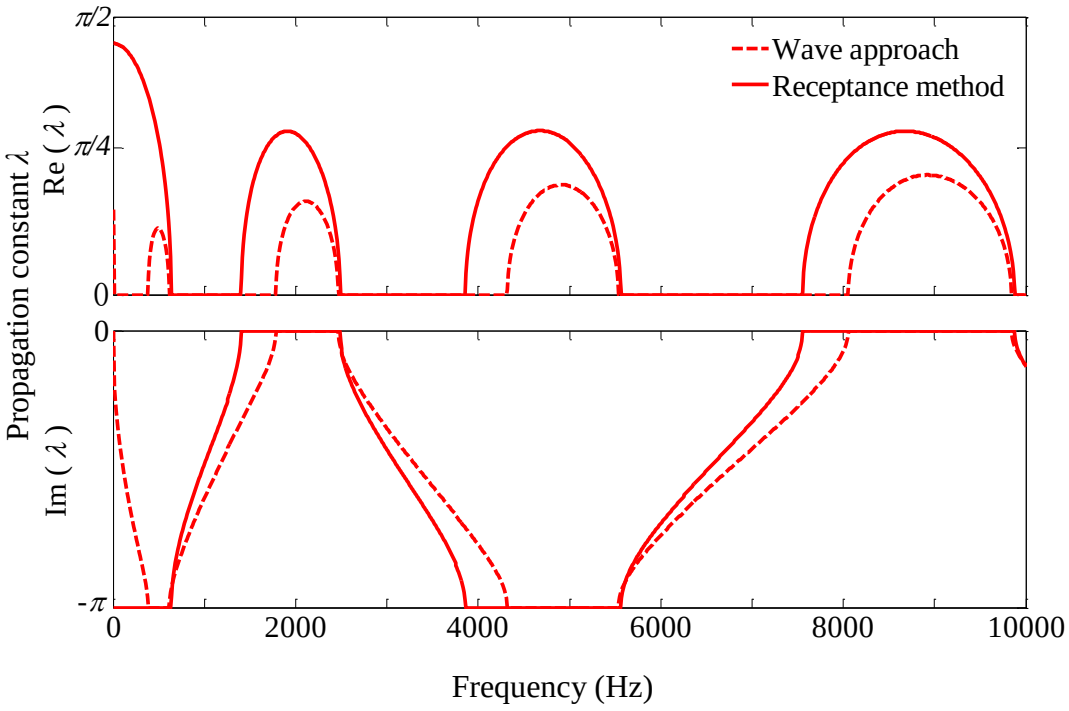

Figure 4.12 Real and imaginary part of the propagation constant calculated from receptance methods for comparison with the wave approach

4.5.5 Calculating natural frequencies of a thin rectangular plate representing a periodic element

The calculation of natural frequencies of thin rectangular plates with various boundary conditions have been widely studied. Leissa [105] calculated the 'exact' first six modes for rectangular thin plate with different length/width ratio of all possible boundary conditions using a numerical method. Dickinson [88] made the approximation of considering the mode shape of a rectangular thin plate is represented by mode shapes of single beams along x and y axes. The solution of natural frequencies of the plate can be developed using energy as the primary parameter and is often referred to as the Rayleigh-Ritz method. The approximate natural frequencies using such a method for the rectangular periodic bay in Figure 4.9 are adapted from Blevins [85] as:

$$f_{ij} = \frac{\pi}{2}\left[\frac{G_1^4}{a^4} + \frac{G_2^4}{b^4} + \frac{2J_1J_2 + 2\mu(H_1H_2 - J_1J_2)}{a^2b^2}\right]^{1/2}\left[\frac{Eh_p^3}{12\rho_S(1-\mu^2)}\right]^{1/2} \quad (4.55)$$

where *i* and *j* are mode number indices corresponding *x* and *y* direction. and *E*, ρ_s, μ are Young's modulus, mass density per unit area and Poisson's ratio respectively. Geometrical dimensions of the plate *a*, *b* and *h* represents length in *x*-direction, width in *y*-direction and plate thickness respectively. Dimensionless constants *G*, *J* and *H* are dependent on the boundary conditions and mode number, which are given in Table 1.

4.5.6 Investigating the relationship between natural frequencies of the periodic element and bounding frequencies for pass/stop bands of periodic ribbed plates

As noted in Section 4.5.3, the bounding frequencies of the pass bands are determined by the natural frequencies of a single periodic element. The boundary conditions must either be free (FFFF) or combinations of simply-supported and clamped (e.g. SSSS, CCCC, SCSC, SSCC) for the two opposite junctions that are connected to adjacent periodic elements. Considering the bay element from the periodic ribbed plate, the natural frequencies with the above boundary conditions can be calculated using equation (4.55). The following results will are calculated from FFFF and SSSS boundary conditions.

For the periodic ribbed plate introduced in chapter 3 as shown in Figure 3.3 (dimensions and material properties in Table 2), Figure 4.13 shows a selection of mode numbers in the *y*-direction (taking values from one to four) alongside their corresponding propagation constants that have been calculated from the receptance method. This shows that all the natural modes for simply-supported boundaries indicate the starting frequency of a pass band (or ending frequency for a stop band). However, it is only for the first mode in the *y*-direction that all the natural modes with free boundaries exactly indicate the starting frequency of a stop band (or ending frequency for a pass band). The latter finding is not

problematic because it has been shown in Figure 4.12 that the simplifications in the receptance method means that this starting frequency is more accurately identified by the wave approach.

Figure 4.14 allows an assessment of whether the natural frequencies indicate the boundaries of pass or stop bands over the full range of mode numbers in the y-direction. As previously indicated by Figure 4.13, it is confirmed that all natural frequencies with simply-supported boundary conditions determine the lower limit of each pass band but for free boundary conditions, the upper bounds of the pass bands are only described by the natural frequency for the first mode. Note that the natural frequencies at 0Hz for FFFF elements are not included on the figures.

In conclusion, the fundamental mode of a bay assuming simply-supported boundaries will always occur at the same frequency as the lower boundary of the first pass band on the periodic ribbed plate. This means that in chapters 6 and 7 it will be reasonable to attempt to treat the bays of the periodic ribbed plate as individual subsystems in SEA and ASEA models above the fundamental mode frequency. This might have been difficult to justify if the fundamental mode always fell within the first stop band where that stop band covered all angles of incidence. Fortunately, all the examples for periodic ribbed plates in section 4.4 show that the first stop band never covers all angles of incidence at any particular frequency. Therefore, at frequencies above the fundamental mode of each bay, there will always be angles of incidence that are in a pass band. However, it will only be once the SEA and ASEA models are analysed in chapters 6 and 7 that we will be able to assess whether the effect of successive spatial filtering across a ribbed plate (which reduces the available angles of incidence) still makes it reasonable to treat bays as individual subsystems.

4.6 Conclusions

This chapter used wave theory and Bloch theory to describe bending wave propagation on a periodic ribbed plate with symmetric ribs. This theory will be incorporated in chapter 5 to determine the SEA coupling loss factor for L-junctions which incorporate this type of periodic ribbed plate.

Geometries for a variety of different periodic ribbed plates were described for analysis in this thesis. Their stop/pass band characteristics have been analyzed to indicate how these geometric parameters can significantly change the distribution of the propagation and attenuation zones.

This chapter also investigates the relations between the bounding frequencies of the stop/pass bands of the periodic ribbed plate and the natural frequencies of the periodic element of the ribbed plate. This analysis is performed in order to examine the validity of SEA and ASEA models in chapter 6 where each bay of the ribbed plate will be treated as a single subsystem in SEA.

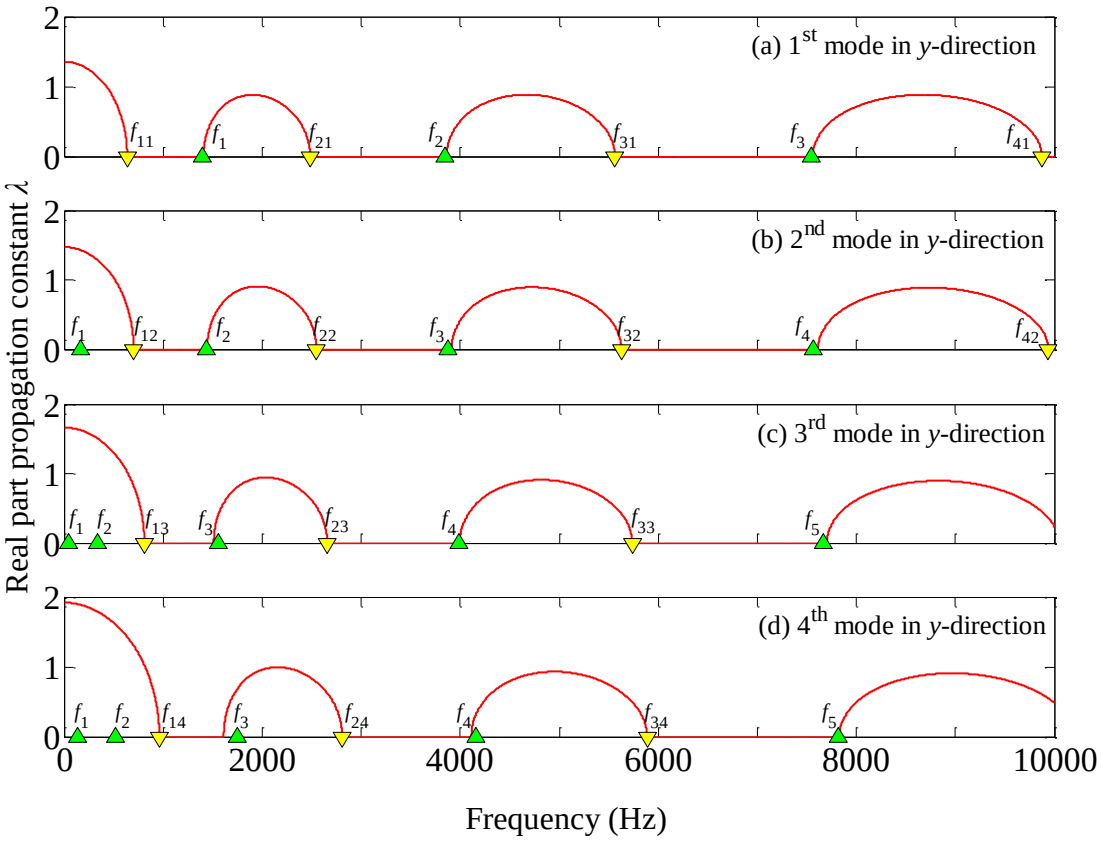

Figure 4.13 Real part of propagation constant for the periodic ribbed plate as shown in Figure 3.3 (dimensions and material properties in Table 2) with natural frequencies of a single periodic element (▽ markers represents the natural modes with simply-supported boundary conditions (SSSS); △ markers with free boundary conditions (FFFF); f_{ij} and f_i means natural frequency with mode number i in x-direction and mode number j in y-direction)

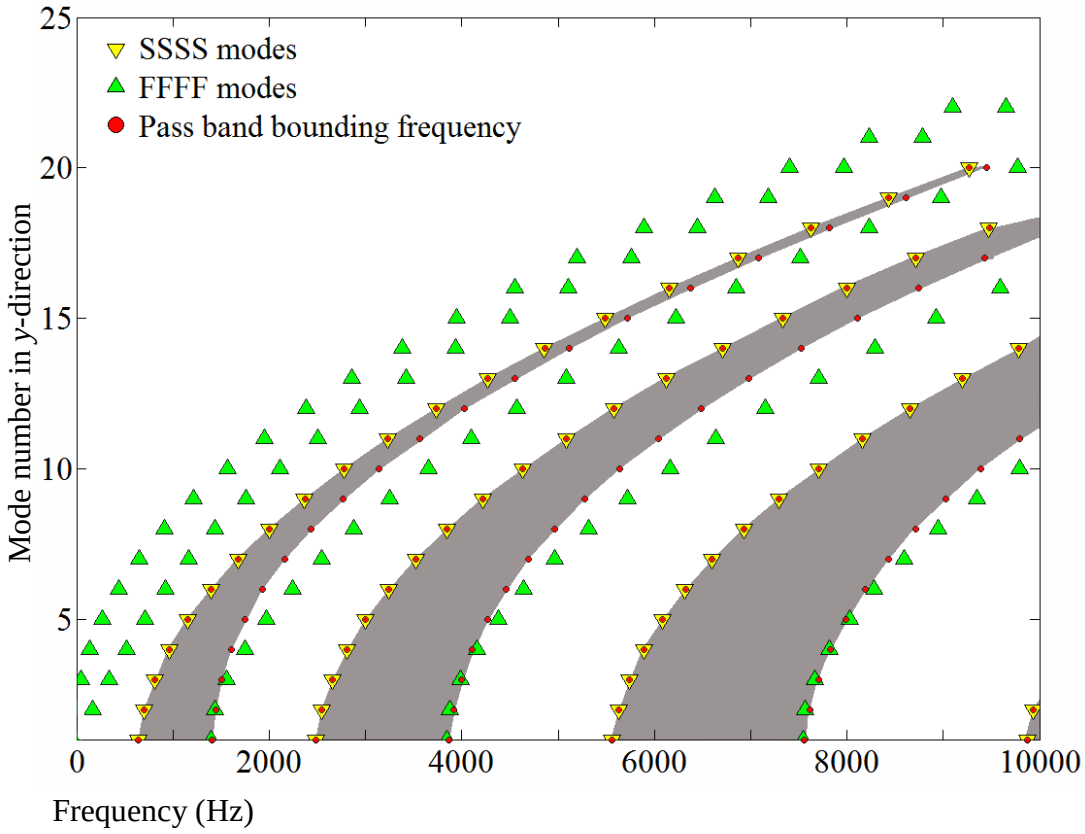

Figure 4.14 Natural modes with different boundary conditions for periodic bay element (▽ markers represents the natural modes with simply-supported boundary conditions; △ markers with free boundary conditions; ● marks the bounding frequencies of pass bands); pass bands are shaded in grey.

5 Structure-borne sound transmission across structural junctions using wave theory

5.1 Introduction

This chapter describes the prediction models for structure-borne sound transmission across structural junctions of semi-infinite plates using the wave approach. The resulting transmission coefficients are used to determine the coupling loss factors for use in SEA and ASEA.

Various structural junctions are discussed in this chapter starting with bending and in-plane wave transmission across an L-junction of two thin, isotropic, homogeneous plates. Secondly, bending wave transmission in a plate with a single reinforcing rib is discussed. Thirdly, considering a plate with periodic reinforcing ribs and an isotropic homogeneous plate forming an L-junction, bending wave transmission in the coupled structure is modelled based on Tso and Hansen [10]. The effect of periodicity of the ribbed plate on the wave transmission is discussed. Finally, the same L-junction is considered but the periodic ribbed plate is modelled as a plate of uniform thickness with orthotropic elastic properties. This allows adaptation of the model for the L-junction with two isotropic homogeneous plates by using angle-dependent bending stiffness instead of isotropic bending stiffness.

5.2 Literature review on vibration transmission through structural junctions

In the wave approach to SEA, the vibration fields on the subsystems are represented by superposition of travelling waves [17] and the power transfer between subsystems through structural junctions is qualified by the transmission coefficient. The transmission coefficient of structural junctions has been carried out by others for different types of structural junction. This section reviews the works on rigid plate/plate and plate/beam junctions.

5.2.1 Plate/Plate junctions

Early publications on the structure-borne sound transmission between structural junctions of semi-infinite plates were limited to normal incidence [106, 107] as

the plates were discretized into a series of strips perpendicular to the junction. Both the bending and in-plane wave transmission across the junction were studied.

The normal incidence case was extended to oblique incidence by Lyon and Eichler [108] in studying a T-junction. They only considered bending wave transmission in the model as the generation of in-plane wave was ignored due to the assumption of a simply-supported junction. Kihlman [109, 110] studied both the bending and in-plane wave transmission for a symmetric cross junction of semi-infinite plates. Due to the symmetric arrangement of the junction, the formulation was simplified as in-plane waves were only generated in the plates perpendicular to the source plate and the plate in the same plane as the source plate only carries bending wave. Cremer *et al.* [34] carried out a comprehensive investigation on wave transmission through various structural junctions, such as L-, T- and cross junctions taking into account bending and in-plane wave transmission. Craik [111] summarized the structure-borne sound transmission for typical types of building structural junctions in the framework of SEA. The work focused on the determination of coupling loss factors from the wave approach. Considering the diffuse vibration field assumption in SEA, the coupling loss factor was calculated from an angular averaged transmission coefficient obtained from an integration of angle-dependent transmission coefficient over all angles of incidence using equation (2.27).

Junctions of plates coupled at arbitrary angles were discussed by Rosenhouse [112] for folded plates and the damping was also considered. A general description of wave transmission at junctions of plates with arbitrary coupling angles was given by Langley and Heron [113] based on a dynamic stiffness matrix formulation.

Many works also studied L-junctions comprised of more complicated plate structures than isotropic, homogeneous plates. Tso and Hansen [10] analyzed the vibration transmission across an L-junction comprised of an isotropic, homogeneous plate and a periodic ribbed plate as the one discussed in chapter 4. Although the vibration field on the periodic ribbed plate is more complicated than the isotropic, homogeneous plate, the wave transmission at the junction is modelled using the same method as for the L-junction of two semi-infinite isotropic, homogeneous plates as discussed by Cremer *et al.* [34]. Bosmans *et al.*

[86, 89] investigated structural junctions comprised of orthotropic plates and the boundary conditions are described in a more complicated way to incorporate in-plane wave transmission and such a description can also be used for other junctions.

In this chapter, wave approaches considering both bending and in-plane wave described by Cremer *et al.* [34] and Bosmans *et al.* [86, 114] are used to calculate the transmission coefficient between isotropic and orthotropic plates. The model from Tso and Hansen is also adopted for the L-junction of isotropic and periodic ribbed plates.

5.2.2 Plate/Beam junctions

The vibration transmission at junctions formed from plates and beams was investigated by Heckl [106] and Cremer *et al.* [34]. The coupling between the plate and beam is usually simplified as a line junction by ignoring beam cross-section deformation. The effect of beam shear deformation and rotational inertia is considered. Wöhle *et al.* [115] theoretically and numerically analyzed the wave transmission in a plate with a single reinforcing rib. This work had been done in the context of SEA aiming to predict the coupling loss factor using angular averaged transmission coefficients for semi-infinite plates. Graven and Gibbs [116] and Gibbs and Graven [117] extended previous methods for a plate/beam junction based on a different formulation of the boundary conditions and incorporated the damping loss factor in the modelling. The effect of plate thickness and material constants in the transmission of bending and in-plane waves was discussed. It also confirmed that when the beams are symmetrically attached to the plate, with an incident bending wave impinging upon the junction, there was no in-plane generation on the plate. Lu *et al.* [118] incorporated the cross-section vibration of the beams in the modelling of wave transmission across plate/beam junctions, and the power conservation error was used to evaluate the accuracy of the method. It was indicated that this method only satisfies the power conservation requirement at low frequencies and large errors could occur in higher frequencies. Steel [119] developed a model using the wave approach and impedance formulations to investigate the wave transmission between columns and walls of framed buildings. This method allows the bending and torsional wave motion in the beam. Craik and

Wilson [120] used a simplified method for vibration transmission across plate/beam junctions by treating the beam as a massless and stiff element. Cremer [121] investigated an ideal plate-beam system considering bending wave propagation on an infinite thin plate with one stiffened beam with the emphasis on the stresses in the plate and the beam. Heckl [106] extended this analytical model to consider finite systems and indicated that very small attenuations due to the beam were found near the resonances of the beam and higher attenuations elsewhere. Both of their studies assumed that the plate was made of a set of narrow strips of plates and the model was simplified into a one-dimensional problem where a set of one-dimensional dynamic elements was considered. However, the major limitation of this analytical approach is that it only allows the wave motion in the direction that is normal to the junction. Cremer *et al.* [34] later developed the analytical expressions of wave propagation on such a structure with infinite extent considering an oblique incident wave angle and showed that the main feature of this type of structure was the 'trace-matching' phenomena when the bending wave attenuation caused by the stiffened beam vanished. Grice and Pinnington [122] discussed the frequency limitation of this approach for finite systems due to the local resonance reacting.

5.3 Wave transmission across an L-junction of thin, homogeneous, isotropic plates

This section describes the structure-borne sound transmission for L-junctions of semi-infinite, thin, homogeneous, isotropic plates using the wave approach. First of all, only bending wave transmission is considered with an oblique incident wave angle impinging upon the junction between the two plates. Secondly, incident bending waves with a wave conversion between bending and in-plane waves at the junction is modelled. The wave approach presented in this section follows that of Cremer *et al*. [34], Craik [111] and Bosmans [87].

5.3.1 Bending waves only

This section only considers the bending wave transmission at the L-junction. The two semi-infinite plates are assumed to be connected to each other by a junction beam as shown in Figure 5.1. The junction beam does not represent a physical part of a real junction. It is assumed to have zero mass and a rigid cross-section [74]. As only the transmission of the bending wave at the junction is allowed, the junction beam is considered to be simply-supported such that there is no lateral displacement of the junction beam although it is free to rotate.

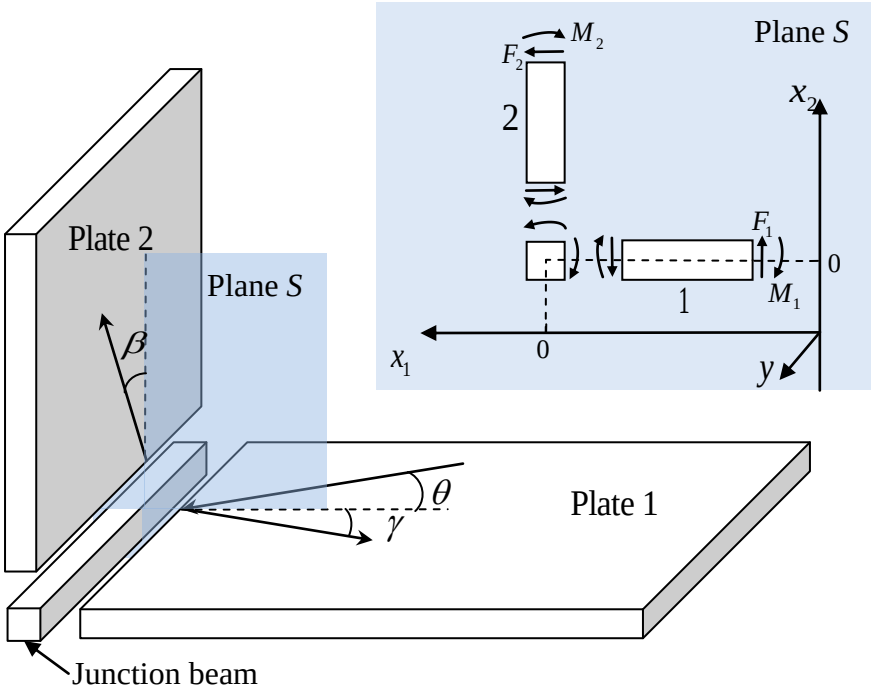

Figure 5.1 Bending wave transmissions between two isotropic homogeneous plates across a junction beam and its corresponding coordinate system

For the source plate (plate 1), carrying an incident bending wave propagating at an angle of θ with a wave amplitude of unity, the displacement of the incident wave, ξ_{inc}, can be expressed as:

$$\xi_{\text{inc}} = \exp(-ik_{\text{B1}}x\cos\theta)\exp(-ik_{\text{B1}}y\sin\theta)\exp(i\omega t) \tag{5.1}$$

where k_{B1} is the bending wavenumber of the plate 1. The first two exponential terms of equation (5.1) represent bending wave propagation in the positive *x*- and *y*-direction, respectively.

When the incident wave reaches the junction, a transmitted wave on plate 2 and a reflected wave on the source plate 1 are generated. The propagation directions of the reflected waves have the same wave angle as expressed in equation (5.2) if a specular reflection is assumed. The wave angles of the transmitted waves can be determined by Snell's Law as shown in equation (5.3).

$$\theta = \gamma \tag{5.2}$$

$$k_{\text{B1}}\sin\theta = k_{\text{B2}}\sin\beta \tag{5.3}$$

where γ is the reflected wave angle and β is the transmitted wave angle. Equation (5.3) also indicates that along the *y*-directions, incident, transmitted and reflected waves have the same wavenumbers so that the *y*-component for these waves are expressed the same as in equation (4.4) as $\exp(-ik_{\text{B1}}\sin\theta y)$.

As indicated by equation (5.3), the transmitted wave angle β increases with the increase of the incident wave angle θ. If the wavenumber of the incident wave is larger than that of the transmitted wave, that is $k_{\text{B2}} < k_{\text{B1}}$, there is an upper limit for the incident wave angle. Above this limit the transmitted wave angles would have complex values and there will be no transmission of propagating waves. This upper limit can be defined as a cut-off angle, θ_{co}, which based on the Snell's law, can be calculated by setting $\beta = \pi/2$ as shown in equation (5.4):

$$\theta_{co} = \arcsin\left(\frac{k_{B2}}{k_{B1}}\right) \tag{5.4}$$

Based on these, the general expressions of transmitted and reflected waves in terms of displacements can be written as:

$$\xi_{trans} = T_2 \exp(\pm k_{B2x} x_2) \exp(-ik_{B1} y \sin\theta) \exp(i\omega t) \tag{5.5}$$

$$\xi_{reflect} = T_1 \exp(\pm k_{B1x} x_1) \exp(-ik_{B1} y \sin\theta) \exp(i\omega t) \tag{5.6}$$

where k_{B1x} represents the bending wavenumber component in *x*-direction for plate 1.

Substituting equation (5.5) and (5.6) into equation (3.1) for bending wave on isotropic plate respectively, two pairs of wavenumbers are obtained for transmitted waves:

$$k_{B2x} = \pm i\sqrt{k_{B2}^2 - k_{B1}^2 \sin^2\theta} = \pm ik_{B2} \cos\beta \tag{5.7}$$

$$k_{B2x} = \pm\sqrt{k_{B2}^2 + k_{B1}^2 \sin^2\theta} = \pm k_{B2}\sqrt{1+\sin^2\beta} \tag{5.8}$$

The wavenumber in *x*-direction can either be real or imaginary. The pair of imaginary wavenumbers corresponds to the travelling wave along positive and negative *x*-direction whereas the real wavenumbers represent the near-field where waves decay exponentially.

(1) Source plate

The total displacement on the source plate consists of the contribution from the incident wave in the positive *x*-direction, the reflected travelling wave and the near-field in the negative *x*-direction. Equation (5.5) can then be rewritten as:

$$\xi_1 = \xi_{\text{inc}} + \xi_{\text{reflect}} + \xi_{\text{nf},1}$$
$$= [\exp(-ik_{\text{B1}}x_1\cos\theta) + T_1\exp(ik_{\text{B1}}x_1\cos\theta) + T_2\exp(k_{\text{B1}}x_1\sqrt{(1+\sin^2\theta)})]\exp(-ik_{\text{B1}}y\sin\theta + i\omega t)$$

(5.9)

(1) Receiving plate

Similarly, the total displacement on the receiving plate is made of a transmitted wave and near-field in the positive *x*-direction.

$$\xi_2 = \xi_{\text{trans}} + \xi_{\text{nf},2}$$
$$= [T_3\exp(-ik_{\text{B2}}x_2\cos\beta) + T_4\exp(-k_{\text{B2}}x_2\sqrt{(1+\sin^2\beta)})]\exp(-ik_{\text{B1}}y\sin\theta + i\omega t)$$

(5.10)

To calculate the four unknown wave amplitudes $\{T_1,\ T_2,\ T_3,\ T_4\}$ in equation (5.9) and (5.10), the corresponding boundary conditions and continuity conditions at the junction beam need to be considered.

(1) Continuity conditions: junction lateral displacement

As the junction beam is simply supported, there is no lateral displacement along the junction.

$$\xi_1(x_1)\big|_{x_1=0} = 0 \tag{5.11}$$

$$\xi_2(x_2)\big|_{x_2=0} = 0 \tag{5.12}$$

Putting equation (5.11) and (5.12) into the wave equations of the source and receiving plates gives:

$$T_1 + T_2 = -1 \tag{5.13}$$

$$T_3 + T_4 = 0 \tag{5.14}$$

(2) Continuity conditions: junction rotation

The continuity of junction rotation requires that the angular rotation of the source plate at the junction equals to the angular rotation of the receiving plate at the junction. The angular rotation of plate can be calculated from equation (3.11), thus this continuity condition can be written as:

$$\left.\frac{\partial \xi_1}{\partial x_1}\right|_{x_1=0} = \left.\frac{\partial \xi_2}{\partial x_2}\right|_{x_2=0} \tag{5.15}$$

Substituting equation (5.9) and (5.10) into (5.15) gives:

$$T_1 ik_{B1}\cos\theta + T_2 k_{B1}\sqrt{(1+\sin^2\theta)} + T_3 ik_{B2}\cos\beta + T_4 k_{B2}\sqrt{(1+\sin^2\beta)} = ik_{B1}\cos\theta \tag{5.16}$$

(3) Equilibrium Condition: Bending moment

The sum of the bending moments at the junction must equal zero, as

$$M_1\big|_{x_1=0} - M_2\big|_{x_2=0} = 0 \tag{5.17}$$

The bending moment per unit length for the isotropic plate is given in equation (3.12) and inserting into (5.17) gives:

$$\left[-B_1\left(\frac{\partial^2 \xi_1}{\partial x_1^2} + \mu_1 \frac{\partial^2 \xi_1}{\partial y^2}\right) + B_2\left(\frac{\partial^2 \xi_2}{\partial x_2^2} + \mu_2 \frac{\partial^2 \xi_2}{\partial y^2}\right)\right]_{x_1=x_2=0} = 0 \tag{5.18}$$

where B_i represents the bending stiffness for plate i calculated from equation (3.2) and μ_i is the Poisson's ratio.

Substituting equations (5.9) and (5.10) into (5.18) gives:

$$T_1 B_1 k_{B1}^2 \cos^2\theta - T_2 B_1 k_{B1}^2 \left(1+\sin^2\theta\right) - T_3 B_2 k_{B2}^2 \cos^2\beta + T_4 k_{B2}^2 \left(1+\sin^2\beta\right)$$
$$= -B_1 k_{B1}^2 \cos^2\theta + k_{B1}^2 \sin^2\theta(\mu_1 B_1 - \mu_2 B_2)$$

(5.19)

Equations (5.13), (5.14), (5.16) and (5.19) can be combined into matrix form as:

$$\begin{bmatrix} 1 & 1 & 0 & 0 \\ 0 & 0 & 1 & 1 \\ ik_{B1}\cos\theta & k_{B1}\sqrt{(1+\sin^2\theta)} & ik_{B2}\cos\beta & k_{B2}\sqrt{(1+\sin^2\beta)} \\ B_1 k_{B1}^2 \cos^2\theta & -B_1 k_{B1}^2 \left(1+\sin^2\theta\right) & -B_2 k_{B2}^2 \cos^2\beta & B_2 k_{B2}^2 \left(1+\sin^2\beta\right) \end{bmatrix} \begin{bmatrix} T_1 \\ T_2 \\ T_3 \\ T_4 \end{bmatrix} = \begin{bmatrix} -1 \\ 0 \\ ik_{B1}\cos\theta \\ -B_1 k_{B1}^2 \cos^2\theta + k_{B1}^2 \sin^2\theta(\mu_1 B_1 - \mu_2 B_2) \end{bmatrix}$$

(5.20)

The unknown amplitudes $\{T_1,\ T_2,\ T_3,\ T_4\}$ can determined by the inversion of the matrix in equation (5.20).

5.3.2 Evaluation of the transmission coefficients

The transmission coefficient is defined as the wave power transmitted across the coupling junction divided by the incident wave power on it. Similarly, the reflection coefficient is the ratio of reflected wave power from the junction to the incident wave power. The transmission coefficient, τ , and reflection coefficient, *r*, can be expressed using the ratio of wave intensities as:

$$\tau(\theta) = \frac{W_{trans}(\theta)}{W_{inc}(\theta)} = \frac{I_{trans}(\theta)}{I_{inc}(\theta)} \qquad (5.21)$$

$$r(\theta) = \frac{W_{\text{reflect}}(\theta)}{W_{\text{inc}}(\theta)} = \frac{I_{\text{reflect}}(\theta)}{I_{\text{inc}}(\theta)} \tag{5.22}$$

As only bending waves are considered, the sum of transmission and reflection coefficients equals unity:

$$\tau + r = 1 \tag{5.23}$$

For the source plate, the incident bending wave upon the junction has unit amplitude and the wave angle of θ. Its wave intensity in the *x*-direction can be expressed based on equation (3.14):

$$I_{\text{B1}x}(\theta) = B_1 \omega k_{\text{B1}}^3 \cos\theta \tag{5.24}$$

The wave intensity is the power flow per unit width, which can be calculated from the force and velocity and moment components as follows:

$$I_{\text{B}}(\theta) = \frac{1}{2}\text{Re}\{M\ \dot{\phi}^* + F\ \dot{\xi}^*\} \tag{5.25}$$

where ϕ is the rotation angle of the plate which can be calculated from equation (3.11). $*$ represents complex conjugate and $\dot{}$ indicates the derivative with respect to time. The bending moment *M* and force *F* for source plate and receiving plate can be calculated from the following equations.

For the transmitted waves on the receiving plate (plate 2) at the junction:

$$M_2 = B_2 T_3 (-k_{\text{B2}}^2 \cos^2\beta + \mu_2 k_{\text{B2}}^2) \tag{5.26}$$

$$\dot{\phi}_2 = T_3 k_{\text{B2}} \omega \cos\beta \tag{5.27}$$

$$F_2 = B_2 T_3 \left[i k_{\text{B2}}^3 \cos^3\beta + (2-\mu_2) i k_{\text{B2}} k_{\text{B1}}^2 \sin^2\theta \cos\beta \right] \tag{5.28}$$

For the reflected waves on the receiving plate at the junction:

$$M_1 = B_1 T_1 (k_{B1}^2 \cos^2\theta - \mu_1 k_{B1}^2 \sin^2\theta) \tag{5.29}$$

$$\dot{\phi}_1 = -T_1 k_{B1} \omega \cos\theta \tag{5.30}$$

$$F_1 = B_1 T_1 \left[i k_{B1}^3 \cos^3\theta + (2-\mu_1) i k_{B1}^3 \sin^2\theta \cos\theta \right] \tag{5.31}$$

The wave intensities for transmitted waves and reflected waves are be calculated by putting equation (5.26) to (5.28) and (5.29) to (5.31) into (5.25) respectively. The transmission coefficient and reflection coefficient can then be calculated from equation (5.21) and (5.22) by using the transmitted and reflected wave intensity and the wave intensity for incident wave in equation (5.24).

Figure 5.2 shows the transmission coefficient between the L-junction of two identical isotropic plates. The transmission coefficient for an incident wave is only a function of incident wave angle and does not vary with frequency. As the two plates are made of the same material and have the same thickness, at normal incidence (θ=0 º), half of the energy carried out by incident wave is transmitted and half is reflected back to the source plate. When θ=90 º, the incident wave travels along the coupling junction; hence there is no energy transmitted to the receiving plate. The angular average transmission coefficient for this type of L-junction is 1/3.

Assuming the source plate has a diffuse vibration field, the angular-average coefficients can be calculated from equation (2.27). The coupling loss factor used in SEA can be calculated from angular-average transmission coefficient as shown in equation (2.26).

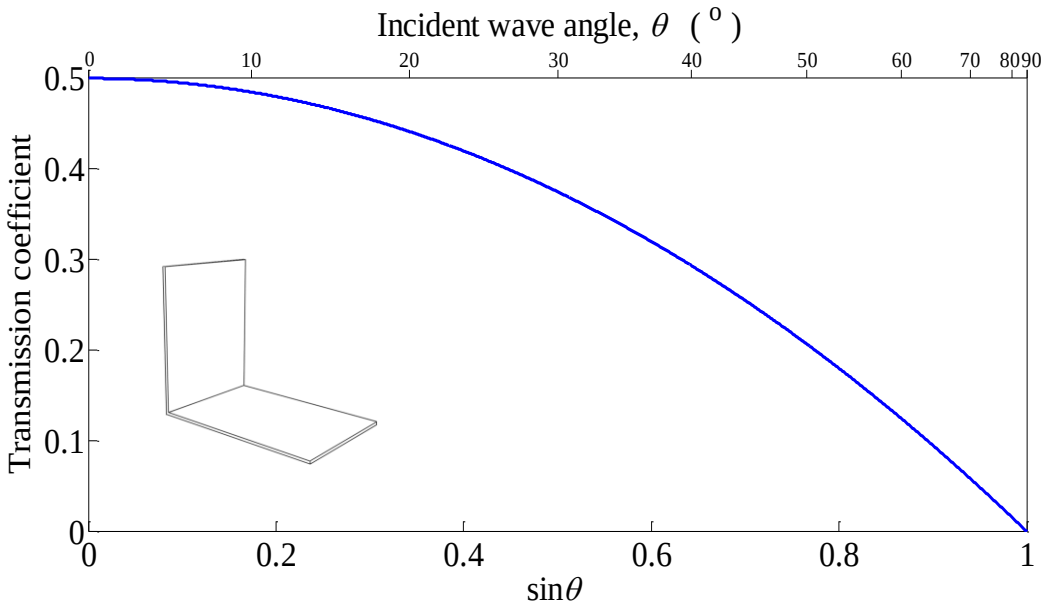

Figure 5.2 Angle-dependent transmission coefficients between L-junction of two identical isotropic homogeneous plates using the wave approach considering bending wave transmission.

5.3.3 Bending and in-plane waves

In the theoretical model for only bending wave transmission through the L-junction, the junction beam is considered to be simply supported. If this constraint is removed, when bending wave incident upon the junction, the incident wave generates not only bending, but also quasi-longitudinal and in-plane waves.

The incident bending wave with unity amplitude is described in equation (5.1), and the transmitted and reflected bending wave field can be expressed in the same way as in equation (5.5) and (5.6).

The wave field of in-plane wave on the receiving plate and source plate can be written as follows based on the equation (3.20) and (3.21).

For the reflected in-plane wave on the receiving plate:

$$\Phi_1 = T_5 \exp(-ik_{L1x}x)\exp(-ik_1 y\sin\theta + i\omega t) \tag{5.32}$$

$$\Psi_1 = T_6 \exp(-ik_{\mathrm{T}1x}x)\exp(-ik_1 y\sin\theta + i\omega t) \tag{5.33}$$

For the transmitted in-plane wave on the receiving plate:

$$\Phi_2 = T_7 \exp(-ik_{\mathrm{L}2x}x)\exp(-ik_{\mathrm{B}1}y\sin\theta + i\omega t) \tag{5.34}$$

$$\Psi_2 = T_8 \exp(-ik_{\mathrm{T}2x}x)\exp(-ik_{\mathrm{B}1}y\sin\theta + i\omega t) \tag{5.35}$$

where $k_{\mathrm{L}i}$ and $k_{\mathrm{T}i}$ represent the in-plane wavenumbers for plate i which can be calculated from equations (3.22) and (3.23). The in-plane wavenumber for plate i in x-direction, $k_{\mathrm{L}ix}$ and $k_{\mathrm{T}ix}$ can be calculated by substituting equation (5.34) and (5.35) into (3.18) and (3.19), then putting them into (3.15) and (3.16).

$$k_{\mathrm{L}ix} = \sqrt{k_{\mathrm{L}i}^2 - k_{\mathrm{B}i}^2 \sin^2\theta} \tag{5.36}$$

$$k_{\mathrm{T}ix} = \sqrt{k_{\mathrm{T}i}^2 - k_{\mathrm{B}i}^2 \sin^2\theta} \tag{5.37}$$

The formulation of bending and in-plane wave field on the source plate and receiving plate leaves eight unknown wave amplitudes $\{T_1, T_2, \ldots, T_8\}$ which can be solved by applied the corresponding boundary conditions at the junction beam.

(1) Continuity conditions

For the rigid junction beam as shown in Figure 5.1, the displacements and rotation at the junction beam are assumed to be equal to the displacements and rotation at the plate edge. Therefore, at the coupling edges of the source and receiving plate, continuity conditions apply for the displacements and rotation as shown in the following equations:

$$\xi_{\mathrm{L}x2} + \xi_{\mathrm{T}x2} = \xi_{\mathrm{L}x1} + \xi_{\mathrm{T}x1} \tag{5.38}$$

$$\xi_{Bx2}=\xi_{Bx1} \tag{5.39}$$

$$\xi_{Ly2}+\xi_{Ty2}=\xi_{Ly1}+\xi_{Ty1} \tag{5.40}$$

$$\phi_1=\phi_2 \tag{5.41}$$

(2) Equilibrium Conditions

Similar to the equilibrium conditions for bending only model, the sum of forces acting on the junction beam equals zero, which leads to the following constraints:

$$F_{z1}+F_{z2}=0 \tag{5.42}$$

$$F_{x1}+F_{x2}=0 \tag{5.43}$$

$$F_{y1}+F_{y2}=0 \tag{5.44}$$

$$M_1=M_2 \tag{5.45}$$

where M and F are calculated from equation (3.12) and (3.13) respectively using the total wave fields in terms of displacement expressed as follows:

$$\xi_1=\xi_{inc}+\xi_{B1}+\xi_{L1}+\xi_{T1} \tag{5.46}$$

$$\xi_2=\xi_{B2}+\xi_{L2}+\xi_{T2} \tag{5.47}$$

By solving the equation group (5.38) to (5.45), the unknown wave amplitudes which are dependent on frequency and incident wave angle can obtained.

Transmission coefficients are used to quantify the energy flow between the two plates and also it allows the evaluation of the wave conversion from incident bending wave to in-plane wave.

The wave intensity of an incident bending wave can be calculated from equation (5.24) and the wave intensities of the transmitted or reflected bending waves can be calculated from equation (5.25) using the expressions of forces, bending moments and rotations from equations (5.26)-(5.31). As for in-plane waves, the total wave intensity for an in-plane wave is given by [34] as:

$$I_{LT}(\theta)=\frac{1}{2}\mathrm{Re}\left\{F_x(-i\omega\xi_{\mathrm{L}})^{*}+F_y(-i\omega\xi_{\mathrm{T}})^{*}\right\} \tag{5.48}$$

F_x and F_y are in-plane forces which can be calculated from equation (3.26) and (3.27). The contribution from quasi-longitudinal and transverse shear waves can be calculated by separating the equation (5.48) into two parts.

The plate junction are assumed to be conservative, therefore the conservation of the energy requires that the sum of the transmission coefficients is equal to unity meaning that the total energy transmitted or reflected at the junction should be equal the energy carried in the incident wave upon the junction. For the L-junction, this requirement can be expressed as:

$$\tau_{\mathrm{B1B2}}+\tau_{\mathrm{B1L2}}+\tau_{\mathrm{B1T2}}+r_{\mathrm{B1B1}}+r_{\mathrm{B1L1}}+r_{\mathrm{B1T1}}=1 \tag{5.49}$$

where the subscript B*i*B*j*, B*i*L*j*, B*i*T*j* represent bending wave (B) to bending wave (B), quasi-longitudinal wave (L) and transverse shear wave (T) transmission or reflection from plate *i* to plate *j*.

Figure 5.3 (a)-(c) show the transmission coefficients between the two plates of L-junction at 100 Hz, 1 kHz and 10 kHz when an incident wave impinges upon the junction from plate 1. In these graphs, the transmission coefficient is represented by the vertical distance between boundary lines. The plate properties remain the same as listed in Figure 5.2. When both bending and in-plane are considered, the angle-dependent transmission coefficient also varies with frequency. With

bending wave incident upon the junction, a wave conversion from bending to in-plane wave appears which can be quantified by a different transmission coefficient. At 100 Hz (Figure 5.3 (a)), the wave conversion from bending wave to in-plane wave occurs at below 5 º, above which almost all incident waves that are transmitted and reflected are bending waves. At 1 kHz (Figure 5.3 (b)), the same trend applies except that the wave conversion range has increased to 10 º. It is found that both the transmission and reflection coefficient from bending to bending waves are reduced by around 0.1 while the bending to in-plane wave transmission is more pronounced than at 100 Hz. At 10 kHz (Figure 5.3 (c)), the wave conversion range is further extended to 32 º. Below 32 º, bending to bending wave transmission and reflection no longer dominates the wave transmission. Below 18 º, bending to quasi-longitudinal transmission dominates the wave conversion and from 18 º to 32 º, bending to transverse shear conversion is dominant.

(a) 100 Hz

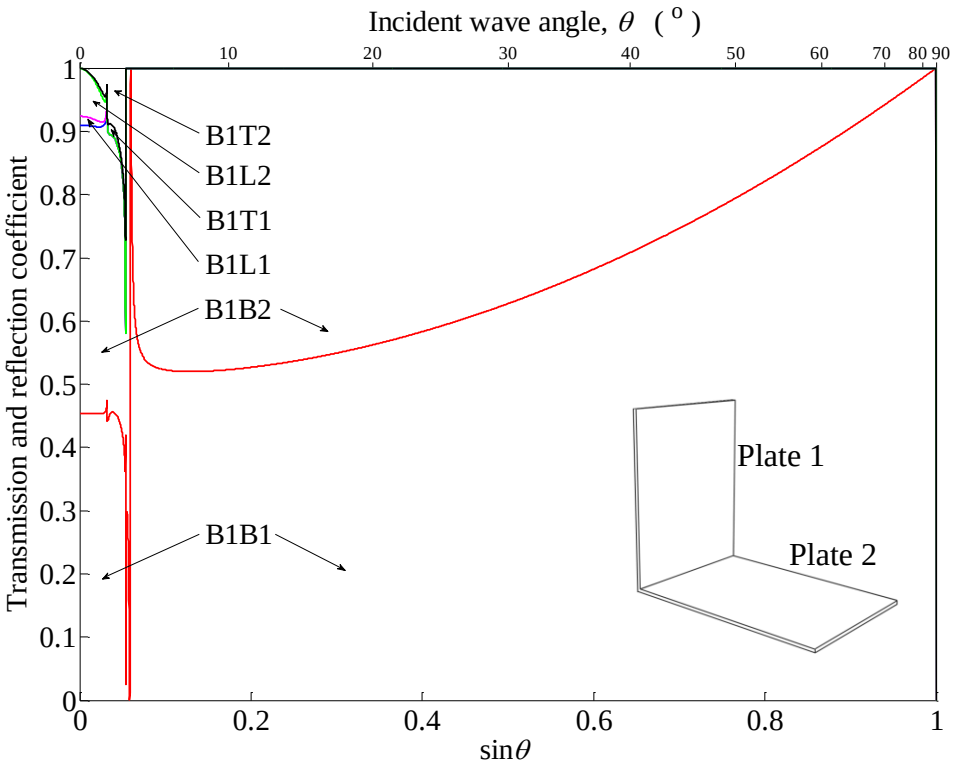

(Continued)

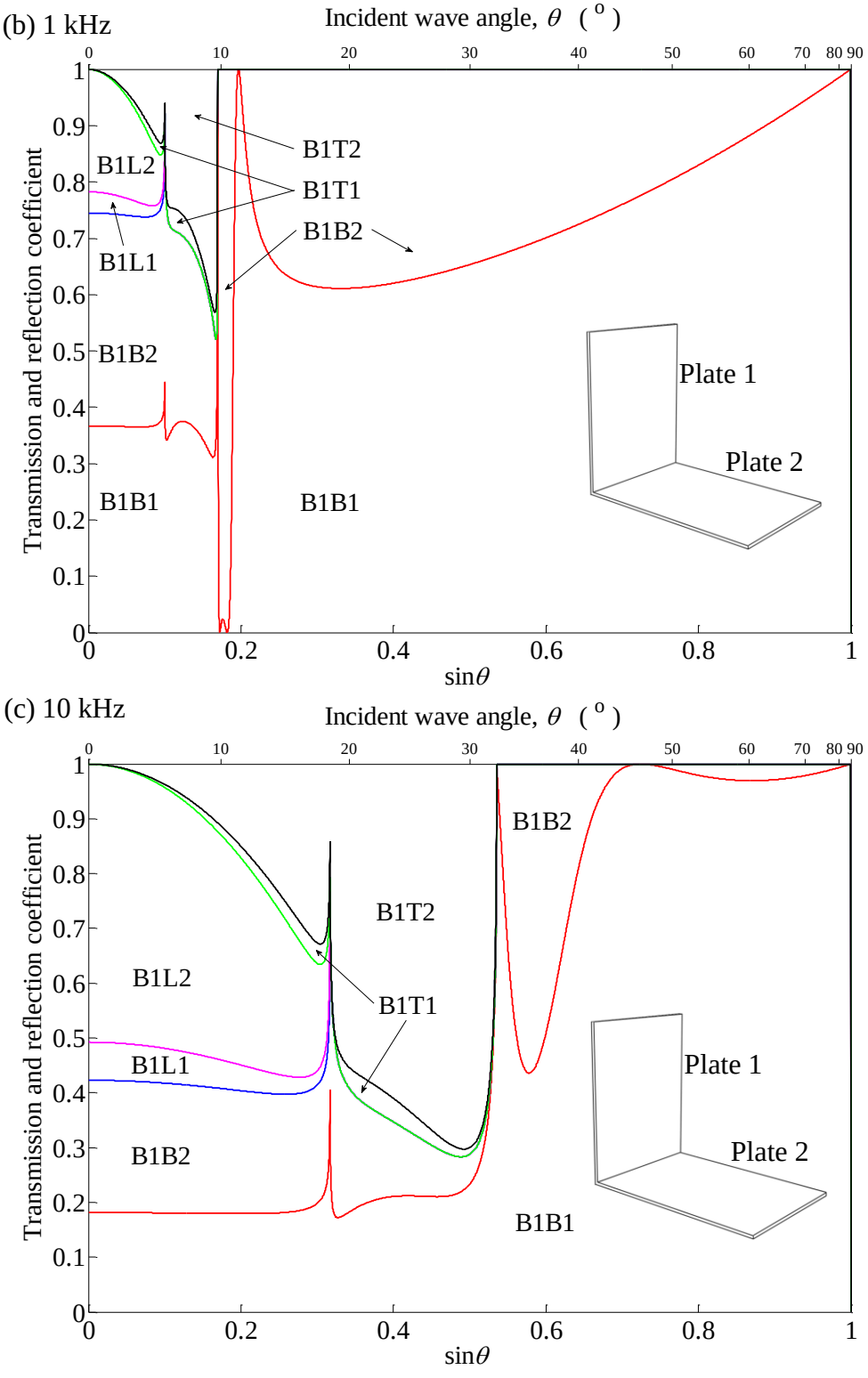

Figure 5.3 Angle-dependent transmission coefficients between L-junction using wave approach considering both bending and in-plane waves when incident bending wave on plate 1 at (a) 100 Hz; (b) 1000 Hz; (c) 10 kHz. B*i*B*j*, B*i*L*j*, B*i*T*j* represent bending wave (B) to bending wave (B), quasi-longitudinal wave (L) and transverse shear wave (T) transmission or reflection from plate *i* to plate *j*.

5.4 Bending wave transmission across plate with a single reinforcing rib

Many engineering structures are composed of plates with one or more reinforcing ribs that can be modelled as a plate/beam junction. The review of literature on vibration transmission across plate/beam junction can be found in section 5.2.2.

In this section, bending wave transmission across two semi-infinite plates separated by a single reinforcing rib shown in Figure 5.4 is considered using the wave approach described by Cremer *et al.* [34]. The junction follows the same type of plate/rib structure that is discussed in Chapter 4 for the periodic ribbed plate, where the generation of in-plane waves is avoided due to the symmetric arrangement of the rib.

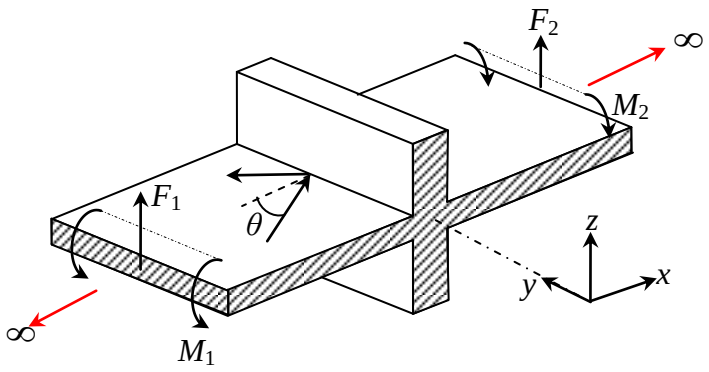

Figure 5.4 Two semi-infinite plates separated by a rib

The boundary conditions at the junction have already been discussed in section 5.3 as illustrated in equation (4.11), (4.12), (4.16) and (4.21). They can be re-written as:

$$\xi_1(x)\big|_{x=0} = \xi_2(x)\big|_{x=0} \tag{5.50}$$

$$\phi_1(x)\big|_{x=0} = \phi_2(x)\big|_{x=0} \tag{5.51}$$

$$F_1(x)\big|_{x=0} - F_2(x)\big|_{x=0} - E_{\mathrm{b}} I_{\mathrm{b}x} \left.\frac{\partial^4 \xi_1(x)}{\partial y^4}\right|_{x=0} = -\rho_{\mathrm{b}} S_{\mathrm{b}} \omega^2 \xi_1(x)\big|_{x=0} \tag{5.52}$$

$$M_1(x)\big|_{x=0} - M_2(x)\big|_{x=0} + G_{\mathrm{b}} J_{\mathrm{b}} \left.\frac{\partial^3 \xi_1(x)}{\partial x \partial y^2}\right|_{x=0} = -I_{\mathrm{bc}} \omega^2 \left.\frac{\partial \xi_1(x)}{\partial x}\right|_{x=0} \tag{5.53}$$

Substituting equation (5.9) and (5.10) into (5.50) to (5.53), the four unknown wave amplitudes can be solved by doing the matrix inversion similarly as for the wave transmission across the L-junction. Furthermore, the angle-dependent transmission coefficients as well as coupling loss factors can be calculated.

The same plate and rib dimensions as shown in Table 2 are chosen as an example. The angle-dependent transmission coefficient at the plate/beam junction is shown in Figure 5.5 (the plate thickness, rib dimensions and material properties are the same as shown in Figure 3.3 (b)).

- As the incident wave angle tends towards 90 º, the transmission coefficient decreases to zero.

- As shown from Figure 5.5, unity transmission coefficient occurs at certain frequencies, which means that the ribs have no blocking effect on wave propagation on the plate. Cremer *et al*. [34] attributes this phenomenon to the results of 'trace-matching' associated with the bending and torsional vibrations of the rib. 'trace-matching' occurs at a certain frequency and a certain incident wave angle where the wavenumber in *x*-direction $k_{\mathrm{B}}\cos\theta$ coincides with the wavenumber of free waves within the rib. By

understanding these ‘trace-matching’ regions, one may manipulate the properties of the plate or the rib and design structures to transmit or block waves at given range of frequency and angle of incidence.

- At low frequencies, it generally shows wider high transmission peaks. Above 3200 Hz, the peak is split into two separate peaks and with the increase of frequency, the two peaks drift apart, but the peak with higher incident wave angle is always wider than the other.

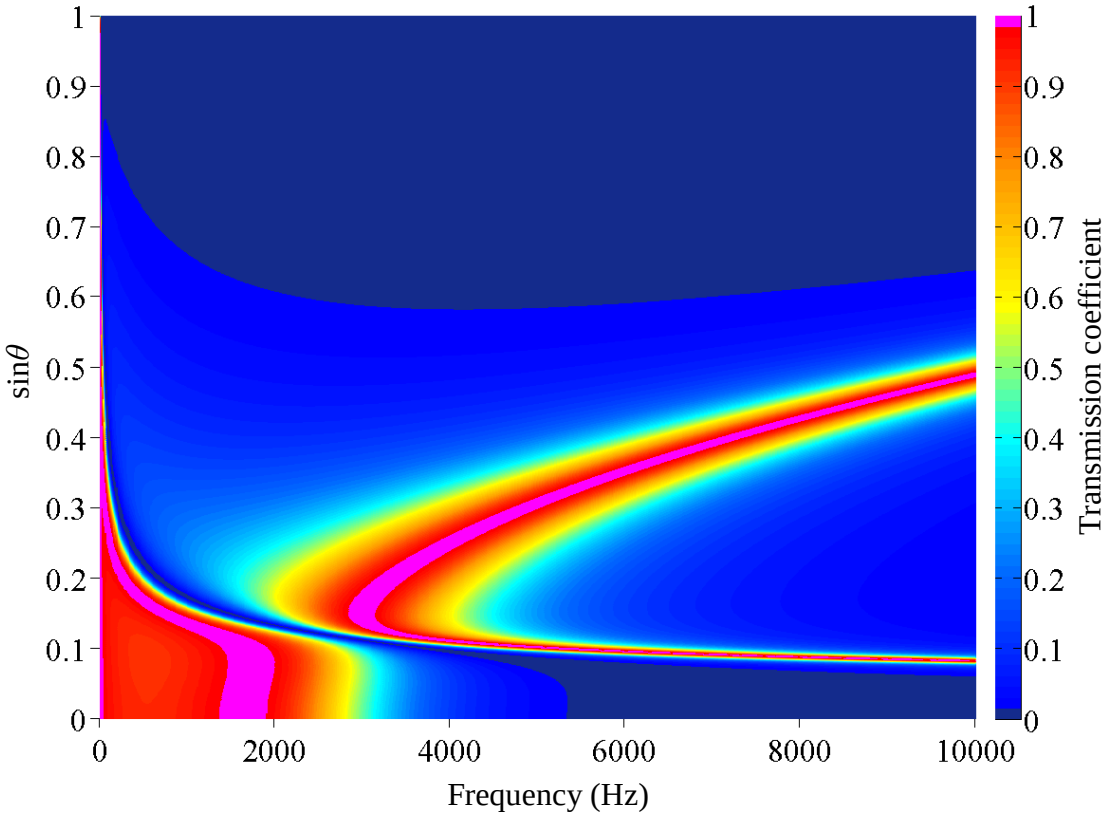

Figure 5.5 Variation of transmission coefficient for two semi-infinite plates separated by a rib with incident wave angle and frequency.

Figure 5.6 to Figure 5.8 investigates the effect of rib and plate dimensions on wave transmission across the junction. Each figure shows the variation of one dimension parameter compared with the default value given in Figure 3.3 (b), and the rest of the dimensions keep the same values as the defaults.

Figure 5.6 (a) and (b) show different width of the rib. With the increase of the rib width, the high transmission peaks are compressed to low angle range and the peaks also become narrower. For the rib width of 15 mm, there is no transmission above 75^{o} in contrast of 60^{o} for 30 mm of rib width and 30^{o} for 60 mm of rib width. At low frequencies with small incidence angles, the transmission is significantly reduced with the increase of the rib width.

Figure 5.7 (a) and (b) show different heights of the rib. With the increase of the rib height, the boundary separating the two main zones with high transmission coefficient is moved towards to lower frequency and the area of the high transmission zones is also reduced. With the increase of the rib height, the two peaks of high transmission at high frequencies are separated wider, which results in narrow peaks at high incidence angle.

Figure 5.8 (a) and (b) show different thicknesses of the plate. With the increase of the plate thickness, the area of high transmission zones is extended and the boundary separating the two main zones with high transmission coefficient is moved towards to higher frequency.

In general, the increase of rib width, rib height and the decrease of plate thickness enhance the wave blocking effect of the rib resulting in larger area of zero transmission in the incidence wave angle-frequency domain.

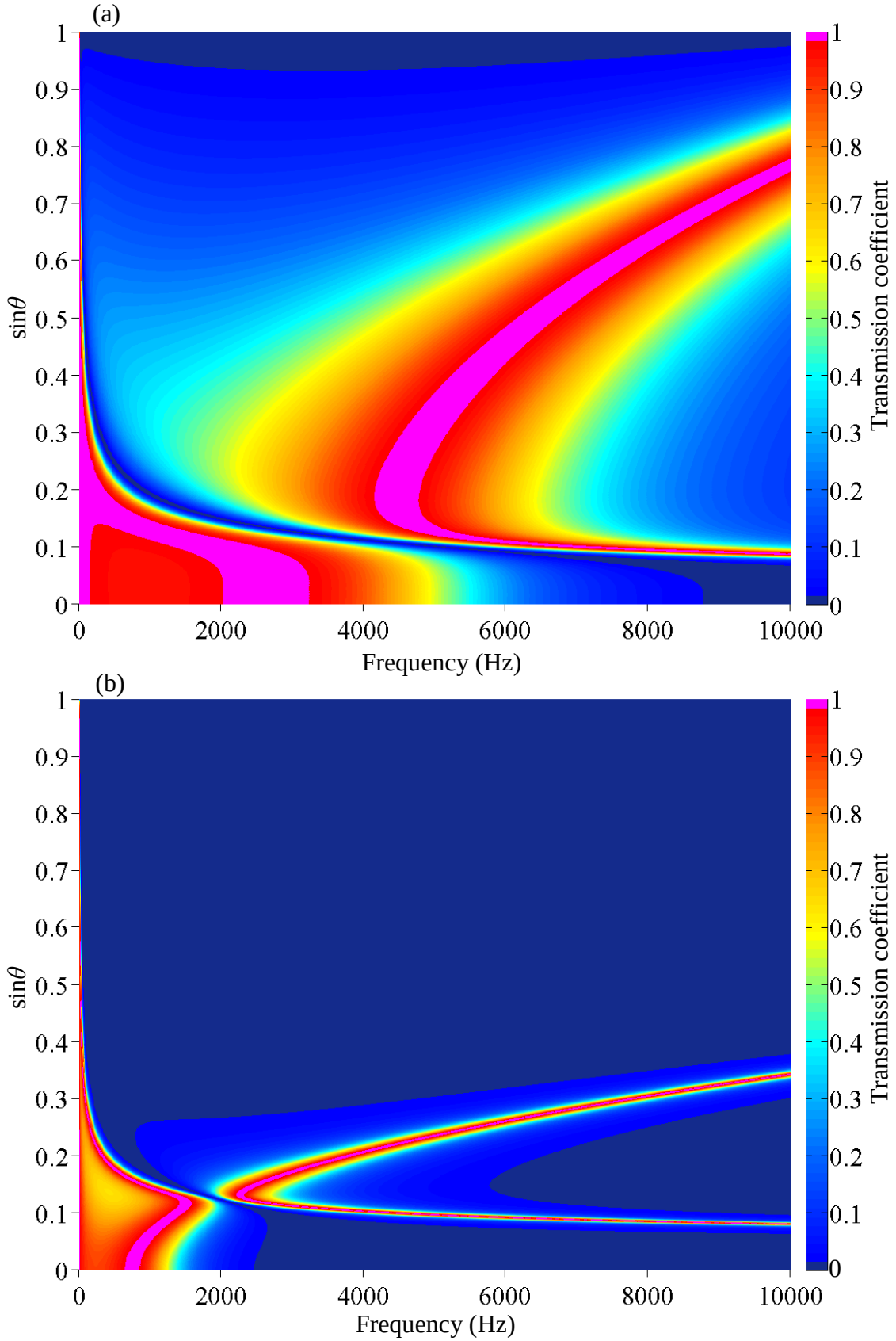

Figure 5.6 Variation of rib width (a) 15 mm, (b) 60 mm on the transmission coefficient. (Compare with Figure 5.5 for 30 mm rib width where all other parameters remains the same with rib height: 50 mm, plate thickness: 13 mm)

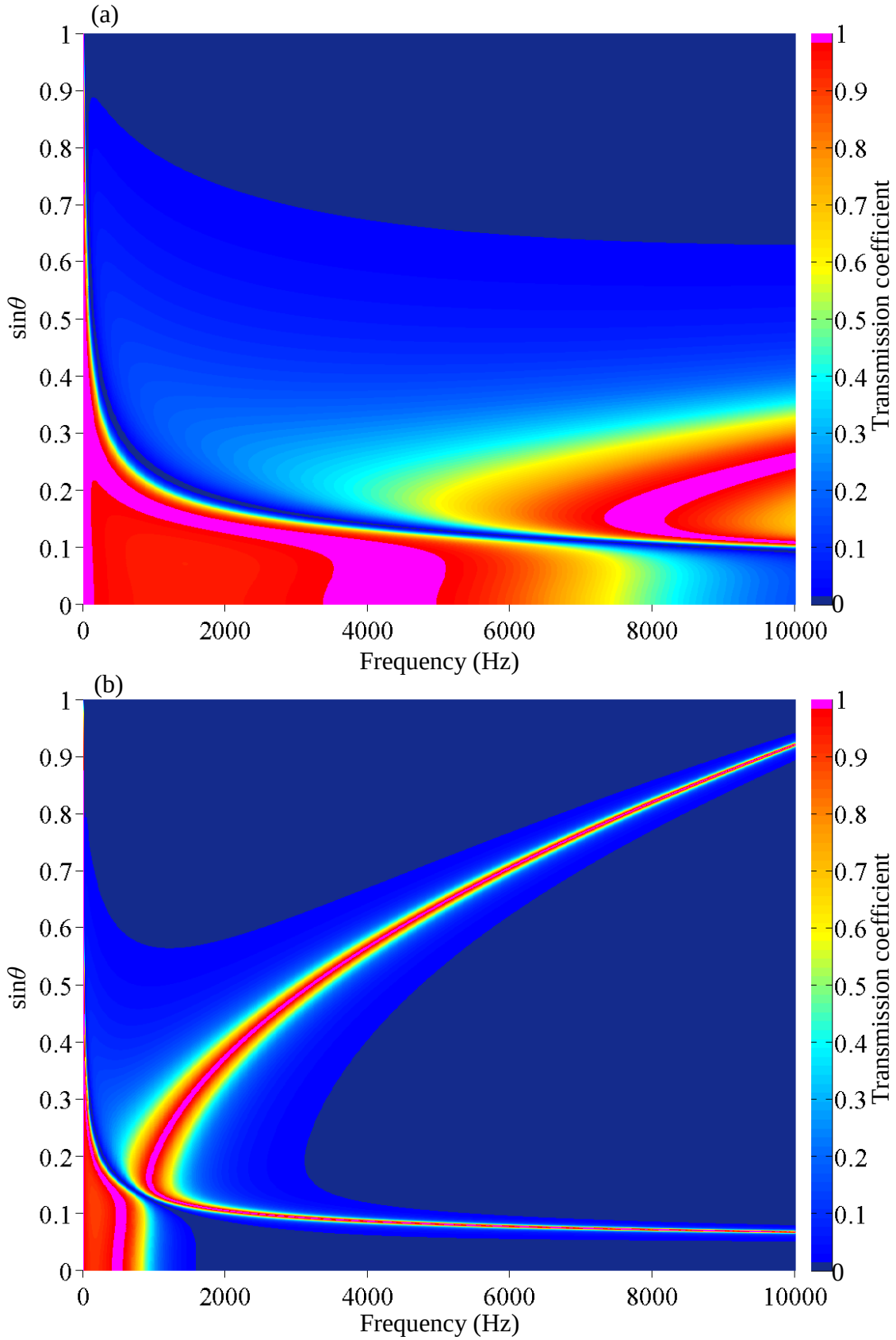

Figure 5.7 Variation of rib height (a) 25 mm, (b) 100 mm on the transmission coefficient. (Compare with Figure 5.5 for 50 mm rib height where all other parameters remains the same with rib width: 30 mm, plate thickness: 13 mm)

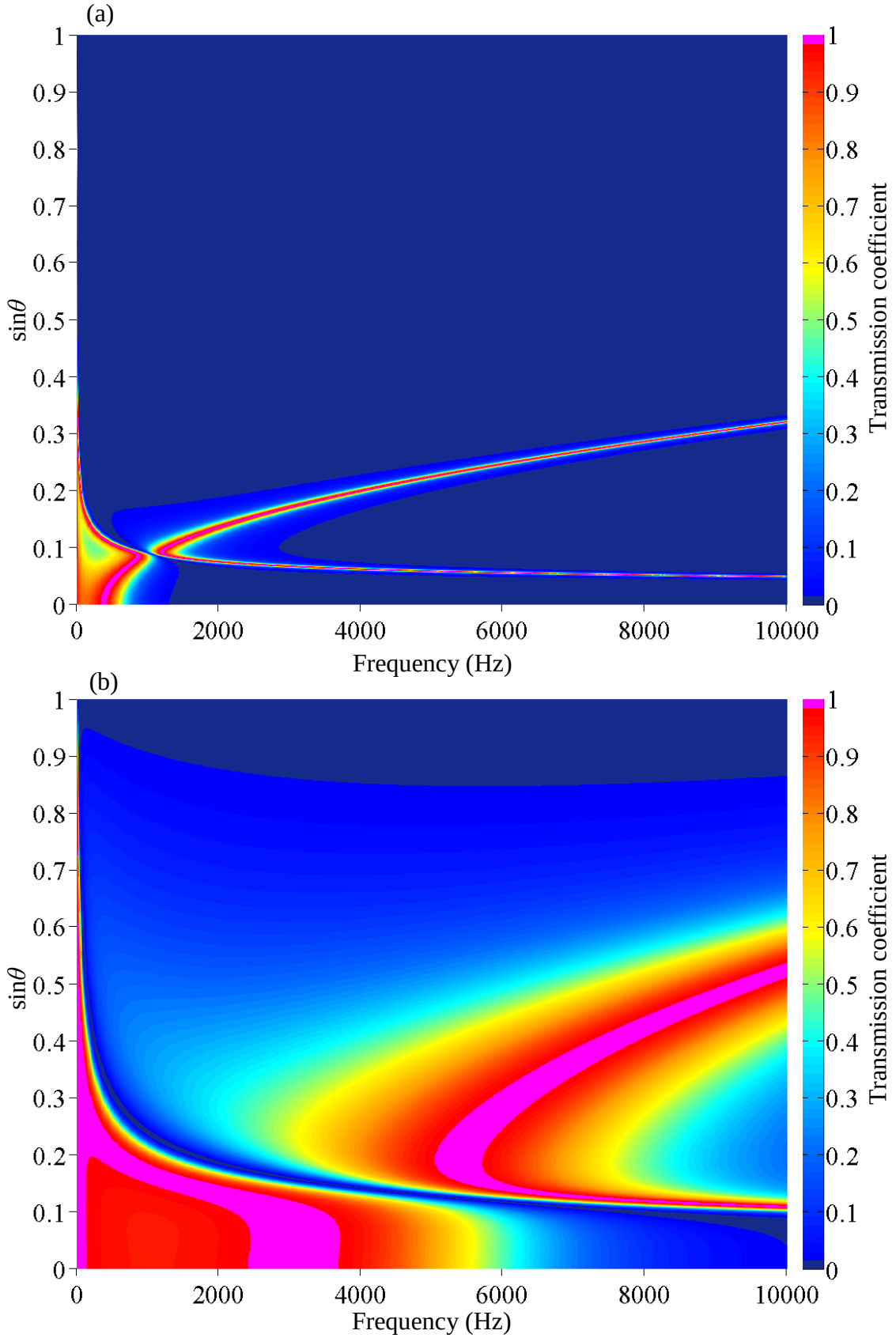

Figure 5.8 Variation of plate thickness (a) 5 mm, (b) 20 mm on the transmission coefficient. (Compare with Figure 5.5 for 13 mm plate thickness where all other parameters remains the same with rib height: 50 mm, rib width: 30 mm)

5.5 Bending wave transmission across an L-junction comprised of a homogeneous isotropic plate and a periodic ribbed plate

This section considers a periodic ribbed plate as described in chapter 4 connected to an isotropic homogeneous plate to form an L-junction where the coupling junction is parallel to the ribs as shown in Figure 5.9. The bending wave transmission across the junction is investigated using the wave approach taken from Tso and Hansen [10]. For bending wave incident upon the junction from the isotropic plate, the displacement field on the isotropic plate is given in equation (5.1). The reflected wave field on the isotropic plate is given by equation (5.9).

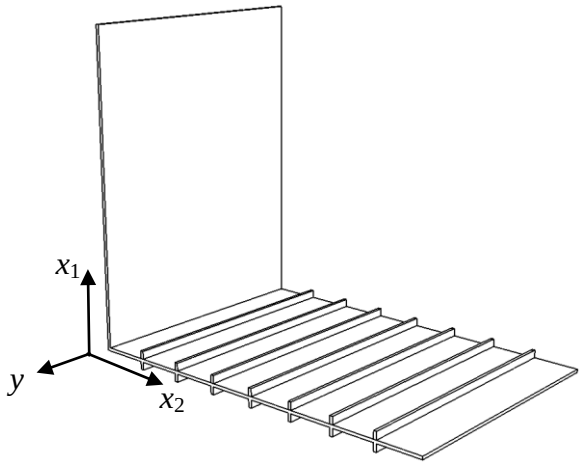

Figure 5.9 L-junction comprised of an isotropic homogeneous plate and a periodic ribbed plate with ribs parallel to the coupling junction

For the ribbed plate, the transverse displacement caused by the transmitted bending waves in the positive x-direction can be written in terms of the two eigenvalues and together with their corresponding eigenvectors:

$$\xi_2 = \left\{ T_3 \left[\exp(\lambda_1) \sum_{m=1}^{4} \frac{A_m}{A_1} \exp(k_{mx} x) \right] + T_4 \left[\exp(\lambda_2) \sum_{m=1}^{4} \frac{A'_m}{A'_1} \exp(k_{mx} x) \right] \right\} \exp(-ik_y y + i\omega t) \tag{5.54}$$

Where T_3 and T_4 are unknown constants associated with the wave amplitudes, λ_1 and λ_2 are a pair of propagation constants determined from matrix equation (4.28) as eigenvalues and vectors $\{A_1, A_2, A_3, A_4\}$ and $\{A_1', A_2', A_3', A_4'\}$ are corresponding eigenvectors.

The junction beam is considered to be simply-supported such that only bending wave are transmitted. The same continuity and equilibrium conditions are considered as in equations (5.11), (5.12), (5.15) and (5.18). Four unknown amplitudes $\{T_1, T_2, T_3, T_4\}$ can be determined from the following equation:

$$\mathbf{L_1}[T_1 \quad T_2 \quad T_3 \quad T_4]^T = \mathbf{L_2} \tag{5.55}$$

where

$$\mathbf{L_1} = \begin{bmatrix} 1 & 1 & 0 & 0 \\ 0 & 0 & \exp(\lambda_1)\sum_{m=1}^{4}\frac{A_m}{A_1} & \exp(\lambda_2)\sum_{m=1}^{4}\frac{A_m'}{A_1'} \\ ik_{\mathrm{B1}x} & k_{\mathrm{B1}}\sqrt{(1+\sin^2\theta)} & \exp(\lambda_1)\sum_{m=1}^{4}k_{mx}\frac{A_m}{A_1} & \exp(\lambda_2)\sum_{m=1}^{4}k_{mx}\frac{A_m'}{A_1'} \\ \mu_1 k_{\mathrm{B1}y}^2 - k_{\mathrm{B1}x}^2 & \mu_1 k_{\mathrm{B1}y}^2 + k_{\mathrm{B1}}^2(1+\sin^2\theta) & \exp(\lambda_1)\sum_{m=1}^{4}(k_{mx}^2+\mu_2 k_{\mathrm{B1}y}^2)\frac{A_m}{A_1} & \exp(\lambda_2)\sum_{m=1}^{4}(k_{mx}^2+\mu_2 k_{\mathrm{B1}y}^2)\frac{A_m'}{A_1'} \end{bmatrix}$$

(5.56)

$$\mathbf{L_2} = \begin{bmatrix} -1 & 0 & ik_{\mathrm{B1}}\cos\theta & k_{\mathrm{B1}}^2\cos^2\theta - \mu_1 k_{\mathrm{B1}y}^2 \end{bmatrix}^T \tag{5.57}$$

where k_{B1} is the bending wavenumber of plate 1, the isotropic homogeneous plate. $k_{\mathrm{B1x}}=k_{\mathrm{B1}}\cos\theta$ and $k_{\mathrm{B1}y}=k_{\mathrm{B1}}\sin\theta$ represent the wavenumbers in *x*- and *y*-direction respectively.

The transmission coefficient is calculated using the wave intensities on the source and receiving plates as described in section 5.3.2. For the transmitted wave on the periodic plate, to calculate the wave intensity, the bending moment, force and angular displacement can be calculated from equations (5.58) to (5.60):

$$M_{\text{trans}} = B_{\text{p}}\left[T_3 \exp(\lambda_1)\sum_{m=1}^{4}\frac{A_m}{A_1}(k_{mx}^2 + \mu_2 k_{\text{B}2y}^2) + T_4 \exp(\lambda_2)\sum_{m=1}^{4}\frac{A'_m}{A'_1}(k_{mx}^2 + \mu_2 k_{\text{B}2y}^2)\right] \quad (5.58)$$

$$F_{\text{trans}} = B_{\text{p}}\left[T_3 \exp(\lambda_1)\sum_{m=1}^{4}(k_{mx}^3 + 2k_{\text{B}2y}^2 - \mu_2 k_{\text{B}2y}^2)\frac{A_m}{A_1} + T_4 \exp(\lambda_2)\sum_{m=1}^{4}(k_{mx}^3 + 2k_{\text{B}2y}^2 - \mu_2 k_{\text{B}2y}^2)\frac{A'_m}{A'_1}\right]$$

(5.59)

$$\phi_{\text{trans}} = i\omega\left[T_3 \exp(\lambda_1)\sum_{m=1}^{4}k_{mx}\frac{A_m}{A_1} + T_4 \exp(\lambda_2)\sum_{m=1}^{4}k_{mx}\frac{A'_m}{A'_1}\right] \quad (5.60)$$

Figure 5.10 shows the transmission coefficient from the isotropic plate to the periodic ribbed plate.

- Referring back to Figure 4.3 which shows the propagation and attenuation zones for the same periodic ribbed plate, the transmission with a certain transmission coefficient only occurs within the propagation zones. The L-junction exhibits wave filtering behaviour over certain ranges of incidence wave angle. Clear boundaries are found between propagation and attenuation zones, and these boundaries correspond with the boundaries shown in Figure 4.3 except for the propagation zone at around 10 kHz with low incident wave angles where the propagation zone for the L-junction is smaller than that of the periodic ribbed plate. It is noted that this conclusion is only true for this specific case where both plates are made of the same material and have the same thickness. As for the cases where the isotropic and periodic ribbed plates have different thickness, further investigation will be made.

- Within the propagation zones, the transmission coefficients vary with frequency as well as with incident wave angle.

- As the incident wave angle tends towards 90 º, the transmission coefficient decreases to zero.

- In the propagation zones, the transmission coefficient only equals unity at specific frequencies with specific incident wave angles. Within such range, the periodic ribs have no blocking effect on wave propagation on the plate.

- It can be seen that no wave transmission occurs above around 60 º. Therefore there exists a cut-off angle for bending wave transmission across an L-junction with periodic ribbed plate. This doesn't happen for the bending wave transmission across an L-junction with two isotropic, homogeneous plates.

- In many practical structures, bending waves will be incident over a range of angles; hence, there will not usually be well-defined pass and stop bands as can occur on one-dimensional periodic systems such as for rods and beams.

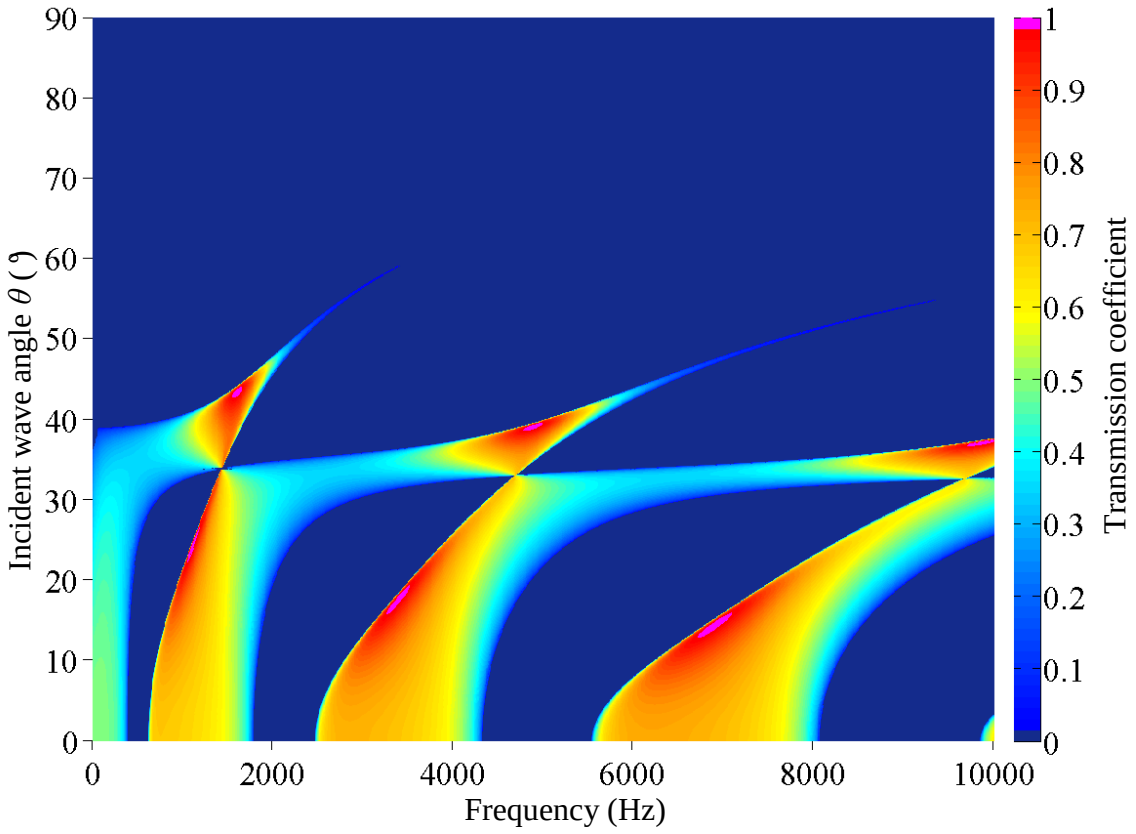

Figure 5.10 Angle-dependent transmission coefficient for an L-junction comprised of isotropic homogeneous plate and a periodic ribbed plate

Figure 5.11 to Figure 5.14 shows the effects of the variations of geometric properties of the plate and ribs on the vibration transmission across the L-junction. Comparing these graphs with the corresponding graphs from Figure 4.4 to Figure 4.7 of the distribution of the propagation and attenuation zones for the periodic ribbed plate, similar conclusions can be made on the effect of the variation of each parameter.

The difference between the two sets of graphs is discussed here. In most cases, the boundaries of each propagation zones for the L-junction correspond with the boundaries for the periodic ribbed plate. At very high frequencies, the propagation zones for the L-junction may be smaller than the periodic ribbed plate (for example, Figure 5.11 (a) and (b), Figure 5.12(a)), and it seems that the wave propagation for L-junction is constrained into the propagation zones of the periodic ribbed plate. However, in some cases, the propagation zones of the L-junction do not fall into the propagation zones of the periodic ribbed plate such as Figure 5.12(b) and Figure 5.14(a) and a frequency shift is shown. It is noticed that this phenomena only occurs when all the propagation zones across the frequency are compressed below 20 º.

It is also observed that for Figure 5.13 (b), there is a large area with scattered high values for the transmission coefficients. This is due to a poorly conditioned matrix with a high condition number ($>10^{15}$) and it can therefore be considered as calculation noise. This indicates potential problems in the approach proposed by Tso and Hansen because it will be not applicable to all geometric permutations for the periodic ribbed plate.

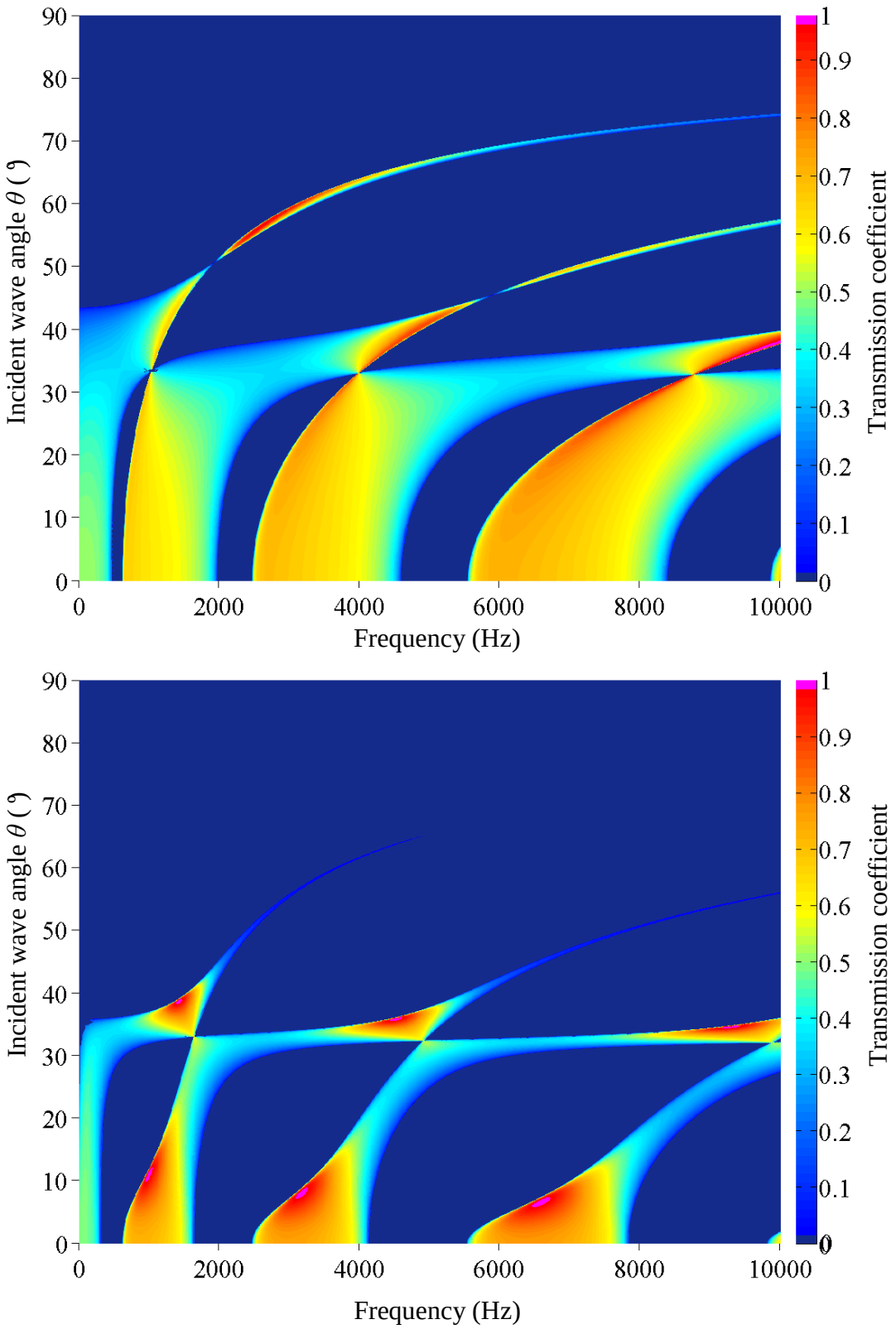

Figure 5.11 Variation of rib width (a) 15 mm, (b) 60 mm on the transmission coefficient of L-junction with periodic ribbed plate. (Compare with Figure 5.10 of 30 mm rib width where all other parameters remains the same with rib height: 50 mm, plate thickness: 13 mm, bay spacing: 150 mm)

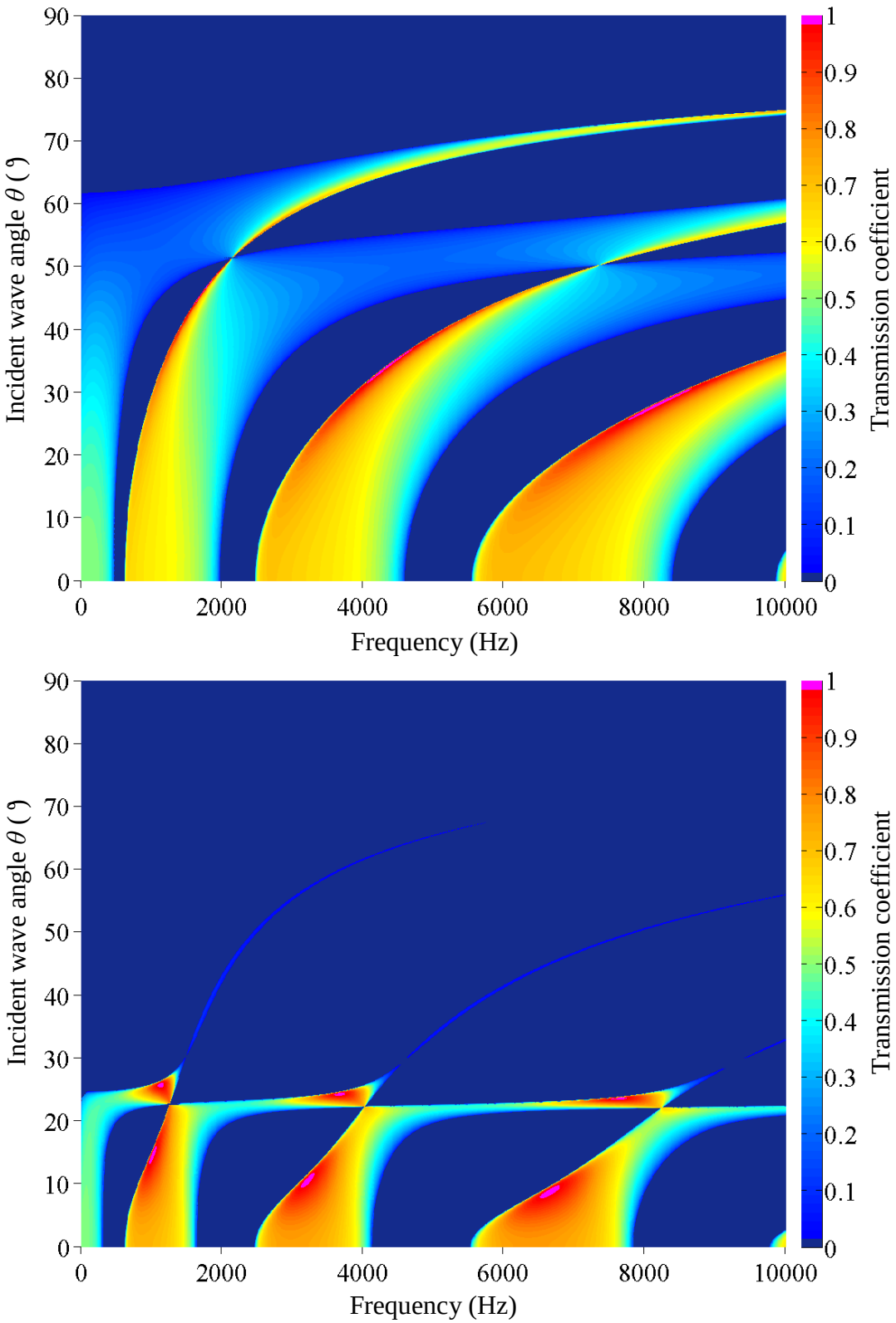

Figure 5.12 Variation of rib height (a) 25 mm, (b) 100 mm on the transmission coefficient of L-junction with periodic ribbed plate. (Compare with Figure 5.10 of 50 mm rib height where all other parameters remains the same with rib width: 30 mm, plate thickness: 13 mm, bay spacing: 150 mm)

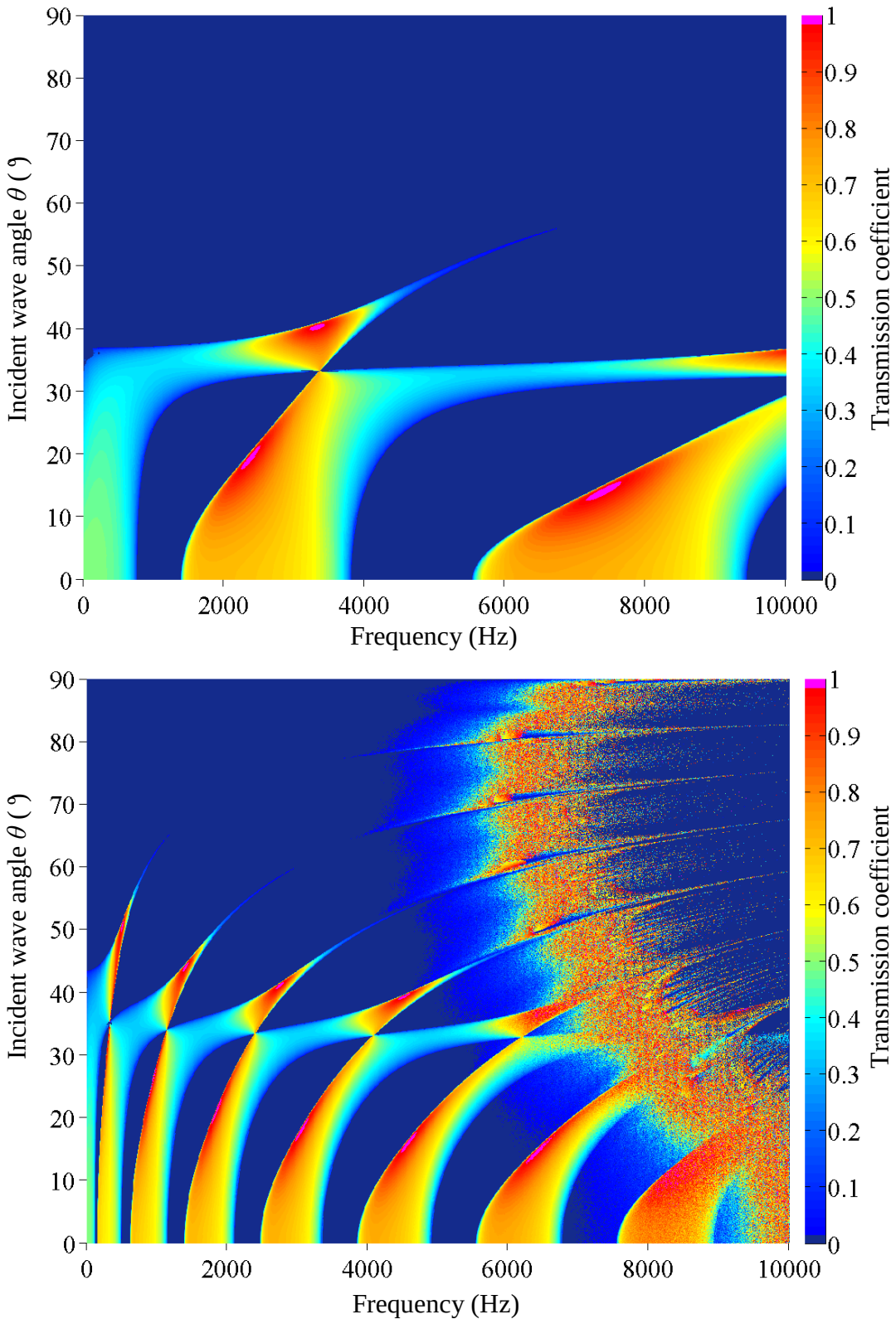

Figure 5.13 Variation of bay spacing (a) 100 mm, (b) 300 mm on the transmission coefficient of L-junction with periodic ribbed plate. (Compare with Figure 5.10 of 150 mm bay spacing where all other parameters remains the same with rib height: 50 mm, rib width: 30 mm, plate thickness: 13 mm)

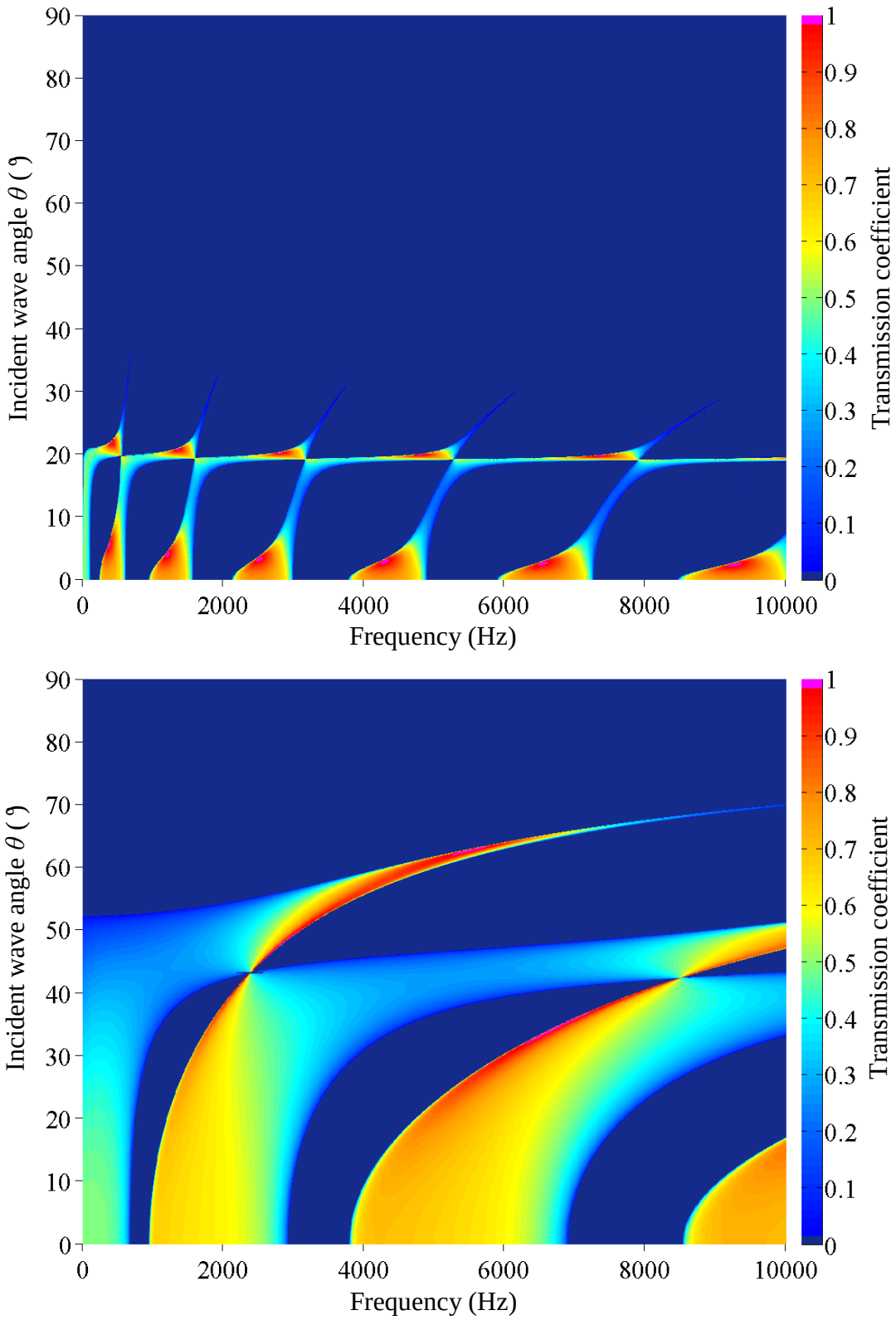

Figure 5.14 Variation of plate thickness for both plates (a) 5 mm, (b) 20 mm on the transmission coefficient of L-junction with periodic ribbed plate. (Compare with Figure 5.10 of 150 mm bay spacing where all other parameters remains the same with rib height: 50 mm, rib width: 30 mm, bay spacing: 150 mm)

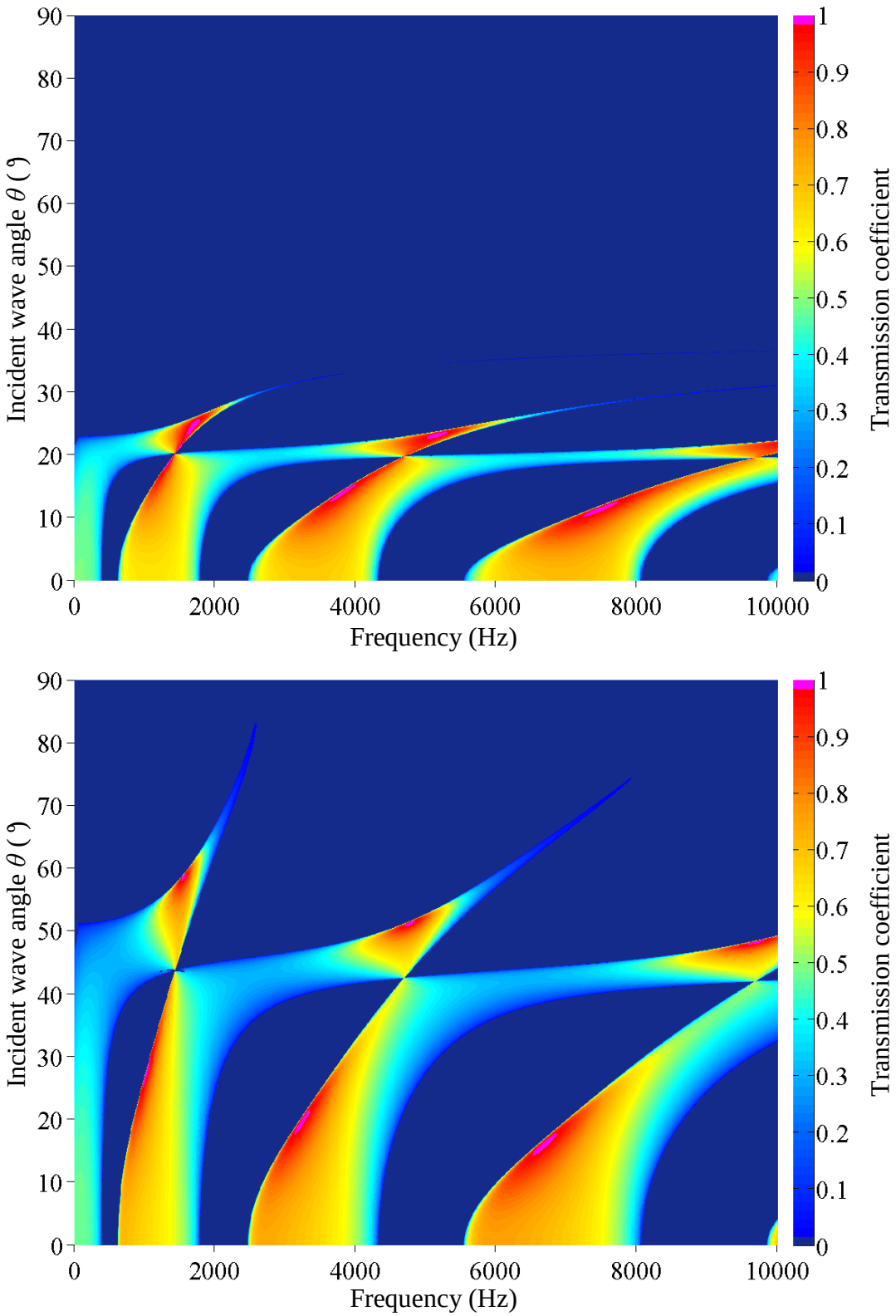

Figure 5.15 Variation of plate thickness for isotropic plate (a) 5 mm, (b) 20 mm on the transmission coefficient of L-junction with periodic ribbed plate. (Compare with Figure 5.10 of 150 mm bay spacing where all other parameters remains the same with rib height: 50 mm, rib width: 30 mm, bay spacing: 150 mm, plate thickness: 13 mm)

5.6 Wave transmission across an L-junction of orthotropic plates using angle-dependent bending stiffness

This section extends the theoretical models for structure-borne sound transmission across L-junctions of isotropic plates to L-junctions of isotropic and orthotropic plates. Due to the wide application of the orthotropic structures in engineering, structural junctions consisting of isotropic and orthotropic plates such as presented in section 6.5 where the periodic ribbed plate can be considered as an orthotropic plate are commonly seen. Theoretical models for structure-borne sound transmission are available for simple periodic structures. However complexity of modern structural engineering has created many orthotropic structures that theoretical solutions are often difficult or impossible to find. Therefore, alternative methods are required. This section considers the periodic plates as orthotropic plates and quantifies the effect of orthotropicity on the vibration transmission at L-junctions.

The derivation of this section is developed mainly based on section 3.2 where the wave equations for orthotropic plates are presented and section 5.2 and 5.6 where the wave approach for bending and in-plane wave transmission across L-junctions are discussed. As the formulation of boundary conditions at the coupling junction is identical to the model for isotropic plates, this section will focus on the effects on vibration transmission caused by the orthotropic characteristics.

5.6.1 Solutions to the wave equations

As previously discussed in chapter 3, wave propagation on the orthotropic plate is subject to an angle-dependent wavenumber. Therefore the solution of the wave equation can be written as:

$$\xi = T \exp[-ik_t(\theta_t)\cos\theta_t x]\exp[-ik_t(\theta_t)\sin\theta_t y]\exp(i\omega t) \tag{5.61}$$

where $k_t(\theta_t)$ the angle-dependent wavenumber of the transmitted(reflected) wavenumber with corresponding wave heading angle θ_t.

Considering the incident bending wave on plate 1 with a heading angle θ_1 and angle-dependent wavenumber $k_{B1}(\theta_1)$, the propagation direction of the transmitted wave is determined from Snell's law as:

$$k_t(\theta_t)\sin\theta_t = k_{B1}(\theta_1)\sin\theta_1 \tag{5.62}$$

Substituting equation (5.62) into (5.61), the solution of the wave equation can be re-written as:

$$\xi = T\exp[-ik_t(\theta_t)\cos\theta_t x]\exp[-ik_{B1}(\theta_1)\sin\theta_1 y]\exp(i\omega t) \tag{5.63}$$

k_t can either be bending or in-plane wave by substituting equation (5.63) into corresponding equations of motion presented in section 3.2.

5.6.2 Angular-average transmission coefficient

Since the boundary conditions for an L-junction of orthotropic plates are identical, the angle-dependent transmission coefficient can be calculated in exactly the same way as discussed in the previous section in this chapter.

The coupling loss factor used in SEA between the two plates of the L-junction is calculated from angular-average transmission coefficient. The angular-average transmission coefficient can be calculated from equation (2.27) assuming a diffuse field where all incident wave angles have equal probability to occur. In a diffuse field on an orthotropic plate, the energy is not distributed uniformly among different directions of propagation [123]. Lyon [7] gave a weighting function $D(\theta)$ to describe the wave distribution in the wavenumber diagram that measures the distribution of area in the interval between $k(\theta, \omega)$ and $k(\theta, \omega+\Delta\omega)$ as given by [123]:

$$D(\theta) = C \cdot k(\theta,\omega)\frac{\partial k(\theta,\omega)}{\partial \omega} \tag{5.64}$$

where the constant C is calculated from the condition:

$$\int_0^{2\pi} D(\theta)\mathrm{d}\theta=2\pi \tag{5.65}$$

The weighting function for bending waves is calculated by substituting equation (3.51) into (5.64) as:

$$D_{\mathrm{B}}(\theta)=C_B/\sqrt{B(\theta)} \tag{5.66}$$

For in-plane waves, the weighting function can be similarly obtained as:

$$D_{\text{in-plane}}(\theta)=C_{\text{in-plane}}k^2(\theta)/\omega \tag{5.67}$$

where the in-plane wavenumber $k(\theta)$ is calculated from equation (3.56)

5.7 Transmission across an L-junction of orthotropic plates using representative bending stiffness

A simplified method is proposed to model the vibration transmission across L-junction of orthotropic plates. Instead of using angle-dependent bending stiffness as discussed in the previous section, only one constant value of bending stiffness is applied for the orthotropic plate so that the orthotropic plate can be considered as an isotropic homogeneous plate. The same models presented in section 5.3 can therefore be used to calculate both bending and in-plane wave transmission across the L-junction.

5.7.1 Using equivalent bending stiffness

Cremer *et al*. [34] suggested that the driving-point impedance of an orthotropic plate is very nearly equal to that of an isotropic homogeneous plate whose bending stiffness is equal to the geometric mean of the bending stiffness in the two principal directions of the orthotropic plate. This equivalent bending stiffness is calculated from:

$$B_{\mathrm{p},\,equiv} = \sqrt{B_{\mathrm{p},\,x} B_{\mathrm{p},\,y}} \tag{5.68}$$

5.7.2 Using bending stiffness in the principal direction of transmission

Another alternative is to only consider the primary wave travelling direction as a representative of the bending stiffness for the entire plate. This is due to the fact that the main power transmission occurs at lower angles of incidence and the bending stiffness in these directions is close to that of the principal direction.

5.8 Conclusions

This chapter contains the wave theory derivations used to calculate transmission coefficients that are needed for subsequent calculation of coupling loss factors for the SEA and ASEA models in chapters 6, 7 and 8. Two types of junction are considered: an L-junction and an in-line junction formed by the presence of a rib.

For an L-junction comprised of a homogeneous isotropic plate and a periodic ribbed plate, Tso and Hansen's model was found to generate numerical errors for certain geometrical arrangements of the ribs and bays. However, these errors do not occur with the periodic ribbed plates considered in chapters 6, 7 and 8.

6 Prediction of structure-borne sound transmission across L-junctions

6.1 Introduction

This chapter implements the theories described in chapters 2, 3, 4 and 5 to model vibration transmission between two plates that form an L-junction. Two L-junctions are considered as shown in Figure 6.1 (a) L-junction of two isotropic homogeneous plates and Figure 6.1 (b): L-junction of an isotropic homogeneous plate and a periodic ribbed plate. All plates are made of Perspex with dimensions and material properties shown in Table 4. Note that the ribbed plate has the same rib arrangement and dimensions as described in Table 2 for which its periodic properties were shown in chapters 4 and 5.

Whilst periodic ribbed plates are the main concern of this thesis, the reason for starting the analysis with an L-junction of isotropic homogeneous plates was that any fundamental problems with FEM can be expected to be highlighted by comparison with SEA on this simpler plate junction.

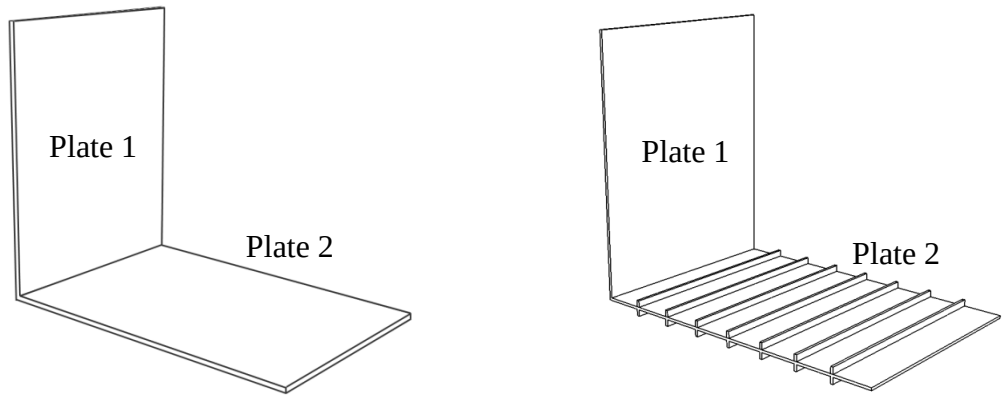

Figure 6.1 Model 1: L-junction comprised of two isotropic homogeneous plates; Model 2: L-junction comprised of an isotropic homogeneous plate and a periodic ribbed plate

Table 4: Dimensions and material properties of L-junctions shown in Figure 6.1

L-junction	Plate 1	Plate 2	Material properties for Perspex
Model 1	L_x=1.0 m L_y=0.8 m h_p = 0.013 m	L_x=1.2 m L_y=0.8 m h_p = 0.013 m	ρ=1180 kg/m^3 c_L=2350 m/s μ=0.3 η_{ii}=0.06
Model 2	L_x=1.0 m L_y=0.8 m h_p = 0.013 m	L_x=1.2 m L_y=0.8 m h_p = 0.013 m h_b=0.05 m b_b=0.03 m l = 0.15 m	

6.2 Numerical experiments with FEM

In this section, numerical experiments using FEM are carried out on the test L-junctions and the sufficiency of mesh is evaluated using mesh error.

6.2.1 ABAQUS processing times

Model 1 consists of 17901 nodes and 17600 elements. There are 10 steps of calculation corresponding to 10 sets of different ROTR and the responses for 70 individual frequencies are calculated for each step. The total calculation time for the job is 1 hour 48 minutes 44 seconds. The post processing including the extraction of the response data from the ABAQUS result file and calculations of kinetic energies for the subsystems is carried out within ABAQUS using codes written in Python scripts [124]. The post processing for model 1 took 28 minutes 27 seconds. Model 2 consists of 21303 nodes and 20960 elements. The same calculation for 10 sets of ROTR took 2 hours 7 minutes 17 seconds and the post processing took 32 minutes 35 seconds.

6.2.2 Mesh errors

It is necessary to ensure that the discretization errors in the FEM modelling are negligible. The S4R finite element size is chosen to be 0.01 m which gives at least seven elements in one wavelength for the highest one-third octave band of analysis at 10 kHz. The adequacy of the mesh element size is evaluated using the mesh errors that are discussed in section 2.5.3 by comparing the injected power with the dissipated power in the system.

The application of ESEA requires numerical experiments using rain-on-the-roof (ROTR) excitations on each subsystem in turn. For each subsystem, 10 sets of different ROTR excitations are used which allows the calculation of 95% confidence intervals using the Student's *t*-distribution. Individual frequency results from FEM are combined into one-third-octave bands for ESEA analysis to determine the coupling loss factors. This general arrangement is applied to all FEM models throughout this thesis.

For Model 1, the average mesh errors are shown in Figure 6.2 where all edges including the junction are simply-supported and in Figure 6.3 when the junction between the two plates is free (i.e. without constraints). The errors are low across the entire frequency range with no indication of significant errors above 6.3 kHz due to the S4R element (refer back to section 2.5.2.1) no longer reproducing thin plate behaviour. At low frequencies, the mesh error tends to fluctuate more than at high frequencies, which results in larger confidence intervals. In most frequency bands, the mesh error is below 10%.

When in-plane waves are generated at the junction, the element mesh error is expected to increase because the mesh error only considers out-of-plane displacement. However, this can be used to indicate the existence of in-plane wave energy. Comparison of Figure 6.2 and Figure 6.3 indicates that in-plane wave energy only occurs above 1.25 kHz although the increase in mesh error is sufficiently small that the values are still below 10%.

The mesh errors for Model 2 with all edges simply-supported are shown in Figure 6.4. Comparison of Figure 6.2 and Figure 6.4 indicates that the errors are similar when the ROTR is applied to the isotropic homogeneous plate, but when the

ROTR is applied to the periodic ribbed plate, the errors increase up to 25% at low frequencies, where the wavelength is larger than the rib spacing. This can be attributed to the fact that the energy of the beams is not included in the calculation of the mesh error.

For the narrow band data in Models 1 and 2, the maximum error is approximately 15% and 25% respectively. These errors are well below the maximum value of 40% which has previously been found to give negligible errors in the vibration response [51]. It is concluded that the mesh errors for this element size are sufficiently low to continue with the modelling in this chapter.

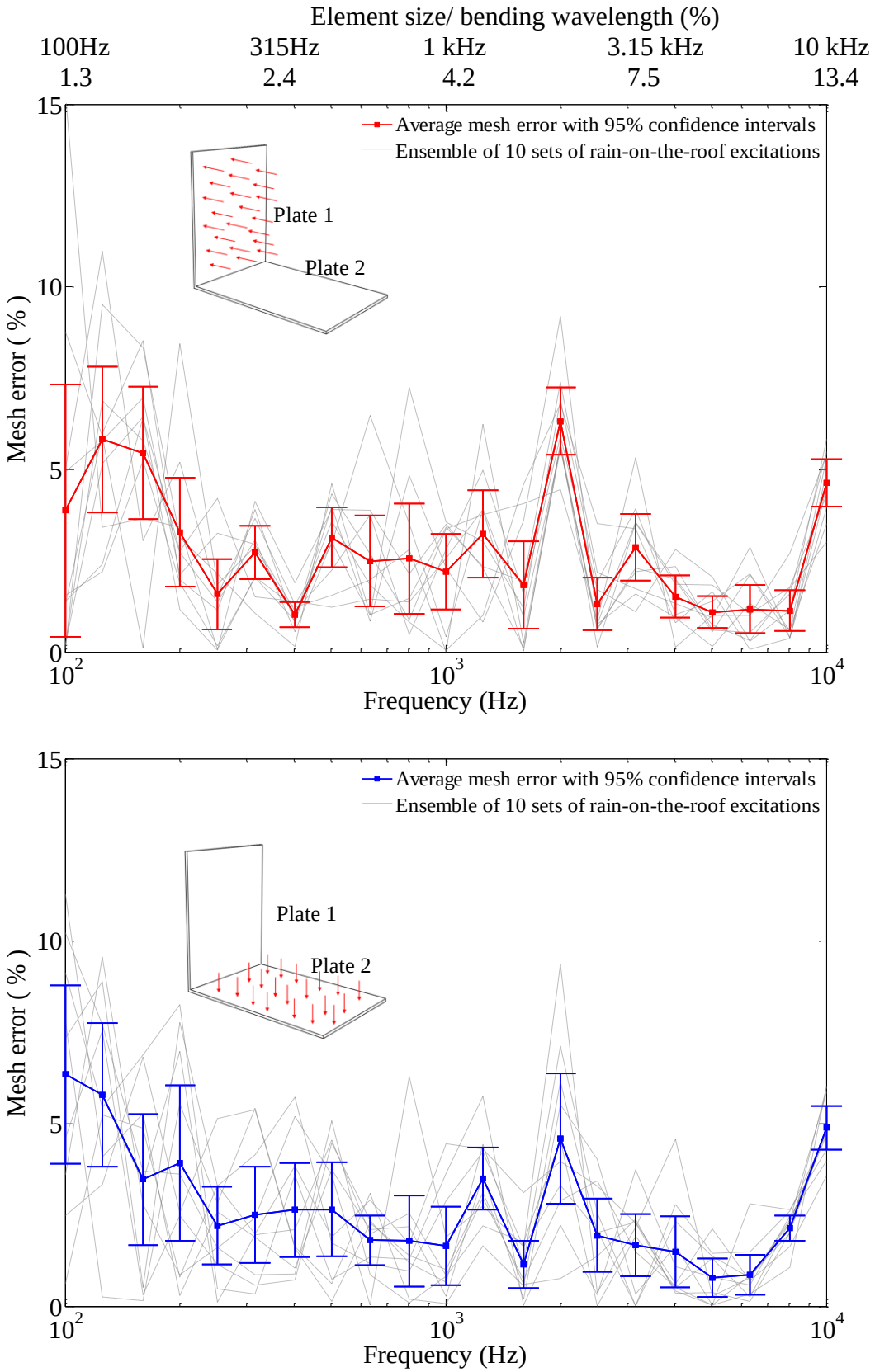

Figure 6.2 Element mesh error for L-junction of two isotropic homogeneous plates (Model 1) with simply-supported boundaries along all edges. (a) rain-on-the-roof on plate 1; (b) rain-on-the-roof on plate 2

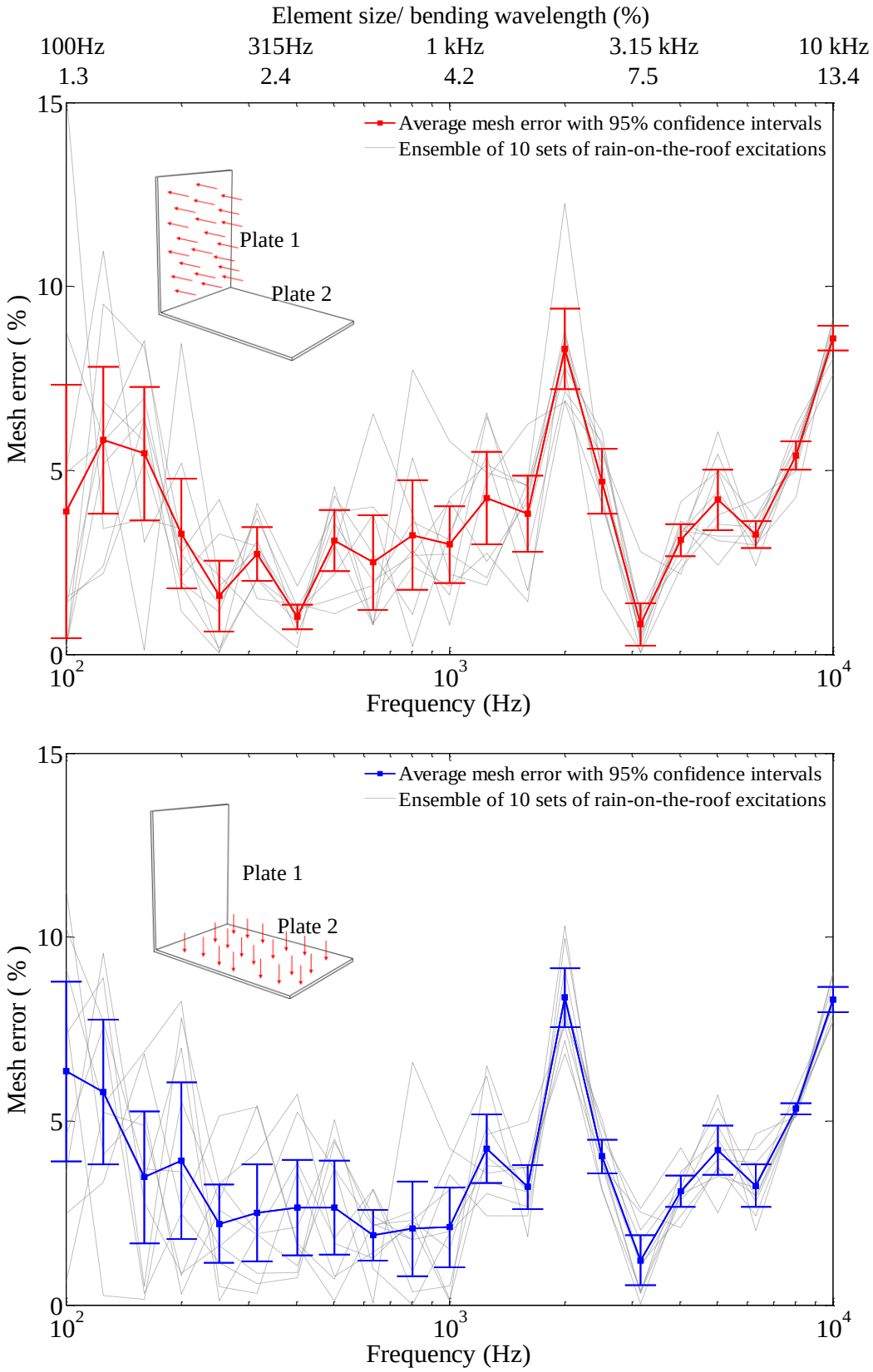

Figure 6.3 Element mesh error for L-junction of two isotropic homogeneous plates (Model 1) with free boundary at the coupling junction. (a) ROTR on plate 1; (b) ROTR on plate 2.

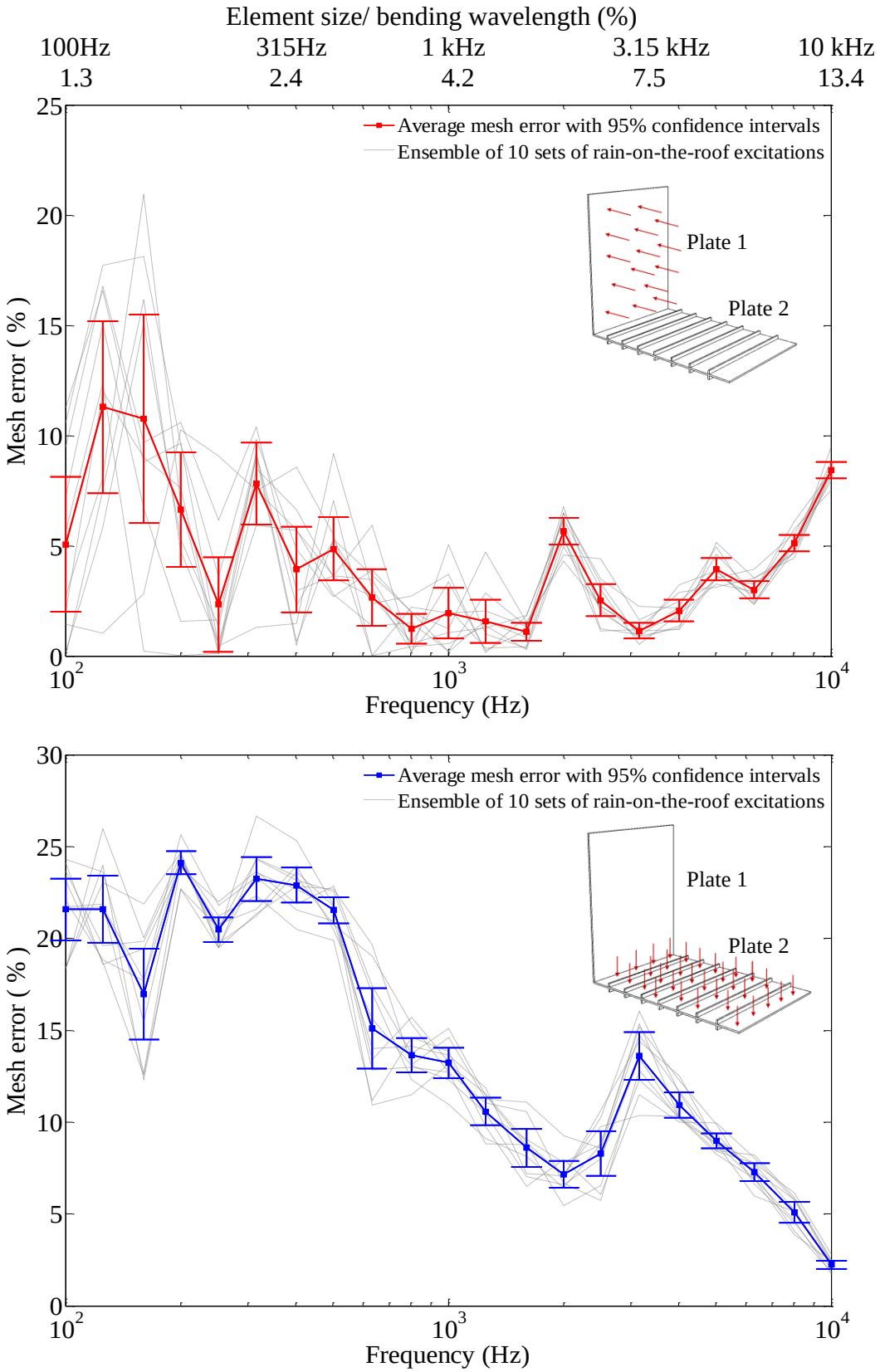

Figure 6.4 Element mesh error for L-junction of an isotropic plate and a periodic plate (Model 2) with simply-supported boundaries along all edges. (a) ROTR on isotropic plate; (b) ROTR on periodic ribbed plate.

6.3 L-junction comprised of two isotropic homogeneous plates

Structure-borne sound transmission across the L-junction comprised of two isotropic homogeneous plates (Model 1: see Figure 6.1) is analyzed in this section based on the discussions in the previous chapters for the prediction of structure-borne sound transmission using ESEA and wave approaches.

In this section, FEM with ESEA as discussed in Chapter 2 is used to calculate the coupling loss factors and the results are compared with the wave approach described in Chapter 5.

6.3.1 Bending waves only

Figure 6.5(a) and Figure 6.6(a) show the coupling loss factors considering only bending wave transmission across the junction. The bending mode counts for the two plates, N_{B1} and $N_{B2,}$ and geometric mean of the modal overlap factors, M_{av} are also shown above the graphs.

In general, the variation of coupling loss factors obtained from different ROTR reduces with increasing frequency resulting in smaller confidence intervals at high frequency bands.

FEM with ESEA generally gives good agreement with coupling loss factors calculated using the wave approach as the latter lie within the 95% confidence intervals of ±2SD. However, there are exceptions at the two ends of the frequency range.

At low frequencies where mode counts and geometric mean of the modal overlap factors are small (from Fahy and Mohammed [40] this condition can be considered as $N_B<5$ and $M_{av}<1$), ESEA is not expected to give a good prediction for individual members of an ensemble. There is a significant variation between individual members of the ensemble of ROTR; hence the FEM result with a single set of ROTR is of little practical use. However, the arithmetic average of the ensemble gives reasonable predictions at low frequencies. This has also been observed with other L- and T-junctions by Hopkins [19].

In the 6.3 kHz, 8 kHz and 10 kHz one-third octave bands on Figure 6.5 (a) and Figure 6.6 (a), there are differences of 1.1 dB to 3.9 dB between the wave approach and the ensemble average from FEM with ESEA. In these frequency bands it is notable that the 95% confidence intervals from FEM with ESEA do not overlap the curve for the wave approach. Referring back to section 2.5.2.1 it is possible that this is caused by the S4R element no longer reproducing thin plate behaviour. However, the mesh error did not indicate significant issues in section 6.2.2.

6.3.2 Bending and in-plane waves

In Figure 6.5 (b) and Figure 6.6 (b), the L-junction is modelled to allow both bending and in-plane waves. Comparison between the wave approach for bending wave only model and bending and in-plane wave model in Figure 6.5 (b) and Figure 6.6 (b) has shown that at low frequencies below 630 Hz where there is no in-plane mode, the two models are equivalent to each other. As frequency increases, the difference between the two models becomes larger due to the increase of the in-plane mode counts.

Between 100 Hz and 5 kHz, the coupling loss factors show good agreement between the wave approach and FEM with ESEA. At higher frequencies, a difference up to 3 dB occurs. This is similar to that seen with the bending only model.

At high frequencies, it appears that FEM with ESEA agrees well with the bending wave only model but this is purely coincidence.

6.3.3 ESEA errors in the internal loss factor

Figure 6.7 (a) and (b) show that the error in the internal loss factor calculated from ESEA is similar for the bending only and bending and in-plane wave models. This shows that there are no significant errors in the internal loss factor between 500 Hz and 10 kHz. Above 5 kHz, the 95% confidence intervals from FEM with ESEA do not overlap the actual value for the internal loss factor but the error is less than 0.5 dB.

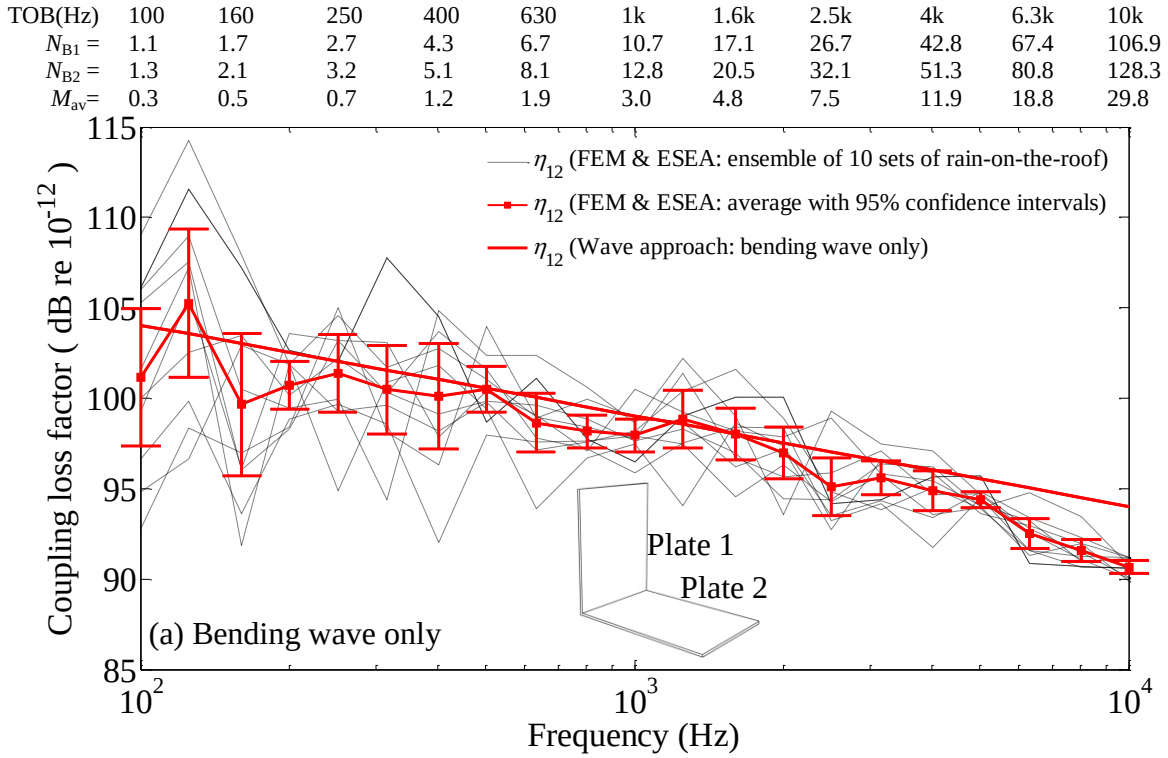

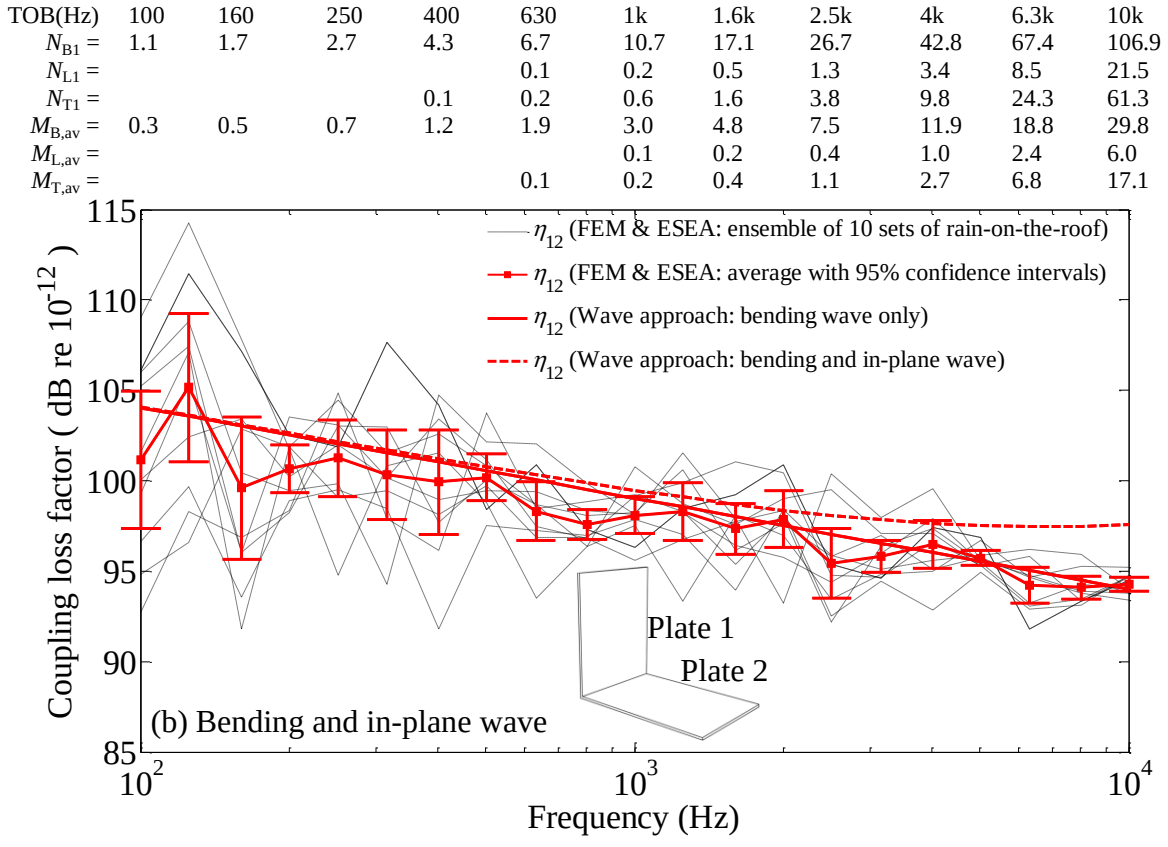

Figure 6.5 Coupling loss factors from plate 1 to 2 determined using FEM with ESEA compared with wave approach with (a) bending wave only; (b) bending and in-plane wave. Mode counts and the geometric mean of the modal overlap factors for different wave types are shown at the top of the figure.

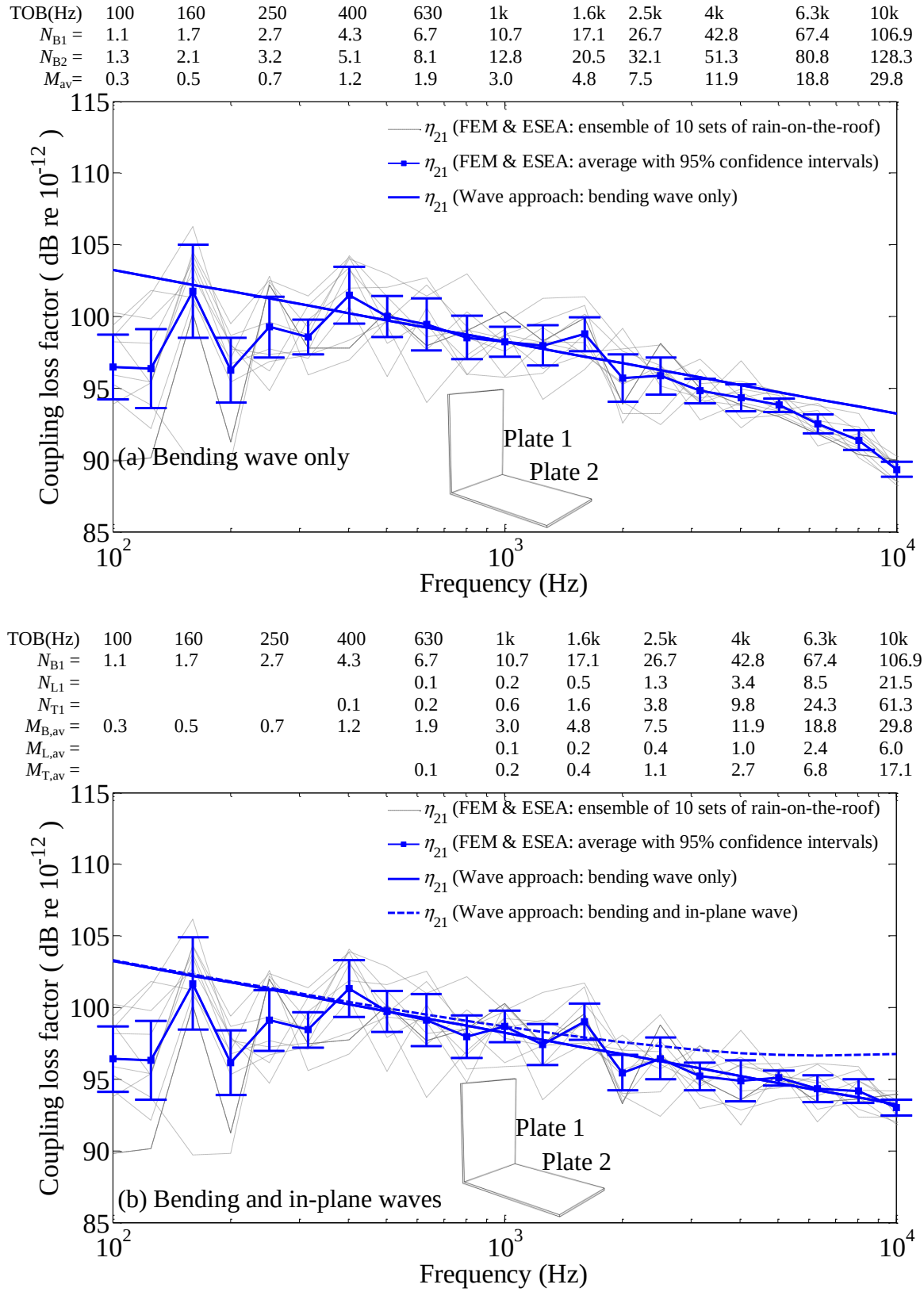

Figure 6.6 Coupling loss factors from plate 2 to 1 determined using FEM with ESEA compared with wave approach with (a) bending wave only; (b) bending and in-plane wave. Mode counts and the geometric mean of the modal overlap factors for different wave types are shown at the top of the figure.

TOB(Hz)	100	160	250	400	630	1k	1.6k	2.5k	4k	6.3k	10k
N_{B1} =	1.1	1.7	2.7	4.3	6.7	10.7	17.1	26.7	42.8	67.4	106.9
N_{B2} =	1.3	2.1	3.2	5.1	8.1	12.8	20.5	32.1	51.3	80.8	128.3
M_{av}=	0.3	0.5	0.7	1.2	1.9	3.0	4.8	7.5	11.9	18.8	29.8

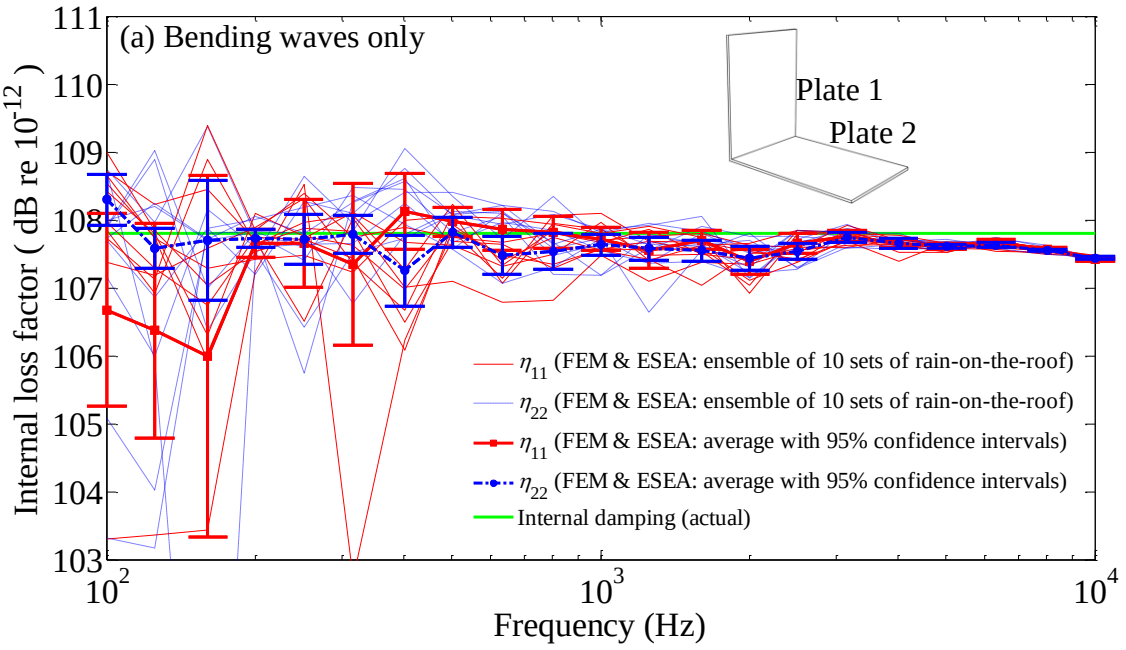

TOB(Hz)	100	160	250	400	630	1k	1.6k	2.5k	4k	6.3k	10k
N_{B1} =	1.1	1.7	2.7	4.3	6.7	10.7	17.1	26.7	42.8	67.4	106.9
N_{L1} =					0.1	0.2	0.5	1.3	3.4	8.5	21.5
N_{T1} =				0.1	0.2	0.6	1.6	3.8	9.8	24.3	61.3
$M_{B,av}$ =	0.3	0.5	0.7	1.2	1.9	3.0	4.8	7.5	11.9	18.8	29.8
$M_{L,av}$ =						0.1	0.2	0.4	1.0	2.4	6.0
$M_{T,av}$ =					0.1	0.2	0.4	1.1	2.7	6.8	17.1

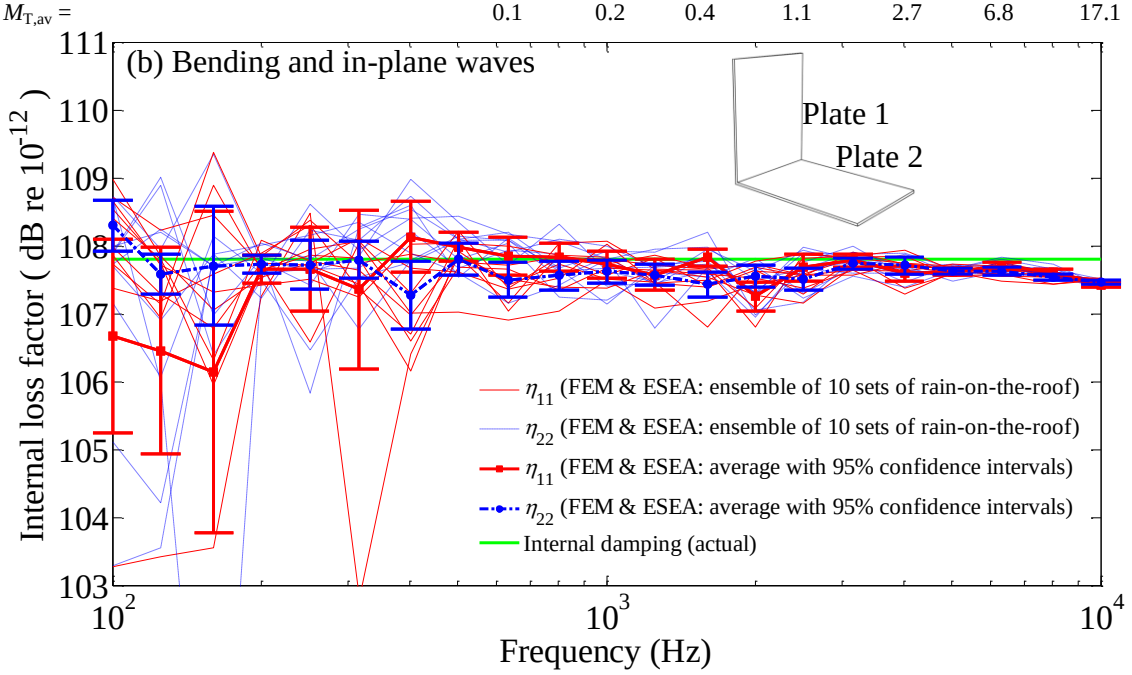

Figure 6.7 Internal loss factors determined using FEM and ESEA compared with actual internal damping used in FEM. Consider (a) bending waves only; (b) bending and in-plane waves. Mode counts and the geometric mean of the modal overlap factors for different wave types are shown at the top of the figure.

6.3.4 Comparison between matrix ESEA and simplified ESEA

As discussed in section 2.3.2, simplified ESEA can be used to predict the coupling loss factors without performing the matrix inversion. Simplified ESEA in equation (2.37) requires the total loss factors to calculate the coupling loss factors, but this is not available from FEM. Therefore the internal loss factor is used to replace the total loss factor. This simplification is only valid when the internal loss factor is much larger than the sum of the coupling loss factors. Hence this section investigates the errors that are incurred when using simplified ESEA with L-junctions.

Figure 6.8 compares the coupling loss factors calculated from matrix ESEA and simplified ESEA for (a) bending wave only model and (b) bending and in-plane wave model. In general, the two methods both give good estimates compared with the wave approach, and the difference between the two methods is less than 3 dB across the whole frequency range.

At low frequencies, matrix ESEA gives a better estimate than simplified ESEA when compared with the wave approach. This is clearly observed for the CLFs from plate 2 to plate 1 in the frequency range of 250 Hz to 1 kHz. This is because the sum of the coupling loss factors is similar to the internal loss factors, thus the assumption to use simplified ESEA is not valid. However it doesn't make a significant difference in this specific model as each subsystem is only coupled to one other subsystem and the internal loss factor is relatively high. At high frequencies where the sum of the coupling loss factors is much smaller compared with the internal loss factor, the difference between the two ESEA methods is negligible (less than 1 dB).

Simplified ESEA provides a quick evaluation of the coupling loss factor between subsystems and is convenient for physical measurements where the coupling loss factor between two subsystems can be calculated by only measuring the responses on the two subsystems. The results in this section indicate that for L-junctions of Perspex plates, simplified ESEA can provide equally good results compared with matrix ESEA in the frequency range from 1 kHz to 10 kHz.

TOB(Hz)	100	160	250	400	630	1k	1.6k	2.5k	4k	6.3k	10k
N_{B1} =	1.1	1.7	2.7	4.3	6.7	10.7	17.1	26.7	42.8	67.4	106.9
N_{L1} =					0.1	0.2	0.5	1.3	3.4	8.5	21.5
N_{T1} =				0.1	0.2	0.6	1.6	3.8	9.8	24.3	61.3
$M_{B,av}$ =	0.3	0.5	0.7	1.2	1.9	3.0	4.8	7.5	11.9	18.8	29.8
$M_{L,av}$ =						0.1	0.2	0.4	1.0	2.4	6.0
$M_{T,av}$ =					0.1	0.2	0.4	1.1	2.7	6.8	17.1

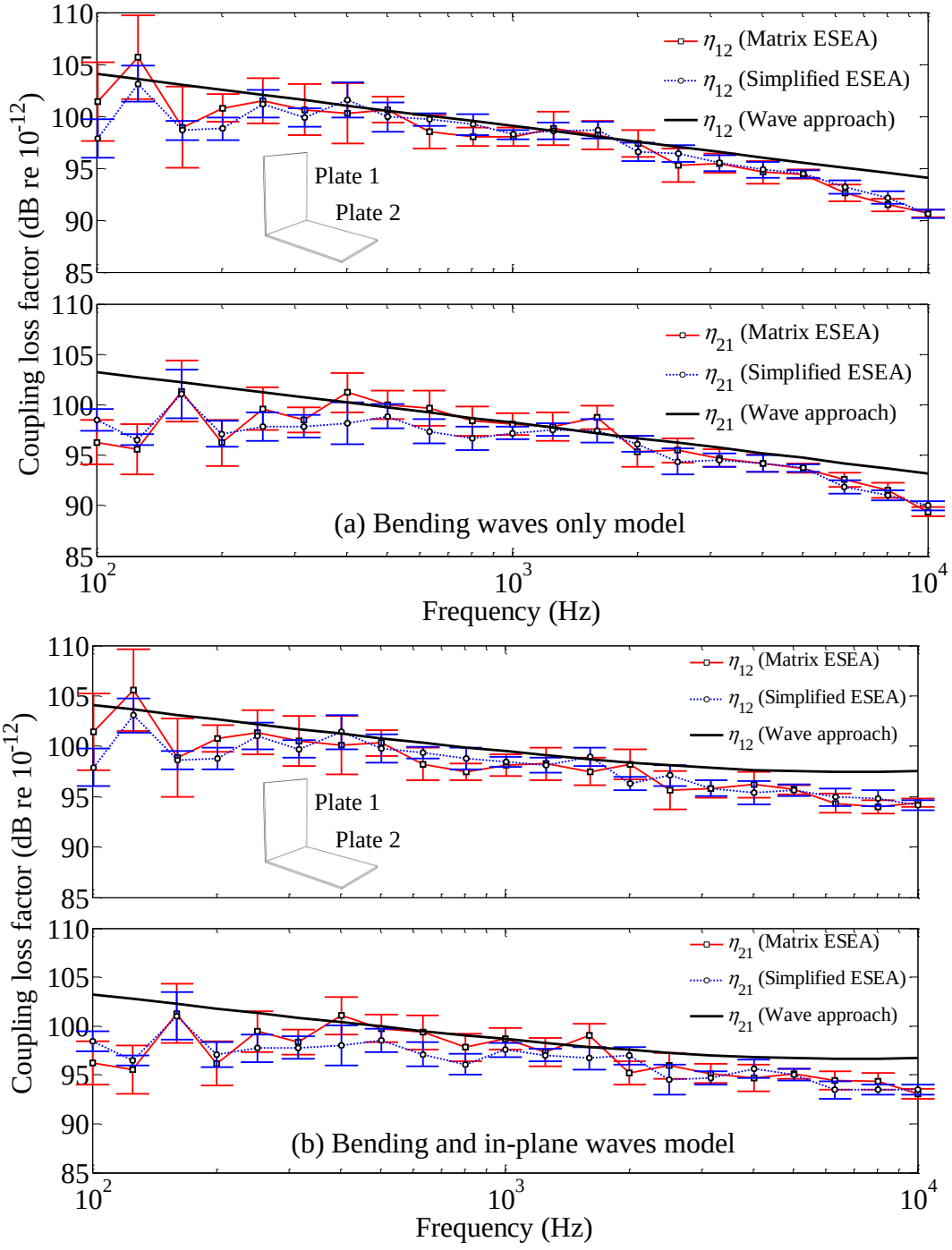

Figure 6.8 Coupling loss factors of between an L-junction with two isotropic, homogeneous plates using matrix ESEA and simplified ESEA. (a) Bending waves only model; (b) Bending and in-plane waves model.

6.4 Effect of the internal loss factor on coupling loss factors determined from FEM with ESEA

SEA assumes a reverberant vibration field on subsystems with no significant decrease in vibration across each subsystem. This assumption may no longer be valid when the internal damping of the subsystem is high, particular at high frequencies. All the plates analyzed in this thesis are made of Perspex whose internal loss factor is 0.06. This can be considered as relatively high damping and its effect therefore requires further investigation here.

The effect of damping is not considered when calculating the coupling loss factors using the wave approach. However, Yap and Woodhouse [26] investigated the damping effect and showed that the coupling loss factors may be strongly dependent on damping when the subsystem is lightly damped.

Figure 6.9 shows the coupling loss factors for the same L-junction analysed in section 6.3 but with internal loss factors ranging from 0.015 to 0.24. Between 100 Hz and 1 kHz, there are differences in the coupling loss factor of up to 10 dB between the lowest damping of 0.015 and the highest damping of 0.24. As the internal loss factor increases, the differences between coupling loss factors reduces. For example, the coupling loss factors calculated with internal loss factor of 0.12 and 0.24 almost overlap with each other. However, the difference between internal loss factor of 0.12 and 0.06 is clearly observed and below 0.06, the differences in CLF are at least 2 dB in most one-third octave bands. Subsystems with the highest internal loss factor of 0.24 show the best agreement with the wave approach with less than 3 dB of discrepancy. This indicates that the errors using the wave approach to predict coupling loss factors at low frequencies can be large for lightly damped subsystems. Also, the ESEA energy matrix (equation (2.39)) is almost singular, hence the inversion is likely to produce errors [125].

The upper x-axis of Figure 6.9 shows the geometric mean of the modal overlap, $M_{\mathrm{B,av}}$. For the indicator for the applicability of SEA, the use of the wave approach in SEA is often considered valid when $M_{\mathrm{B,av}}$ is greater than unity. On this basis the wave approach is valid above 100 Hz for subsystems with internal loss factor of

0.24, 400 Hz for internal loss factor of 0.06 and 1.6 kHz for internal loss factors of 0.015.

At high frequencies, Figure 6.9 shows that varying internal loss factors has little effect on the coupling loss factors. CLFs calculated from different internal loss factor tend to merge together with differences less than 2 dB.

Figure 6.10 shows the energy level differences between the source subsystem and receiving subsystem with different internal loss factors. Between 1 kHz and 5 kHz, there is good agreement with discrepancies less than 3 dB. These results confirm the finding of Villot and Bosmans [126] that when using distributed excitation such as rain-on-the-roof, SEA can be applied to highly damped subsystems.

It is also shown that the discrepancy between the wave approach and FEM with ESEA that occurs above 6.3 kHz is not due to the internal loss factor of Perspex being relatively high.

In section 2.2.8 the requirement on maximum subsystem dimensions due to high internal losses were discussed. The upper frequency limits for the L-junction with different internal loss factors calculated using these criteria is shown in Table 5. This indicates that for subsystems made of Perspex (internal loss factor of 0.06), this requirement is met up to 15 kHz so the SEA assumptions of uniform distribution of energy over each subsystem or a reverberant field on the subsystem is satisfied for results shown up to 10 kHz in this thesis. However, it also shows that for higher internal losses, the frequency limit significantly decreases to below 5 kHz. Therefore, to model the L-junction using SEA would not be valid based on this requirement. However, the results presented in this section do not show significant error with internal loss factors larger than 0.06. This may be due to the criterion being developed for subsystems that are connected on all sides rather than only on one side as with the isolated L-junction.

Table 5: Frequency limit due to damping based on the criteria given in section 2.2.8

Internal loss factor	0.015	0.03	0.06	0.12	0.24
Upper frequency limit (Hz)	238840	59710	14927	3732	933

	M_{av}										
$\eta_{11}=\eta_{22}$=0.24	1.2	1.9	3.0	4.8	7.5	11.9	19.1	29.8	47.7	75.1	119.2
$\eta_{11}=\eta_{22}$=0.12		1.0	1.5	2.4	3.8	6.0	9.5	14.9	23.8	37.6	59.6
$\eta_{11}=\eta_{22}$=0.06				1.2	1.9	3.0	4.8	7.5	11.9	18.8	29.8
$\eta_{11}=\eta_{22}$=0.03						1.5	2.4	3.7	6.0	9.4	14.9
$\eta_{11}=\eta_{22}$=0.015							1.2	1.9	3.0	4.7	7.5
TOB(Hz)	100	160	250	400	630	1k	1.6k	2.5k	4k	6.3k	10k

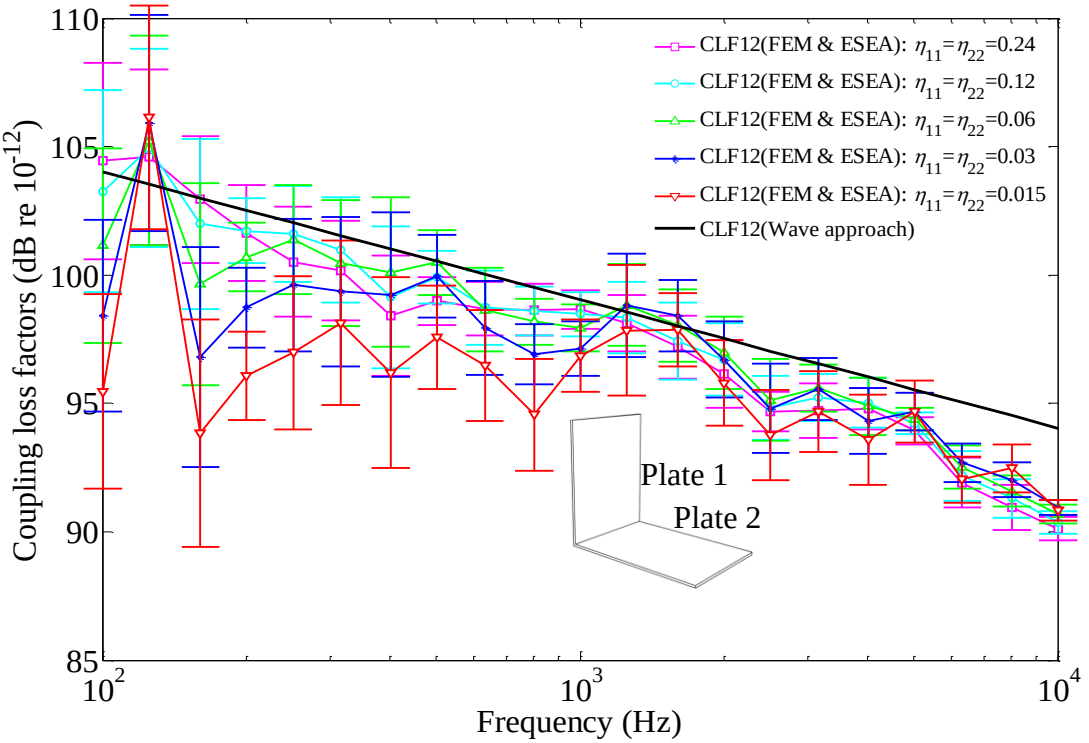

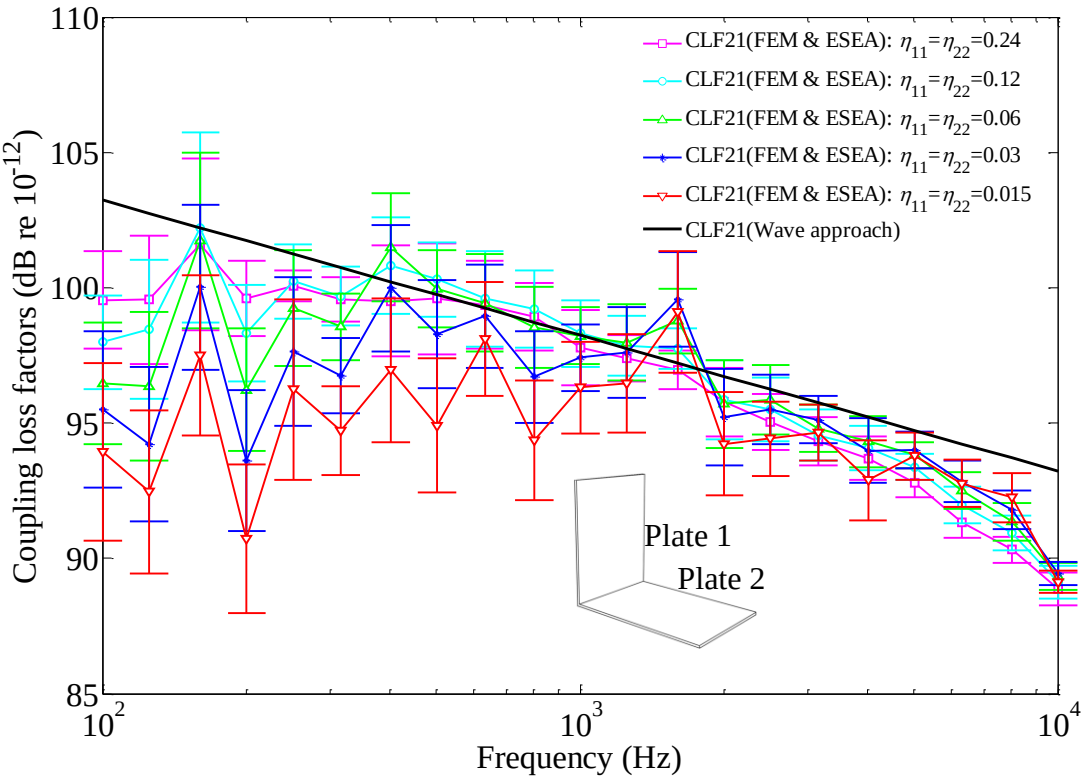

Figure 6.9 Coupling loss factors (FEM with ESEA averaged 10 sets of ROTR) with different internal loss factors

	M_{av}										
$\eta_{11}=\eta_{22}=0.24$	1.2	1.9	3.0	4.8	7.5	11.9	19.1	29.8	47.7	75.1	119.2
$\eta_{11}=\eta_{22}=0.12$		1.0	1.5	2.4	3.8	6.0	9.5	14.9	23.8	37.6	59.6
$\eta_{11}=\eta_{22}=0.06$				1.2	1.9	3.0	4.8	7.5	11.9	18.8	29.8
$\eta_{11}=\eta_{22}=0.03$						1.5	2.4	3.7	6.0	9.4	14.9
$\eta_{11}=\eta_{22}=0.015$							1.2	1.9	3.0	4.7	7.5
TOB(Hz)	100	160	250	400	630	1k	1.6k	2.5k	4k	6.3k	10k

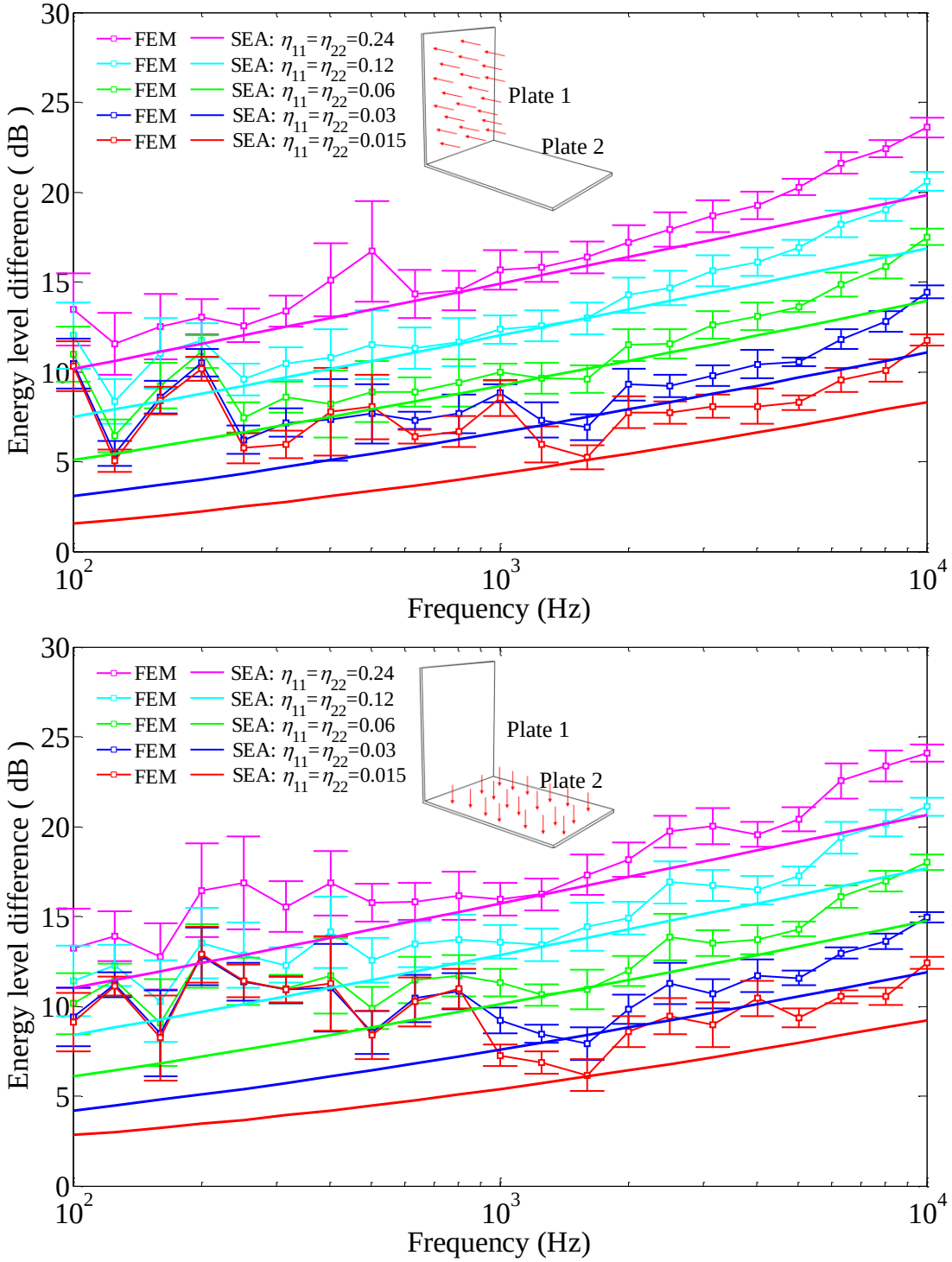

Figure 6.10 Ensemble average of energy level difference between the source subsystem and receiving subsystem (10 sets of ROTR). Different internal damping loss factors are used in FEM.

6.5 L-junction with a periodic ribbed plate modelled as a single subsystem

The L-junction comprised of an isotropic plate and a periodic ribbed plate (Model 2 - see Figure 3.3) is analyzed using the wave approach from Tso and Hansen [10] (section 5.5) and FEM with ESEA where the ribbed plate is treated as a single subsystem.

6.5.1 Low frequency model treating the periodic ribbed plate as an orthotropic plate

At low frequencies where the bending wavelength is larger the bay spacing of the periodic ribbed plate, the ribbed plates can be treated as uniform plates with orthotropic elastic properties. Wave propagation on orthotropic plate is discussed in section 3.2 and theoretical models for wave transmission across structural junctions of orthotropic plates are presented in section 5.6 and 5.7.

Figure 6.11 shows the coupling loss factors across the same L-junction in section 6.5 calculated from FEM with ESEA where the periodic ribbed plate is modelled as an orthotropic plate in ABAQUS. Both FEM models give large fluctuations at low frequencies and good agreement is found at high frequencies with confidence intervals overlapping with each other in most frequency bands although the orthotropic models are considered not valid at high frequencies where the bending wavelength is smaller than the bay spacing. For the complete FEM model, the coupling loss factor curves show four clear troughs which is explained in the next section as caused by the stop bands of the periodic ribbed plate identified in Figure 4.3. However, these troughs have not been picked up by the orthotropic FEM model. It is also noticed that for the coupling loss factors from the ribbed plate to the isotropic plate, the orthotropic FEM with ESEA slightly overestimates the coupling loss factors. This discrepancy can be explained as follows: in the FEM model for the complete ribbed plate, the energies of the ribs are not accounted in the calculation of the coupling loss factors so when the ribbed plate is excited, the transmission coefficient from the ribbed plate to the isotropic plate will be underestimated which will result in an underestimated coupling loss factor.

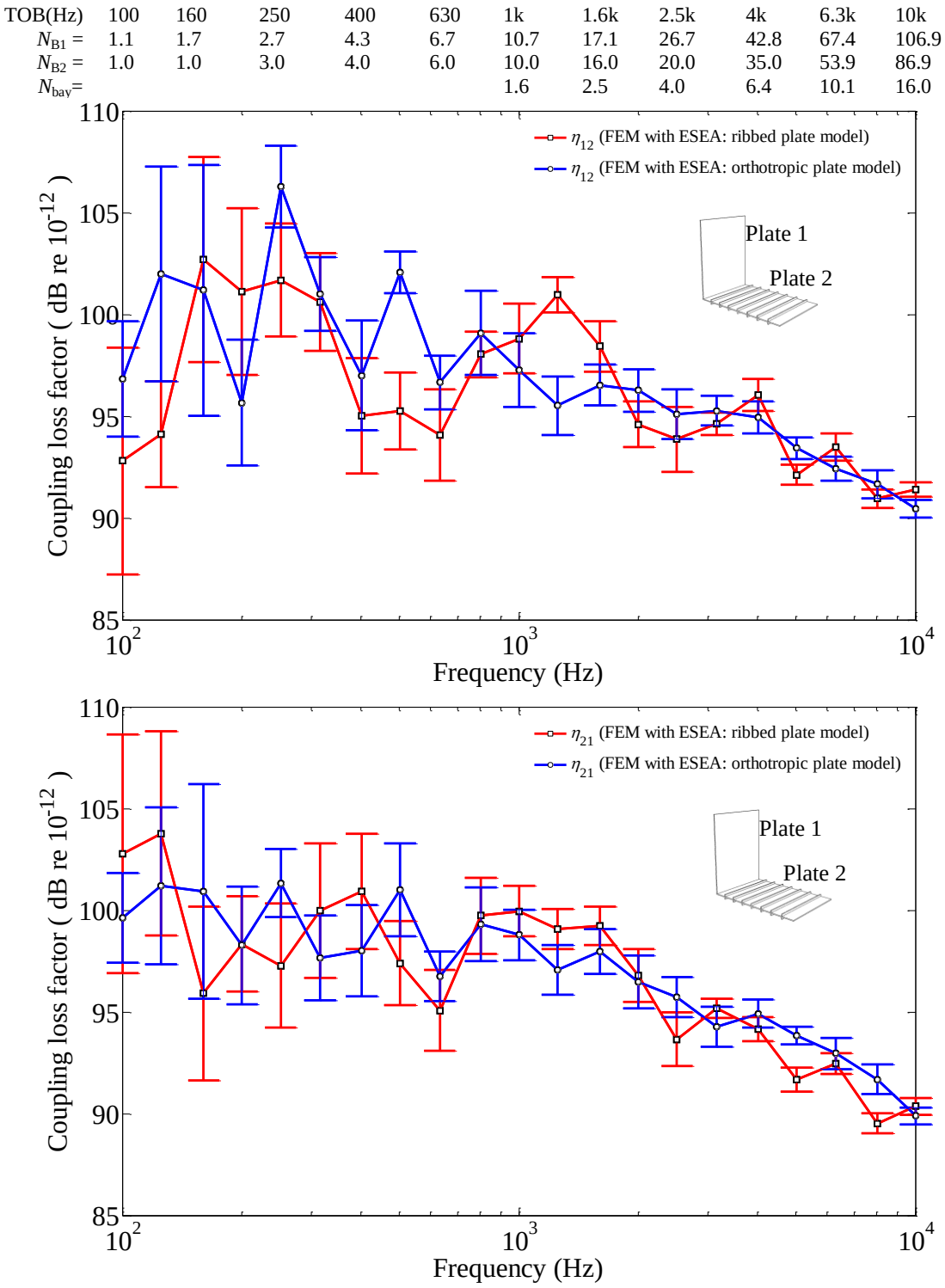

Figure 6.11 Coupling loss factors of between an L-junction with a uniform plate and a periodic ribbed plate determined using FEM with ESEA (10 sets of ROTR) where ribbed plate is modelled as a plate with orthotropic elastic properties in FEM compared with the model in section 6.6. Mode counts and the geometric mean of the modal overlap factors of the two subsystems are shown at the top of the figure.

Figure 6.12 shows a comparison of theoretical results with the wave approach using different bending stiffness presented in section 5.6 and 5.7. The models are shown for the entire frequency range although strictly speaking they are only valid below the fundamental mode of the bay or at frequencies where the bay spacing is less than half of the bending wavelength. This is purely done to illustrate the relatively good agreement that can exist even when the models are not strictly valid. The wave approach using the equivalent bending stiffness gives the best agreement with FEM with ESEA where ribbed plate is modelled as an orthotropic plate. The wave approach using angle-dependent bending stiffness tends to underestimate the CLFs while using the bending stiffness in the *x*-direction overestimate the CLFs. It is noticed that these two methods seemed to give an upper and lower envelop of the ESEA predictions.

Figure 6.13 shows the theoretical results with the wave approach using different bending stiffness compared with FEM with ESEA where the ribbed plate is modelled exactly in FEM. It is found that the wave approach using angle-dependent bending stiffness gives a slightly better estimate than using the equivalent bending stiffness in terms of the number of frequency bands that the theoretical results falls into the 95% confidence intervals of FEM with ESEA.

In summary, FEM with ESEA where the ribbed plate is modelled as an orthotropic plate generally gives close prediction compared with the complete FEM model. Theoretical models using the wave approach with different bending stiffness yield close results at low frequencies with less than 2 dB of discrepancy and the predictions also agree well with FEM with ESEA. At high frequencies, the discrepancies become larger between different bending stiffness models. Compared with FEM with ESEA, wave approaches using equivalent bending stiffness and angle-dependent bending stiffness give the best estimates while using bending stiffness in only the *x*-direction overestimates the CLFs.

The problem with the orthotropic plate models is that they are not able to predict the troughs in the CLF that are caused by the stop bands of the periodic ribbed plate. Hence in the next section, the wave approach from Tso and Hansen will be used to incorporate this phenomenon.

TOB(Hz)	100	160	250	400	630	1k	1.6k	2.5k	4k	6.3k	10k
N_{B1} =	1.1	1.7	2.7	4.3	6.7	10.7	17.1	26.7	42.8	67.4	106.9
N_{B2} =	1.0	1.0	3.0	4.0	6.0	10.0	16.0	20.0	35.0	53.9	86.9
N_{bay}=						1.6	2.5	4.0	6.4	10.1	16.0

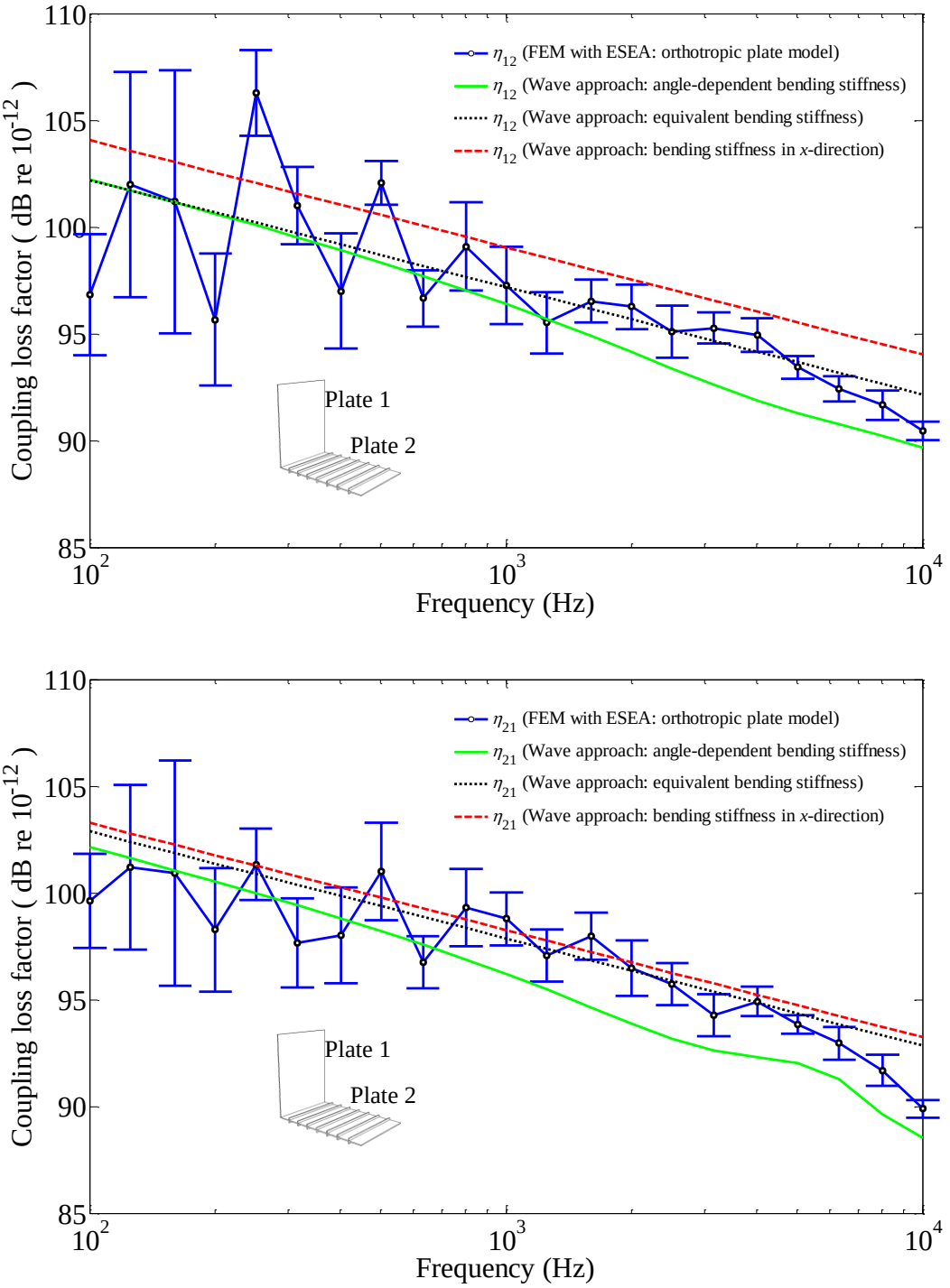

Figure 6.12 Coupling loss factors of between an L-junction with a uniform plate and a periodic ribbed plate determined using FEM with ESEA (10 sets of ROTR) where ribbed plate is modelled as a plate with orthotropic elastic properties in FEM compared with wave approach using different bending stiffness.

TOB(Hz)	100	160	250	400	630	1k	1.6k	2.5k	4k	6.3k	10k
N_{B1} =	1.1	1.7	2.7	4.3	6.7	10.7	17.1	26.7	42.8	67.4	106.9
N_{B2} =	1.0	1.0	3.0	4.0	6.0	10.0	16.0	20.0	35.0	53.9	86.9
N_{bay}=						1.6	2.5	4.0	6.4	10.1	16.0

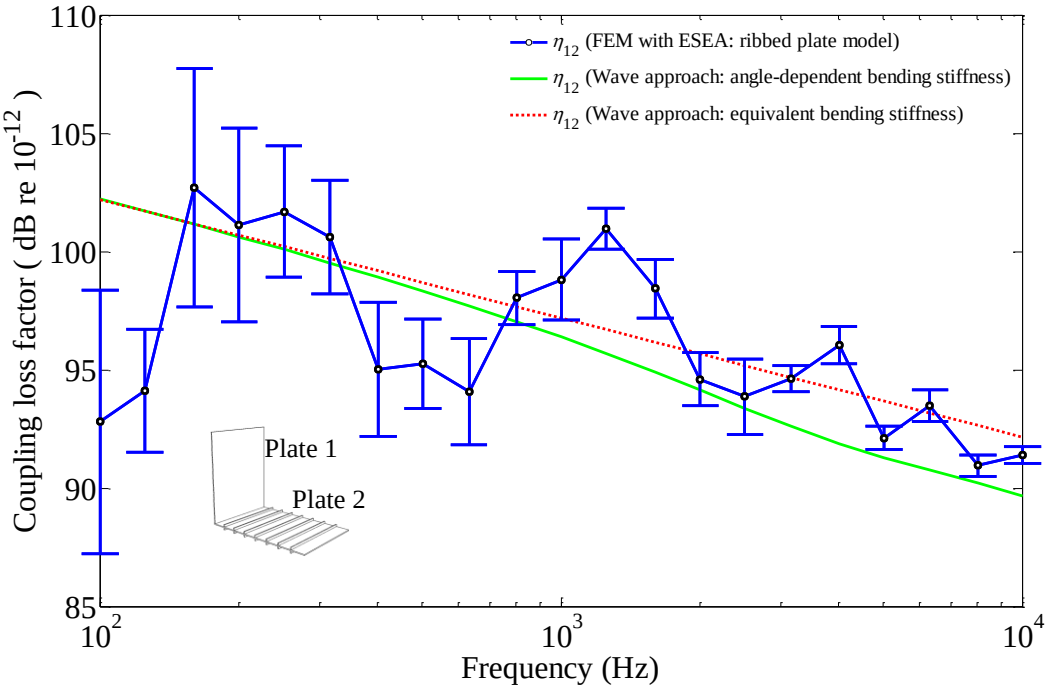

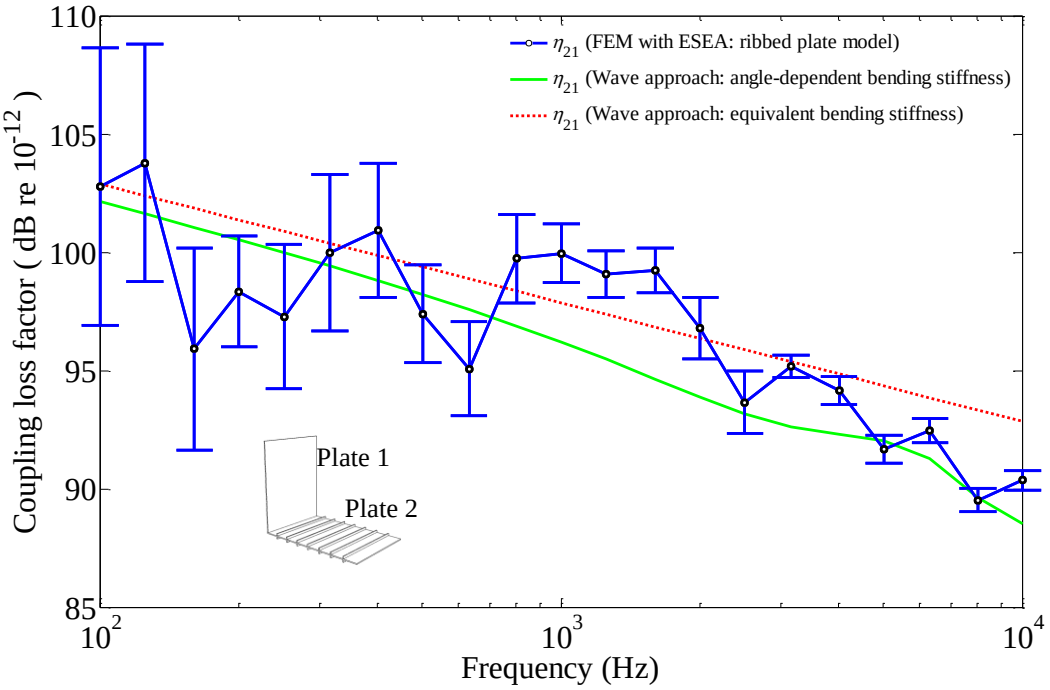

Figure 6.13 Coupling loss factors of between an L-junction with a uniform plate and a periodic ribbed plate determined using FEM with ESEA (10 sets of ROTR) compared with wave approach from Tso and Hansen and wave approach using angle-dependent bending stiffness.

6.5.2 Low-, mid- and high-frequency models using the wave approach from Tso and Hansen

6.5.2.1 Coupling loss factors from FEM with ESEA

The coupling loss factors calculated from FEM with ESEA are shown in Figure 6.14 in comparison with results from the wave approach from Tso and Hansen [10]. The CLFs from the isotropic plate to the ribbed plate are calculated using this wave approach and the CLFs in the opposite direction are calculated from the consistency relationship using the modal density for the periodic ribbed plate from Bosmans and Vermeir[89] described in section 3.2.6.

Both the wave approach and FEM with ESEA show troughs in the coupling loss factors at 630 Hz, 2500 Hz and 5000 Hz. These troughs correspond to the first three attenuation zones that can be identified in Figure 4.3.

In general, good agreement is found, with the results from the wave approach falling within the 95% confidence intervals of FEM with ESEA in most one-third octave bands. The maximum discrepancy is 3 dB except for η_{12} in the 100 Hz and 125 Hz one-third octave bands. Between 100 Hz and 500 Hz where the geometric mean of modal overlap factors is less than unity, large variations occur with individual rain-on-the-roof excitation resulting in large confidence intervals.

ESEA gives accurate predictions for the internal loss factors as shown in Figure 6.15. Between 1 kHz and 10 kHz, the ILF for the isotropic homogeneous plate is underestimated by up to 1 dB and for the periodic ribbed plate it is overestimated by up to 1 dB.

On the basis of this section it appears that the Tso and Hansen model is adequate. However, it will be shown in section 6.5.2.3 that above 1kHz this model is not appropriate because it is not correct to assume that the ribbed plate can be modelled as a single subsystem.

TOB(Hz)	100	160	250	400	630	1k	1.6k	2.5k	4k	6.3k	10k
N_{B1} =	1.1	1.7	2.7	4.3	6.7	10.7	17.1	26.7	42.8	67.4	106.9
N_{B2} =	1.0	1.0	3.0	4.0	6.0	10.0	16.0	20.0	35.0	53.9	86.9
M_{av}=	0.3	0.3	0.6	0.7	1.5	2.9	5.3	8.7	17.1	26.3	47.9

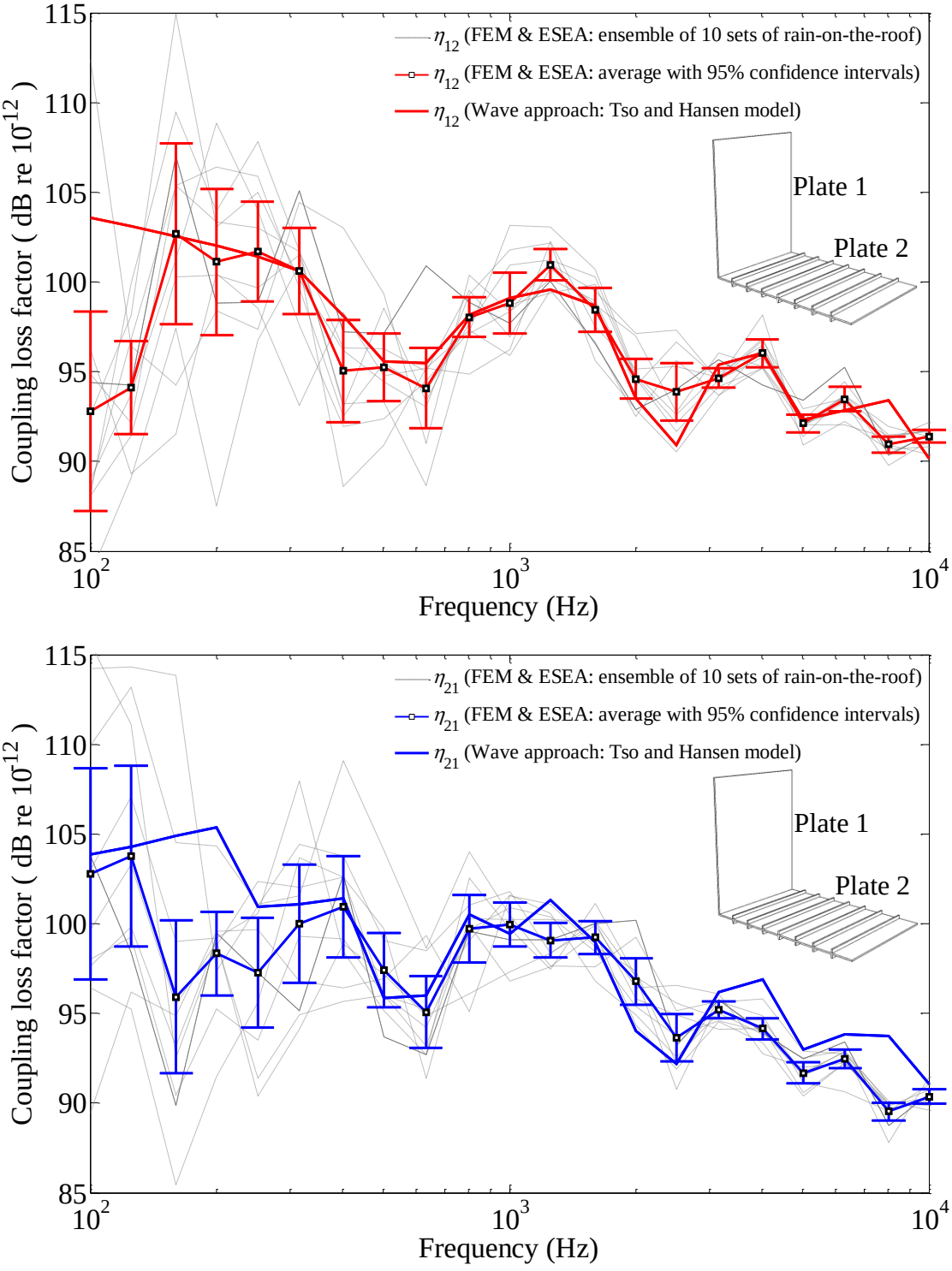

Figure 6.14 Coupling loss factors of between an L-junction with a uniform plate and a periodic ribbed plate determined using FEM and ESEA (10 sets of ROTR) compared with theoretical results using wave approach from Tso and Hansen [10]. Mode counts and the geometric mean of the modal overlap factors of the two subsystems are shown at the top of the figure.

TOB(Hz)	100	160	250	400	630	1k	1.6k	2.5k	4k	6.3k	10k
N_{B1} =	1.1	1.7	2.7	4.3	6.7	10.7	17.1	26.7	42.8	67.4	106.9
N_{B2} =	1.0	1.0	3.0	4.0	6.0	10.0	16.0	20.0	35.0	53.9	86.9
M_{av}=	0.3	0.3	0.6	0.7	1.5	2.9	5.3	8.7	17.1	26.3	47.9

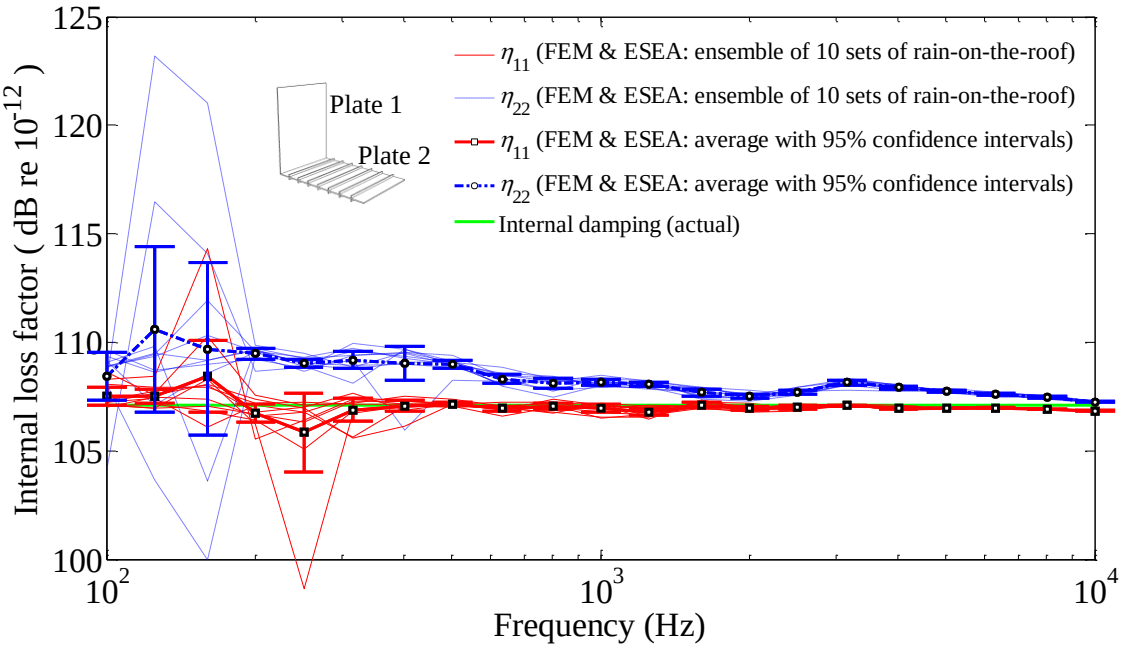

Figure 6.15 Internal loss factors of the two subsystems determined using FEM and ESEA (10 sets of ROTR with 95% confidence intervals) compared with the actual internal loss factor used in FEM. Mode counts and the geometric mean of the modal overlap factors of the two subsystems are shown at the top of the figure.

6.5.2.2 Comparison between matrix ESEA and simplified ESEA

Figure 6.16 shows comparison of the coupling loss factors calculated from matrix ESEA and simplified ESEA.

In contrast to the L-junction of isotropic homogeneous plates in section 6.3.3, it is seen in Figure 6.16 that there is a difference between matrix ESEA and simplified ESEA across the frequency range. One cause of the difference between matrix ESEA and simplified ESEA is that the total energy determined for the ribbed plate excludes the vibration on the ribs. These ribs undergo a combination of bending and torsional motion which results in displacements in all three coordinate directions that is difficult to identify as the modal energy is purely associated with bending waves. In section 6.2 it was shown that the mesh error was highest between 100 Hz and 500 Hz for the L-junction when the periodic ribbed plate was

excited with ROTR rather than when the isotropic homogeneous plate was excited. However, this mesh error only gave a discrepancy in the power of approximately 1 dB.

In the next section it will be shown that the Tso and Hansen model is not appropriate because it is not correct to assume that the ribbed plate can be modelled as a single subsystem. Hence, the fact that it is not possible to identify whether simplified ESEA or matrix ESEA is more accurate is not problematic.

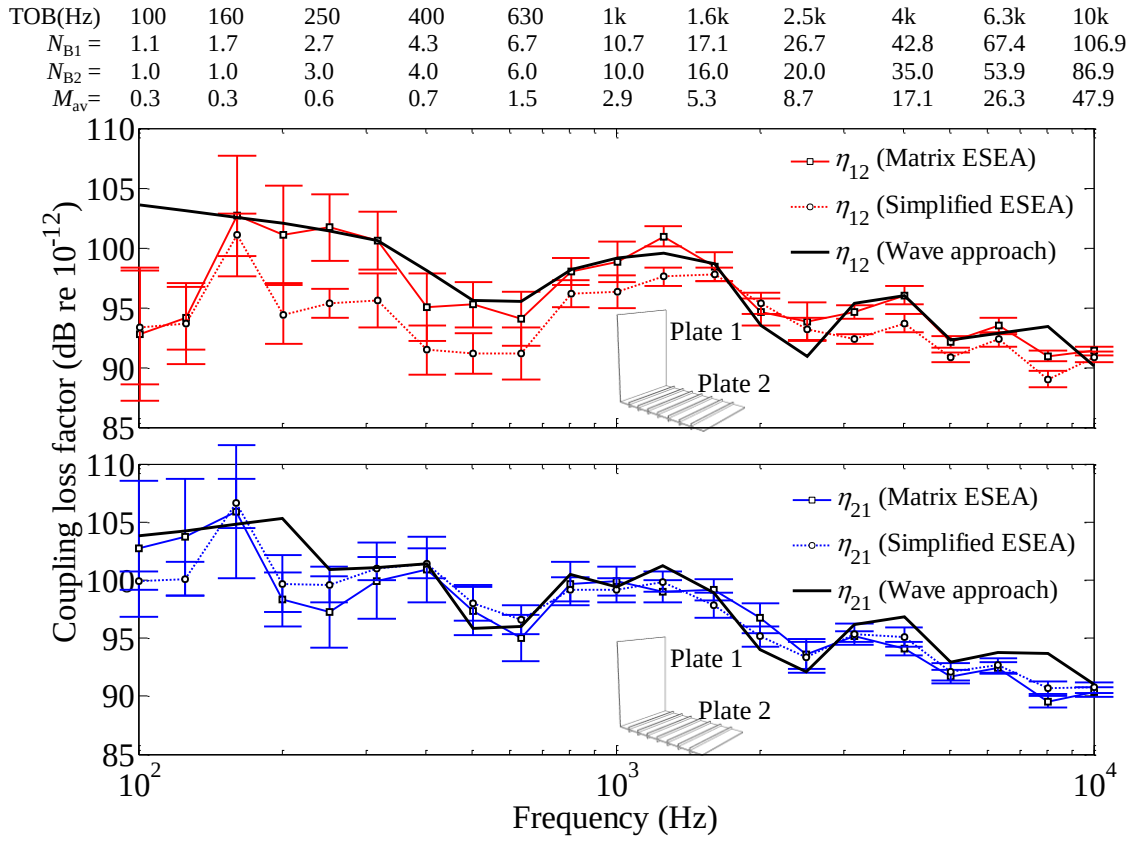

Figure 6.16 Coupling loss factors of between an L-junction with a uniform plate and a periodic ribbed plate using matrix ESEA and simplified ESEA averaged from 10 sets of ROTR with 95% confidence intervals compared with the wave approach from Tso and Hansen.

6.5.2.3 Decrease in vibration level across the bays of the periodic plate

Up to this point in this chapter, the periodic plate has been treated as a single subsystem in the SEA model. However the approach from Tso and Hansen to treat the periodic ribbed plate as a single subsystem is only valid if there is no significant decrease in vibration across successive bays.

Figure 6.17 shows the energy level difference between the source plate (plate 1) and the bays on plate 2. Assuming simply-supported boundaries for each bay, the fundamental local mode for bending occurs at 637 Hz. Below this fundamental mode there is no significant decrease in level across the periodic ribbed plate; hence it is reasonable to treat the periodic plate as a single subsystem. However, above this fundamental mode, the energy levels in each bay differ and when the mode counts for each bay, $N_{bay}>5$ (i.e. above the 3.15 Hz one-third octave band) there are large energy level differences between the bays. At 10 kHz, the energy level difference between the first bay that is closest to the junction and the furthest bay is more than 50 dB. This indicates that at high frequencies, the periodic plate cannot be modelled as a single subsystem in SEA. Therefore it is concluded that the two subsystem model using the Tso and Hansen wave approach gave good agreement with FEM with ESEA in Figure 6.14 for the wrong reason. Therefore at high frequencies, it is now reasonable to consider alternative SEA models which treat each bay on the periodic plate as a separate subsystem.

TOB(Hz)	100	160	250	400	630	1k	1.6k	2.5k	4k	6.3k	10k
N_{plate1} =	1.1	1.7	2.7	4.3	6.7	10.7	17.1	26.7	42.8	67.4	106.9
N_{plate2} =	1.0	1.0	3.0	4.0	6.0	10.0	16.0	20.0	35.0	53.9	86.9
N_{bay}=						1.6	2.5	4.0	6.4	10.1	16.0

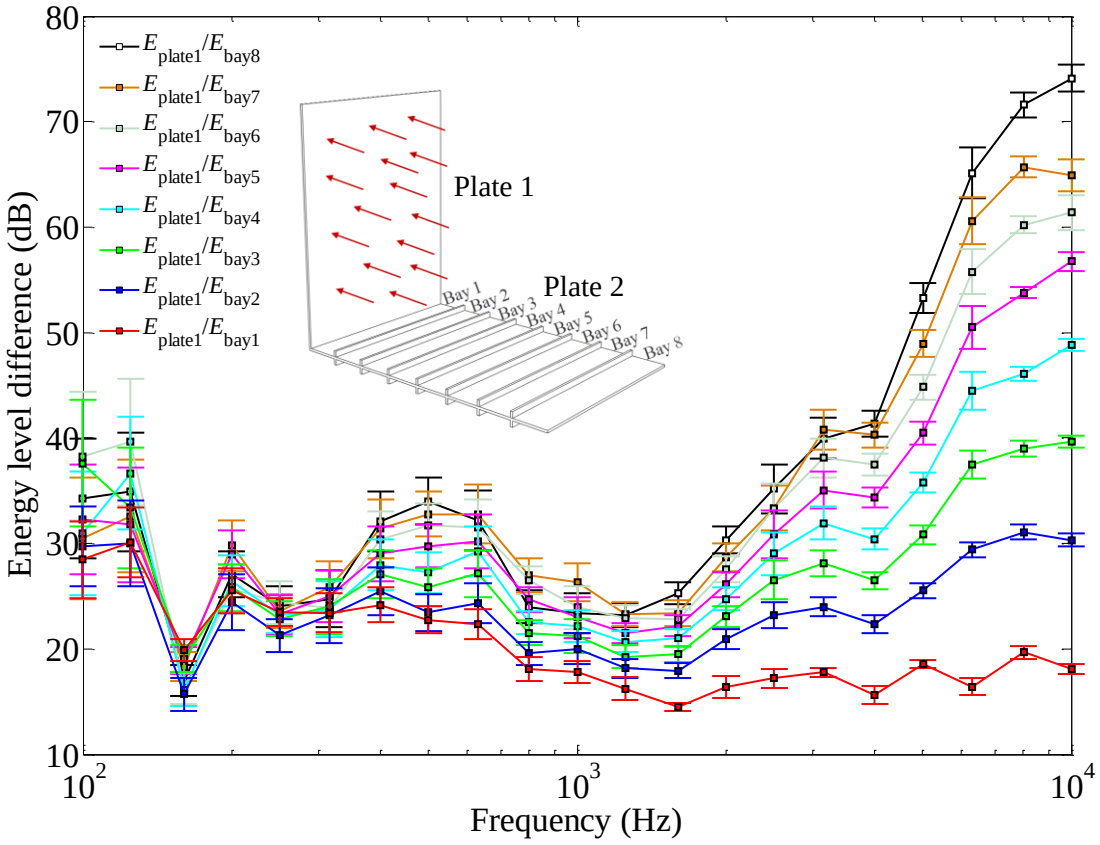

Figure 6.17 Energy level difference between the source subsystem (Plate 1) and bays on the periodic plate (Plate 2) from FEM (10 sets of ROTR with 95% confidence intervals). Mode counts for the two plates as well as the mode counts for an individual bay of the periodic plate are shown on the upper *x*-axis.

6.6 L-junction with a periodic ribbed plate: High frequency model treating the bays of the periodic plate as individual subsystems

6.6.1 SEA model with CLFs calculated using a wave approach (nine-subsystems)

This section considers an SEA model treating each bay of the periodic plate as an individual subsystem. The coupling loss factors are calculated using the wave approach for a rib junction (section 5.4). All the coupling loss factors between physically unconnected subsystems are set to zero in the SEA formulation.

Figure 6.18 shows the SEA prediction for the nine-subsystem model compared with FEM results averaged from 10 sets of ROTR on plate 1. As noted in section 6.5.2.3, the SEA model is only appropriate above the fundamental bending mode of the bay, therefore the results are only shown at and above the 1 kHz one-third octave band. Figure 6.18 shows that SEA only agrees with the FEM model for the first four bays that are closest to the junction. For more distant bays, SEA underestimates the response by up to 25 dB.

It is concluded that this nine-subsystem model using coupling loss factors from the wave approach does not provide an improved prediction when compared with the two-subsystem model. Hence the next step is to see whether using coupling loss factors determined from ESEA would improve the prediction.

TOB(Hz)	100	160	250	400	630	1k	1.6k	2.5k	4k	6.3k	10k
N_{B1} =	1.1	1.7	2.7	4.3	6.7	10.7	17.1	26.7	42.8	67.4	106.9
N_{bay}=						1.6	2.5	4.0	6.4	10.1	16.0
M_{av}=	0.1	0.2	0.3	0.4	0.7	1.1	1.7	2.6	4.2	6.6	10.5

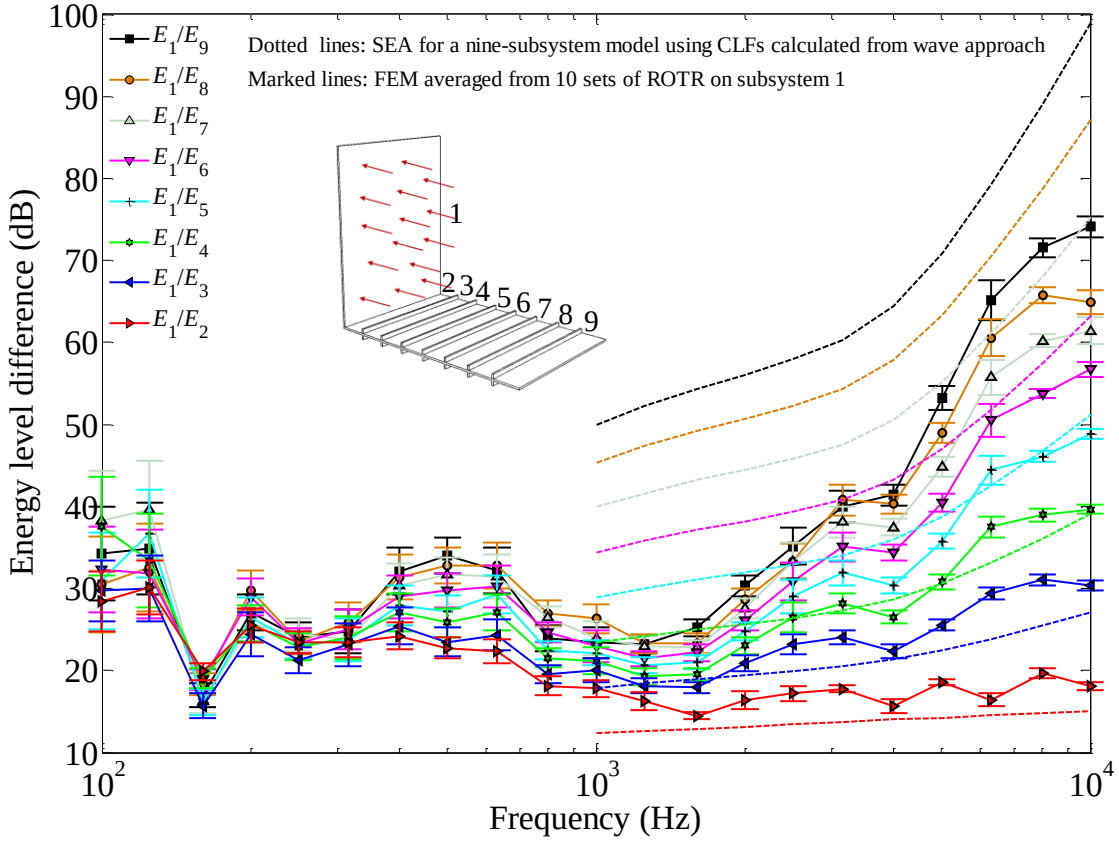

Figure 6.18 Energy level difference between the source subsystem (Plate 1) and bays on the periodic plate (Plate 2) from FEM (10 sets of ROTR) compared with SEA for a nine-subsystem model using coupling loss factors calculated from wave approach. Mode counts for plate 1 and the bays of the ribbed plate, geometric mean of modal overlap for plate 1 and any individual bay are shown on the upper *x*-axis.

6.6.2 SEA model with CLFs calculated from FEM with ESEA (nine-subsystems)

In order to investigate the large discrepancies with the nine-subsystem SEA model using coupling loss factors calculated from wave approach, this section uses FEM with ESEA to determine the coupling loss factors. The nine subsystems are excited in turn with ROTR and standard ESEA formulation in equation (2.39) is used to calculate the coupling loss factors.

Figure 6.19 shows the coupling loss factors between adjacent subsystems. Above the 1 kHz one-third octave band, η_{12} calculated from ESEA (see Figure 6.19 a) shows good agreement with wave approach. However, for the CLFs between adjacent bays (see Figure 6.19 b), good agreement is only observed above the 1.6 kHz one-third octave band when the mode count of the bay N_{bay}>2.5.

Figure 6.20 (a)-(d) show that matrix ESEA for a nine-subsystem model does not only give CLFs between physically connected subsystems, but also gives CLFs between physically unconnected subsystems. The strength of the CLFs between physically unconnected subsystems decreases with increasing distance between the two subsystems. For example, the CLF from plate 1 to bay 2 at 10 kHz is 65 dB which is lower than the CLF from plate 1 to bay 1 of 86 dB. The CLF from plate 1 to the furthest bay at 10 kHz is 70 dB lower than the CLF from subsystem plate 1 to bay 1. Although it is very small, it still indicates positive coupling between the two subsystems.

Figure 6.21 (a) and (b) show the internal loss factors calculated from ESEA for the isotropic plate (plate 1) and bays on the periodic ribbed plate. The internal loss factor for plate 1 (see Figure 6.21 (a)) calculated from ESEA shows good agreement with actual values for all one-third octave bands starting from 100 Hz with a discrepancy less than 1 dB. For the internal loss factors of the bays as shown in Figure 6.21 (b), good agreement only occurs at and above the 1.6 kHz one-third octave band. This indicates that the bays of the periodic plate can only be treated as individual subsystems when the mode count of the bays $N_{\text{bay}} \geq 1.6$.

(a) Coupling loss factors between subsystem 1 and 2

TOB(Hz)	100	160	250	400	630	1k	1.6k	2.5k	4k	6.3k	10k
N_{B1} =	1.1	1.7	2.7	4.3	6.7	10.7	17.1	26.7	42.8	67.4	106.9
N_{bay}=						1.6	2.5	4.0	6.4	10.1	16.0
M_{av}=	0.1	0.2	0.3	0.4	0.7	1.1	1.7	2.6	4.2	6.6	10.5

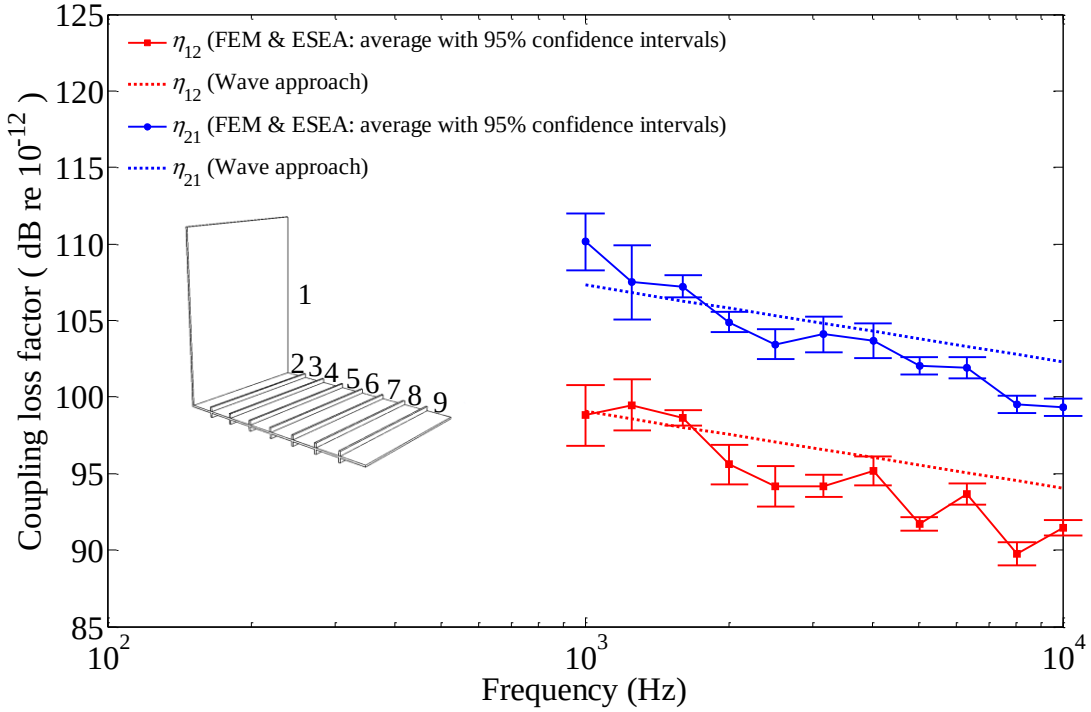

(b) Coupling loss factors between adjacent bays

TOB(Hz)	100	160	250	400	630	1k	1.6k	2.5k	4k	6.3k	10k
N_{B1} =	1.1	1.7	2.7	4.3	6.7	10.7	17.1	26.7	42.8	67.4	106.9
N_{bay}=						1.6	2.5	4.0	6.4	10.1	16.0
M_{av}=	0.1	0.2	0.3	0.4	0.7	1.1	1.7	2.6	4.2	6.6	10.5

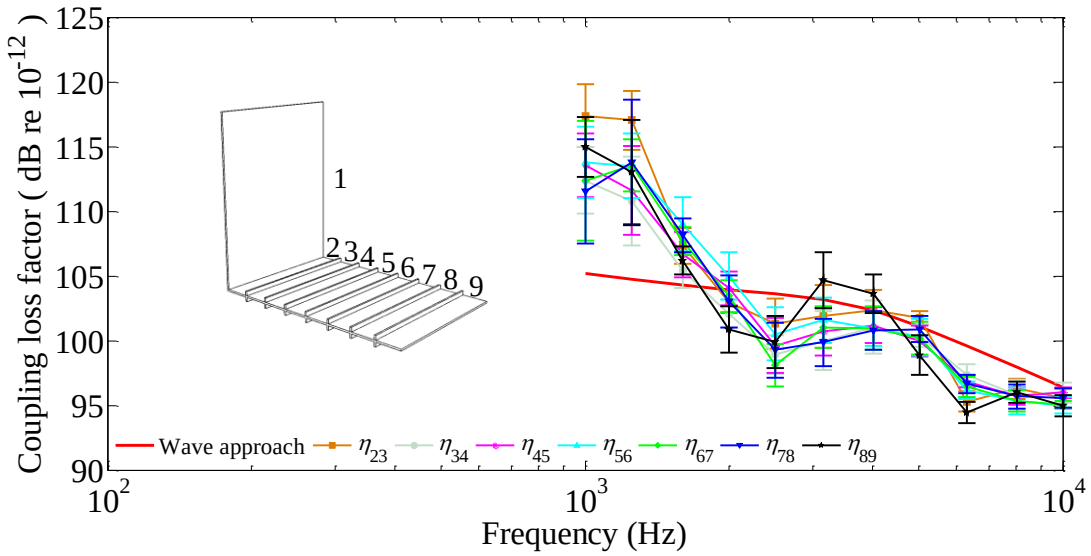

Figure 6.19 Coupling loss factors between physically connected subsystems for a nine-subsystem model determined using FEM with ESEA (10 sets of ROTR) compared with the wave approach. Mode counts, geometric mean of modal overlap for subsystem 1 and any individual bay are shown on the upper *x*-axis.

(a) Coupling loss factors between subsystem 1 and all other subsystems

TOB(Hz)	100	160	250	400	630	1k	1.6k	2.5k	4k	6.3k	10k
N_{B1} =	1.1	1.7	2.7	4.3	6.7	10.7	17.1	26.7	42.8	67.4	106.9
N_{bay}=						1.6	2.5	4.0	6.4	10.1	16.0
M_{av}=	0.1	0.2	0.3	0.4	0.7	1.1	1.7	2.6	4.2	6.6	10.5

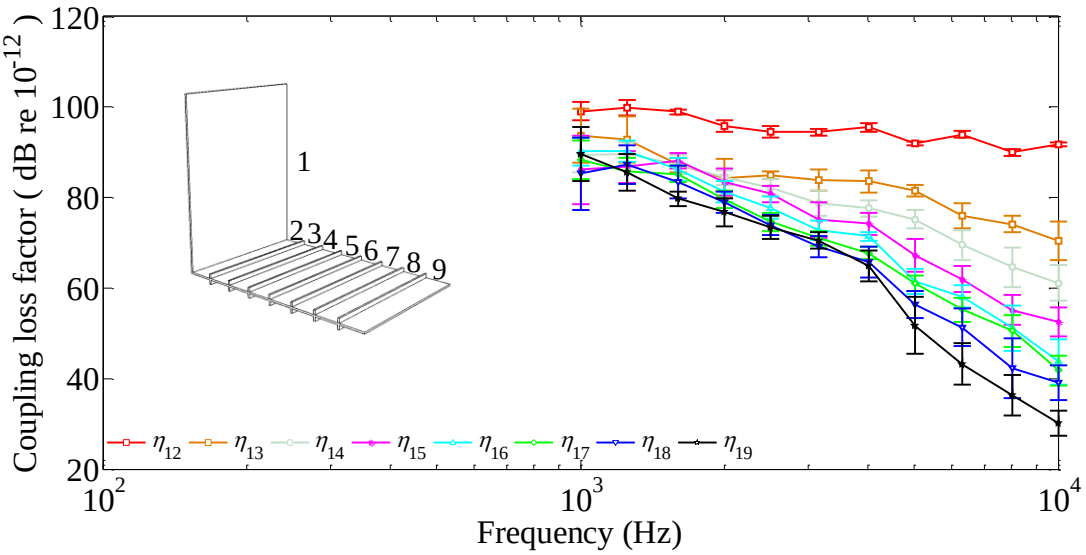

(b) Coupling loss factors between subsystem 2 and all other subsystems

TOB(Hz)	100	160	250	400	630	1k	1.6k	2.5k	4k	6.3k	10k
N_{B1} =	1.1	1.7	2.7	4.3	6.7	10.7	17.1	26.7	42.8	67.4	106.9
N_{bay}=						1.6	2.5	4.0	6.4	10.1	16.0
M_{av}=	0.1	0.2	0.3	0.4	0.7	1.1	1.7	2.6	4.2	6.6	10.5

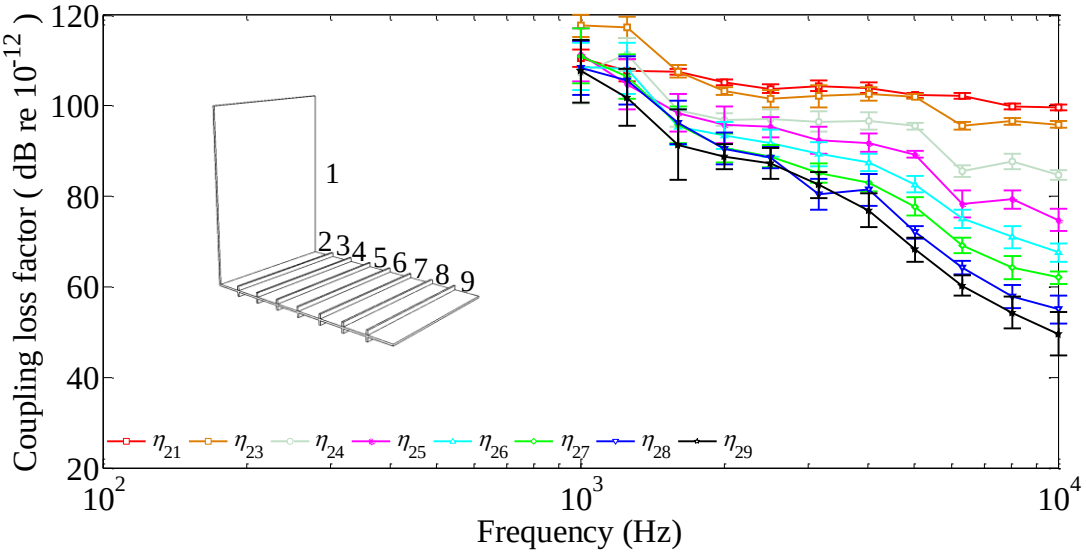

(Continued)

(c) Coupling loss factors between subsystem 5 and all other subsystems

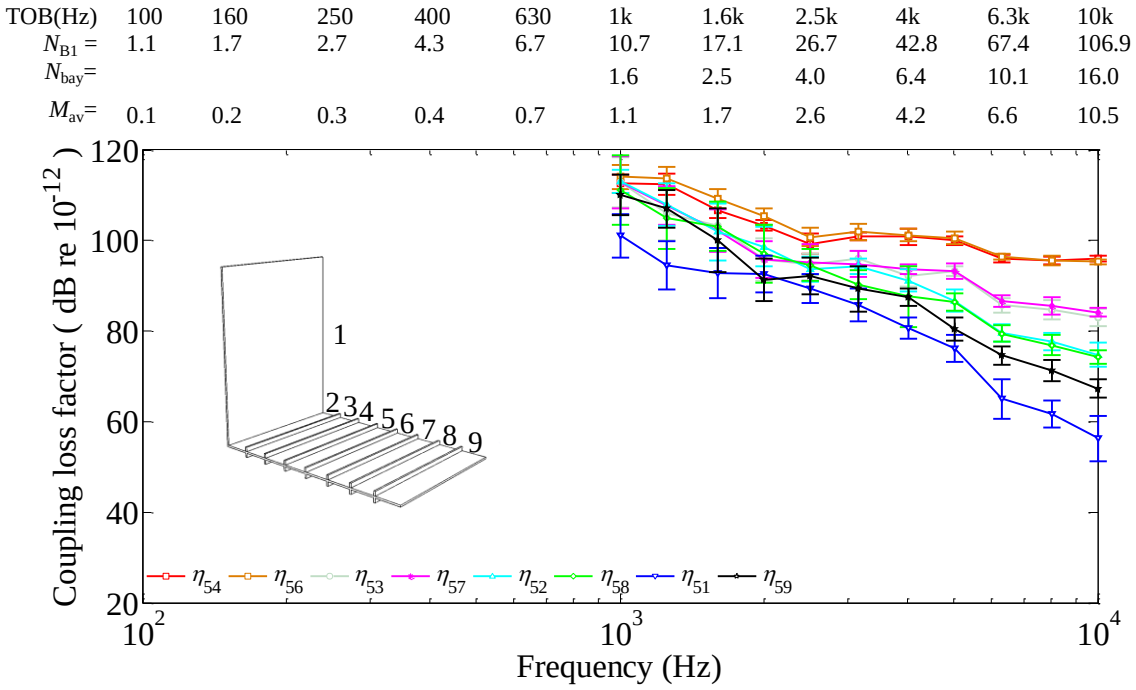

(d) Coupling loss factors between subsystem 9 and all other subsystems

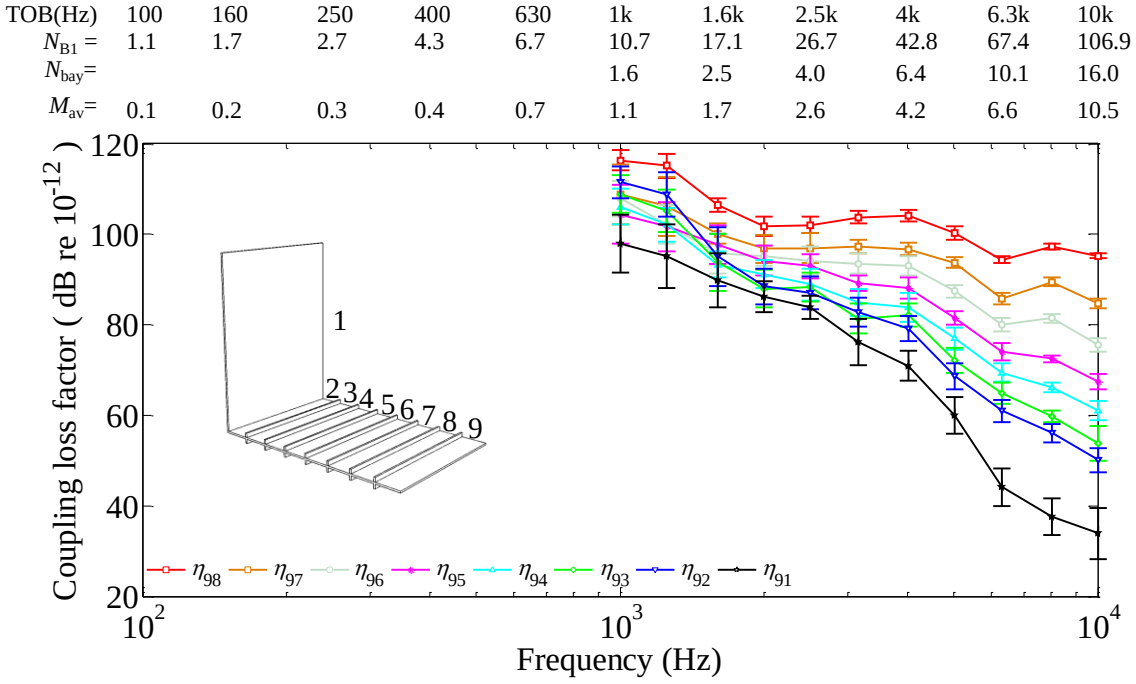

Figure 6.20 Coupling loss factors between physically unconnected subsystems for a nine-subsystem model determined using FEM with ESEA (10 sets of ROTR) compared with wave approach. Mode counts, geometric mean of modal overlap for subsystem 1 and any individual bay are shown on the upper *x*-axis.

TOB(Hz)	100	160	250	400	630	1k	1.6k	2.5k	4k	6.3k	10k
N_{B1} =	1.1	1.7	2.7	4.3	6.7	10.7	17.1	26.7	42.8	67.4	106.9
N_{bay}=						1.6	2.5	4.0	6.4	10.1	16.0
M_{av}=	0.1	0.2	0.3	0.4	0.7	1.1	1.7	2.6	4.2	6.6	10.5

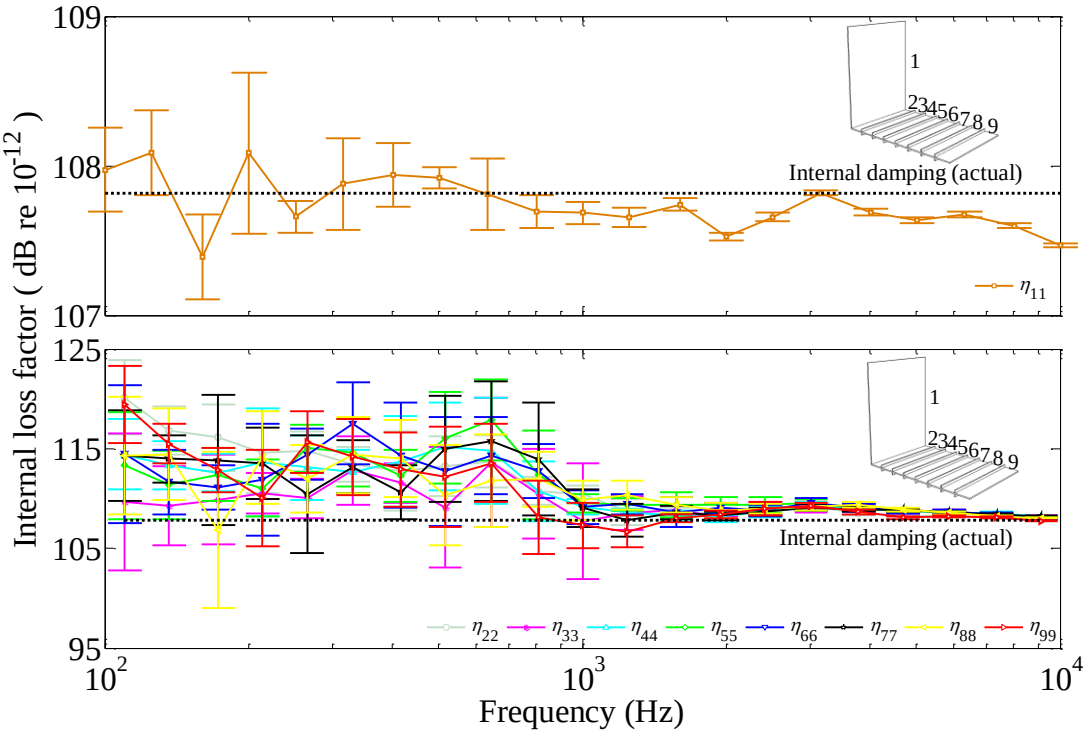

Figure 6.21 Internal loss factors for a nine-subsystem model determined using FEM and ESEA from 10 sets of ROTR compared with theoretical results using wave approach. The results are averaged from 10 sets of ROTR with 95% confidence intervals. Mode counts, geometric mean of modal overlap for subsystem 1 and any individual bay are shown on the upper *x*-axis.

Figure 6.22 shows the energy level difference calculated from ensemble average of FEM in comparison with the prediction using SEA where the coupling loss factors are obtained from FEM with ESEA (general matrix formulation). Good agreement is found between the two methods. It also shows that using these CLFs from FEM with ESEA gives a distinct improvement compared to using the CLFs from the wave approach. One may claim that this is a circular process as the CLFs are determined from FEM data using ESEA, subsequently incorporated in SEA and then compared with FEM. However, the process of using ESEA with more than two subsystems will only result in coupling loss factors if it is possible to treat the system as an SEA system. This is critical if an assessment is to be made of the importance of indirect coupling loss factors.

Use of the general ESEA matrix formation for the nine-subsystem model has identified the coupling between physically unconnected subsystems, which can be referred as indirect coupling.

The next step is to investigate how indirect coupling would affect the prediction of the energy responses in the nine-subsystem SEA model. Therefore, the alternative ESEA matrix formation equation (2.40) is used which allows the coupling loss factors between physically unconnected subsystems to be forced to zero. The CLFs between physically connected subsystems are determined from FEM with ESEA (alternative matrix formulation) and then used in an SEA model to calculate the subsystem energies.

Figure 6.23 shows the energy level differences from SEA using CLFs from the alternative ESEA matrix where CLFs between physically unconnected subsystems are forced to zero. Again, a large discrepancy is found compared with FEM results. Therefore, it is clear that even though the CLFs between physically unconnected subsystems are small compared with the CLFs for direct coupling, they play an important role in vibration transmission across the periodic plate and cannot be ignored. This non-resonant transmission phenomenon for coupling between physically unconnected subsystems is referred to as ‘tunnelling’. However, we cannot incorporate tunnelling into a standard SEA model without ESEA and this is of little use for predictive engineering design. For this reason the

next section implements Advanced SEA for the nine-subsystem model which incorporates tunnelling.

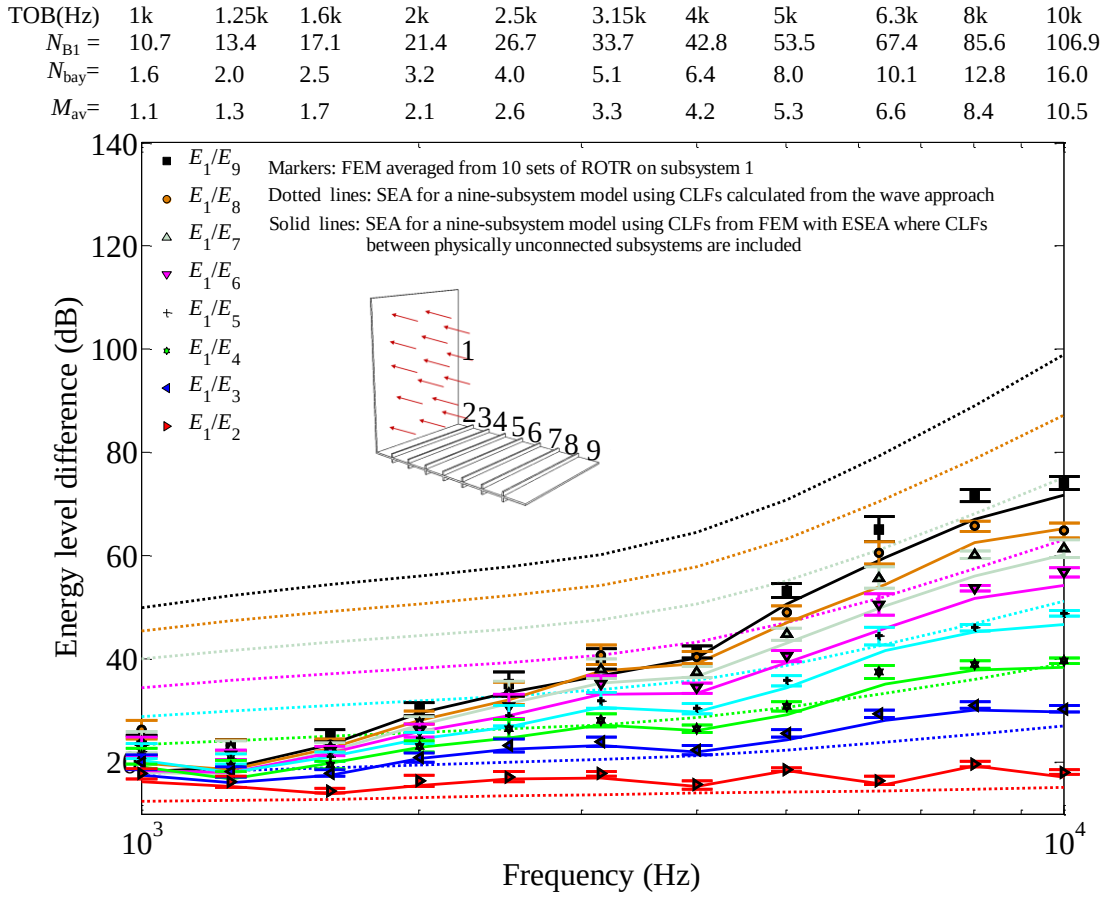

Figure 6.22 Energy level difference between the source subsystem (Plate 1) and bays on the periodic plate (Plate 2) from FEM averaged from 10 sets of ROTR compared with SEA for a nine-subsystem model using CLFs from wave approach and SEA using CLFs from alternative ESEA where CLFs between physically unconnected subsystems are forced to zero. Mode counts for subsystem 1 and the bays of the ribbed plate, geometric mean of modal overlap for subsystem 1 and any individual bay are shown on the upper *x*-axis.

TOB(Hz)	1k	1.25k	1.6k	2k	2.5k	3.15k	4k	5k	6.3k	8k	10k
N_{B1} =	10.7	13.4	17.1	21.4	26.7	33.7	42.8	53.5	67.4	85.6	106.9
N_{bay}=	1.6	2.0	2.5	3.2	4.0	5.1	6.4	8.0	10.1	12.8	16.0
M_{av}=	1.1	1.3	1.7	2.1	2.6	3.3	4.2	5.3	6.6	8.4	10.5

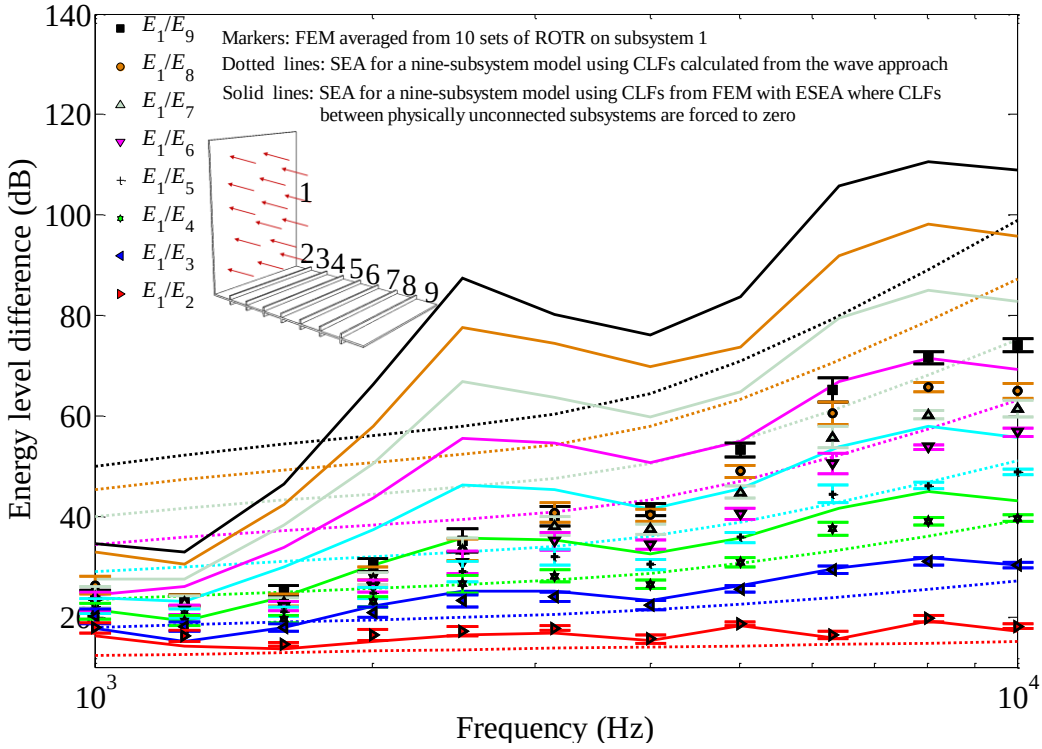

Figure 6.23 Energy level difference between the source subsystem (Plate 1) and bays on the periodic plate (Plate 2) from FEM averaged from 10 sets of ROTR compared with SEA for a nine-subsystem model using CLFs from wave approach and SEA using CLFs from alternative ESEA where CLFs between physically unconnected subsystems are forced to zero. Mode counts for subsystem 1 and the bays of the ribbed plate, geometric mean of modal overlap for subsystem 1 and any individual bay are shown on the upper *x*-axis.

6.6.3 ASEA model (nine-subsystems)

Advanced Statistical Energy Analysis (ASEA) described in section 2.3 is used here to incorporate tunnelling mechanisms between physically unconnected subsystems for the L-junction with ribbed plate that were identified in the previous section.

6.6.3.1 Computation times

As ASEA gives different results with different level number representing different number of power transfers for each subsystem, the calculations proceed until convergence occurs for all subsystems. The ASEA calculation has been carried out using Matlab on a PC with Intel Core 2 Duo CPU @ 3.00 GHz and 4 GB RAM from 100 Hz to 10 kHz.

As described in section 2.3, the ray tracing algorithm in ASEA involves intensive calculations and could be computationally expensive. However, for this specific model, the ray tracing algorithm can be significantly simplified. This is due to the fact that all junctions are parallel to each other and all subsystems are rectangular with the same thickness and material; thus no matter how far the ray is traced, the wave angle impinging upon the junction always stays the same and the wave propagation path for each subsystem is only related to the initial wave angle and the length of the subsystem in the direction perpendicular to the junction.

Table 6 shows the CPU times for running ASEA models with different level numbers. When narrow bands at 10 Hz intervals are used to calculate the one-third octave bands, the computation time significantly increases compared with using only the one-third octave band centre frequencies.

Figure 6.24 shows the difference between ASEA8 calculations using centre frequencies of the one-third octave bands and narrow bands at intervals of 10 Hz combined into one-third octave bands. In most frequency bands, the difference between the two calculations is less than 1 dB for all bays. However, for the last two bays (subsystems 7, 8 and 9) at 2.5 kHz and 4 kHz, the difference is up to 3 dB. It will be shown in later calculations that this error is negligible in the

context of the errors incurred with SEA. In this chapter, all ASEA calculations use narrow band calculations at 10 Hz intervals. However, to reduce computation times the results in chapters 7 and 8 use one-third octave band centre frequencies.

Table 6: ASEA computation time with different level numbers using 0.01° angular resolution for each one-third octave band centre frequency and narrow bands with 10 Hz resolution between 1 kHz and 10 kHz.

ASEA with different level number	CPU time	
	One-third octave bands	Narrow bands (10 Hz interval)
ASEA1	88s	1h 48m 44s
ASEA2	127s	2h 41m 20s
ASEA3	162s	3h 24m 57s
ASEA4	188s	4h 2m 12s
ASEA5	210s	4h 34m 17s
ASEA6	237s	4h 59m 20s
ASEA7	242s	5h 21m 30s
ASEA8	240s	5h 26m

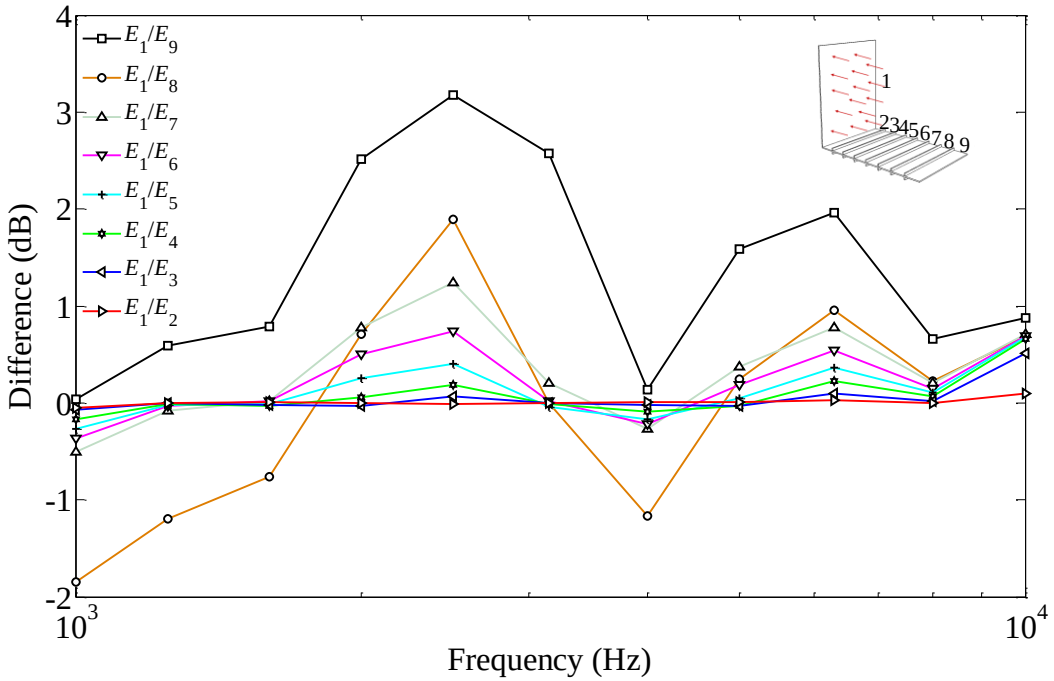

Figure 6.24 Difference between the ASEA8 energy level differences calculated using narrow band calculations at 10 Hz intervals minus the ASEA8 energy level difference calculations using only the one-third octave band centre frequencies.

6.6.3.2 Effect of nearfields

ASEA uses ray tracing theory to track the propagating waves and therefore it essentially assumes that the effect of any nearfield originating from one junction and arriving at the next junction is negligible. It is therefore necessary to investigate whether this assumption is reasonable. This is done by considering whether the mean-square velocity of the nearfield generated on a bay is negligible when it reaches the next rib compared with the mean-square velocity of the free propagating wave. Bending waves on the source plate would impinge upon the junction from all angles, but here we only consider the worst-case situation for normal incidence on the ribs. This can be calculated by converting equations (5.9) and (5.10) from displacement to velocity and creating a velocity level difference between the free propagating wave and the nearfield along the first bay as shown in Figure 6.25 and Figure 6.26 for the start and end frequencies to which ASEA applies which are 1 kHz and 10 kHz respectively. These calculations show that by the time that the nearfield has travelled the full length of the bay (150 mm) to the next rib, the velocity level difference is at least 50 dB. Therefore, the assumption made in ASEA to ignore the nearfield is reasonable.

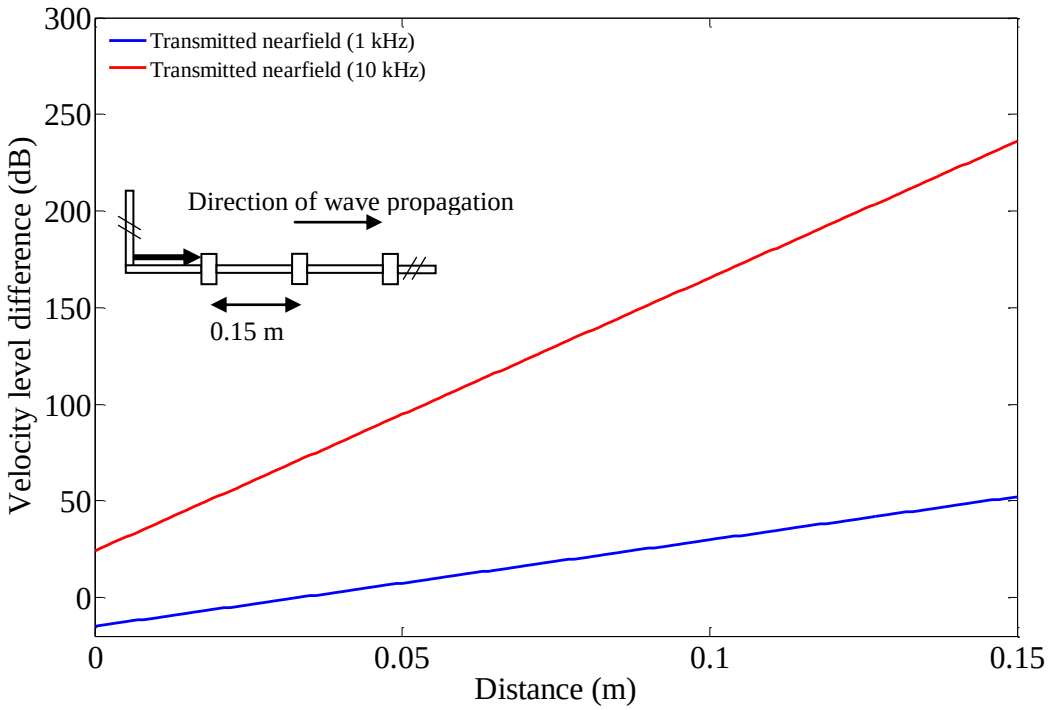

Figure 6.25 Velocity level difference between the free wave and the nearfield at various distances along the first bay near the junction on the periodic ribbed plate at 1 kHz and 10 kHz.

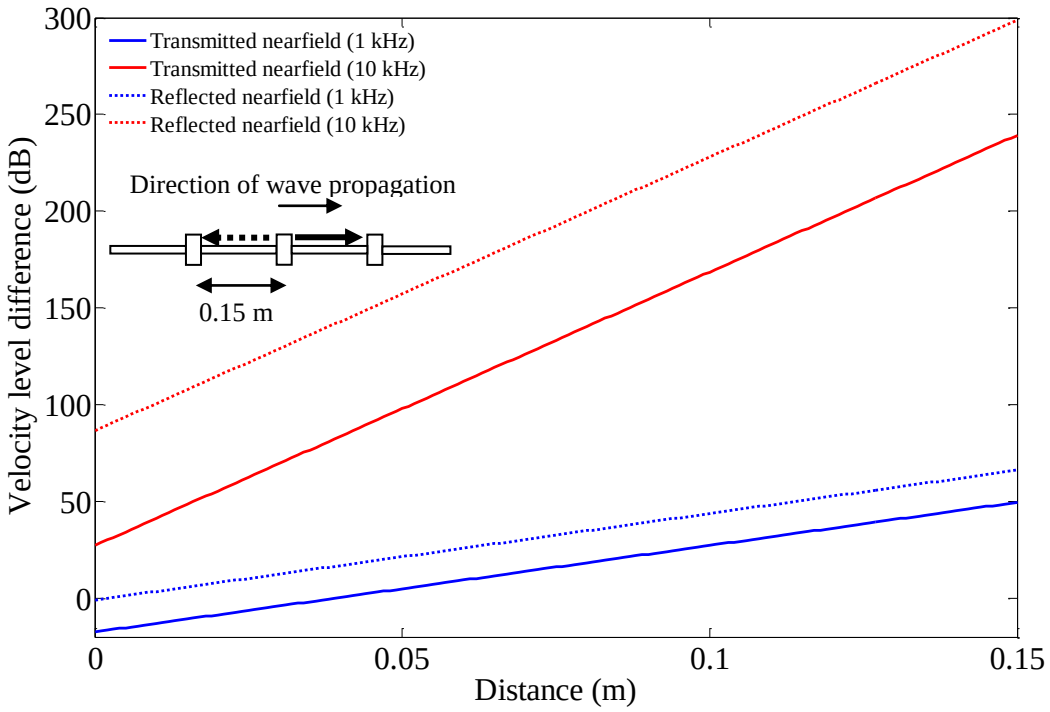

Figure 6.26 Velocity level difference between the free wave and the nearfield at various distances along a bay for waves leaving the rib junction on the periodic ribbed plate at 1 kHz and 10 kHz.

6.6.3.3 Comparison of FEM and ASEA

Figure 6.27 (a)-(h) show the energy level difference between the source subsystem (subsystem 1) and the bays of the periodic ribbed plate with different ASEA level number for comparison with FEM.

Comparison of FEM with SEA (ASEA0) indicates that the latter only gives a reasonable prediction for the three bays nearest the junction (subsystems 2, 3 and 4). For the bays that are further away, SEA significantly underestimates vibration transmission.

Convergence with ASEA occurs for the furthest bay away from the junction at ASEA8. For the first four subsystems that are closest to the source subsystem, all ASEA predictions are very close to FEM. For more distant subsystems, low levels of ASEA show discrepancies compared with FEM, whereas high levels of ASEA always gives good agreement with FEM. In some cases the ASEA prediction does not always improve with the increase of ASEA level number, for example, ASEA 6 for bay 6 gives slightly better results than ASEA8. However, this is purely coincidence because it is only after convergence that ASEA can be compared with FEM.

Figure 6.28 compares ASEA8 with FEM and SEA (ASEA0). For the last bay (subsystem 9), ASEA8 only gives a discrepancy up to 3 dB compared with FEM whereas SEA (ASEA0) has a discrepancy of more than 25 dB. It is also observed that in the frequency range between 1 kHz and 2.5 kHz, there is a discrepancy between ASEA8 and FEM especially for the furthest four bays away from the junction; however, it is seen that above 2.5 kHz when the mode count of the bay $N_{bay}>5$, closer agreement is achieved. Recalling that by using ray tracing ASEA does not account for phase effects, so it is possible that the discrepancies with FEM between 1 kHz and 2.5 kHz are due to coherence between the waves that impinge on the junctions.

Earlier in this chapter it was seen that at high frequencies (6.3 kHz to 10 kHz) there was a small error (up to a few decibels) which was attributed to the fact that the S4R element did not exactly replicate thin plate theory near and above the thin

plate limit (8 kHz one-third octave band). However, considering that the energy level differences for individual bays are at least 15 dB and at most 72 dB at these high frequencies it is clear that this FEM error is generally negligible.

For periodic ribbed plates the agreement between SEA and FEM for the first few bays nearest the junction indicates that tunnelling mechanisms are not significant. However for more distant bays, SEA significantly underestimates vibration transmission whereas ASEA is able to successfully incorporate tunnelling and provide a significantly more accurate prediction. As periodic ribbed plates in engineering structures typically have many bays, ASEA should therefore have practical applications.

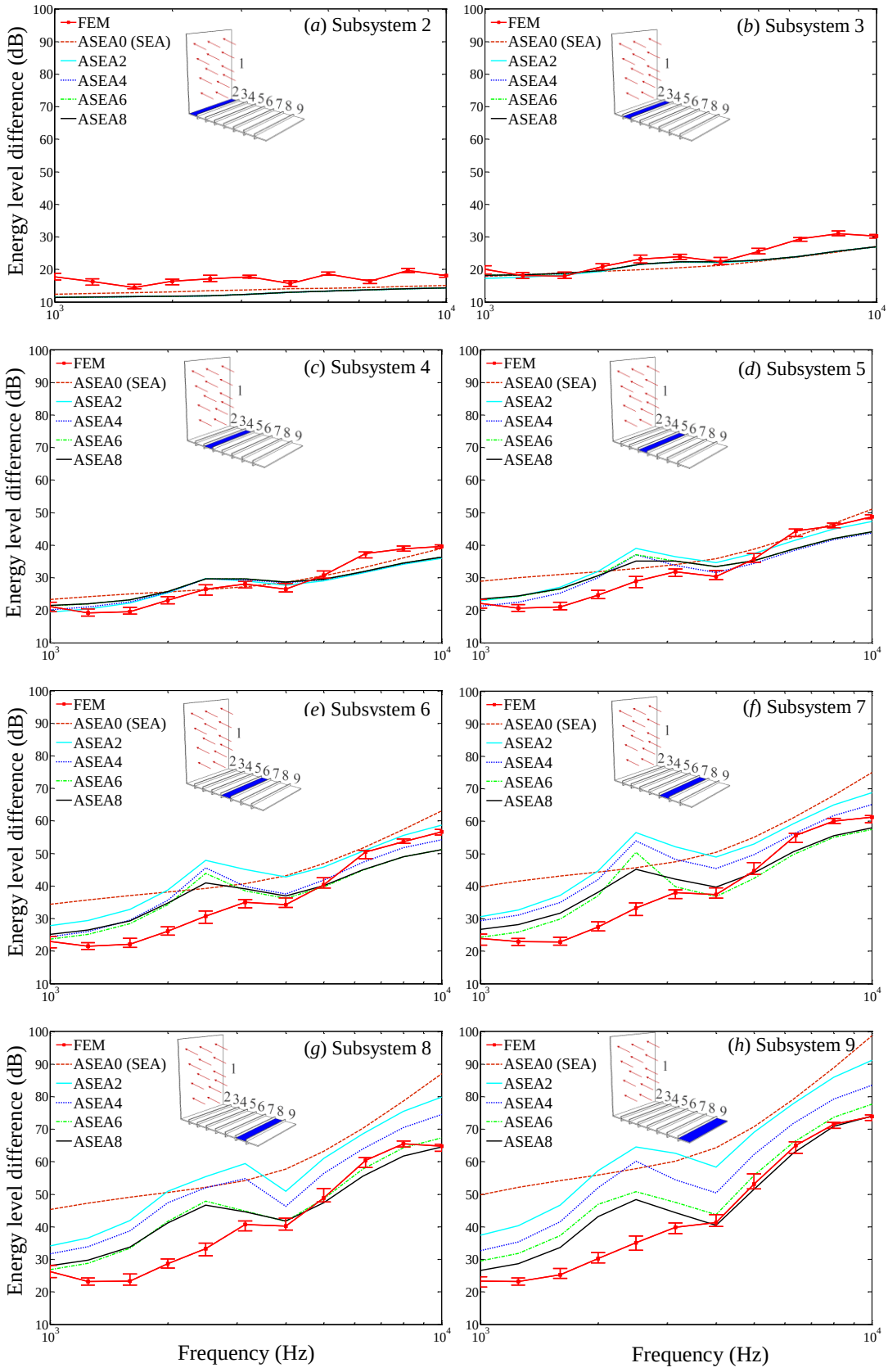

Figure 6.27 Energy level difference between the subsystem 1 (source subsystem) and the bays of the periodic plate predicted from ASEA with different level numbers compared with FEM.

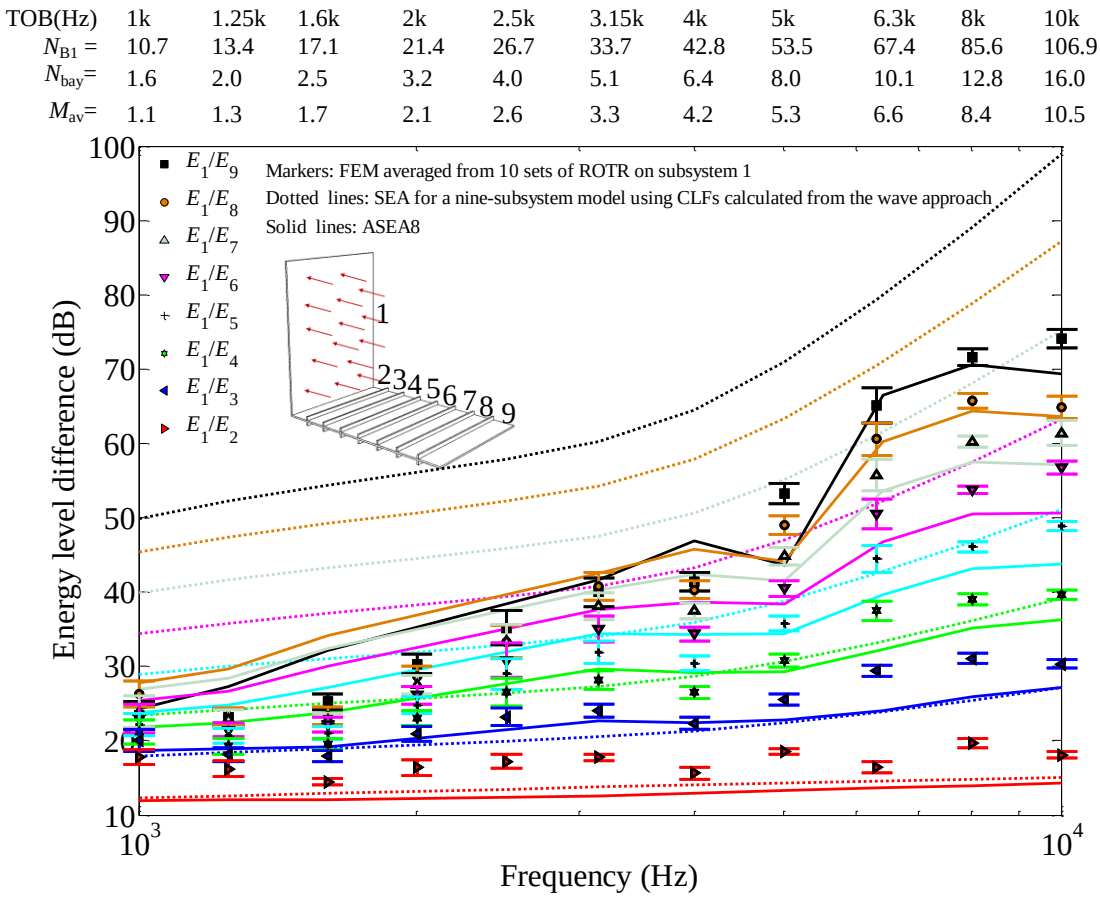

Figure 6.28 Energy level difference between the source subsystem (subsystem 1) and the bays of the periodic plate predicted from ASEA8 compared with FEM and SEA. Mode counts for subsystem 1 and the bays of the ribbed plate, geometric mean of modal overlap for subsystem 1 and any individual bay are shown on the upper *x*-axis.

6.7 Conclusions

This chapter compared FEM, SEA and ASEA for L-junctions formed by a homogeneous isotropic plate and a periodic ribbed plate.

In the low-frequency range below the fundamental local mode of the bay on the ribbed plate, the main conclusion is that the periodic ribbed plate can be modelled as a single subsystem either using the wave approach from Tso and Hansen, or using orthotropic plate theory with the wave approach from Bosmans and Vermeir.

In the high-frequency range above the fundamental local mode of the bay on the ribbed plate there is a significant decrease in energy along successive bays of the periodic ribbed plate; hence it is no longer appropriate to model this periodic plate as a single subsystem. For this reason it is not appropriate to use the wave approach from Tso and Hansen. Therefore SEA models were investigated that treat each bay as an individual subsystem using wave theory to model transmission across each rib. The good agreement between SEA and FEM for the first few bays near the junction indicates that tunnelling mechanisms are not significant. However, there is less agreement for more distant bays and SEA underestimates the response in the furthest bay by up to 25 dB. ESEA was then used to investigate this large discrepancy. ESEA indicates the existence of tunnelling between physically unconnected subsystems, which is not usually incorporated in SEA with plate subsystems. To incorporate this tunnelling mechanism, ASEA is used to track the energy flow across the plate system. In this chapter ASEA is shown to be able to successfully incorporate tunnelling and provide a significantly more accurate prediction for the furthest bay with discrepancies less than 3 dB. As periodic ribbed plates in engineering structures typically have many bays, ASEA should find practical applications.

The main conclusion is that ASEA is able to successfully incorporate tunnelling for plate junctions that incorporate periodic ribbed plates and that ASEA provides a significantly more accurate predictive approach to vibration transmission across periodic ribbed plates than SEA. The good agreement between ASEA and FEM above 2.5 kHz indicates that the ASEA assumptions that phase effects can be ignored and that the nearfield plays a negligible role are both appropriate for this particular L-junction.

Further investigations on the application of ASEA to other L-junctions incorporating a periodic ribbed plate and to systems with more than two plates are carried out in chapter 8.

7 Experimental verification

This chapter discusses the measurement of vibration transmission across L-junctions formed from isotropic, homogeneous plates and periodic ribbed plates. The results from these physical experiments are compared with numerical calculations using FEM, SEA and ASEA to confirm the validity of the theoretical models discussed in the previous chapters. The measurements used to determine material properties of the plates are also discussed.

Two L-junctions are assembled for the experiments and fixed into a specially designed frame to simulate simply-supported boundary conditions along the plate edges.

7.1 Measurement of material properties

This section discusses the experimental determination of material properties of the plate structures including Young's modulus, quasi-longitudinal phase speed and internal loss factor. These parameters are needed for the FEM, SEA and ASEA models.

7.1.1 Measurement of the bending stiffness

For homogeneous materials such as Perspex, Young's modulus can be experimentally determined using modal analysis by measuring the point input impedance as a function of frequency at the centre of a strip specimen made from the material. This method is described in ISO/PAS 16940:2004 for glass specimens [127]. The input impedance is given as the transfer function between the injected force at one point and the velocity. This impedance shows the property of resonances corresponding to the resonance frequencies of the beam. The resonance frequencies of the beam can be used to calculate the bending stiffness for a plate of the same material according to [19]:

$$B_{\mathrm{p},i} = \rho_s \left(\frac{\pi L^2 f_i}{2 C_i^2} \right)^2 \tag{7.1}$$

where L is the length of the beam, ρ_s is the surface density and f_i is the i^{th} resonant frequency. C_i is a parameter dependent on the number of resonance frequency. For free boundary conditions, it is given as: C_1=1.87510, C_2=4.69410, C_3=7.85476 and C_4=10.99554.

Equation (3.2) can then be used to calculate Young's modulus of the material and equation (3.24) can be used to calculate the quasi-longitudinal wave speed.

The measurement setup is shown in Figure 7.1, the centre of beam sample is mounted using beeswax onto a force transducer which is screwed onto the shaker. An accelerometer is mounted on top of the beam. When the accelerometer is fixed to the surface of the beam, the mass of it has effectively been added to the beam that can reduce the vibration level at the measurement point. The effect of the mass can be ignored when the accelerometer impedance is much less then the beam impedance as given by Hopkins [19]:

$$\omega m_{ac} \ll \left| Z_{dp} \right| \tag{7.2}$$

where m_{ac}, the mass of the accelerometer of B&K 4393, is 2.4 grams and the driving-point imdedance for inifine beam excited at the middle can be calculated from [34]:

$$Z_{dp} = 2\rho S c_B (1+i) \tag{7.3}$$

where S is the beam cross-section area. After evaluation for the beams used in the measurements and the equation (7.2) is satisfied so that the mass loading of the accelerometer won't affect the measurement results.

The beam samples made from Perspex^{TM} are chosen with different lengths (0.1 m, 0.2 m, 0.3 m, 0.5 m and 1 m) in order to measure a wider frequency range. The cross-section of the beam samples are all the same with 20 mm width and 10 mm thickness. The density of the material is measured as 1218 kg/m^3 and the Poisson's ratio is taken as 0.3 [128].

Figure 7.2 shows an example of the beam input impendence spectrum from the measurements. Each trough corresponds to a natural frequency that will be used in equation (7.1) to calculate the bending stiffness and other material properties. The measurement results from different lengths of beams are shown in Table 7. As a result, the estimated Young's modulus averaged over the results from all beam samples in the frequency range of 25 Hz to 5k Hz is 4.54×10^9 Pa with a standard deviation of 1.03×10^9 Pa. The corresponding quasi-longitudinal phase speed is calculated as 2045 m/s with a standard deviation of 230 m/s.

Table 7: Measurements of material properties using beam impedance method

Beam length (m)	Mode number	Resonant frequency (Hz)	Quasi-longitudinal wave speed (m/s)	Young's modulus (GPa)
0.2	1	423.4	2298.8	5.86
	2	2256	1954.5	4.23
	3	5670	1754.3	3.41
0.3	1	188	2296.6	5.85
	2	1025	1998.0	4.42
	3	2590	1803.1	3.60
	4	4830	1715.9	3.26
0.5	1	69	2341.4	6.08
	2	384	2079.2	4.79
	3	981	1897.1	3.99
	4	1849	1824.7	3.69
1	1	17.5	2375.4	6.25
	2	97	2100.9	4.89
	3	246.5	2306.7	4.03
	4	464	1931.6	3.72
Average			2045	4.54
Standard deviation			230	1.03

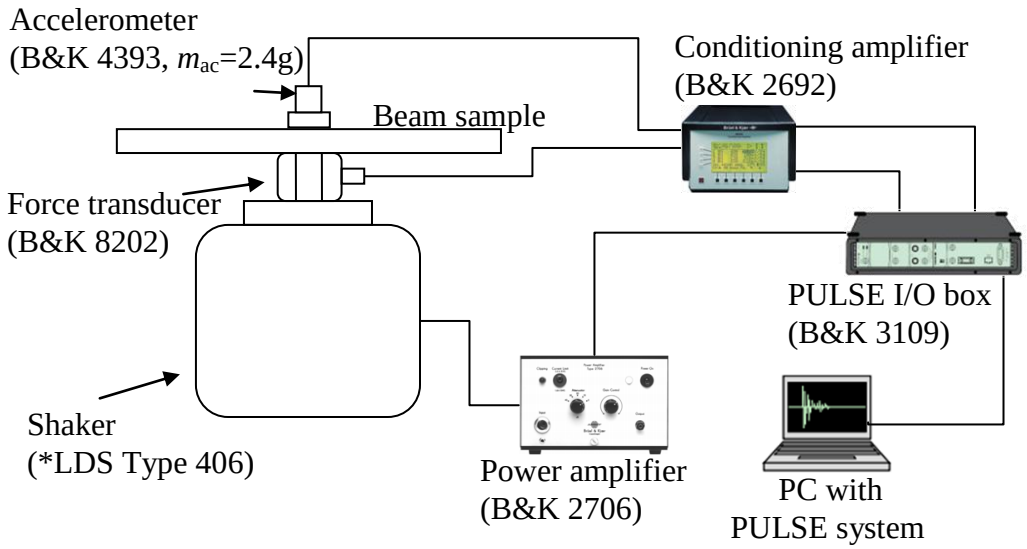

Figure 7.1 Experiment setup for measuring the impedance of a beam sample.

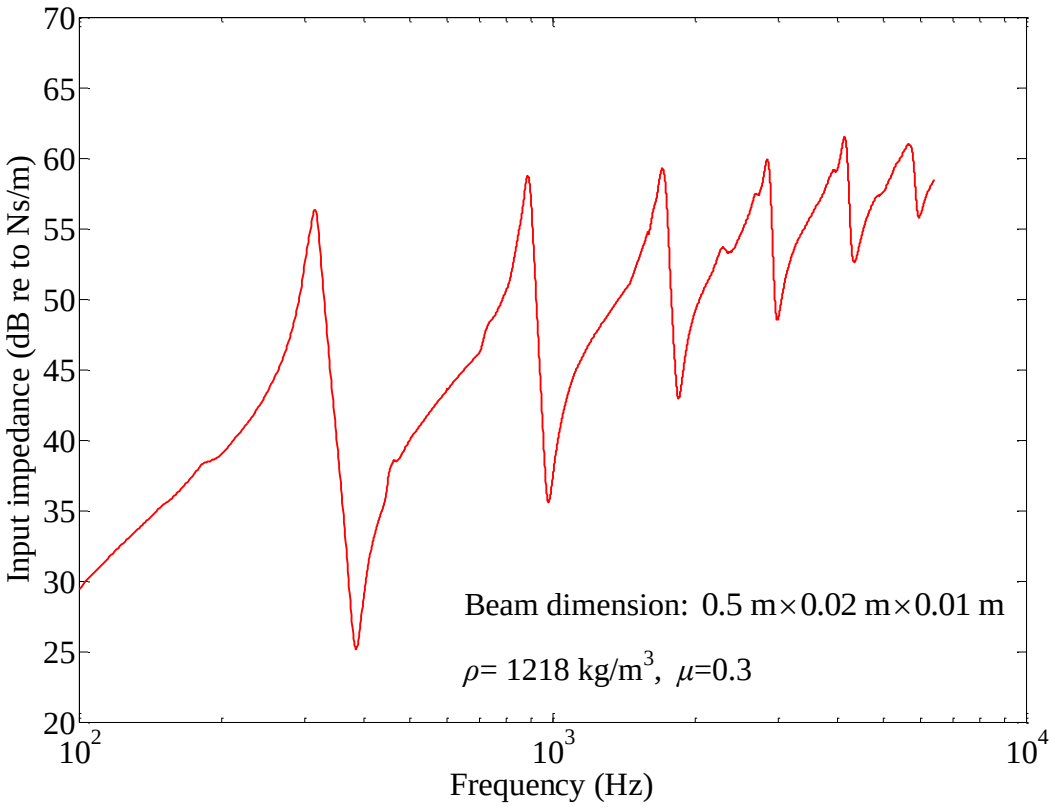

Figure 7.2 Example of input impedance spectrum from a measurement with troughs corresponding to the resonant frequencies.

7.1.2 Measurement of the internal loss factor

The internal loss factor can be can be calculated from the results of the measurement procedure presented in section 7.1.1 by determining the half-power bandwidth (3 dB reduction) at each resonant peak as using:

$$\eta_{\text{int},\,i} = \frac{\Delta f_{3\text{dB},i}}{f_i} \tag{7.4}$$

where $\Delta f_{3\text{dB},i}$ is the half-power bandwidth for the i^{th} resonance frequency, f_i.

The results of the individual measurements for different length of beams are shown in Table 8. The average internal loss factor is 0.06 with a standard derivation of 0.01. This method allows the determination of internal loss factor over a wide frequency range. However, only the internal loss factors at the resonance frequencies can be calculated and if the internal loss factor is highly dependent on the frequency, the use of the input impedance method may be limited. This method is based on modal analysis where the internal loss factors are dependent on the mode shapes of the structure. Therefore, it can result in significant differences between the measured internal loss factors of beams and plates [19].

This internal loss factor will be compared with the measured total loss factor on each plate of the L-junction. This measurement procedure using structural reverberation time is discussed in the next section.

Table 8: Measurements of Internal loss factor using beam impendence method

Beam length (m)	Mode number	Resonant frequency (Hz)	Internal loss factor
0.2	1	423.4	0.068
	2	2256	0.042
	3	5670	0.076
0.3	1	188	0.072
	2	1025	0.040
	3	2590	0.052
	4	4830	0.089
0.5	1	69	0.072
	2	384	0.057
	3	981	0.051
	4	1849	0.052
1	1	17.5	0.057
	2	97	0.042
	3	246.5	0.069
	4	464	0.070
Average			0.06
Standard deviation			0.01

7.2 Measurement of structural reverberation time

7.2.1 Introduction

In section 2.2.5, the internal loss factor and total loss factor in SEA were introduced and can be calculated from structural reverberation time. When a subsystem is isolated from the whole system (i.e. suspended by bungee cords or supported by soft elastic layers), the measurement of the structural reverberation time can be used to calculate the internal loss factor of this subsystem using equation (2.21). When the reverberation time of a subsystem is measured *in situ*, the results can be used to assess the total loss factor of this subsystem as in equation (2.22). This section therefore discusses the measurement of structural reverberation time for bending waves on plates to determine the total loss factors.

The measurement of structural reverberation time uses the integrated impulse response method described in ISO 3382 [129] for determining the reverberation

time in space. This method was introduced by Schroeder [130] to calculate the vibrational energy decay using reverse-time integration of an impulse response. A Maximum Length Sequence (MLS) is generated internally in B&K DIRAC system as the impulse signal. This is a periodic, pseudo-random white noise signal, having the desirable property that its frequency spectrum over one period is as flat as the spectrum of an ideal impulse [131]. It is then fed into a shaker via a power amplifier to excite the plate. The impulse response is obtained by cross-correlating the excitation signal with the measured response signal which is measured using an accelerometer. After one-third octave band filtering, the impulse response is integrated in the time domain and results in a single curve representing the decay of vibration levels with time. As a result, the reverberation time can be estimated by apply a linear curve fitting to the most linear and clear part of the decay curve.

In order to determine the structural reverberation time in octave-band or one-third octave bands, the impulse response is usually sent through some filters before the decay time is calculated. The effect of the filters on the decay time is thoroughly discussed by Jacobsen [132]. As a filter also has its own impulse response, the decay time of the filter must be shorter than the actual structural decay time in order that it can be measured with a good accuracy [19]. The effect of the filter is dependent upon the filter bandwidth, B, and the actual reverberation time, T. It is suggested by Jacobsen [132] that the product of these two, BT, can be used to assess the effect of the filter on the decay curve. ISO 3382 [129] requires that $BT>8$ in order to ensure that the measured decay curve is unaffected by the impulse response filter. As the bandwidth of a filter varies with band central frequency, f_c, for one-third octave bands, the bandwidth $B=0.236f_c$. The actual reverberation time T is obtained from measurement.

7.2.2 Measurement set-up

The measurement set-up is shown as in Figure 7.3. An external sound card is used and the excitation MLS signal is obtained from B&K DIRAC system through the sound card output.

Three excitation positions and for each excitation, four accelerometer positions are chosen for measurements. The accelerometers need to be positioned in the

reverberant field of the plate. The reverberant distance, r_{rd}, from the excitation point at which the energy density in the direct field is equal that in the reverberant field can be approximately calculated using [19] for plates:

$$r_{\mathrm{rd}} \approx \frac{\omega \eta_i S}{4\pi c_{\mathrm{B,p}}} \tag{7.5}$$

where η_i is the total loss factor of the plate.

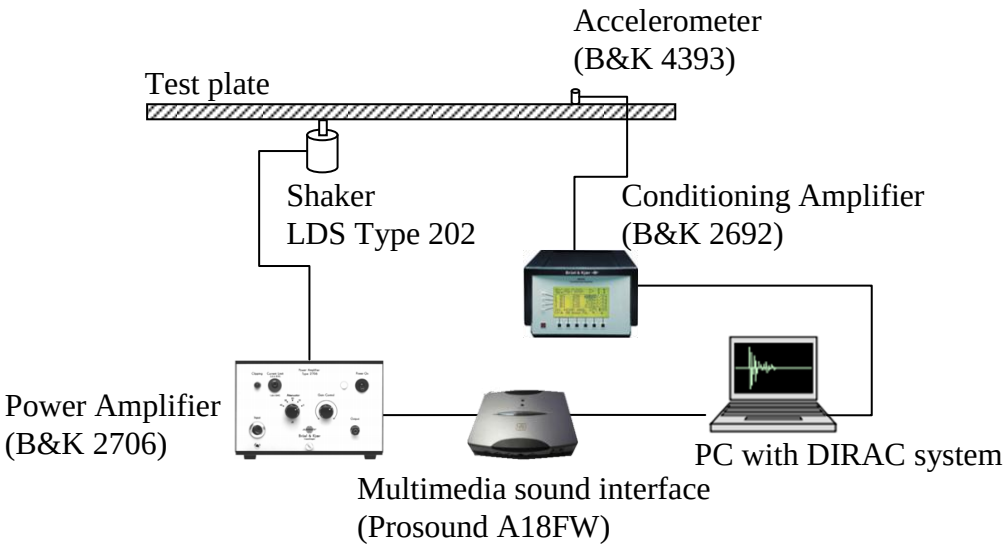

Figure 7.3 Experiment setup for measuring the reverberation time

7.2.3 Evaluation of the decay curve

Figure 7.4 shows an example of the decay curve measured *in situ* on one of the plates of the L-junction with two isotropic, homogeneous plates. As one plate is coupled to another with different thickness and slightly different material properties, energy measured is returning from the excitation but also from the other plate. Therefore, the corresponding decay curve is not a straight line, but instead, with many slopes. The evaluation normally starts from 5 dB below the

initial vibration level to minimise the curvature introduced by the detector [19]. Using different range of the curves for the linear curve fitting will result in different reverberation time (as shown in Figure 7.4, the difference between T_{10} and T_{20}). With the evaluation range increasing, the decay time increases due to the effect of the returning energy coming from the other coupled plate. Therefore, in order to measure the total loss factor of the plate, short evaluation range such as T_5 and T_{10} should be used before the energy comes back from the other plate.

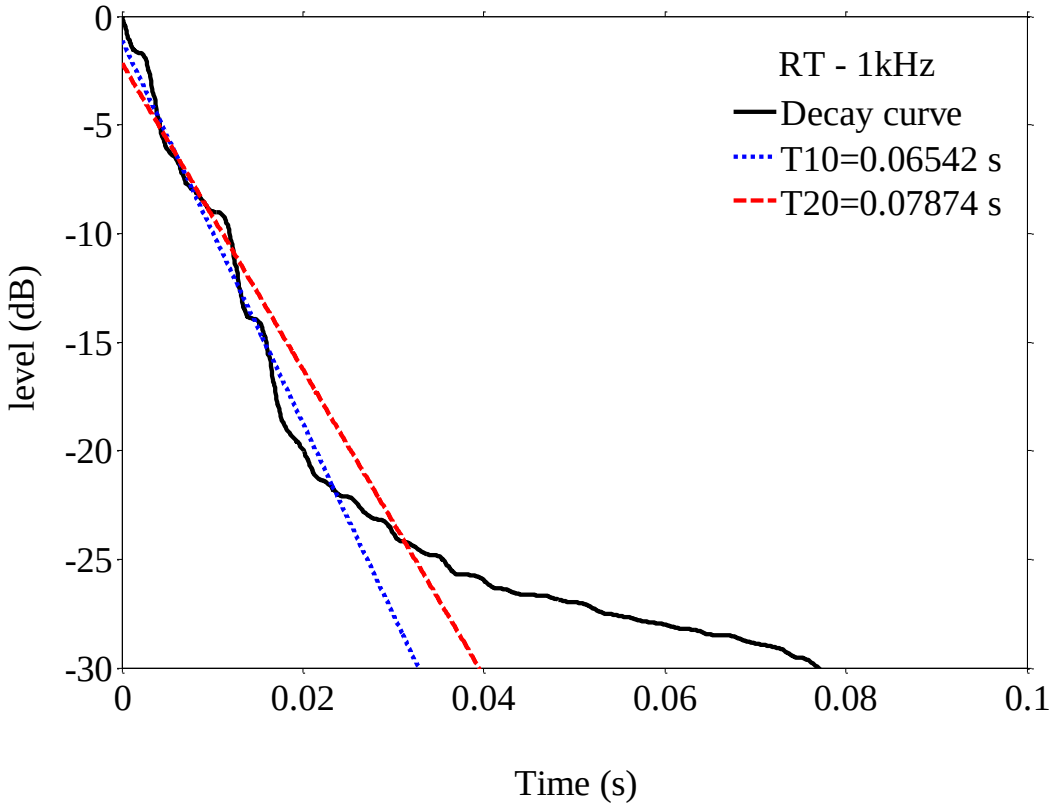

Figure 7.4 Decay curve measured *in situ* on one plate of the L-junction with two isotropic, homogeneous plates, and the evaluation reverberation time using different range of the decay curve of T_{10} and T_{20}

7.3 Measurement of vibration transmission across L-junctions of simply-supported plates

7.3.1 Introduction

Many engineering structures have complex geometries and the coupling between structures can be non-rigid, dissipative and non-uniform. In some situations, it is difficult or even impossible to theoretically calculate the coupling loss factors. FEM is one solution, but as discussed in Chapters 2 and 6, it comes with certain limitations and uncertainties. Therefore, another possibility is to measure the coupling loss factor through physical experiments.

In the theoretical analysis of the structure, simply-supported boundary conditions are often considered which allows free rotation of the edge about its centre tangent line while the displacements in all three dimensions are restricted. This is a mathematically idealized boundary condition and difficult to arrange in a laboratory. Works such as in [133, 134] have addressed the experimental methods to support structures in a way close to the idealized simply-supported boundary conditions.

It is useful to have a reliable experimental test rig to investigate the structure behaviour under controlled boundary conditions and also provide verification for the theoretical models. In this section, the design of the experimental frame to support the L-junctions is presented to allow a close approximation of the simply-supported boundary conditions and the frame was tested by the measurement of the driving-point mobilities for both the isotropic, homogeneous plate and the ribbed plate. Then the design for the experiment frame for the L-junction is illustrated and the measurement step-up and procedures are discussed.

Due to the material limitations, the plate material properties and dimensions used in the actual experiments differ from the analytical models discussed in Chapter 6. The plates available for experimental test make two L-junctions: one with two isotropic, homogeneous plates and the other is comprised of an isotropic plate and a periodic ribbed plate. Young's modulus, internal damping, and quasi-longitudinal wave speed are measured using the methods discussed in section 7.1. The dimensions and material properties are summarized in Table 9. Accordingly,

theoretical and numerical models based on these properties are built for comparison with the experimental results.

Note that the thin plate limit for plates 1 and 2 for Model 1 are 9038 Hz and 10456 Hz respectively, whereas for Model 2 they are both 10456 Hz.

Table 9: Plate dimensions and material properties used in the experiments

Model	Plate 1	Plate 2	Material properties for the plates
1	L_x=1.0 m L_y=0.8 m h_p = 0.010 m	L_x=1.2 m L_y=0.8 m h_p = 0.010 m	ρ_1=1180 kg/m^3 $c_{L,1}$=2350 m/s ρ_2=1218 kg/m^3 $c_{L,2}$=2045 m/s μ_1= μ_2=0.3
2	L_x=1.0 m L_y=0.8 m h_p = 0.010 m	L_x=1.2 m L_y=0.8 m h_p = 0.01 m h_b=0.025 m b_b=0.03 m l = 0.15 m	ρ_1=ρ_2=1218 kg/m^3 $c_{L,1}$=$c_{L,2}$=2045 m/s μ_1= μ_2=0.3

7.3.2 Design of the experimental frame to provide simply-supported boundary conditions

Most theoretical methods to analyze structure-borne sound transmission through coupled structures are built up based on idealized boundary conditions in place of actual boundary conditions in real world. Although the mathematical idealization of the boundary conditions can greatly simplify the theoretical modelling, the justification of it in real practice can be largely dependent upon the test structures and their corresponding boundary conditions. Among all the idealized boundary conditions, it is known that simply-supported boundary condition is most difficult to achieve in the laboratory as it requires a continuous support of the edges of the structure that the edges are free to rotate but no lateral displacement in all three directions. Some works have been reported to try to support the structure in a way that is close to the idealized boundary conditions. M ńguez [135] presented a design to create approximately simply-supported boundary conditions in the laboratory for compression test of panels. As it is sketched in Figure 7.5, the unloaded edges of plate were supported by attaching high strength steel wires into a set of machined slots along the edges of the plate using a brass collar with s set of screw and a piece of structural-steel angel section. The ends of the steel wires were fixed to a metal frame. Wilson [136] suggested two different methods to stimulate the simply-supported boundary condition. Figure 7.6 uses a set of metal pins to support the plate edge. The pins are fixed to a timber baffle by using grooved aluminium strips. Figure 7.10 uses a 'z' shaped thick metal strip as a rotational spring to support the edges of the plate. Unlike the other methods reviewed in this section where the plates are supported at discrete distances, this method could provide continuous supports, which seems closer to the idealized boundaries. Lacour *et al*. [137], Putra and Thompson [138] and Maillard and Fuller [139] all followed a similar method by using metal strips to support the plates.

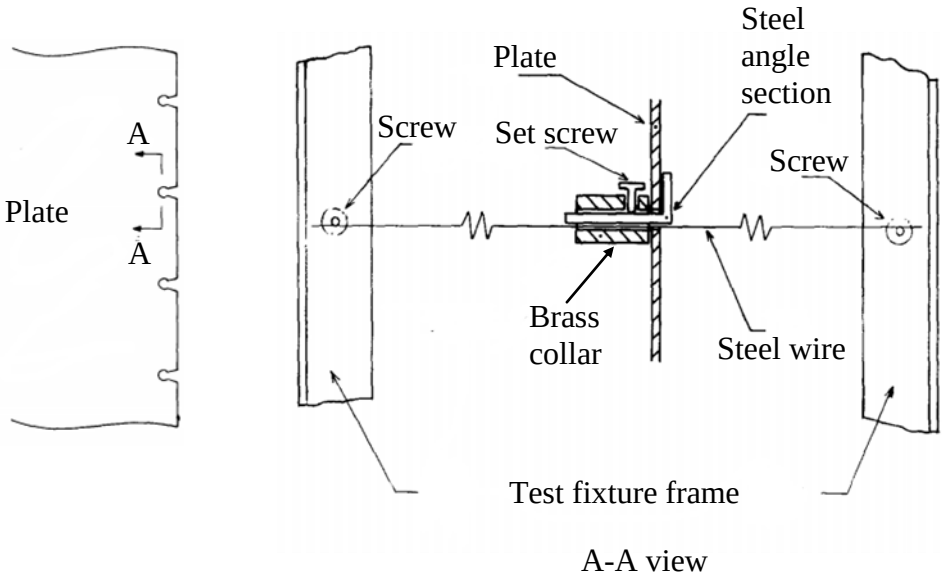

Figure 7.5 Design for simply-supported boundary conditions in laboratory by M ńguez [135] using steel wires as supports.

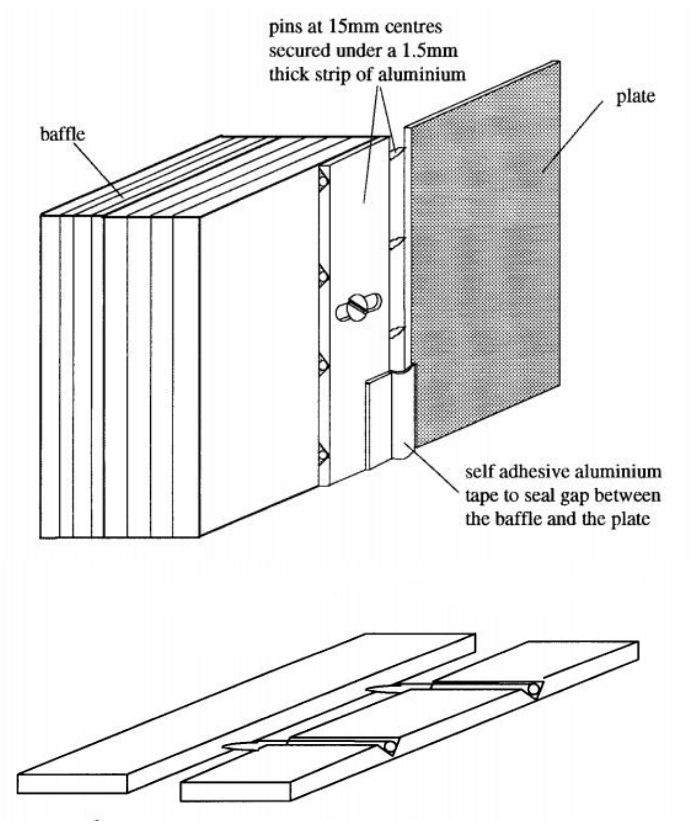

Figure 7.6 Design 1 for simply-supported boundary conditions in laboratory from Wilson [136] using metal pins as supports

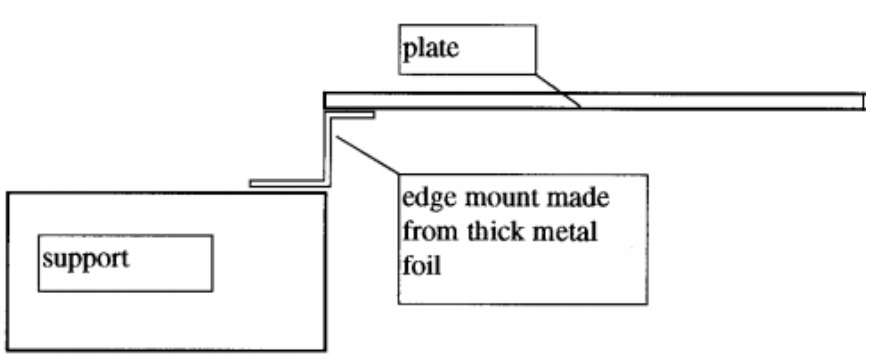

Figure 7.7 Design 2 for simply-supported boundary conditions in laboratory from Wilson [136] using rotational spring with a 'z' shaped metal strip

In this thesis, the design of this frame allows tests both on the single rectangular plates and the L-junctions of two rectangular plates. The simply-supported boundary conditions are achieved by supporting the edges of plates with a set of pins distributing in a periodic distance along the edges.

As shown in Figure 7.8, the sharp ends of the pins support the plate edges along the centre line. The supporting pins are fitted into a heavy steel frame (dimensions see in the figure) to minimise flanking transmission through pins and the frame into the plate. The metal frame is isolated from the ground using resilient layers.

The ideal simply-supported boundary is a continuous condition along the boundary. In practice, it is only possible to use the pins at discrete distances. However, if the distance between any two adjacent pins is sufficiently small such that the bending wavelength is much larger than the pin spacing, it should give a close approximation to the continuous condition. In the design of the frame, the distance between two pins next to each other is chosen to be 20 mm which is much less than the bending wavelength of 60 mm at 10 kHz for a Perspex plate with 10 mm thickness.

The frame for an individual plate is shown in Figure 7.9. There are 196 pins to support the four edges of the plate. The installation of plate starts by adjusting the free plate to the right height (pins pointing at the centre line of the plate edge) and horizontal position using large blocks and smaller spacers. The pins at the centre

and two ends of each edge are first fixed using a screw driver to the point that the sharp end of the pin is tightly pointing against the edge of the plate at the central line of the edge. The rest of the pins are fixed from centre to the ends. The distance between the frame and the plate edge is designed to be 5 mm, and it is important to keep this distance consistence. As the pins will introduce a compression force to the plate, and the Perspex plate has a relatively low bending stiffness, too much compression may results in a large lateral displacement at the middle of the plate.

The frame for L-junction comprises of two U-shaped frames (see Figure 7.10 (a) using the same design of pins for the individual plate frame. The two frames are not connected with each other (as shown in Figure 7.10 (b)) in order to prevent flanking transmission between the two plates through the coupling of the frame. All the edges of the L-junction are simply-supported except the coupling junction which has no supports.

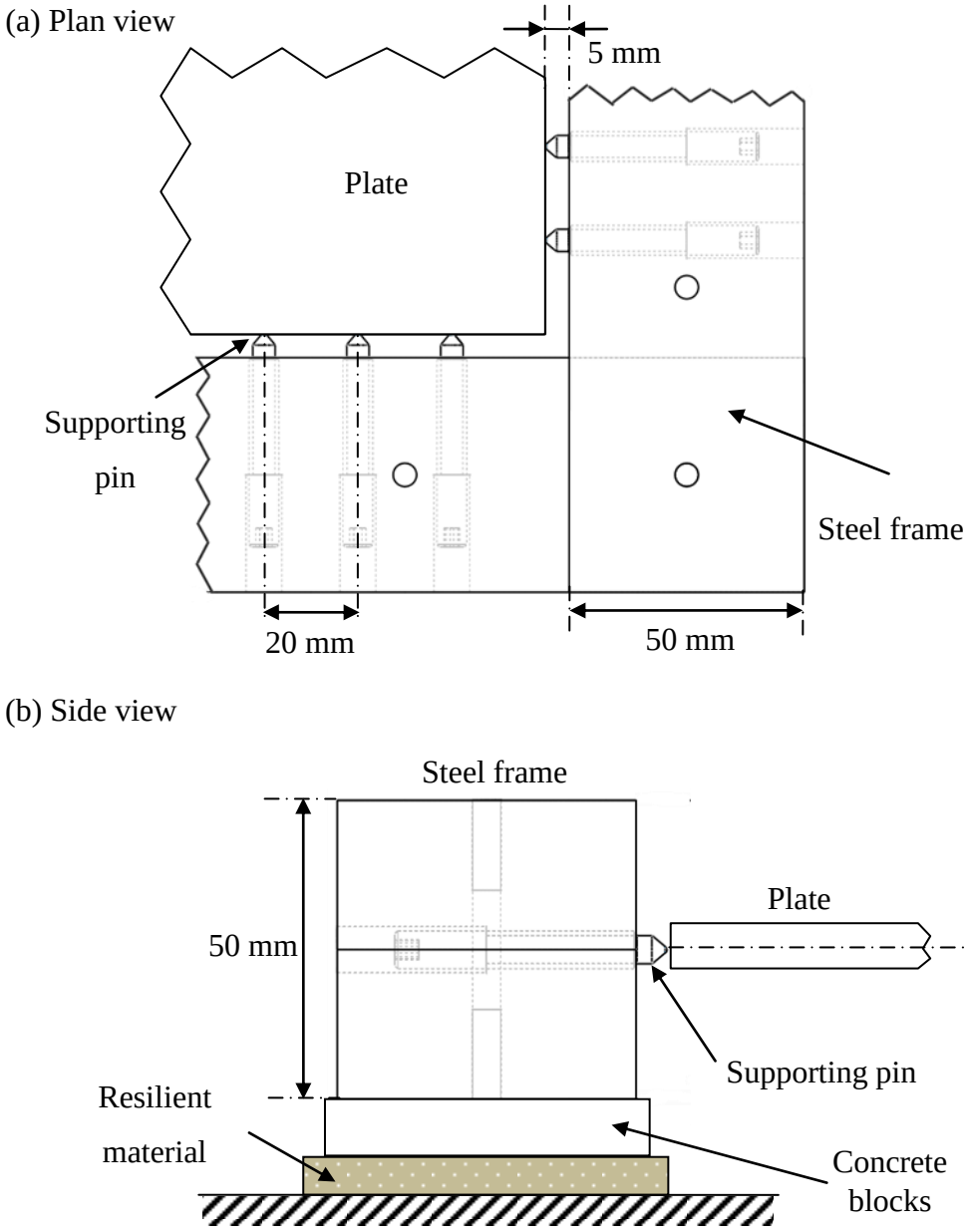

Figure 7.8 Supporting pins and steel frame

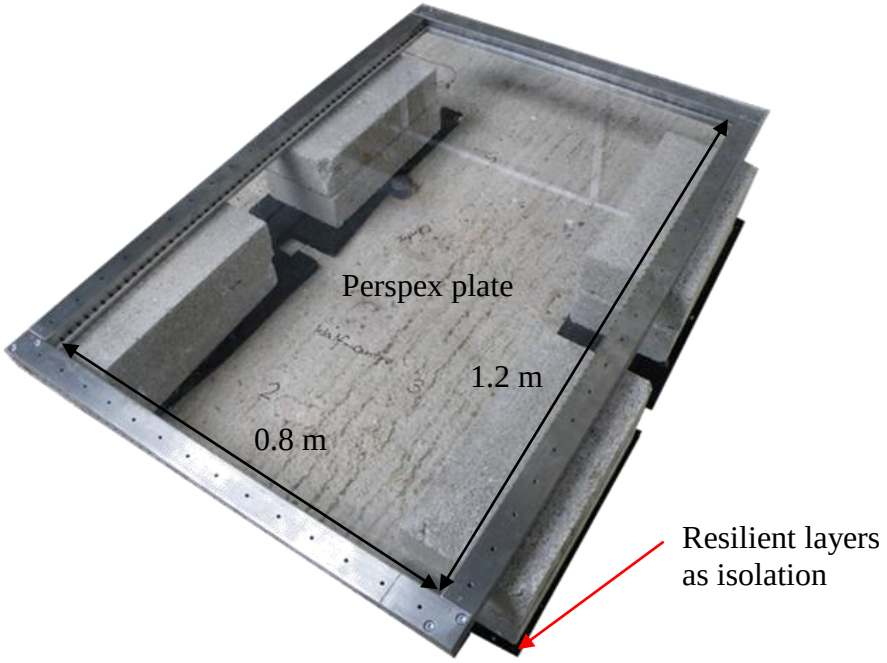

Figure 7.9 Frame used for measurements on an individual rectangular plate

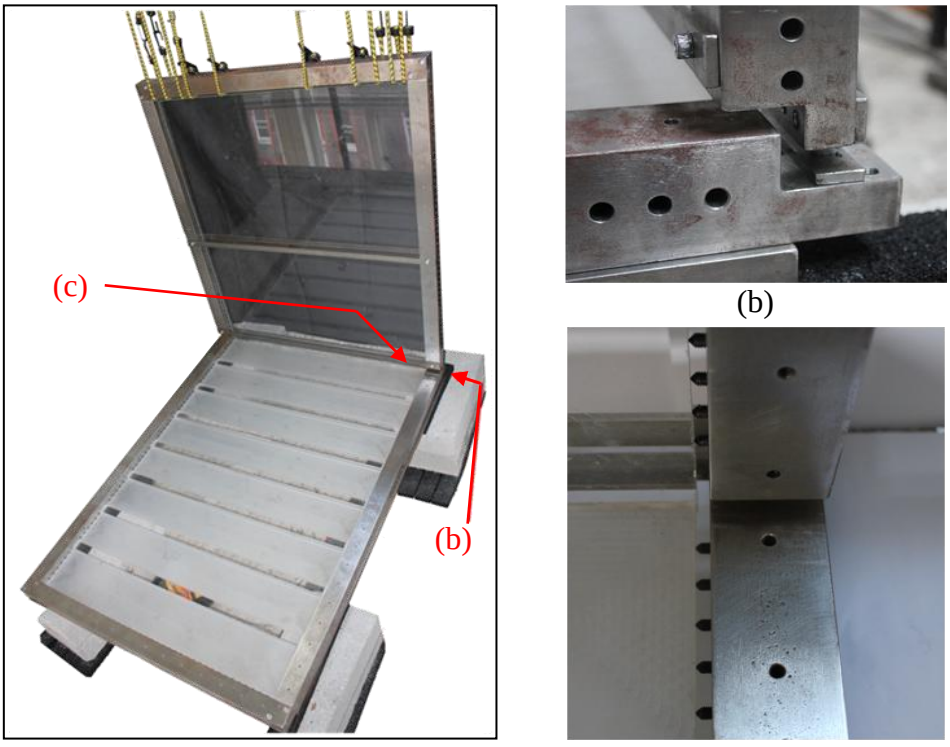

Figure 7.10 Frame for the two rectangular plates. (a) Overview of the frame design (b) The individual frames for each plate are not connected with each other to prevent flanking transmission (c) View of the supporting pins on each plate.

7.3.3 Experimental validation of the simply-supported boundary conditions

In order to test validity of using the pins to approximate simply-supported boundary conditions, the frame for single plate is used to measure the driving-point mobility on both the isotropic, homogeneous plate (plate 2 of model 1 in Table 9) and the periodic ribbed plate (plate 2 of model 2 in Table 9).

The driving-point mobility of a finite rectangular isotropic plate with simply-supported boundaries can be calculated using Rayleigh-Ritz method [38] described in section 2.2.4. The driving-point mobility of the periodic ribbed plate can also be estimated using the similar method; however discrepancies are expected due to the error in the calculation of natural modes for the ribbed plate as discussed in section 3.3.4. For this reason, FEM is also used for ribbed plate to calculate the mobilities for the periodic ribbed plate. The theoretical results are used as comparison with the measurement to validate the effectiveness of the pins.

Figure 7.11 shows the driving-point mobility at two positions of an isotropic, homogeneous plate. The measurement shows excellent agreement with the theoretical results at both positions by capturing the majority of peaks in the mobility up to 3 kHz, although there is a 10 Hz shift for the fundamental mode. Above 2 kHz, the measured results tend towards infinite plate theory.

Figure 7.12 shows the driving-point mobility measured at both the ribs and the bays. The measured driving-point mobilities both at the rib and the bay follow the same trend as the theoretical prediction, though the peaks from the measured mobility cannot be predicted by the theoretical method. The discrepancy is caused by the simplification of the Rayleigh-Ritz method where the ribbed plate is treated as a plate of uniform thickness with orthotropic properties. Comparing with measurement with FEM results, better agreement is found but this still shows a shift in resonance peaks. The discrepancies are caused by using the shell element to model the ribs. Figure 7.13 averages the results into one-third octave bands. It is shown that the measurement has a close agreement with FEM while the theoretical results overestimate the mobilities at high frequencies above 4 kHz.

The results indicate that simply-supported boundary conditions can be achieved with sufficient accuracy in the laboratory using metal pins along the edges.

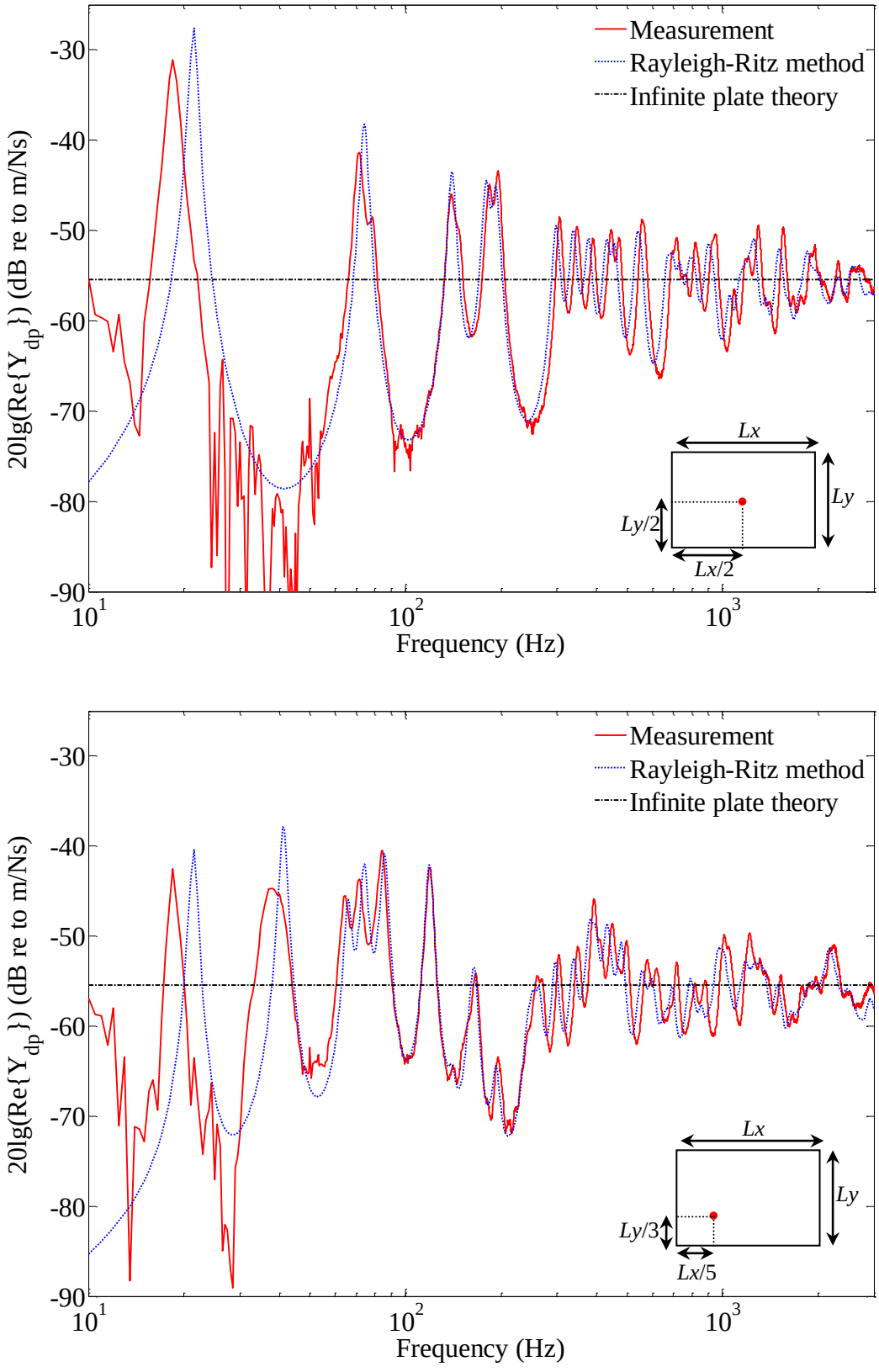

Figure 7.11 Driving-point mobilities (narrow band) for simply-supported isotropic plate. The measurement is compared with Rayleigh-Ritz theory for an finite plate and infinite plate theory

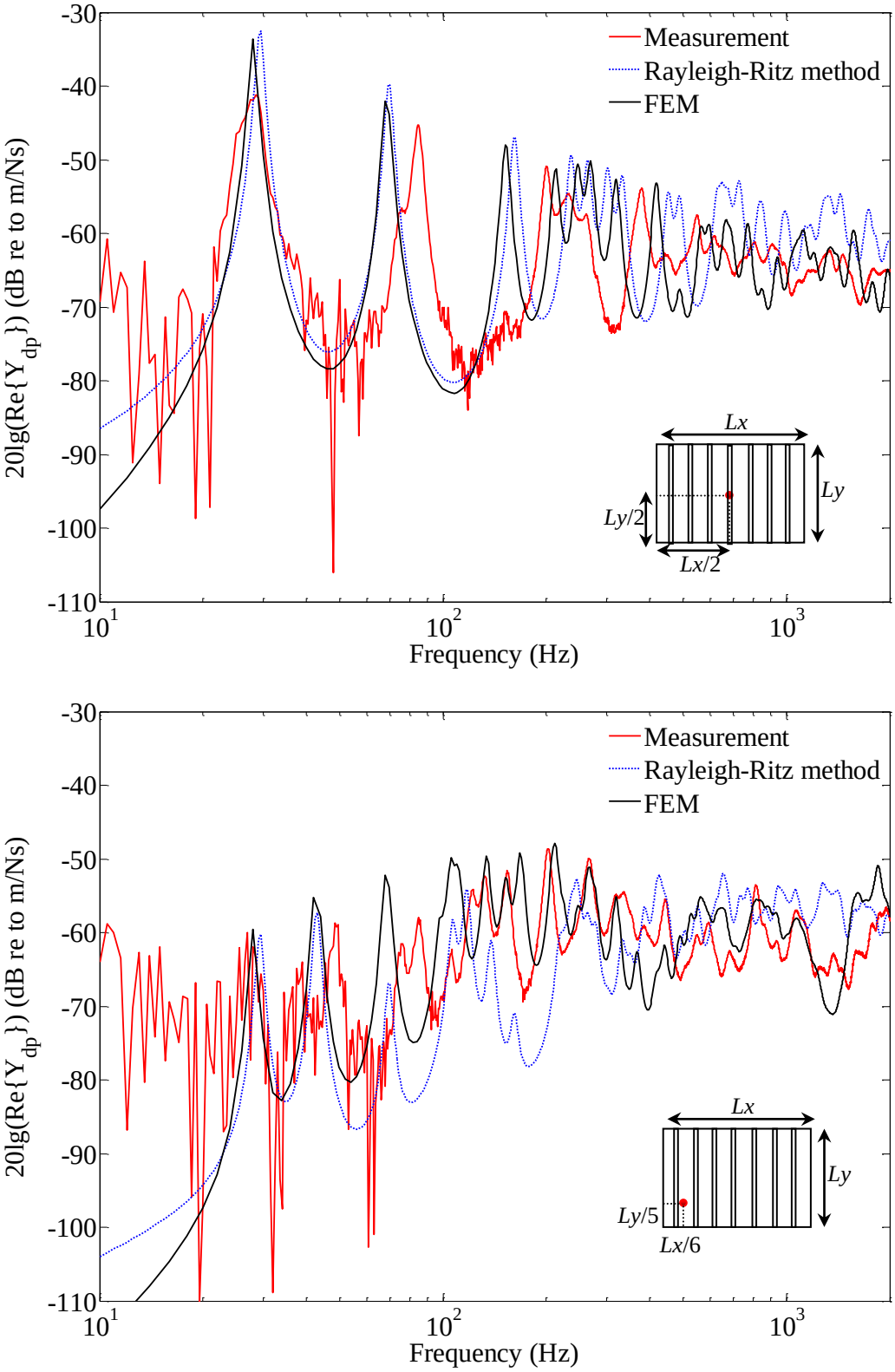

Figure 7.12 Driving-point mobilities (narrow band) for simply-supported periodic ribbed plate. The measurement is compared with theoretical results for finite plate and FEM results.

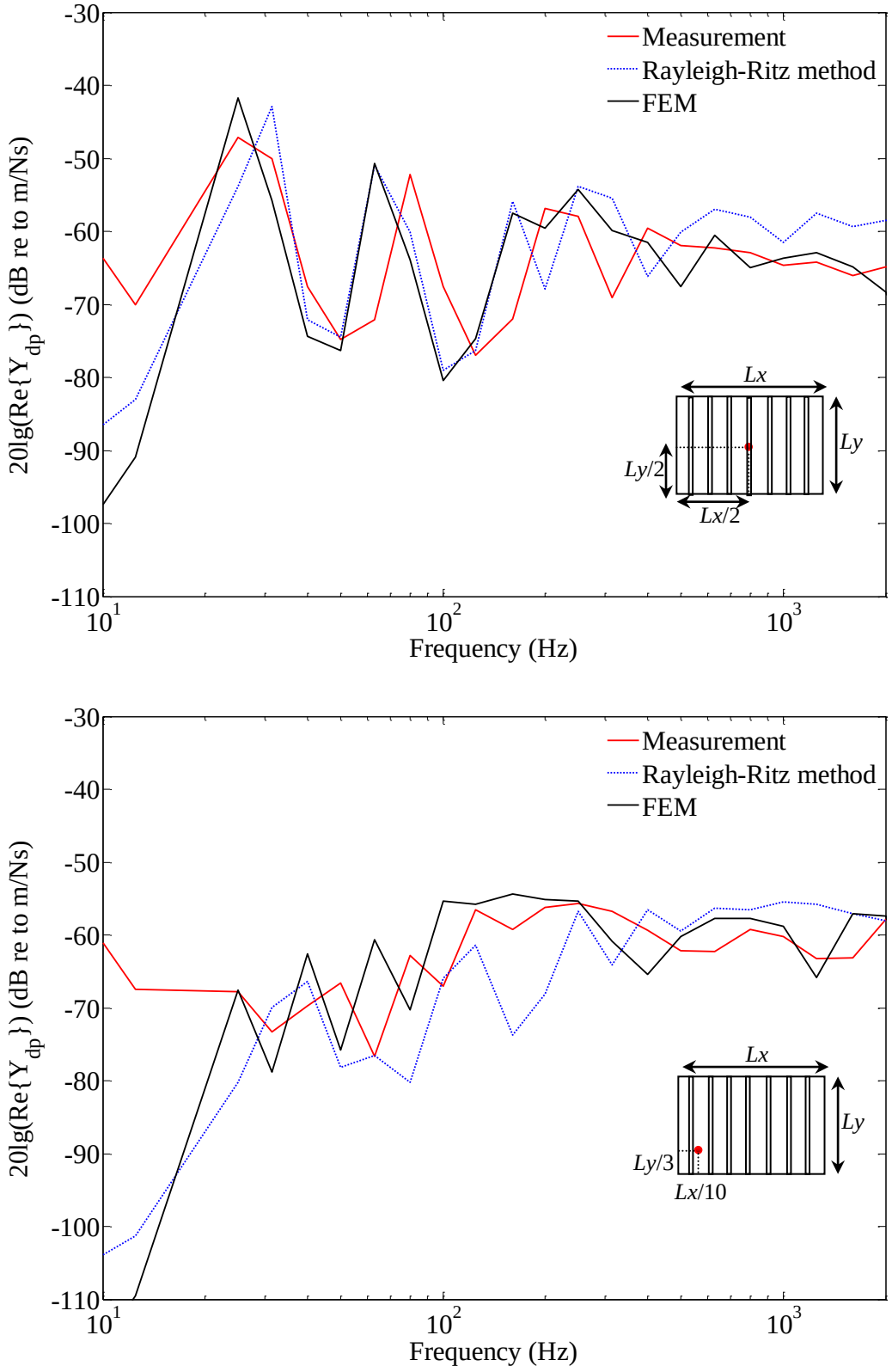

Figure 7.13 Driving-point mobilities (one-third octave band) for simply-supported periodic ribbed plate. The measurement is compared with theoretical results for finite plate and FEM results.

7.3.4 Measurement of bending wave transmission across L-junctions

In order to measure vibration transmission up to 10 kHz, a broadband signal via a shaker is used as the excitation source because it is difficult to provide such a signal using an impact hammer. The flat spectrum of excitation is achieved by using a graphic equalizer to adjust the amplification for each one-third octave band in the range of 500 Hz to 10 kHz with fluctuations less than 2 dB in acceleration.

The bending wave transmission between two plates of L-junction is determined by measuring the out-of-plane vibration. In order to represent the vibration level of the entire plate, a spatial average of velocity levels is performed over several randomly chosen accelerometer position with each excitation position.

In the experiments, three excitation positions are chosen on each plate and with each excitation position, four accelerometer positions are randomly chosen on each plate to measure the rms velocity.

The surface averaged velocity of plate *i* is calculated using:

$$<v_i^2>_{\mathrm{sa}} = \frac{1}{N \cdot M} \sum_{\mathrm{e}=1}^{N} \sum_{m=1}^{M} <v_i^2>_{\mathrm{e},m} \tag{7.6}$$

where N and M represent the number of excitations and number of measurements per excitation. $<v_i^2>_{\mathrm{e},m}$ is the rms velocity measured at accelerometer position m for the excitation position e.

The spatial-average mean-square velocity $<v_i^2>_{\mathrm{sa}}$ can then be used to calculate the energy level difference, $D_{\mathrm{E},ij}$, between plate *i* and plate *j* of the L-junction as:

$$D_{\mathrm{E},ij} = 10\lg\left(\frac{\rho_{\mathrm{s},i} <v_i^2>_{\mathrm{sa}}}{\rho_{\mathrm{s},j} <v_j^2>_{\mathrm{sa}}}\right) \tag{7.7}$$

where $\rho_{\mathrm{s},i}$ is the surface density of plate *i*.

The measurements of the spatial-average mean-square velocity on the source and receiving plates give a standard deviation for the source and receiving plates. The standard deviation of the energy level difference calculated from the velocity levels can be calculated by combining the standard deviations from two sets of measurements, which is given by [140] as:

$$s=\sqrt{s_1^2+s_2^2} \tag{7.8}$$

where s is the combined standard deviation, s_1 and s_2 are standard deviations of individual sets of measurement.

The 95% confidence interval of the combined measurement can be calculated using:

$$95\%CC=\left(\frac{s_1^2}{n_1}+\frac{s_2^2}{n_2}\right)^{\frac{1}{2}} t_{v,0.975} \tag{7.9}$$

where n_1 and n_2 are sample size of the two measurement sets and $t_{v,0.975}$ is the student t-distribution of 95% confidence interval with a degree of freedom of v which can be calculated from:

$$\frac{1}{v}=\frac{1}{n_1\text{-}1}\left(\frac{\frac{s_1^2}{n_1}}{\frac{s_1^2}{n_1}+\frac{s_2^2}{n_2}}\right)^2+\frac{1}{n_2\text{-}1}\left(\frac{\frac{s_2^2}{n_2}}{\frac{s_1^2}{n_1}+\frac{s_2^2}{n_2}}\right)^2 \tag{7.10}$$

7.3.5 Measurement procedure for velocity levels

The measurement setup to measure the velocity level difference between the two coupled plates of the L-junction is shown as in Figure 7.14. In the real measurement, there are four channels available to analyze the velocities. So there will be two accelerometers on each plate for every measurement.

The L-junction is formed by two Perspex plates which are bonded together at the junction line using cyanoacrylate glue. The glue is applied uniformly along the connecting surface and after it dries, the junction can be considered relatively rigid.

The measured acceleration is analyzed in one-third octave bands from 100 Hz to 10 kHz. The results for the two L-junctions are discussed in the next section.

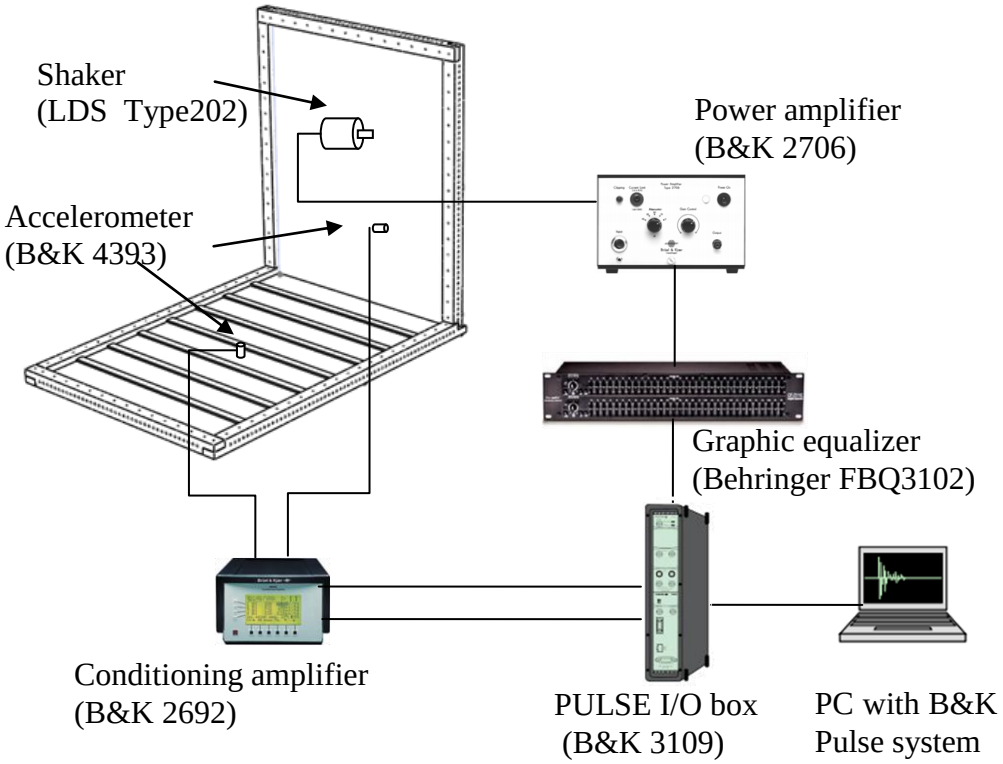

Figure 7.14 Experiment setup for measuring the velocity level difference on the L-junction.

7.4 Comparison between analytical and experimental results

The physical experiments designed for measuring vibration transmission across L-junction are used to confirm the theoretical models presented in the previous chapters of the thesis.

7.4.1 L-junction of two isotropic, homogeneous plates

7.4.1.1 Measurement of vibration levels

Figure 7.15 shows the energy level difference between the two coupled isotropic plates obtained from measurement for comparison with SEA (wave approach) and FEM. The FEM model uses an ensemble formed using 10 different sets of ROTR. At low frequencies, large variations are observed for the measurement results and there are 1 to 5 dB discrepancies between the averaged measurement energy level difference and the theoretical results. Both the measurement and FEM with ESEA show such tendency due to the low modal overlap. Above 400 Hz up to 10 kHz, the measurement gives good agreement with the theoretical results with a maximum of 2.5 dB discrepancy. There is no evidence that the layer of super glue at the junction has a significant effect on vibration transmission. The results also show that above 6.3 kHz, FEM overestimates the energy level difference by up to 6 dB. However this cannot be attributed to the S4R element because the thin plate limit is 10 kHz.

TOB(Hz)	100	160	250	400	630	1k	1.6k	2.5k	4k	6.3k	10k
N_{B1} =	1.1	1.7	2.7	4.3	6.7	10.7	17.1	26.7	42.8	67.4	106.9
N_{B2} =	1.3	2.1	3.2	5.1	8.1	12.8	20.5	32.1	51.3	80.8	128.3
M_{av}=	0.3	0.5	0.7	1.2	1.9	3.0	4.8	7.5	11.9	18.8	29.8

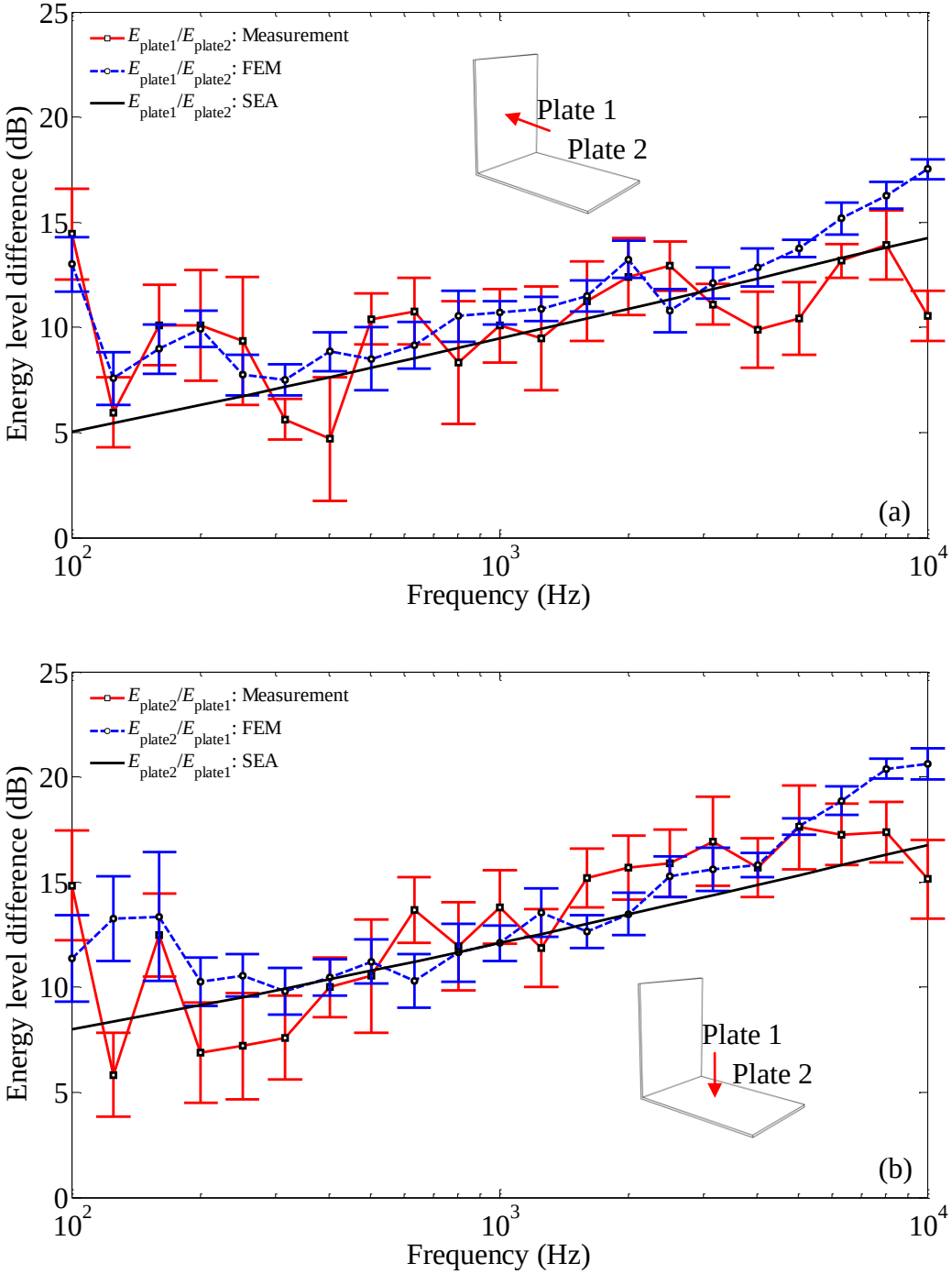

Figure 7.15 Energy level difference between two coupled isotropic plates from measurement compared with SEA (wave approach) and FEM models. (a) source on plate 1; (b) source on plate 2.

7.4.1.2 Measurement of total loss factors

Reverberation time measurements are carried out as discussed in section 7.2 to determine the total loss factor of the two plates. For each plate, three excitation positions are chosen and with each excitation, four accelerometer positions are chosen to measure the reverberation time using a Brüel & Kjær DIRAC system. Table 10 shows the average reverberation time for each plate and the product of bandwidth and reverberation time, *BT*, as an evaluation of the one-third octave band filter effect. It is confirmed in most one-third octave bands, the measurements of reverberation time on the two plates are not be affected ($BT>8$) by the band filter. As the plate size is relatively small (1.0 m×0.8 m and 1.2 m×0.8 m), the accelerometers may be impossible to be positioned in the reverberant field using the evaluation in equation (7.5) (i.e. at 10 kHz, r_{rd} for the two plates are 0.39 m and 0.47 m respectively). This may also cause some error in the measurements.

Figure 7.16 shows the total loss factor for the two plates measured using the reverberation time method compared with the internal loss factor measured using beam samples. At low frequencies, the total loss factor is higher than the internal loss factor because the coupling loss factor is higher than the internal loss factor at low frequencies. Above 630 Hz the mean total loss factor is slightly lower than the internal loss factor although the 95% confidence intervals for the total loss factor often overlap the internal loss factor. As noted in section 7.1, there can be small differences between material properties measured on beam samples and large plates.

Table 10: Reverberation time measured *in situ* for the two plates of the L-junction using Brüel & Kjær DIRAC system

Frequency (Hz)	Plate 1		Plate 2	
	T (s)	BT (Hz·s)	T (s)	BT (Hz·s)
100	0.28450	6.7	0.26883	6.3
125	0.26800	7.9	0.26125	7.7
160	0.34158	12.9	0.20558	7.8
200	0.25158	11.9	0.13608	6.4
250	0.19808	11.7	0.12492	7.4
315	0.33908	25.2	0.13608	10.1
400	0.08750	8.3	0.12583	11.9
500	0.11425	13.5	0.07908	9.3
630	0.13442	20.0	0.07325	10.9
800	0.11117	21.0	0.06183	11.7
1000	0.05358	12.6	0.05317	12.5
1250	0.05233	15.4	0.04733	14.0
1600	0.03450	13.0	0.03967	15.0
2000	0.03183	15.0	0.03342	15.8
2500	0.01892	11.2	0.01708	10.1
3150	0.01767	13.1	0.01650	12.3
4000	0.01917	18.1	0.01508	14.2
5000	0.01150	13.6	0.01283	15.1
6300	0.00933	13.9	0.01133	16.9
8000	0.00875	16.5	0.00983	18.6
10000	0.00717	16.9	0.00658	15.5

TOB(Hz)	100	160	250	400	630	1k	1.6k	2.5k	4k	6.3k	10k
N_{B1} =	1.1	1.7	2.7	4.3	6.7	10.7	17.1	26.7	42.8	67.4	106.9
N_{B2} =	1.3	2.1	3.2	5.1	8.1	12.8	20.5	32.1	51.3	80.8	128.3
M_{av}=	0.3	0.5	0.7	1.2	1.9	3.0	4.8	7.5	11.9	18.8	29.8

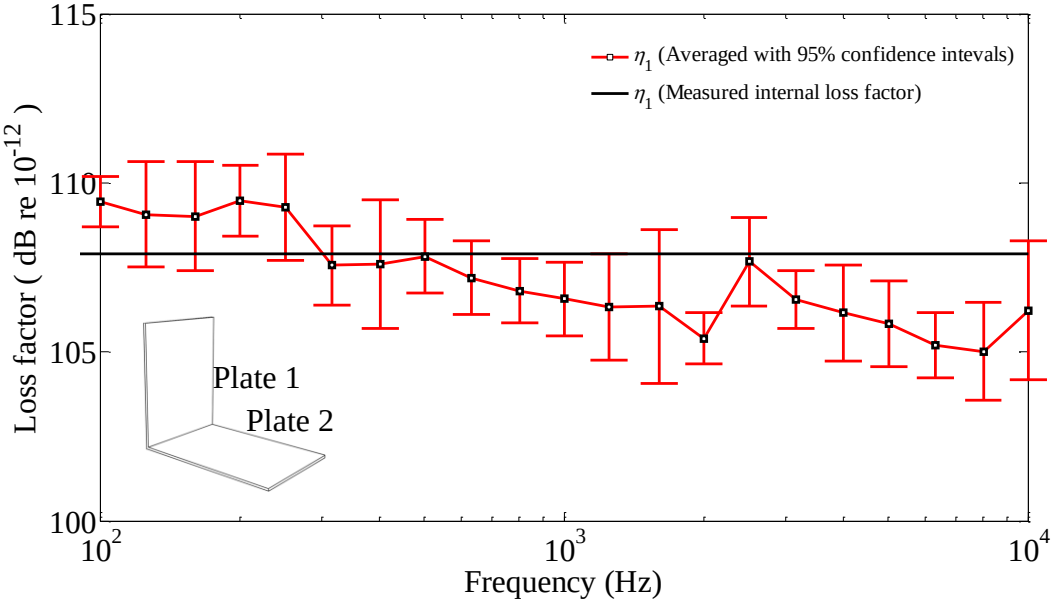

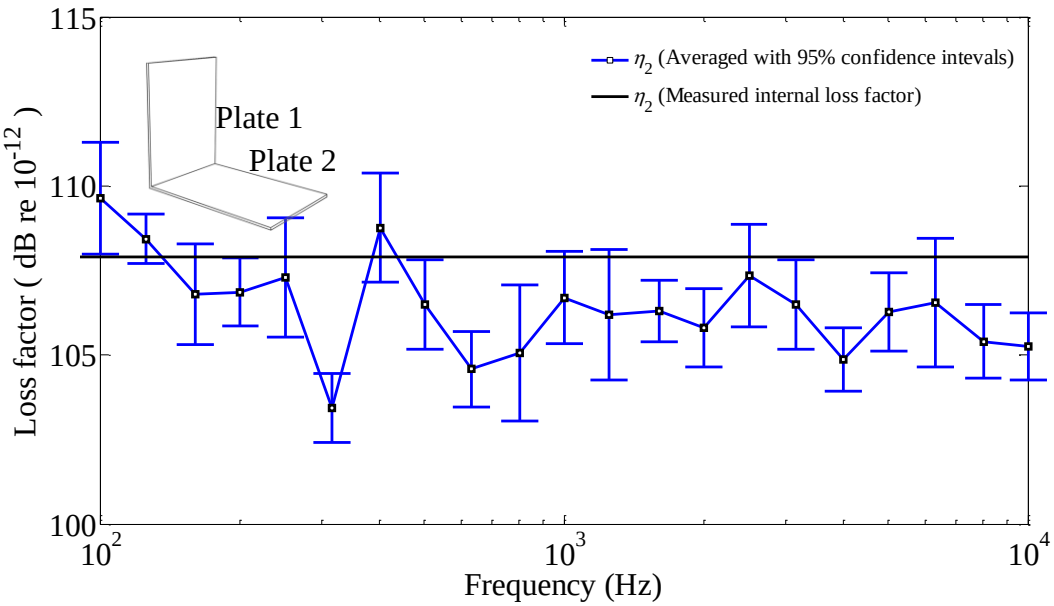

Figure 7.16 Total loss factors for the two coupled plates of L-junction measured using reverberation time method compared with the measured internal loss factor (see in section 7.2.3).

7.4.2 L-junction of an isotropic, homogeneous plate and a periodic ribbed plate

The measurement of vibration transmission across the L-junction of an isotropic plate and periodic ribbed plate is carried out using the same technique discussed in section 7.3. For the periodic ribbed plate, each bay is excited at three random positions and the vibration levels of the ribbed plate are also measured in bays with four accelerometer positions on each bay.

7.4.2.1 Two subsystem SEA model

Figure 7.17 shows the energy level difference from measurements, FEM, and SEA using CLFs calculated from the wave approaches with Tso and Hansen's model and the orthotropic plate model using angle-dependent bending stiffness. Figure 7.18 shows the coupling loss factors calculated using ESEA from measurements, FEM with ESEA and the two wave approaches. The results in both figures confirm the conclusions from section 6.7 that below the fundamental local mode of the bays (630 Hz one-third octave band) both the wave approaches using Tso and Hansen's model and the orthotropic plate model provide reasonable predictions using SEA. Although measurements and the Tso and Hansen's model closely agree on the attenuation in the first attenuation zone (400 Hz one-third octave band) for η_{12}, it appears that the consistency relationship does not correctly calculate η_{21} in the 400Hz band. However, the measurements do indicate the same pattern of troughs in the CLF due to attenuation zones as the Tso and Hansen's model.

TOB(Hz)	100	160	250	400	630	1k	1.6k	2.5k	4k	6.3k	10k
N_{B1} =	1.6	2.5	3.9	6.2	9.8	15.6	25.0	39.1	62.5	98.4	156.2
N_{B2} =	2.3	3.7	5.8	9.4	14.7	23.4	37.4	58.5	93.6	147.4	234.0
N_{bav}=						1.4	2.2	3.4	5.4	8.5	13.5

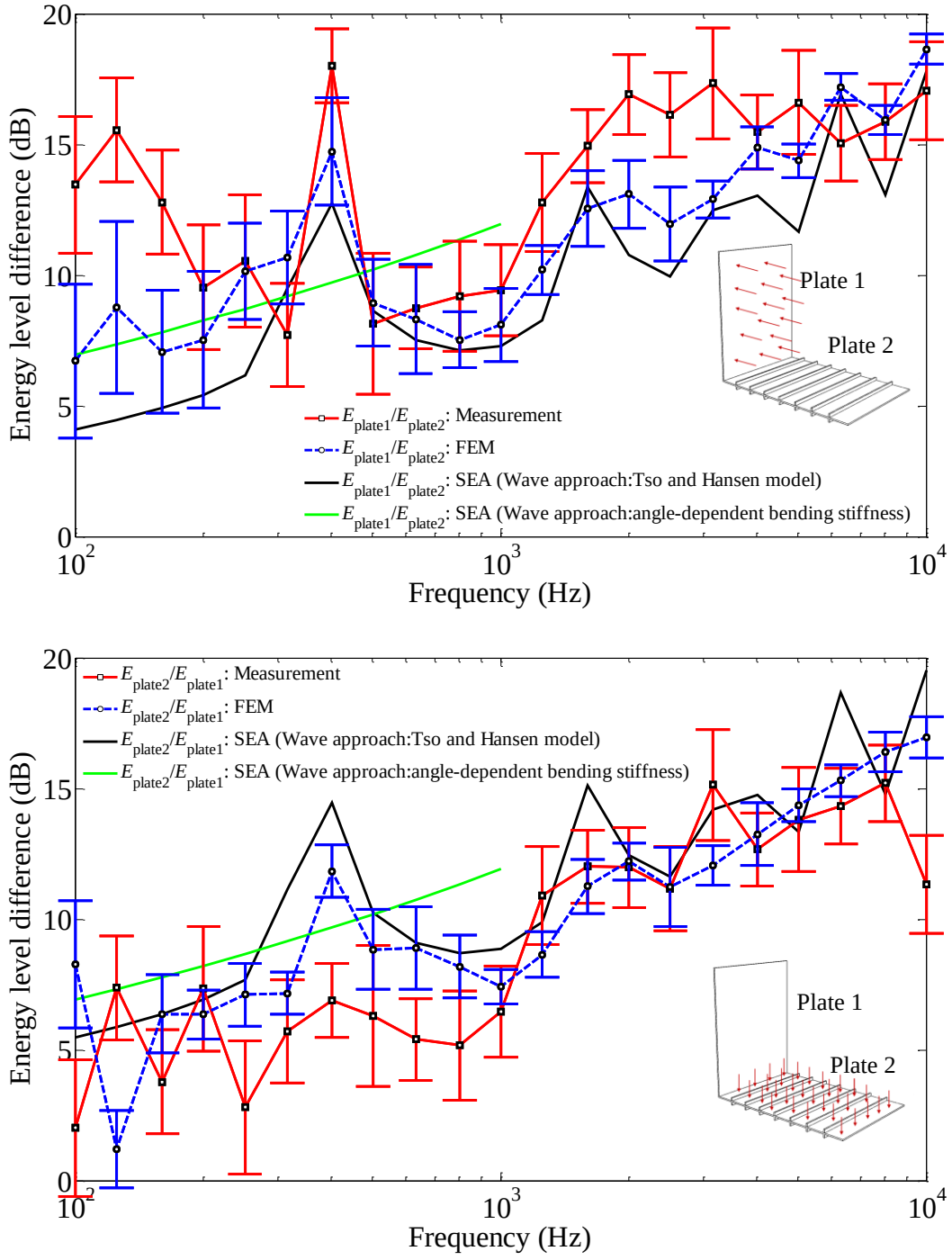

Figure 7.17 Energy level difference between the isotropic plate and the periodic ribbed plate calculated from measurement data compared with FEM and the wave approach using Tso and Hansen's model and the wave approach using angle-dependent bending stiffness.

TOB(Hz)	100	160	250	400	630	1k	1.6k	2.5k	4k	6.3k	10k
N_{B1} =	1.6	2.5	3.9	6.2	9.8	15.6	25.0	39.1	62.5	98.4	156.2
N_{B2} =	2.3	3.7	5.8	9.4	14.7	23.4	37.4	58.5	93.6	147.4	234.0
N_{bay}=						1.4	2.2	3.4	5.4	8.5	13.5

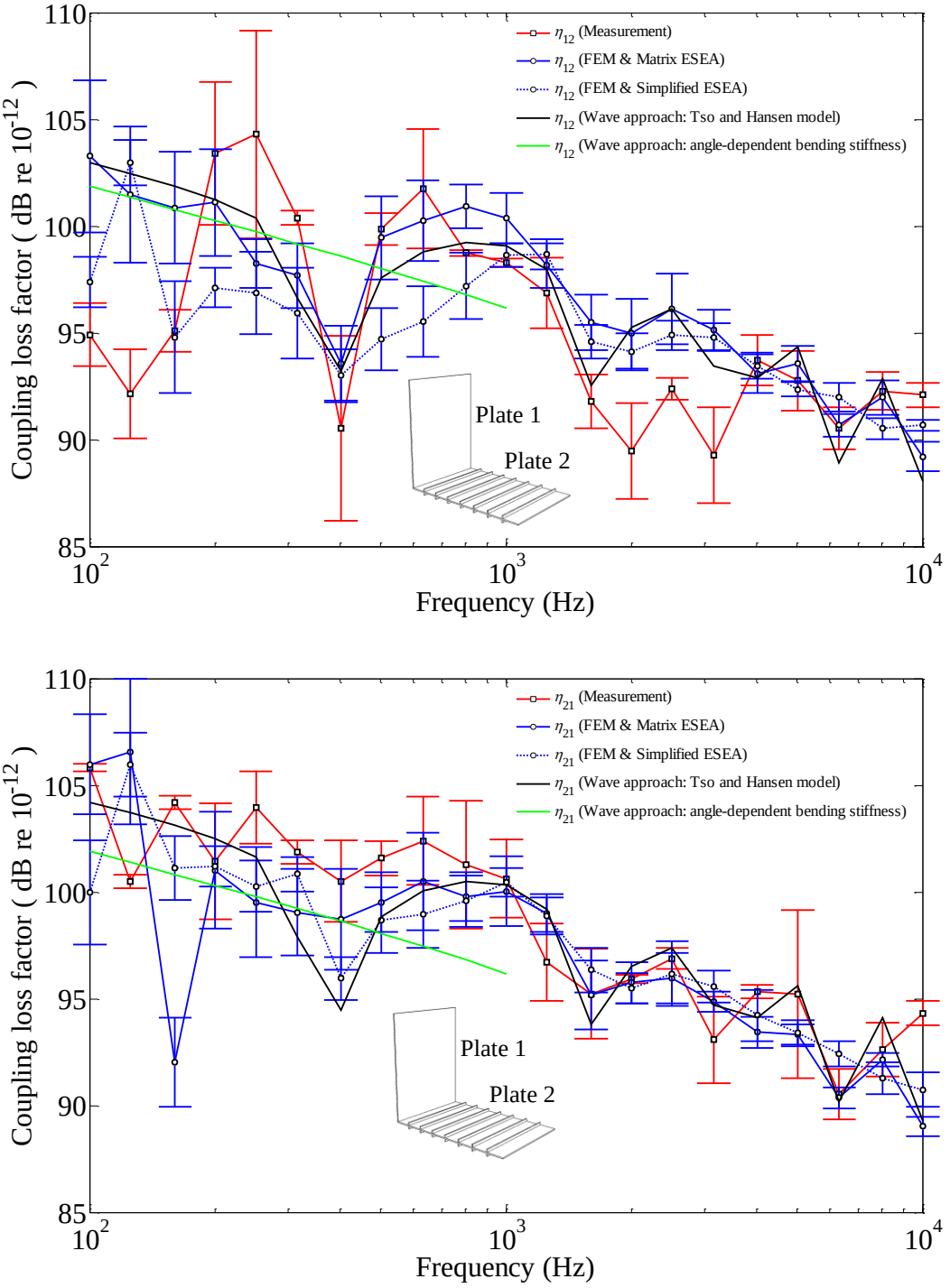

Figure 7.18 Coupling loss factors between the isotropic plate and the periodic ribbed plate calculated from measurement data compared with FEM with ESEA and theoretical results.

7.4.2.2 Decrease in energy level decrease across the bays of the nine-subsystem model

As discussed in section 6.5, although SEA of the two-subsystem model for L-junction of isotropic plate and ribbed plate gives good estimation compared with the measurement data, it needs to be examined at high frequencies, whether it is appropriate to treat the ribbed plate as a single subsystem.

Figure 7.19 plots the energy level difference between the isotropic plate (source subsystem) and the bays of the ribbed plate. At 10 kHz, the measurement shows that there is a 30 dB energy level difference between the bay closest to the junction and the furthest bay. The biggest energy decrease occurs from the first to the second bay with 5 to 10 dB of decrease at high frequencies. Smaller energy decreases are observed across bay 2 to 5 followed by another large decrease from bay 5 to bay 6. However, after bay 6, the energy levels for the last three bays are very close to each other with almost no energy decrease.

As discussed in section 6.7, due to the large energy level decrease across bays of the periodic ribbed plate at high frequencies, it is not appropriate to treat the ribbed plate as a single subsystem. Therefore, Figure 7.20 shows the results from a nine-subsystem SEA model in terms of an energy level difference for measurements, FEM and ASEA.

From Figure 7.20 it is seen that SEA predictions start to depart from the measurement results from bay 3 onwards and this discrepancy increases with increasing distance of each bay from the junction. For the furthest bay, SEA overestimates the energy level difference by 40 dB. This confirms the earlier finding in section 6.6.1 that SEA using CLF from wave approach is not appropriate for the nine-subsystem model. ASEA makes a significant improvement in the prediction by reducing the discrepancy to less than 5 dB.

The good agreement between measurements, FEM and ASEA provides further evidence that the conclusions from Chapter 6 are correct.

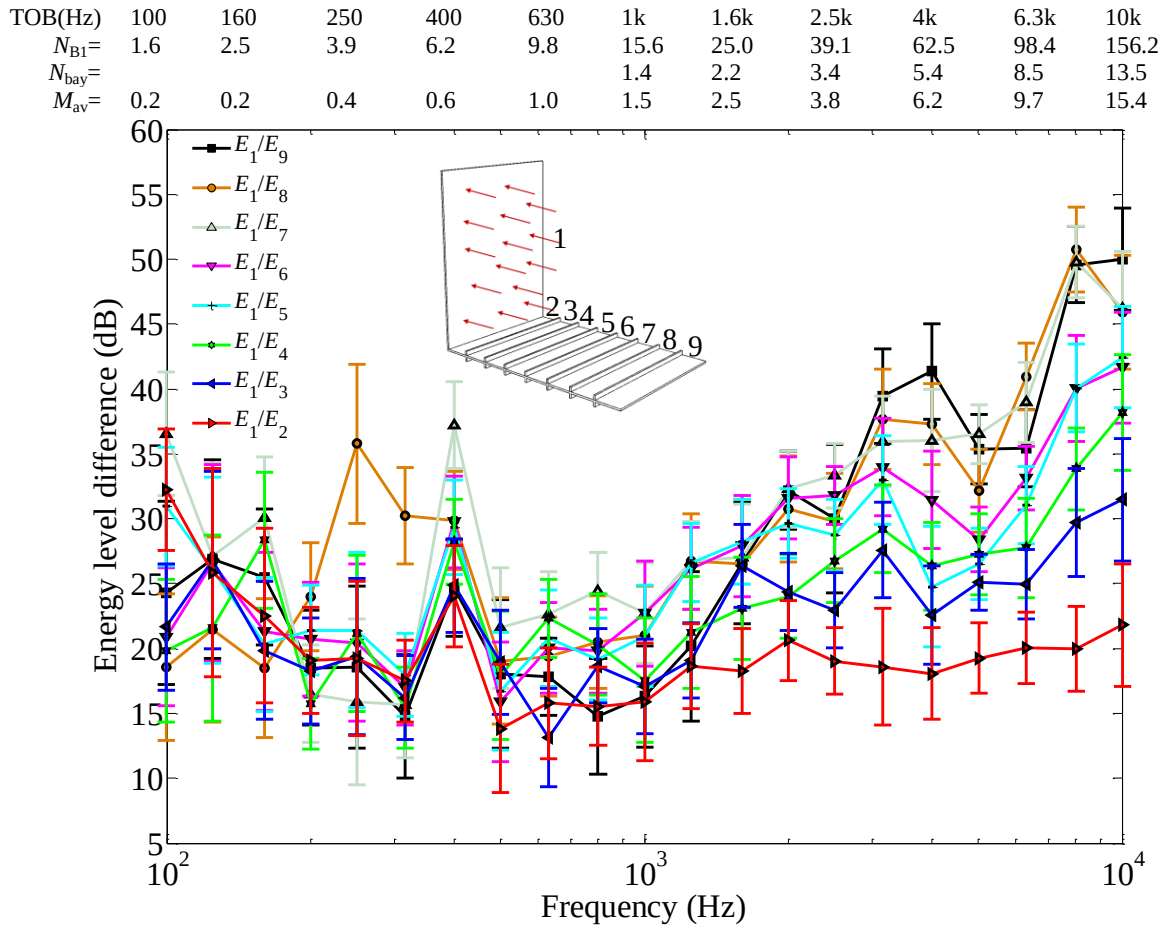

Figure 7.19 Measured energy level difference between the source subsystem (subsystem 1) and the successive bays of the periodic ribbed plate with 95% confidence intervals. Mode counts for subsystem 1 and the bays of the ribbed plate, geometric mean of modal overlap for subsystem 1 and any individual bay are shown on the upper *x*-axis.

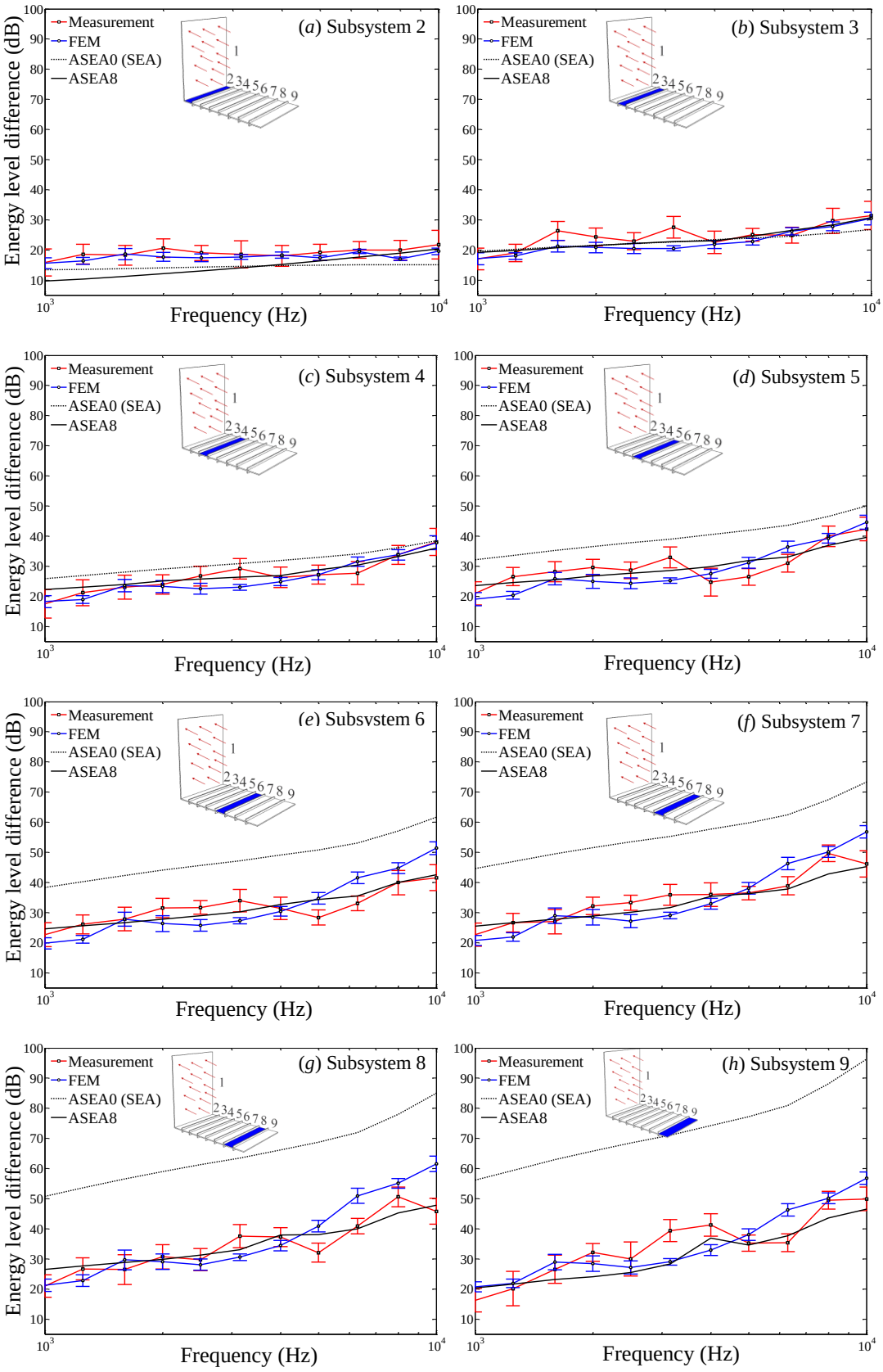

Figure 7.20 Measured energy level difference between the source subsystem (subsystem 1) and the successive bays of the periodic ribbed plate compared with FEM, SEA and ASEA predictions.

7.5 Conclusions

In this chapter, experimental work in the laboratory has been used to quantify material properties and to measure vibration transmission on L-junction of plates.

A specially designed frame has been created to simulate simply-supported boundary conditions using metal pins along the edges of the plates. Close agreement between the driving-point mobility from measurements and an analytical model confirm the effectiveness of the frame to provide a simply-supported boundary condition.

The first L-junction under test was comprised of two isotropic homogeneous plates for which good agreement between measurements and FEM provided validation of the FEM model.

The second junction under test comprised an isotropic homogeneous plate and a periodic ribbed plate. The measurements show good agreement with both FEM and ASEA up to 10 kHz. Along with the findings from chapter 6 this confirms that for L-junctions of isotropic and periodic ribbed plates above the fundamental mode of each bay, ASEA gives significantly better estimates of the energy levels in individual bays than SEA.

8 Application of ASEA to built-up structures incorporating periodic ribbed plates

In chapters 6 and 7, ASEA was successfully used to predict vibration transmission across L-junctions comprised of an isotropic, homogeneous plate and a periodic ribbed plate. In chapter 6 it was shown that ASEA can take into account the tunnelling mechanism between physically unconnected subsystems and the results show a significant improvement in predicting subsystem responses on a periodic ribbed plate compared with SEA.

In order to confirm that ASEA is appropriate for more general use with periodic plates, this chapter first considers the application of ASEA to a similar L-junction but with different geometric parameters for the periodic ribbed plate to change the distribution of the attenuation and propagation zones. Secondly, the effect of internal loss factor on the ASEA results is analyzed. Thirdly, larger built-up structures are analyzed with ASEA to evaluate its performance for (a) a folded plate structure comprising a chain of L-junctions of isotropic, homogeneous plates, (b) an in-line periodic structure created by connecting another isotropic, homogeneous plate to the periodic plate and (c) flanking transmission introduced by adding another plate to the L-junction coupling both plates to form a more complicated built-up structure.

8.1 Effect of stop/pass bands on the application of ASEA

It is now appropriate to consider whether the L-junction analysed in detail in chapter 6 was a special case, or whether ASEA can be used to model a wider range of periodic ribbed plates. Section 4.4 discussed the effect of geometric parameters on wave propagation on the periodic ribbed plate due to the stop/pass bands. It was shown that by altering the dimensions of the periodic ribbed plate, the vibration propagation could be significantly changed. These results are now used to consider two different L-junctions compared with the ‘default’ L-junction considered in chapter 6. These L-junctions have periodic ribbed plates with different geometric properties that result in distinctly different stop/pass bands. The geometric properties are listed in Table 11.

Table 11: Dimensions of the periodic ribbed plate in different L-junctions used to study the effect of stop/pass bands on the efficacy of ASEA

	Dimensions (mm)	Figure references for angle-dependent transmission coefficients of the plate/beam junction	Figure references for propagation and attenuation zones of the periodic ribbed plate
L-junction (Default)	h_p=13 h_b=50 b_b=30 l=150	Figure 5.5	Figure 4.3
L-junction 1	h_p=13 h_b=25 b_b=30 l=150	Figure 5.7 (a)	Figure 4.5 (a)
L-junction 2	h_p=5 h_b=50 b_b=30 l=150	Figure 5.8 (a)	Figure 4.7 (a)

For L-junctions 1 and 2, Figure 8.1 and Figure 8.2 respectively show the energy level difference calculated from FEM, SEA and ASEA between the source subsystem 1 (the isotropic, homogeneous plate) and the bays of the periodic plate. For both junctions, ASEA gives a significant improvement compared with SEA. The mode counts for the isotropic plate and the bay of the periodic plate are shown on the upper x-axis. These indicate that ASEA provides a good prediction above the limiting frequency where the mode count of the bay, N_{bay}>1. For L-junction 1, this limiting frequency is the 800 Hz one-third octave band and for L-junction 2 it is the 250 Hz one-third octave band.

L-junction 1 has a reduced rib height compared with the default junction; hence the angle-dependent transmission coefficient for the L-junction has a wider range of transmission angles (see Figure 5.12 (a)). For this reason the energy decrease across the subsystems tends to be lower than with the default junction. It is also seen that a peak occurs for ASEA predictions in the 6.3 kHz one-third octave band. Figure 5.7 (a) indicates that the 6.3 kHz band is located at the trough between two high transmission zones at 5 kHz and 8 kHz. Figure 8.3 plots the angle-dependent transmission coefficient for these three frequency bands. When the incident wave angle below 15 º, both 5 kHz and 8 kHz bands have a range of angles with high transmission coefficients (i.e. 0.98 to 1), while for 6.3 kHz bands,

no high values exist below 15°. Therefore, a significant reduction in vibration transmission is expected which results in a high peak for energy level difference. This effect is significant for this particular L-junction because all the subsystems are rectangular with the same thickness and material. Therefore, because specular reflection is assumed, the wave angle upon each junction is always the same and equal to the incident wave angle. For this reason, the same wave filtering effect is caused by each rib so that the total effect is strengthened as the wave travels across the bays. These peaks are not picked up by FEM which indicates that the specular reflection assumption may not hold true due to the motion of the ribs.

For L-junction 2 which has a reduced plate thickness, the angle-dependent transmission coefficient is compressed to a smaller range of angles (see Figure 5.14 (a)) compared with default L-junction and it also has more propagation zones. The energy level difference has been significantly increased compared with the default L-junction. Above 250 Hz where N_{bay}>1, ASEA typically improves the prediction by 20 dB to 55 dB compared with SEA for the furthest bay of the ribbed plate. ASEA shows three troughs in the energy level difference at 1.6 kHz, 3.15 kHz and 6.3 kHz. FEM also predicts three troughs at 1.25 kHz, 3.15 kHz and 5 kHz; which are within one one-third octave band of the ASEA predicted troughs.

For all three L-junctions analysed in this thesis, ASEA generally gives good agreement with FEM for periodic ribbed plates with different geometric properties. This is important as it demonstrates that it was not a fortuitous event that ASEA gave good agreement with FEM for the L-junction in chapter 6.

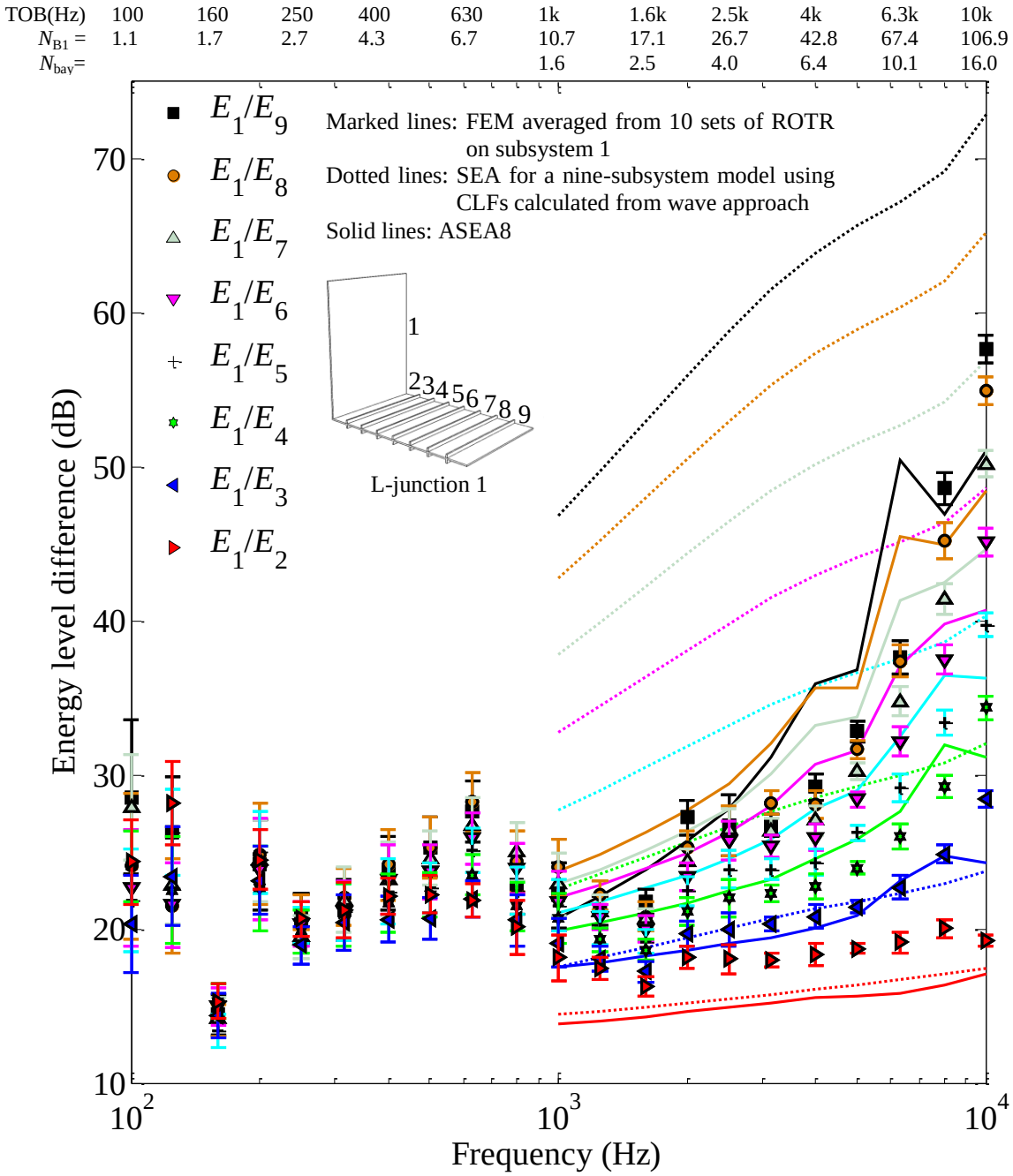

Figure 8.1 Energy level difference between the source subsystem (subsystem 1) and the bays of the periodic plate (L-junction 1: see Table 11) predicted from ASEA8 compared with FEM and SEA (ASEA0). Mode counts for subsystem1 and the bays (subsystem 2 to 9) are shown at the top of the figure.

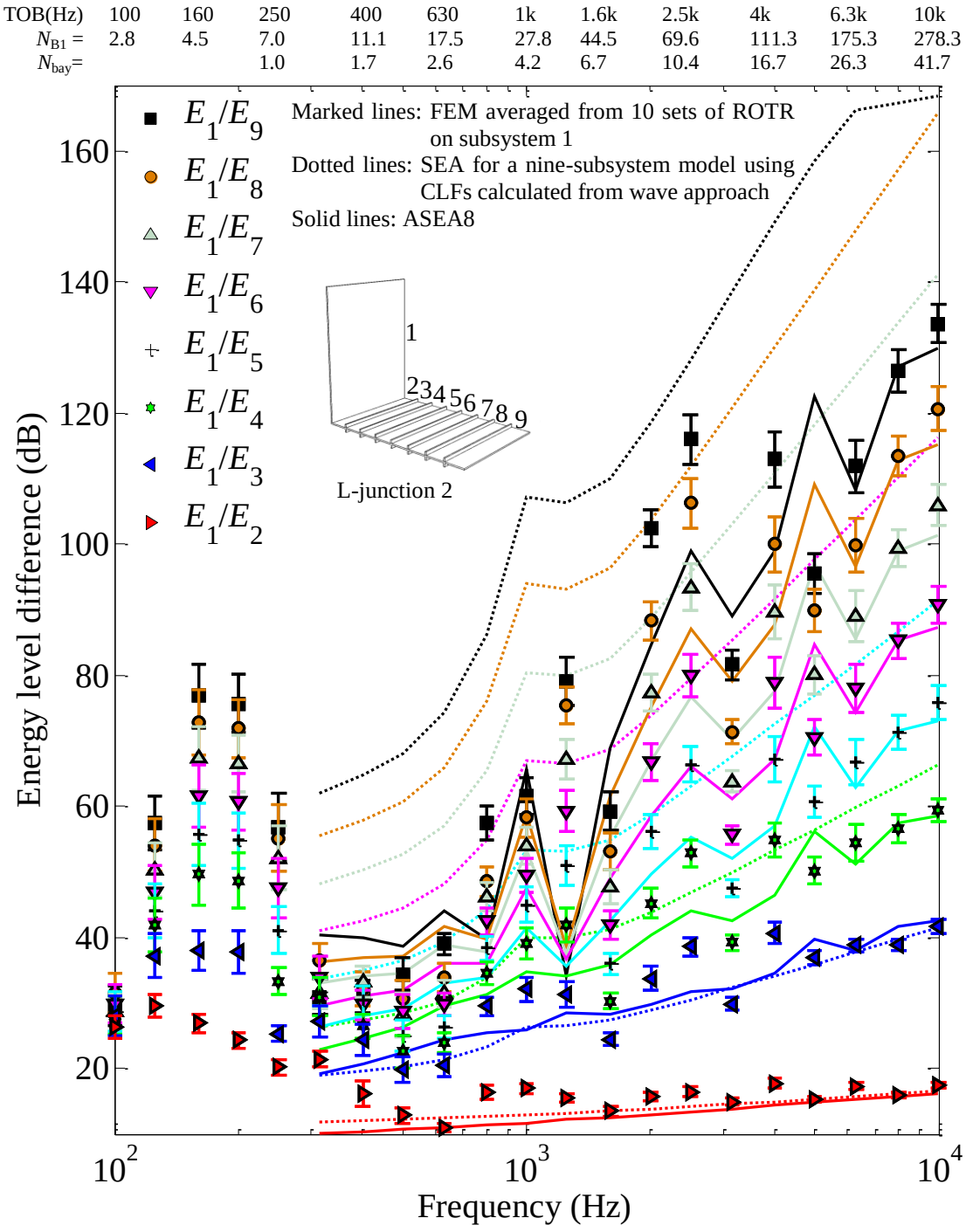

Figure 8.2 Energy level difference between the source subsystem (subsystem 1) and the bays of the periodic plate (L-junction 2 in Table 11) predicted from ASEA8 compared with FEM and SEA (ASEA0). Mode counts for subsystem1 and the bays (subsystem 2 to 9) are shown at the top of the figure.

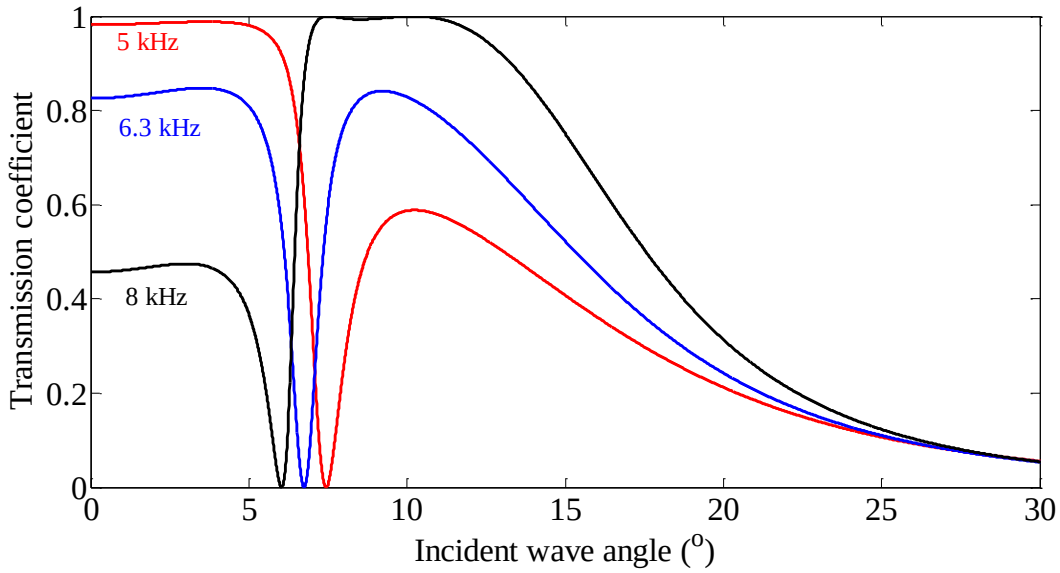

Figure 8.3 Transmission coefficient cross a rib (L-junction 1: see Table 11) at 5 kHz, 6.3 kHz and 8 kHz.

8.2 Effect of internal loss factor on the application of ASEA

This section investigates the effect of the internal loss factor on the efficacy of ASEA for the L-junction from chapter 6. In section 6.4, the effect of damping on the application of ESEA is discussed, which indicates that at high frequencies, internal damping has little effect on the SEA prediction when ROTR excitation is used. However, it is necessary to determine whether ASEA only gives good predictions when the internal loss factor is relatively high, as with Perspex. For this reason a range of internal loss factors are investigated from 0.015 to 0.24.

Figure 8.4 (a)-(d) shows the energy level differences between the source subsystem (subsystem 1) and the four bays furthest from the junction (subsystems 6-9) with internal loss factors from 0.015 to 0.24. The energy level differences are calculated using ASEA8 (it was checked that convergence was achieved using ASEA8), FEM and SEA using CLFs from the wave approach.

With increasing internal loss factor for the subsystems, the energy level difference also increases and it is observed that the errors of SEA prediction also increase. Contrary to the conclusion in section 6.4, when there is tunnelling involved, even

with ROTR excitation on the source subsystem, SEA gives inaccurate predictions and the error is dependent upon the internal loss factor.

For the highest loss factor of 0.24, ASEA generally shows good agreement with FEM except for the last two bays (subsystem 8 and 9) where there is a discrepancy up to 10 dB between ASEA and FEM. However, ASEA still gives a better prediction than SEA and this is likely to represent the highest loss factor that would be practically achievable on an engineering structure.

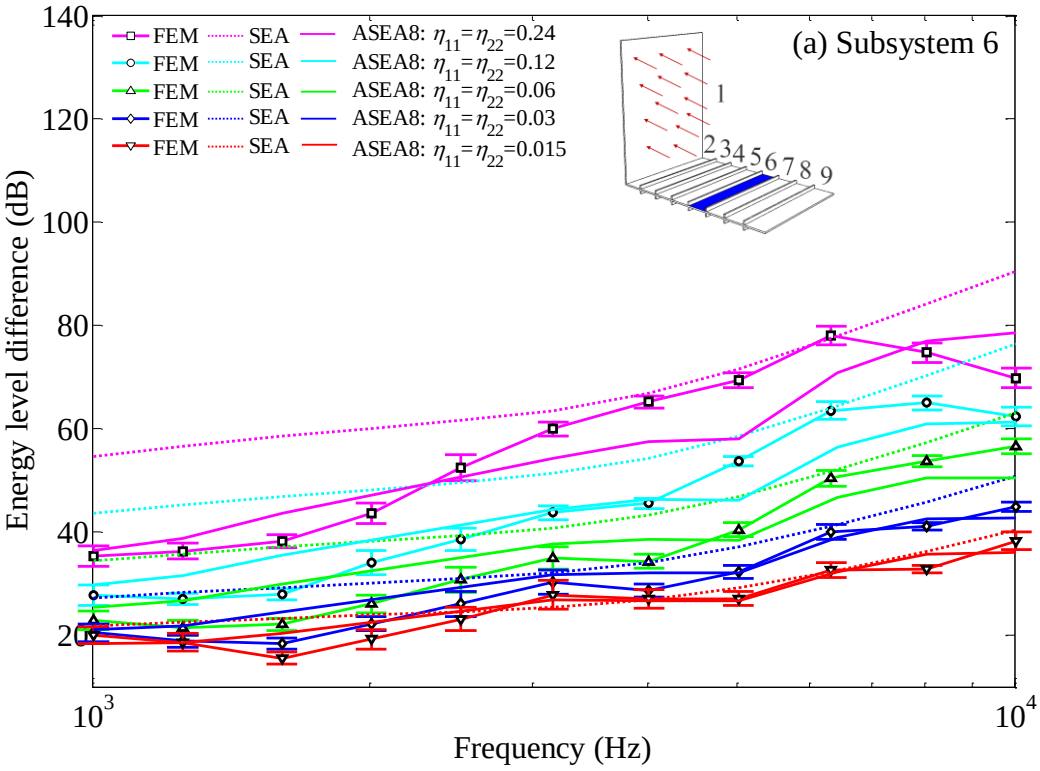
(a) Subsystem 6
FEM SEA ASEA8: $\eta_{11}=\eta_{22}=0.24$
FEM SEA ASEA8: $\eta_{11}=\eta_{22}=0.12$
FEM SEA ASEA8: $\eta_{11}=\eta_{22}=0.06$
FEM SEA ASEA8: $\eta_{11}=\eta_{22}=0.03$
FEM SEA ASEA8: $\eta_{11}=\eta_{22}=0.015$
1 2 3 4 5 6 7 8 9
Energy level difference (dB)
140
120
100
80
60
40
20
10^3
10^4
Frequency (Hz)

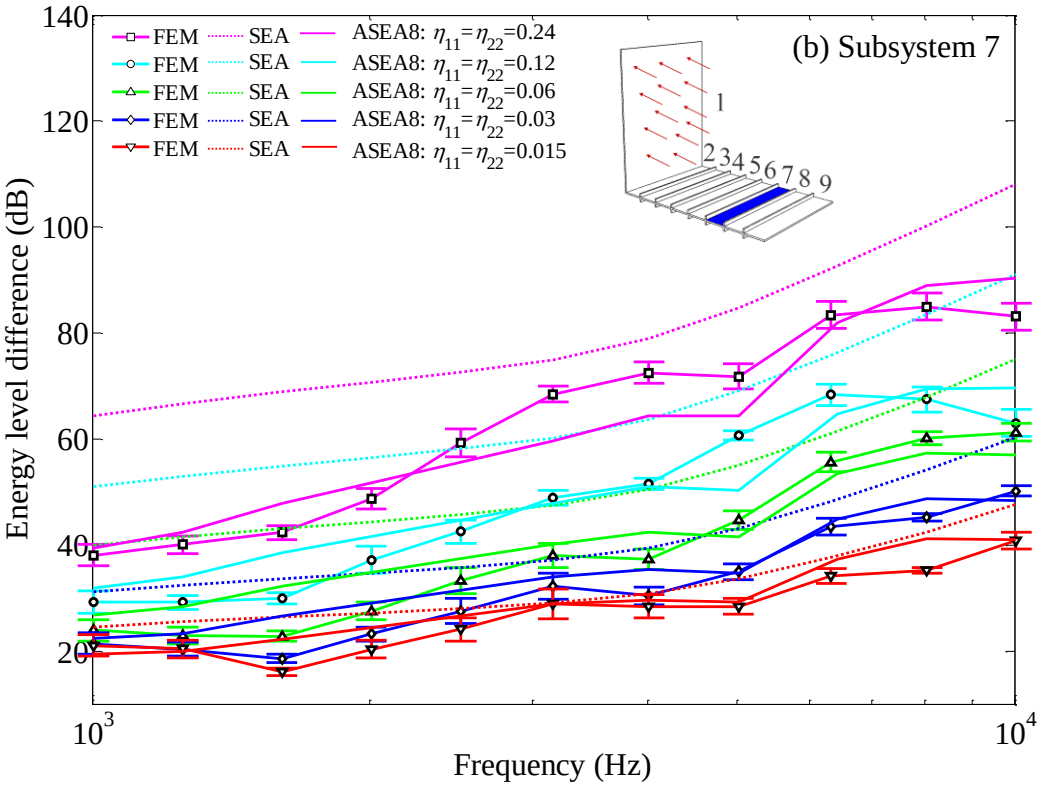
(b) Subsystem 7
FEM SEA ASEA8: $\eta_{11}=\eta_{22}=0.24$
FEM SEA ASEA8: $\eta_{11}=\eta_{22}=0.12$
FEM SEA ASEA8: $\eta_{11}=\eta_{22}=0.06$
FEM SEA ASEA8: $\eta_{11}=\eta_{22}=0.03$
FEM SEA ASEA8: $\eta_{11}=\eta_{22}=0.015$
1 2 3 4 5 6 7 8 9
Energy level difference (dB)
140
120
100
80
60
40
20
10^3
10^4
Frequency (Hz)

(Continued)

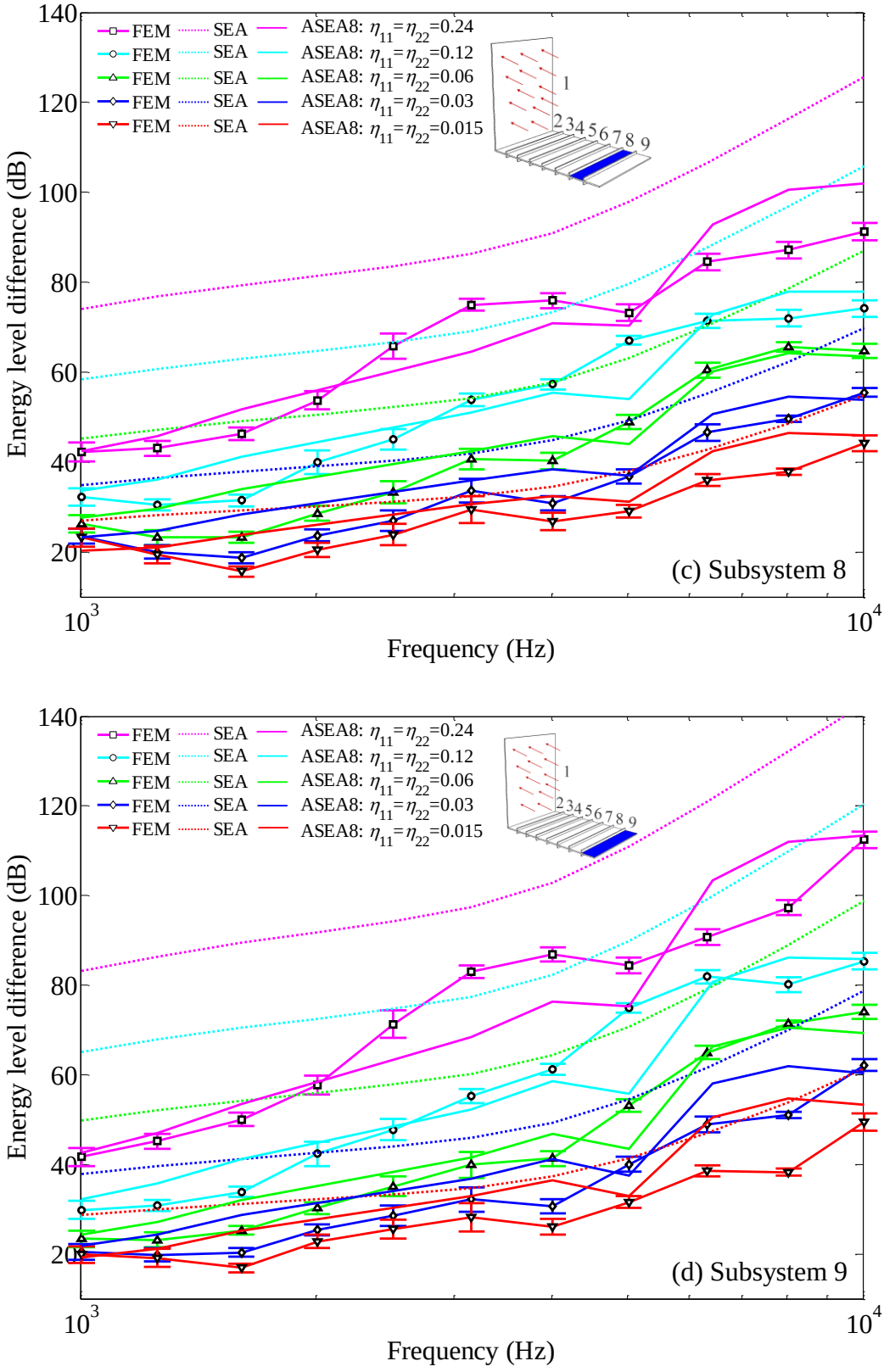

Figure 8.4 Energy level difference between the source subsystem (subsystem 1) and (c) Subsystem 8; (d) Subsystem 9 predicted from ASEA8 compared with FEM and SEA (ASEA0).

8.3 Nine-subsystem model with a folded plate

In this thesis, the main focus has been on periodic ribbed plates for which the transmission coefficient between adjacent bays used in ASEA is calculated using a wave approach described in section 5.4. Each rib results in a transmission coefficient that has sharp peaks with high transmission at specific angles of incidence. In addition, this type of junction has a limiting angle above which no wave transmission occurs. Having demonstrated in section 8.1 that different periodic ribbed plates can successfully be modelled using ASEA it is now appropriate to look at modelling periodic plates where the transmission coefficient has (a) smooth variation with angle of incidence (i.e. no rapid transitions between high and low transmission) and (b) no limiting angle for transmission below 90°. Hence this section considers a nine-subsystem model of a folded plate formed by eight L-junctions in a chain as shown in Figure 8.5. All the plates are isotropic and homogeneous and made of Perspex as in previous chapters and only bending wave transmission is considered so that all boundaries are simply supported. Subsystem 1 of this nine-subsystem model has the same plate dimensions as plate 1 from chapter 6 and all the other subsystems have the same dimensions as the bays of the periodic plate. These material properties and dimensions are given in Table 4.

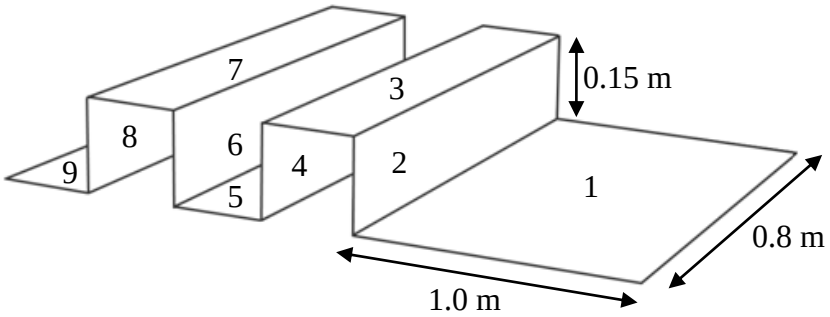

Figure 8.5 Folded isotropic, homogeneous plate formed from eight L-junctions connected in a chain.

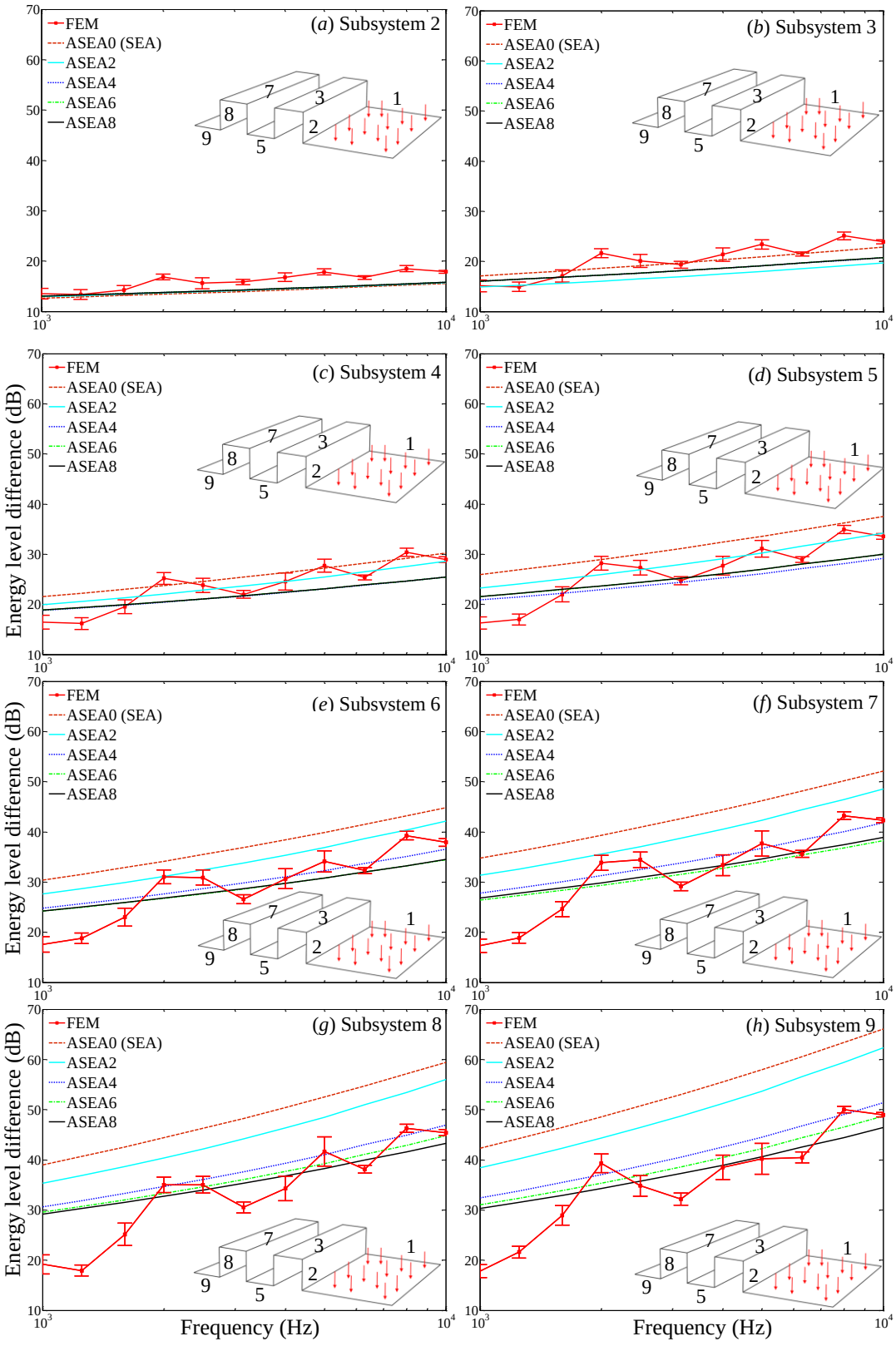

Figure 8.6 Energy level difference between the source subsystem (subsystem 1) and subsystems 2 to 9 predicted from ASEA with different ASEA level numbers compared with FEM.

TOB(Hz)	1k	1.25k	1.6k	2k	2.5k	3.15k	4k	5k	6.3k	8k	10k
N_{B1} =	10.7	13.4	17.1	21.4	26.7	33.7	42.8	53.5	67.4	85.6	106.9
$N_{B2,3,..9}$=	1.6	2.0	2.5	3.2	4.0	5.1	6.4	8.0	10.1	12.8	16.0
M_{av}=	1.1	1.3	1.7	2.1	2.6	3.3	4.2	5.3	6.6	8.4	10.5

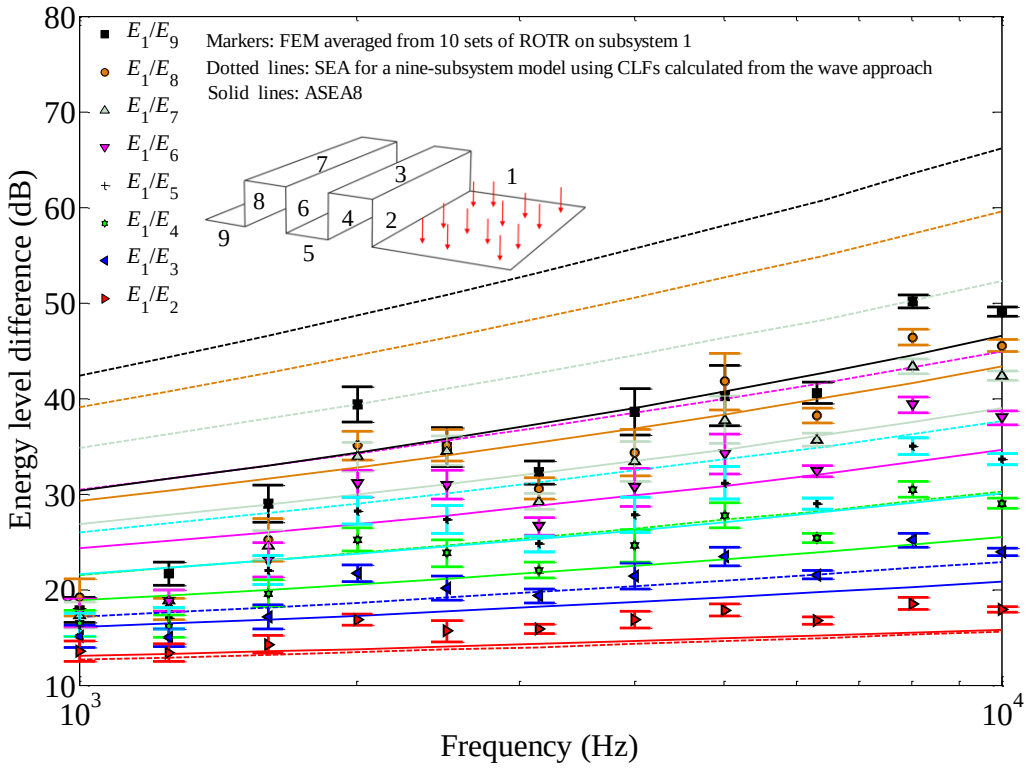

Figure 8.7 Energy level difference between the source subsystem (subsystem 1) and subsystems 2 to 9 of the folded plate predicted from ASEA8 compared with FEM and SEA. Mode counts for subsystem 1 and the smaller subsystem (2-9), geometric mean of modal overlap for subsystem 1 and any individual subsystem among 2 to 9 are shown on the upper *x*-axis.

Figure 8.6 (a)-(h) show all the energy level differences with different ASEA level numbers between source subsystem 1 and the other subsystems. Convergence was achieved at ASEA8 for the furthest subsystem, subsystem 9. SEA underestimates the energy levels for the last three subsystems by up to 15 dB compared with FEM. In contrast, ASEA significantly improves the prediction of energy levels for the last three subsystems by reducing the discrepancy to less than 5 dB.

Figure 8.7 compares ASEA8 in comparison with FEM and SEA (ASEA0). In section 6.6.3, it was observed that when $1<N_{bay}<5$, discrepancies occurred between ASEA and FEM. Figure 8.7 indicates a similar finding, but with good agreement achieved after $N_{bay}>3$.

8.4 Ten-subsystem model: validation of ASEA for a larger structure formed by two L-junctions

In this section, a 10-subsystem model is considered where a third plate is added to the L-junction at the far end of the periodic ribbed plate to form two connected L-junctions as shown in Figure 8.8. This results in a chain of subsystems where the source and receiver subsystems at the ends of the chain are both isotropic, homogeneous plates.

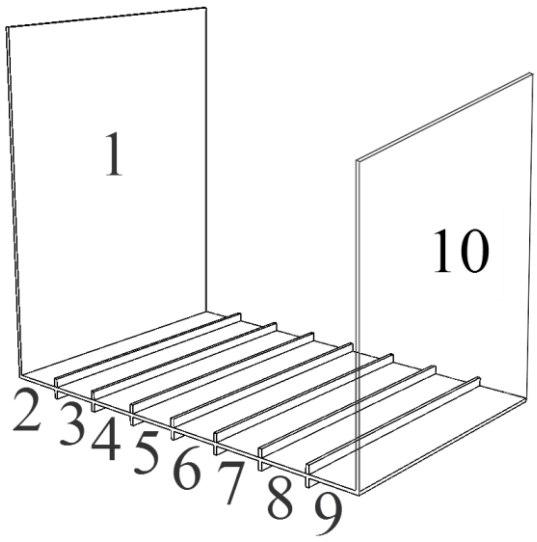

Figure 8.8 Two connected L-junctions including a periodic ribbed plate forming a 10-subsystem model

Figure 8.9 shows the ASEA9 predictions for comparison with FEM and SEA. SEA gives a poor estimate of the energy level in subsystem 10 by up to 50 dB. ASEA gives a significant improvement compared to SEA with discrepancies from FEM up to 10 dB above 2.5 kHz where N_{bay} >3.

For the three bays closest to the junction between subsystem 1 and the ribbed plate (subsystems 2, 3 and 4), ASEA slightly underestimates the energy levels by up to 5 dB. In contrast, for more distant bays (subsystems 5, 6, 7, 8 and 9) and the receiving plate (subsystem 10), ASEA generally overestimates the energy levels by up to 11 dB.

It is concluded that ASEA is a significant improvement on SEA particularly when N_{bay}>5, but there are still differences between ASEA and FEM which are unlikely to be due to phase effects because they occur even when N_{bay} >10.

TOB(Hz)	1k	1.25k	1.6k	2k	2.5k	3.15k	4k	5k	6.3k	8k	10k
$N_{B1,10}$ =	10.7	13.4	17.1	21.4	26.7	33.7	42.8	53.5	67.4	85.6	106.9
$N_{B2,3,..9}$=	1.6	2.0	2.5	3.2	4.0	5.1	6.4	8.0	10.1	12.8	16.0

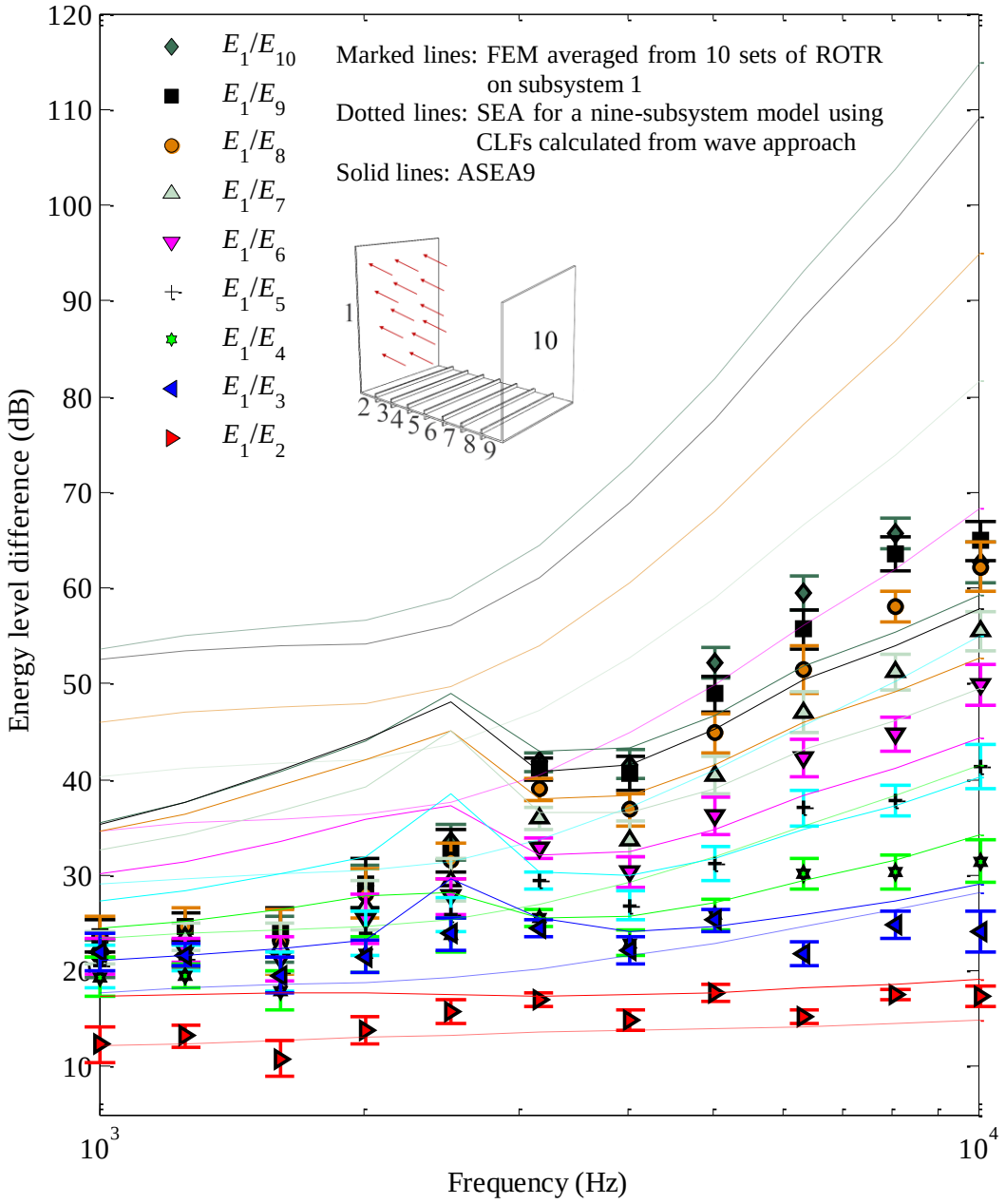

Figure 8.9 Energy level difference between the source subsystem (subsystem 1) and subsystems 2 to 10 representing three coupled plates including a periodic ribbed plate. ASEA9 is shown for comparison with FEM and SEA.

8.5 Ten-subsystem model: validation of ASEA for a larger structure with flanking transmission

In this section, flanking transmission is introduced for the L-junction with the periodic ribbed plate by adding a third plate to connect the isotropic, homogeneous plate and the periodic ribbed plate as shown in Figure 8.10. The third plate (subsystem 10) is made of the same material and has the same thickness as subsystem 1.

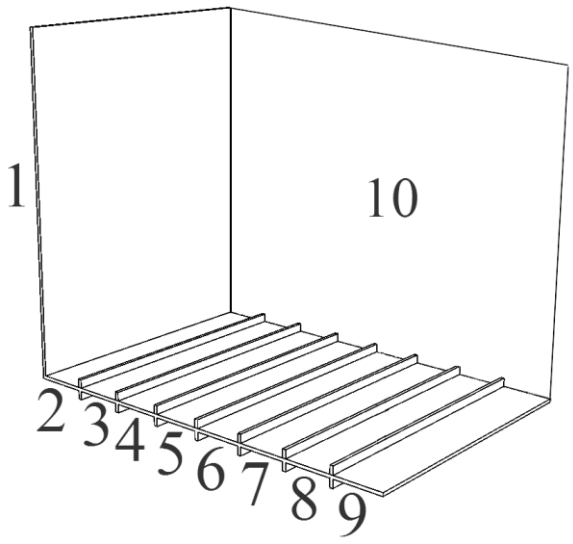

Figure 8.10 Three coupled plates including a periodic ribbed plate forming a ten-subsystem model.

In the FEM model, the ribs of the periodic plate are not connected to the third plate (subsystem 10). This is achieved by assigning a small gap (10^{-6} m) between the edge of the rib and the surface of subsystem 10. This is to ensure that the coupling between each bay of the ribbed plate and subsystem 10 can be modelled as an L-junction between two isotropic, homogeneous plates without considering the ribs. Future work will consider the more practical situation where the ribs are connected to the adjacent plate.

Subsystem 10 introduces flanking transmission paths between the source subsystem (subsystem 1) and the bays of the periodic ribbed plate. Energy level differences between the source subsystem and other subsystems calculated from FEM, SEA and ASEA are shown in Figure 8.11.

The FEM results show that the decrease in energy level mainly occurs for the five bays closest to the junction between the ribbed plate and subsystem 1 (subsystems 2, 3, 4, 5 and 6). In addition, the energy levels above 4 kHz for the adjacent bays in the furthest three bays (subsystems 7, 8 and 9) are similar with differences only up to 2 dB. Referring back to Figure 6.28 for the isolated L-junction the energy levels above 4 kHz for the furthest three bays were up to 10 dB apart. This indicates that flanking transmission is significant for the three bays that are furthest away from the source subsystem.

Comparison of FEM with SEA indicates that SEA gives a good prediction for the three bays closest to the junction between subsystem 1 and the ribbed plate (subsystems 2, 3 and 4). However, there is less agreement for more distant bays and SEA overestimates vibration transmission to the last bay by up to 20 dB. Note that this is an overestimate whereas for the isolated L-junction, SEA underestimates vibration transmission to the last bay by up to 25 dB (see section 6.6).

The FEM results can now be compared with ASEA9 where convergence occurs. For the three bays closest to the junction between subsystem 1 and the ribbed plate (subsystems 2, 3 and 4), ASEA gives an equally good prediction to SEA above 4 kHz. However, ASEA gives a significantly improved prediction for the more distant bays (subsystems 5, 6, 7, 8 and 9) above 4 kHz. For the furthest bay, ASEA improves the prediction by around 15 dB compared to SEA. However, for the furthest three bays ASEA slightly overestimates the transmission predicted by FEM by 3 to 7 dB.

For this structure where flanking transmission is introduced, ASEA is able to provide a significantly better prediction than SEA for the individual bays, particularly when $N_{\text{bay}} > 5$.

TOB(Hz)	1k	1.25k	1.6k	2k	2.5k	3.15k	4k	5k	6.3k	8k	10k
N_{B1}=	10.7	13.4	17.1	21.4	26.7	33.7	42.8	53.5	67.4	85.6	106.9
N_{B10}=	16.0	20.1	25.7	32.1	40.1	50.6	64.2	80.2	101.1	128.4	160.5
$N_{B2,3,..9}$=	1.6	2.0	2.5	3.2	4.0	5.1	6.4	8.0	10.1	12.8	16.0

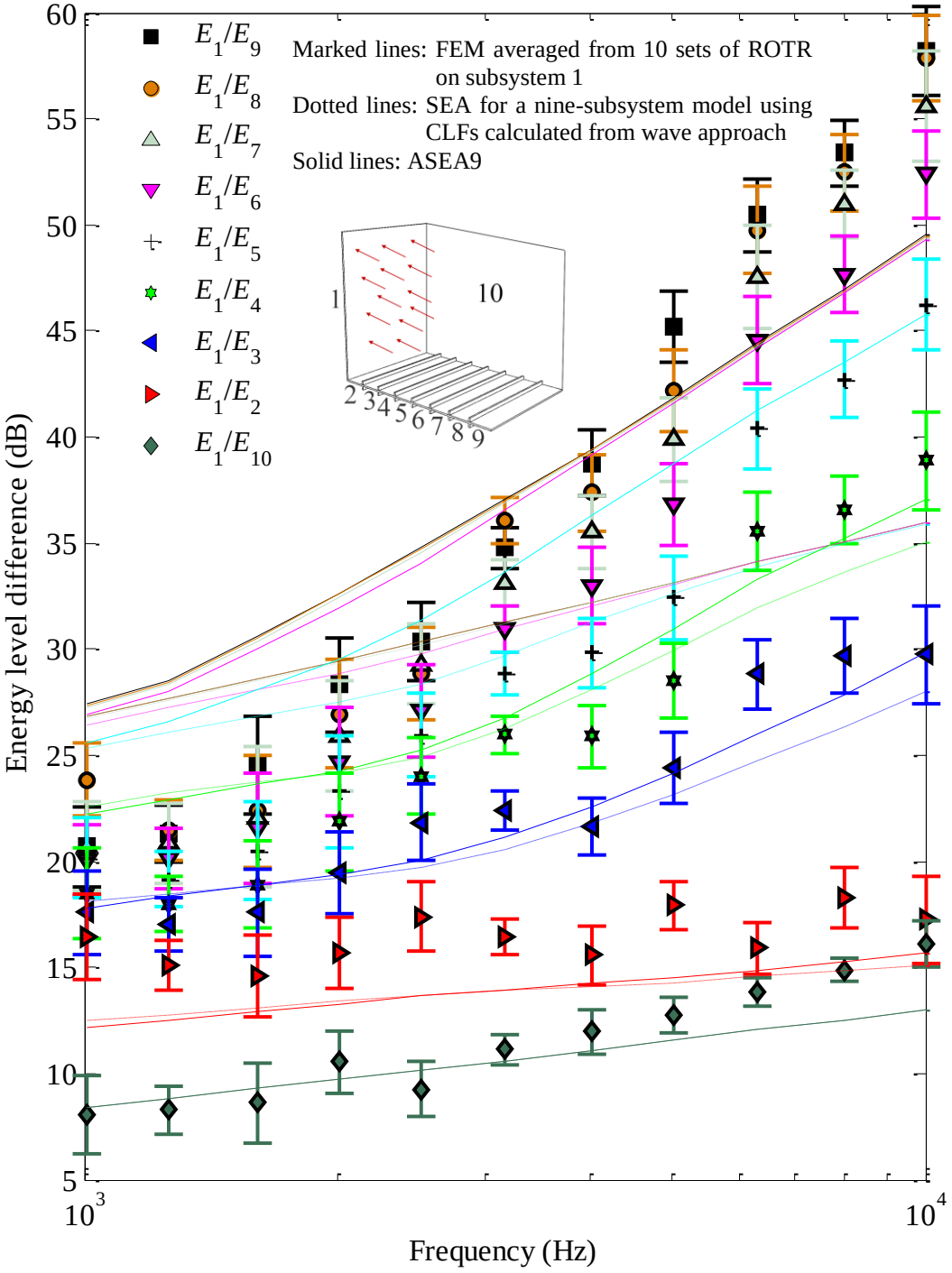

Figure 8.11 Energy level difference between the source subsystem (subsystem 1) and subsystems 2 to 10 of three coupled plates including a periodic ribbed plate predicted from ASEA9 compared with FEM and SEA.

8.6 Conclusions

This chapter extends the application of ASEA to more complicated built-up structures and investigates factors that could reduce the accuracy of ASEA.

For L-junctions comprised of an isotropic, homogeneous plate and a periodic ribbed plate, the geometric properties of the ribbed plate can significantly affect vibration transmission due to the distribution of the stop/pass bands. The transmission coefficient across the rib is highly variable depending on the angle of incidence and frequency resulting in a transmission coefficient with peaks and troughs. Hence in some cases, the assumption of specular reflection in ASEA will cause significant peaks or troughs in the ASEA prediction of energy response on the bays. However, FEM does not always predict these peaks or troughs to be in the same frequency band as ASEA and this may be attributed to the fact that specular reflection is not always an appropriate assumption.

The effect of different internal loss factors for the plates in the L-junction was assessed using FEM and ASEA. This indicates that ASEA works well with both lightly and highly damped plates. However, discrepancies between ASEA and FEM can occur with high damping for bays on the periodic ribbed plate that are distant from the source subsystem.

For ribbed plates, the ribs cause the transmission coefficient between adjacent bays to have sharp peaks with high transmission at specific angles of incidence. For this reason, a nine-subsystem model of a folded plate formed by eight L-junctions was used to assess ASEA when there is a smooth variation of transmission coefficient with angle of incidence. The results showed good agreement between ASEA and FEM indicating that the use of ASEA is likely to be applicable to many other types of junction that connect long, narrow bays in a periodic array.

The effect of flanking transmission is investigated by adding a third plate to the L-junction that couples the isotropic plate and the periodic ribbed plate. For this structure where flanking transmission is introduced, ASEA is able to provide a significantly better prediction than SEA for the individual bays. It is found that flanking via the third plate has a more significant effect on the subsystems that are

far away from the source subsystem than the subsystems close to the source subsystem. Unlike the isolated L-junction where SEA tends to underestimate the energy levels on the subsystems, introducing flanking transmission in this structure caused SEA to significantly overestimate the energy level differences.

Considering all the L-junctions in this chapter as well as in chapters 6, 7, and the larger structures in this chapter, ASEA tends to give reasonable agreement with FEM when N_{bay} >3.

From the ASEA models analysed in this chapter and in chapter 6, it is reasonable to conclude that in order to achieve convergence for all subsystems the level number should be at least equal to the subsystem number minus one. This is slightly different to Heron [16] who, based upon a chain of rod subsystems, proposed that it should be at least equal to the subsystem number minus two.

In all the models presented in this chapter, ASEA has proved to be an effective method to predict vibration transmission at high frequencies for built-up structures where tunnelling is involved.

9 Conclusions and future work

This section summarises the main findings and conclusions in this thesis and gives suggestions for potential future work.

9.1 Conclusions

This thesis has validated theoretical and experimental models for structure-borne sound transmission in built-up structures which incorporates periodic ribbed plates. Theories for different prediction models were presented in chapters 2, 3, 4 and 5. Chapter 6 and 8 implemented these theories on examples of L-junctions and larger built-up structures. Chapter 7 validated the theories using physical experiments.

Chapter 2 outlined the principles of SEA, FEM and ASEA as prediction models for structure-borne sound transmission. ESEA was introduced as an approach to estimate coupling loss factors from numerical experiments with FEM which will be compared with coupling loss factors determined from wave theory that was described in chapter 5. ASEA was presented as an extension to SEA which can incorporate tunnelling mechanisms between physically unconnected subsystems. A ray-tracing algorithm used to track power flow among subsystems in ASEA was described in detail. ASEA was validated on structural junctions including periodic ribbed plates in chapters 6, 7 and 8.

The models in chapter 2 were often described in a generic form that applies to many different kinds of vibration fields. Therefore Chapter 3 described the theory for bending and in-plane wave fields on isotropic and orthotropic plates. Calculations were carried out for a periodic ribbed plate which was treated as a flat plate with orthotropic material properties. This was used to illustrate the important features that were relevant to the predictions in chapters 5 and 6. In order to incorporate the orthotropic plate in SEA, eigenfrequencies of the orthotropic plates were needed to calculate the mode count and modal overlap. Concerning the prediction of eigenfrequencies on a periodic ribbed plate as an orthotropic plate, it was shown that the Rayleigh-Ritz method missed a significant

number of modes at high frequencies in comparison with FEM. For modal densities, approximated equations from both Lyon and Heckl give close estimations of the modal densities compared with the theory from Bosmans and Vermeir.

Chapter 4 used wave theory and Bloch theory to describe bending wave propagation on a periodic ribbed plate with symmetric ribs. This theory was then incorporated in chapter 5 to determine the SEA coupling loss factor for L-junctions which incorporate this type of periodic ribbed plate. Stop/pass band characteristics of different periodic ribbed plates were analyzed to indicate how these geometric parameters can significantly change the distribution of the propagation and attenuation zones. Chapter 4 also investigated the relations between the bounding frequencies of the stop/pass bands of the periodic ribbed plate and the natural frequencies of the periodic element of the ribbed plate. This analysis was performed in order to examine the validity of SEA and ASEA models in chapter 6 where each bay of the ribbed plate was treated as a single subsystem in SEA.

Chapter 5 contained the wave theory derivations used to calculate transmission coefficients that are needed for subsequent calculation of coupling loss factors for the SEA and ASEA models in chapters 6, 7 and 8. Two types of junction were considered: an L-junction and an in-line junction formed by the presence of a rib.

For an L-junction comprised of a homogeneous isotropic plate and a periodic ribbed plate, Tso and Hansen's model was found to generate numerical errors for certain geometrical arrangements of the ribs and bays. However, these errors do not occur with the periodic ribbed plates considered in chapters 6, 7 and 8.

Chapter 6 compared FEM, SEA and ASEA for L-junctions formed by a homogeneous isotropic plate and a periodic ribbed plate.

In the low-frequency range below the fundamental local mode of the bay on the ribbed plate, an important conclusion is that the periodic ribbed plate can be modelled as a single subsystem either using the wave approach from Tso and Hansen, or using orthotropic plate theory with the wave approach from Bosmans and Vermeir.

In the high-frequency range above the fundamental local mode of the bay it was shown that on the ribbed plate there is a significant decrease in energy along successive bays. Hence it is no longer appropriate to model the periodic plate as a single subsystem. For this reason it is not appropriate to use the wave approach from Tso and Hansen. Therefore SEA models were investigated that treated each bay as an individual subsystem using wave theory to model transmission across each rib. However, SEA was found to underestimate the response in each bay up to 25 dB. ESEA was then used to investigate this large discrepancy. ESEA indicated the existence of tunnelling between physically unconnected subsystems, which is not usually incorporated in SEA with plate subsystems. To incorporate this tunnelling mechanism, ASEA was used to track the energy flow across the plate system. In contrast to SEA, ASEA gave good agreement with FEM by reducing the discrepancies to less than 3 dB.

The main conclusion is that ASEA is able to successfully incorporate tunnelling for plate junctions that incorporate periodic ribbed plates and that ASEA provides a significantly more accurate predictive approach to vibration transmission across periodic ribbed plates than SEA.

In chapter 7, experimental work in the laboratory was used to quantify material properties and to measure vibration transmission on L-junctions of isotropic, homogeneous plates and periodic ribbed plates to validate SEA and ASEA models. A specially designed frame has been created to simulate simply-supported boundary conditions using metal pins along the edges of the plates. Close agreement between the driving-point mobility from measurements and an analytical model confirmed the effectiveness of the frame to provide a simply-supported boundary condition. The first L-junction under test was comprised of two isotropic homogeneous plates for which good agreement between measurements and FEM provided validation of the FEM model. The second junction under test comprised an isotropic homogeneous plate and a periodic ribbed plate. The measurements showed good agreement with both FEM and ASEA up to 10 kHz. Along with the findings from chapter 6 this confirmed that for L-junctions of isotropic and periodic ribbed plates above the fundamental mode of each bay, ASEA gives significantly better estimates of the energy levels in individual bays than SEA.

Chapter 8 extended the application of ASEA to more complicated built-up structures and also investigated the factors that would affect the performance of ASEA. In all the models presented in this chapter, ASEA has proved to be an effective method to predict the vibration transmission at high frequencies for built-up structures where tunnelling is involved.

For L-junctions comprised of an isotropic, homogeneous plate and a periodic ribbed plate, the geometric properties of the ribbed plate can significantly affect vibration transmission due to the distribution of the stop/pass bands. The transmission coefficient across the rib is highly variable depending on the angle of incidence and frequency resulting in a transmission coefficient with peaks and troughs. Hence in some cases, the assumption of specular reflection in ASEA will cause significant peaks or troughs in the ASEA prediction of energy response on the bays. However, FEM does not always predict these peaks or troughs to be in the same frequency band as ASEA and this may be attributed to the fact that specular reflection is not always an appropriate assumption.

The effect of internal loss factor on ASEA was also analyzed and the results indicated that ASEA works well with highly damped subsystems if ROTR excitation is used on the source subsystem. However, discrepancies between ASEA and FEM can occur with high damping for subsystems that are far away from the source subsystem.

For ribbed plates, the ribs cause the transmission coefficient between adjacent bays to have sharp peaks with high transmission at specific angles of incidence. For this reason, a nine-subsystem model of a folded plate formed by eight L-junctions was used to assess ASEA when there is a smooth variation of transmission coefficient with angle of incidence. The results showed good agreement between ASEA and FEM indicating that the use of ASEA is likely to be applicable to many other types of junction that connect long, narrow bays in a periodic array.

The effect of flanking transmission is investigated by adding a third plate to the L-junction that couples the isotropic plate and the periodic ribbed plate. For this structure where flanking transmission is introduced, ASEA is able to provide a significantly better prediction than SEA for the individual bays. It is found that

flanking via the third plate has a more significant effect on the subsystems that are far away from the source subsystem than the subsystems close to the source subsystem. Unlike the isolated L-junction where SEA tends to underestimate the energy levels on the subsystems, introducing flanking transmission in this structure caused SEA to significantly overestimate the energy level differences.

This thesis comprehensively discussed the applicability of different prediction models for structure-borne sound transmission in built-up structures including periodic ribbed plates at both low frequencies and high frequencies. When modelling periodic ribbed plate with classical SEA, large errors can occur due to a tunnelling mechanism at high frequencies which is not incorporated. Considering the four L-junctions analysed in chapters 6, 7 and 8 at frequencies where the mode count in the bay is greater than 5, SEA has been shown to be in error by up to 60 dB for the bay that is most distant from the junction, but this discrepancy can be reduced to less than 6 dB by using ASEA. Hence, the validity of ASEA has been confirmed by numerical and physical experiments and it can be concluded that ASEA is a robust and effective methods when tunnelling is involved.

9.2 Future work

The specific periodic ribbed plate considered in this thesis has ribs attached symmetrically on both sides of the plate in order to prevent the generation of in-plane wave in the plate. In reality, many engineering structures have stiffened ribs on only one side of the plate which allows in-plane waves to be generated. Hence, using ASEA on such periodic structures would be worth studying.

There is also potential in extending the work of Tso and Hansen as a low-frequency solution for L-junctions and also to T- and cross junctions comprised of either all periodic ribbed plates or in combination with isotropic homogeneous plates.

In this thesis the focus has been on treating the bays as subsystems because the relatively large bay areas are (a) more important for sound radiation and (b) more likely to be used to connect machinery/equipment either acting as a structure-borne sound source or as a vibration-sensitive receiver. However there is potential

to investigate the prediction of vibration on the ribs as these can also be used to connect machinery or equipment.

Further work could also investigate the application of ASEA to imperfectly periodic structures to assess the effect of Anderson localization on vibration transmission.

References

[1] I. Conn. *Acoustics and ship design*. Proceedings of International Symposium on Shipboard Acoustics, Noordwijkerhout, Netherlands (1976).

[2] F. P. Grad, A. J. Rosenthal, L. R. Rockett, J. A. Fay, J. Heywood, J. F. Kain, G. K. Ingram, D. Harrison Jr, T. Tietenberg. *Automobile and the regulation of its impact on the environment*., University of Oklahoma Press, Norman, USA (1975).

[3] M. S. Qatu, M. K. Abdelhamid, J. Pang, G. Sheng. *Overview of automotive noise and vibration.* International Journal of Vehicle Noise and Vibration (2009) **5**(1) 1-35.

[4] B. Rasmussen, J. H. Rindel. *Sound insulation between dwellings--Descriptors applied in building regulations in Europe*. Applied Acoustics (2010) **71**(3) 171-180.

[5] L. Brillouin. *Wave propagation in periodic structures*. Dover Publications Inc, New York, USA (1953).

[6] O. C. Zienkiewicz, R. L. Taylor, R. L. Taylor. *The finite element method for solid and structural mechanics*. Sixth Edition. Butterworth-Heinemann (2005) ISBN: 0-7506-6321-9.

[7] R. H. Lyon, R. G. DeJong. *Theory and application of Statistical Energy Analsysis*. Second Edition. Butterworth-Heinemann (1995) ISBN: 0-7506-9111-5.

[8] D. A. Bies, S. Hamid. *In situ determination of loss and coupling loss factors by the power injection method.* Journal of Sound and Vibration (1980) **70**(2) 187-204.

[9] C. Hopkins. *Statistical energy analysis of coupled plate systems with low modal density and low modal overlap.* Journal of Sound and Vibration (2002) **251**(2) 193-214.

[10] Y. K. Tso, C. H. Hansen. *The transmission of vibration through a coupled periodic structure.* Journal of Sound and Vibration (1998) **215**(1) 63-79.

[11] R. S. Langley. *A wave intensity technique for the analysis of high frequency vibrations.* Journal of Sound and Vibration (1992) **159**(3) 483-502.

[12] S. McWilliam, R. S. Langley. *Extreme values of first- and second-order wave-induced vessel motions.* Applied Ocean Research (1993) **15**(3) 169-181.

[13] B. R. Mace. *Statistical energy analysis: coupling loss factors, indirect coupling and system modes.* Journal of Sound and Vibration (2005) **279**(1-2) 141-170.

[14] M. Blakemore, J. Woodhouse, D. Hardie. *Statistical power-flow analysis of an imperfect ribbed cylinder.* Journal of Sound and Vibration (1999) **222**(5) 813-832.

[15] M. Blakemore, J. Woodhouse. *Power-flow analysis of quasi-one-dimensional systems with distributed coupling*. IUTAM Symposium on Statistical Energy Analysis, Kluwer Academic Publishers, London (1998), 163-174.

[16] K. H. Heron. *Advanced statistical energy analysis.* Philosophical Transactions of the Royal Society of London. Series A: Physical and Engineering Sciences (1994) **346**(1681) 501-510.

[17] F. J. Fahy. *Statistical energy analysis: a critical overview.* Philosophical Transactions of the Royal Society of London. Series A: Physical and Engineering Sciences (1994) **346**(1681) 431-447.

[18] R. G. D. Richard H. Lyon. *Theory and application of Statistical Energy Analsysis*. Second. Butterworth-Heinemann (1995).

[19] C. Hopkins. *Sound insulation*. Butterworth-Heinemann, Oxford, UK (2007) ISBN: 978-0-7506-6526-1.

[20] B. R. Mace. *Weak and strong coupling in statistical energy analysis: quantification and consequences*. Proceedings of 10th International Congress on Sound and Vibration (2003).

[21] R. S. Langley. *A general derivation of the statistical energy analysis equations for coupled dynamic systems.* Journal of Sound and Vibration (1989) **135**(3) 499-508.

[22] R. S. Langley. *A derivation of the coupling loss factors used in statistical energy analysis.* Journal of Sound and Vibration (1990) **141**(2) 207-219.

[23] F. J. Fahy, P. P. James. *A study of the kinetic energy impulse response as an indicator of the strengh of coupling between SEA subsystems.* Journal of Sound and Vibration (1996) **190**(3) 363-386.

[24] P. P. James, F. J. Fahy. *A technique for the assessment of strength of coupling between sea subsystems: experiments with two coupled plates and two coupled rooms.* Journal of Sound and Vibration (1997) **203**(2) 265-282.

[25] B. Mace. *Statistical energy analysis, energy distribution models and system modes.* Journal of Sound and Vibration (2003) **264**(2) 391-409.

[26] F. F. Yap, J. Woodhouse. *Investigation of damping effects on statistical energy analysis of coupled structures.* Journal of Sound and Vibration (1996) **197**(3) 351-371.

[27] B. Mace. *Statistical energy analysis, energy distribution models and system modes.* Journal of Sound and Vibration (2003) **264**(2) 391-409.

[28] B. R. Mace, P. J. Shorter. *Energy flow models from finite element analysis.* Journal of Sound and Vibration (2000) **233**(3) 369-389.

[29] L. Maxit, J. L. Guyader. *Extension of SEA model to subsystems with non-uniform modal energy distribution.* Journal of Sound and Vibration (2003) **265**(2) 337-358.

[30] R. Craik, J. A. Steel, D. I. Evans. *Statistical energy analysis of structure-borne sound transmission at low frequencies.* Journal of Sound and Vibration (1991) **144**(1) 95-107.

[31] C. Hopkins. *Statistical energy analysis of coupled plate systems with low modal density and low modal overlap.* Journal of Sound and Vibration (2002) **251**(2) 193-214.

[32] T. D. Scharton, R. H. Lyon. *Power flow and energy sharing in random vibration.* Journal of the Acoustical Society of America (1968) **43**(6) 1332-1343.

[33] B. R. Mace, J. Rosenberg. *The sea of two coupled plates: an investigation into the effects of subsystem irregularity.* Journal of Sound and Vibration (1998) **212**(3) 395-415.

[34] L. Cremer, M. Heckl, E. E. Ungar. *Structure-Borne Sound*. Second Edition. Springer-Verlag, Berlin, Germany (1988) ISBN: 0-3871-8241-1.

[35] B. L. Clarkson, R. J. Pope. *Experimental determination of modal densities and loss factors of flat plates and cylinders.* Journal of Sound and Vibration (1981) **77**(4) 535-549.

[36] W. Soedel. *Vibrations of shells and plates*. Third Edition. Dekker, New York, USA (2005) ISBN: 0-8247-5629-0.

[37] G. B. Warburton. *The vibration of rectangular plates.* Proceedings of the Institution of Mechanical Engineers (1954) **168**(1) 371-384.

[38] F. Fahy, J. Walker. *Advanced applications in acoustics, noise, and vibration*. Taylor & Francis (2004) ISBN: 0-4152-3729-7.

[39] A. W. Leissa. *The free vibration of rectangular plates.* Journal of Sound and Vibration (1973) **31**(3) 257-293.

[40] F. J. Fahy, A. D. Mohammed. *A study of uncertainty in applications of sea to coupled beam and plate systems, part I: Computational experiments.* Journal of Sound and Vibration (1992) **158**(1) 45-67.

[41] N. Lalor. *Practical considerations for the measurement of internal and coupling loss factors on complex structures*. ISVR Technical Report No. 182, University of Southampton (1990).

[42] D. A. Bies, S. Hamid. *In situ determination of loss and coupling loss factors by the power injection method.* Journal of Sound and Vibration (1980) **70**(2) 187-204.

[43] B. R. Mace. *On The Statistical Energy Analysis Hypothesis Of Coupling Power Proportionality And Some Implications Of Its Failure*. Journal of Sound and Vibration (1994) **178**(1) 95-112.

[44] B. L. Clarkson, M. F. Ranky. *On the measurement of the coupling loss factor of structural connections.* Journal of Sound and Vibration (1984) **94**(2) 249-261.

[45] J. Woodhouse. *An introduction to statistical energy analysis of structural vibration.* Applied Acoustics (1981) **14**(6) 455-469.

[46] C. H. Hodges, P. Nash, J. Woodhouse. *Measurement of coupling loss factors by matrix fitting: An investigation of numerical procedures.* Applied Acoustics (1987) **22**(1) 47-69.

[47] N. Lalor. *The practical implementation of SEA.* IUTAM Symposium on Statistical Energy Analysis. Springer (1999) 257-268.

[48] N. Lalor. *The measurement of SEA loss factors on a fully assembled structure*. ISVR Technical Memorandum No. 150, University of Southampton (1987).

[49] N. Lalor. *Experimental determination of vibrational energy balance in complex structures*. Society of Photo-Optical Instrumentation Engineers (SPIE) Conference Series (1989).

[50] P. G. Lat, N. Lalor. *The role and experimental determination of equivalent mass in complex SEA models.* Journal of Sound and Vibration (2002) **255**(1) 97-110.

[51] C. Hopkins. *Experimental statistical energy analysis of coupled plates with wave conversion at the junction.* Journal of Sound and Vibration (2009) **322**(1-2) 155-166.

[52] R. J. M. Craik. *The prediction of sound transmission through buildings using statistical energy analysis.* Journal of Sound and Vibration (1982) **82**(4) 505-516.

[53] G. Borello, L. Gagliardini. *Virtual SEA: towards an industrial process*. SAE Noise and Vibration Conference Proceedings (2007).

[54] M. P. Sheng, M. Q. Wang, J. C. Sun. *Effective internal loss factors and coupling loss factors for non-conservatively coupled systems.* Journal of Sound and Vibration (1998) **209**(4) 685-694.

[55] N. Lalor. *Practical considerations for the measurement of internal and coupling loss factors on complex structures*. ISVR Technical Report No. 182, University of Southampton (1990).

[56] J. J. Sakurai, S. F. Tuan. *Modern quantum mechanics*. Addison-Wesley California (1985) ISBN: 0-8053-7501-5.

[57] A. J. Price, M. J. Crocker. *Sound transmission through double panels using statistical energy analysis.* Journal of the Acoustical Society of America (1970) **47** 683.

[58] F. G. Leppington, E. G. Broadbent, K. H. Heron, S. M. Mead. *Resonant and non-resonant acoustic properties of elastic panels. I. The radiation problem.* Proceedings of the Royal Society of London. A. Mathematical and Physical Sciences (1986) **406**(1831) 139-171.

[59] F. G. Leppington, K. H. Heron, E. G. Broadbent, S. M. Mead. *Resonant and non-resonant acoustic properties of elastic panels. II. The transmission problem.* Proceedings of the Royal Society of London. A. Mathematical and Physical Sciences (1987) **412**(1843) 309-337.

[60] R. S. Langley. *The response of two-dimensional periodic structures to impulsive point loading.* Journal of Sound and Vibration (1997) **201**(2) 235-253.

[61] R. S. Langley, A. N. Bercin. *Wave intensity analysis of high frequency vibrations.* Philosophical Transactions of the Royal Society of London. Series A: Physical and Engineering Sciences (1994) **346**(1681) 489-499.

[62] J. M. Cuschieri, J. C. Sun. *Use of Statistical Energy Analysis for Rotating Machinery, Part II: Coupling Loss Factors Between Indirectly Coupled Substructures.* Journal of Sound and Vibration (1994) **170**(2) 191-201.

[63] C. R. Fredö. *A modification of the SEA equations: a proposal of how to model damped car body systems with SEA*. SAE Technical Paper, No. 2005-01-2436 (2005).

[64] K. H. Heron. *Advanced statistical energy analysis.* Philosophical Transactions of the Royal Society of London. Series A: Physical and Engineering Sciences (1994) **346**(1681) 501-510.

[65] H. Kuttruff. *Room Acoustics*. Fourth. Taylor & Francis Group, London (2000).

[66] R. Gunda, S. M. Vijayakar, R. Singh. *Method of images for the harmonic response of beams and rectangular plates.* Journal of Sound and Vibration (1995) **185**(5) 791-808.

[67] V. Cotoni, A. Le Bot. *Specular and diffuse reflections of rays in coupled thin plates at high frequencies.* Journal of Sound and Vibration (2003) **265**(1) 23-41.

[68] C. Simmons. *Structure-borne sound transmission through plate junctions and estimates of sea coupling loss factors using the finite element method.* Journal of Sound and Vibration (1991) **144**(2) 215-227.

[69] J. A. Steel, R. J. M. Craik. *Statistical energy analysis of structure-borne sound transmission by finite element methods.* Journal of Sound and Vibration (1994) **178**(4) 553-561.

[70] C. Hopkins. *Vibration transmission between coupled plates using finite element methods and statistical energy analysis. Part 1: Comparison of measured and predicted data for masonry walls with and without apertures.* Applied Acoustics (2003) **64**(10) 955-973.

[71] C. R. Fredö. *A SEA-like approach for the derivation of energy flow coefficients with a finite element model.* Journal of Sound and Vibration (1997) **199**(4) 645-666.

[72] H. Karlsson, S. Hibbitt. *ABAQUS/Standard: user's manual*. Hibbitt, Karlsson & Sorensen Inc., Pennsylvania State University (1998).

[73] C. E. Crede, C. M. Harris. *Shock and vibration handbook*. McGraw-Hill (1976) ISBN: 0-0702-6799-5.

[74] C. Hopkins. *Structure-borne sound transmission between coupled plates*. PhD thesis, Department of Building Engineering and Surveying, Heriot-Watt University, Edinburgh, UK (2000).

[75] S. Troitsky. *Stiffened plates: bending, stability, and vibrations*. Elsevier Scientific Pub. Co. (1976) ISBN: 978-0444415301.

[76] R. H. Lyon. *In-plane contribution to structural noise transmission.* Noise Control Engineering Journal (1986) **26**(1) 22-27.

[77] R. J. M. Craik, A. Thancanamootoo. *The importance of in-plane waves in sound transmission through buildings.* Applied Acoustics (1992) **37**(2) 85-109.

[78] S. Timoshenko, S. Woinowsky-Krieger, S. Woinowsky. *Theory of plates and shells*. McGraw-hill, New York, USA (1959).

[79] R. D. Mindlin. *Influence of rotatory inertia and shear on flexural motions of isotropic, elastic plates.* Journal of Applied Mechanics (1951) **18**(1) 31-38.

[80] G. Xie, D. J. Thompson, C. Jones. *Mode count and modal density of structural systems: relationships with boundary conditions.* Journal of Sound and Vibration (2004) **274**(3) 621-651.

[81] S. G. Lechnitsky. *Theory of elasticity for the anisotropic media*. Moscow (1951).

[82] S. G. Lekhnitskii. *Anisotropic plates*. DTIC Document (1968).

[83] G. Venkateswara Rao, K. Kanaka Raju, I. S. Raju. *Finite element formulation for the large amplitude free vibrations of beams and orthotropic circular plates.* Computers & Structures (1976) **6**(3) 169-172.

[84] L. R. Deobald, R. F. Gibson. *Determination of elastic constants of orthotropic plates by a modal analysis/Rayleigh-Ritz technique.* Journal of Sound and Vibration (1988) **124**(2) 269-283.

[85] R. D. Blevins. *Formulas for natural frequency and mode shape*. Van Nostrand Reinhold, NewYork, USA (1979) ISBN: 0-4422-0710-7.

[86] I. Bosmans, P. Mees, G. Vermeir. *Structure-borne sound transmission between thin orthotropic plates:analytical solutions.* Journal of Sound and Vibration (1996) **191**(1) 75-90.

[87] I. L. Bosmans. *Analytical modelling of structure-borne sound transmission and modal interaction at complex plate junctions*. PhD thesis, Katholieke Universiteit Leuven, Belgium (1998).

[88] S. M. Dickinson. *The buckling and frequency of flexural vibration of rectangular isotropic and orthotropic plates using Rayleigh's method.* Journal of Sound and Vibration (1978) **61**(1) 1-8.

[89] I. Bosmans, P. Mees, G. Vermeir. *Structure-borne transmission between thin orthotropic plates: analytical solutions*. Proceedings of the CIB-W51 Meeting, Warsaw, Poland (1994).

[90] M. Heckl. *Investigation on orthotropic plates (in German).* Acustica (1960) **10** 109-115.

[91] M. A. Heckl. *Investigations on the vibrations of grillages and other simple beam structures.* Journal of the Acoustical Society of America (1964) **36** 1335.

[92] M. L. Rumerman. *Vibration and wave propagation in ribbed plates.* Journal of the Acoustical Society of America (1975) **57** 370.

[93] D. J. Mead, E. G. Wilby. *The random vibrations of a multi-supported heavily damped beam.* The Shock and Vibration Bulletin (1966) **35**(3) 45-55.

[94] D. J. Mead. *Wave propagation in continuous periodic structures: Research contributions from Southampton, 1964-1995.* Journal of Sound and Vibration (1996) **190**(3) 495-524.

[95] B. L. Clarkson, D. J. Mead. *High frequency vibration of aircraft structures.* Journal of Sound and Vibration (1973) **28**(3) 487-504.

[96] R. S. Langley, J. Smith, F. J. Fahy. *Statistical energy analysis of periodically stiffened damped plate structures.* Journal of Sound and Vibration (1997) **208**(3) 407-426.

[97] S. S. Mester, H. Benaroya. *Periodic and near-periodic structures.* Shock and Vibration (1995) **2**(1) 69-95.

[98] T. R. Lin. *A study of modal characteristics and the control mechanism of finite periodic and irregular ribbed plates.* Journal of the Acoustical Society of America (2008) **123** 729.

[99] C. H. Hodges, J. Woodhouse. *Vibration isolation from irregularity in a nearly periodic structure: Theory and measurements.* Journal of the Acoustical Society of America (1983) **74** 894.

[100] S. P. Timoshenko, J. N. Goodier. *Theory of Elasticity*. McGraw-Hill, New York (1970) ISBN: 978-0070858053.

[101] G. S. Gupta. *Natural frequencies of periodic skin-stringer structures using a wave approach.* Journal of Sound and Vibration (1971) **16**(4) 567-580.

[102] D. J. Mead. *Wave propagation and natural modes in periodic systems: I. Mono-coupled systems.* Journal of Sound and Vibration (1975) **40**(1) 1-18.

[103] R. E. D. Bishop, D. C. Johnson. *The mechanics of vibration*. Cambridge University Press (1960).

[104] S. Azimi, J. F. Hamilton, W. Soedel. *The receptance method applied to the free vibration of continuous rectangular plates.* Journal of Sound and Vibration (1984) **93**(1) 9-29.

[105] A. W. Leissa. *The free vibration of rectangular plates.* Journal of Sound and Vibration (1973) **31**(3) 257-293.

[106] M. Heckl. *Wave Propagation on Beam-Plate System.* Journal of Acoustical Society of America (1961) **33**(5) 640-652.

[107] S. V. Budrin, A. S. Nikiforov. *Wave transmission through assorted plate joints.* Soviet Physics - Acoustics (1964) **9**(4) 333-336.

[108] R. H. Lyon, E. Eichler. *Random vibration of connected structures.* Journal of the Acoustical Society of America (1964) **36** 1344.

[109] T. Kihlman. *Transmission of Structure-borne Sound in Buildings: A Theoretical and Experimental Investigation*. National Swedish Institute for Building Research (1967).

[110] T. Kihlman. *Sound transmission in building structures of concrete.* Journal of Sound and Vibration (1970) **11**(4) 435-445.

[111] R. J. M. Craik. *Structure Transmission Through Buildings using Statistical Energy Analysis*. Gower, Hampshire (1996) ISBN: 0-5660-7872-5.

[112] G. Rosenhouse. *Acoustic wave propagation in bent thin-walled wave guides.* Journal of Sound and Vibration (1979) **67**(4) 469-486.

[113] R. S. Langley, K. H. Heron. *Elastic wave transmission through plate/beam junctions.* Journal of Sound and Vibration (1990) **143**(2) 241-253.

[114] I. Bosmans, G. Vermeir. *The use of semi-analytical calculation models to verify SEA predictions*. Proceedings of CIB Meeting, Paris, France (1998).

[115] W. Wöhle, T. Beckmann, H. Schreckenbach. *Coupling loss factors for statistical energy analysis of sound transmission at rectangular structural slab joints, part I.* Journal of Sound and Vibration (1981) **77**(3) 323-334.

[116] P. G. Craven, B. M. Gibbs. *Sound transmission and mode coupling at junctions of thin plates, part I: Representation of the problem.* Journal of Sound and Vibration (1981) **77**(3) 417-427.

[117] B. M. Gibbs, P. G. Craven. *Sound transmission and mode coupling at junctions of thin plates, part II: Parametric survey.* Journal of Sound and Vibration (1981) **77**(3) 429-435.

[118] I. T. Lu, H. L. Bertoni, H. Y. Chen. *Coupling of plate waves at joints.* Journal of the Acoustical Society of America (1992) **92** 510.

[119] J. A. Steel. *Sound transmission between plates in framed structures.* Journal of Sound and Vibration (1994) **178**(3) 379-394.

[120] R. J. M. Craik, R. Wilson. *Sound transmission through parallel plates coupled along a line.* Applied Acoustics (1996) **49**(4) 353-372.

[121] L. Cremer. *The propagation of structure-borne sound*. Department of Scientific and Industrial Research (1952).

[122] R. M. Grice, R. J. Pinnington. *A method for the vibration analysis of built-up structures, Part I: Introduction and analytical analysis of the plate-stiffened beam.* Journal of Sound and Vibration (2000) **230**(4) 825-849.

[123] I. Bosmans, P. Mees, G. Vermeir. *Structure-borne sound transmission between thin orthotropic plates: analytical solutions.* Journal of Sound and Vibration (1996) **191**(1) 75-90.

[124] G. Puri. *Python Scripts for Abaqus (preview version)*. Dassault Systèmes Simulia Corporation, http://www.abaquspython.com/ (2011) ISBN: 978-0-615-52050-6.

[125] M. R. Spiegel. *Schaum's outline of theory and problems of advanced mathematics for engineers and scientists*. Schaum's Outline Series (1971) ISBN: 0-0706-0216-6.

[126] M. Villot, I. Bosmans. *Modeling and characterizing flanking transmissions in lightweight considerations*. Proceedings of INTER-NOISE and NOISE-CON Congress and Conference, Dearborn, Michigan, USA (2002), 946-953.

[127] ISO/PAS 16940:2004 Glass in building-Glazing and airborne sound insulation-Measurement of the mechanical impedence of laminated glass. International Organization for Standardization. (2004).

[128] A. Kumar, T. Jayakumar, B. Raj, K. K. Ray. *Correlation between ultrasonic shear wave velocity and Poisson's ratio for isotropic solid materials.* Acta Materialia (2003) **51**(8) 2417-2426.

[129] ISO 3382. Acoustics--Measurement of the reverberation time of rooms with reference to other acoustical parameters. International Organization for Standardization. (1997).

[130] M. R. Schroeder. *New method of measuring reverberation time.* Journal of the Acoustical Society of America (1965) **37** 409.

[131] R. B. Randall. *Frequency analysis*. Third Edition. Bruel & Kjaer (1987) ISBN: 978-8787355070.

[132] F. Jacobsen. *A note on acoustic decay measurements.* Journal of Sound and Vibration (1987) **115**(1) 163-170.

[133] J. M ńguez. *An experimental investigation of how accurate, simply supported boundary conditions can be achieved in compression testing of panels*. (1986).

[134] L. Leniowska. *Active vibration control of the circular plate with simply-supported boundary condition.* Molecular and Quantum Acoustics Journal (2003) **24** 109-124.

[135] J. M ńguez. *An experimental investigation of how accurate, simply supported boundary conditions can be achieved in compression testing of panels.* Experimental Mechanics (1986) **26** 238-244.

[136] R. Wilson. *Plate mounting for simply-supported boundaries*. Personal communication to C. Hopkins (1996).

[137] O. Lacour, M. A. Galland, D. Thenail. *Preliminary experiments on noise reduction in cavities using active impedance changes.* Journal of Sound and Vibration (2000) **230**(1) 69-99.

[138] A. Putra, D. J. Thompson. *Sound radiation from perforated plates.* Journal of Sound and Vibration (2010) **329**(20) 4227-4250.

[139] J. P. Maillard, C. R. Fuller. *Advanced time domain wave-number sensing for structural acoustic systems. Part III. Experiments on active broadband radiation control of a simply supported plate.* The Journal of the Acoustical Society of America (1995) **98** 2613.

[140] C. Chatfield. *Statistics for technology: a course in applied statistics*. Third Edition. Chapman & Hall (1983) ISBN: 0-4122-5340-2.